A Study and Optimization of a Radial Ball Piston Pump for High-Speed Applications

A THESIS

SUBMITTED TO THE FACULTY OF THE

UNIVERSITY OF MINNESOTA

BY

Garrett Bohach

IN PARTIAL FULFILLMENT OF THE REQUIREMENTS

FOR THE DEGREE OF

Master of Science

Dr. James D. Van de Ven

January 2021

© Garrett Bohach 2020
ALL RIGHTS RESERVED

Acknowledgements

"This material is based upon work supported by the U.S. Department of Energy's Office of Energy Efficiency and Renewable Energy (EERE) under the Award Number DE-EE0008384."

Disclaimer: "This report was prepared as an account of work sponsored by an agency of the United States Government. Neither the United States Government nor any agency thereof, nor any of their employees, makes any warranty, express or implied, or assumes any legal liability or responsibility for the accuracy, completeness, or usefulness of any information, apparatus, product, or process disclosed, or represents that its use would not infringe privately owned rights. Reference herein to any specific commercial product, process, or service by trade name, trademark, manufacturer, or otherwise does not necessarily constitute or imply its endorsement, recommendation, or favoring by the United States Government or any agency thereof. The views and opinions of authors expressed herein do not necessarily state or reflect those of the United States Government or any agency thereof."

Dedication

This work is dedicated to my wife Kennidee. Her unwavering confidence, incredible patience, and constant support motivated me to pursue my dreams. Her love and steadfast dedication was the foundation that made this work possible.

Abstract

Ever increasing concern and regulations related to climate change has prompted hydraulic research to focus on improving energy efficiency and reducing emissions, with electrifying hydraulic systems considered a promising solution. This thesis studies the radial ball piston hydraulic architecture, and its capability to efficiently and compactly be integrated with a high-speed electric motor. A combination of analytical, numerical, and empirical models are utilized to create a detailed model of a radial ball piston unit and its losses. The model is experimentally validated using an off-the-shelf radial ball piston pump. After updating the model parameters, the model predicted the efficiency within 3-10 percent across the range of operating conditions. The model is then implementing within a genetic algorithm optimization framework that predicts performance across multiple operating conditions. The preferred embodiment discovered by the optimization reached 12,500 rpm while maintaining 80 – 90 percent efficiency across four quadrants of operation and packaged a 20kW machine within approximately 100mm outside diameter. The work within this thesis represents the first computationally fast and accurate model of a radial ball piston unit that was utilized within an optimization framework for design purposes. The results of this optimization demonstrate that the radial ball piston is an acceptable hydraulic architecture for four quadrant operation and integration with a high-speed electrical motor. However, a challenge with the architecture is that the ball piston kinematics generate an uneven clearance around the ball that results in a nearly constant torque loss independent of piston-cylinder clearance, creating an upper bound on the efficiency.

Contents

List of Tables

List of Figures

1 Introduction

1.1 Background

Electrification has been an area of increasing interest within the transportation sector, from the production of all electric on-highway vehicles to the concept of more electric aircraft. The ever growing concern about global warming has made electrification and zero emissions a goal of the next several decades [1]. Regulations have already been put in place to limit emissions within cities and more stringent guidelines will be going into effect on large engine vehicles creating a challenge for construction and other large off-highway equipment. Today, many off-highway vehicles utilize hydraulics due to their impressive power and force density. Unfortunately, hydraulics are almost exclusively powered by a combustion engine because liquid fuels are the only practical energy storage available today for high power machines that operate for long periods of time. Current battery technology does not have the energy density to feasibly power these applications.

This thesis presents a promising step towards integrating hydraulic and electrical systems. The proposed architecture uses both an internal combustion engine (ICE) and electrical motors/generators to create a hybrid hydraulic power system. The Hybrid Hydraulic-Electric Architecture or HHEA was formally proposed by Li et al. [2] as a method to improve the efficiency of hydraulic systems by utilizing electrically powered control units for energy boosting and regeneration, see Figure 1.1. The foundation of the HHEA architecture is the elevated hydraulic pressure rails. These rails are pressurized using an ICE attached to a main pump and is very similar to the STEAM architecture [3]. Each pressure rail is set to distinct pressure and includes an accumulator to smooth out pressure variation that could occur during operation.

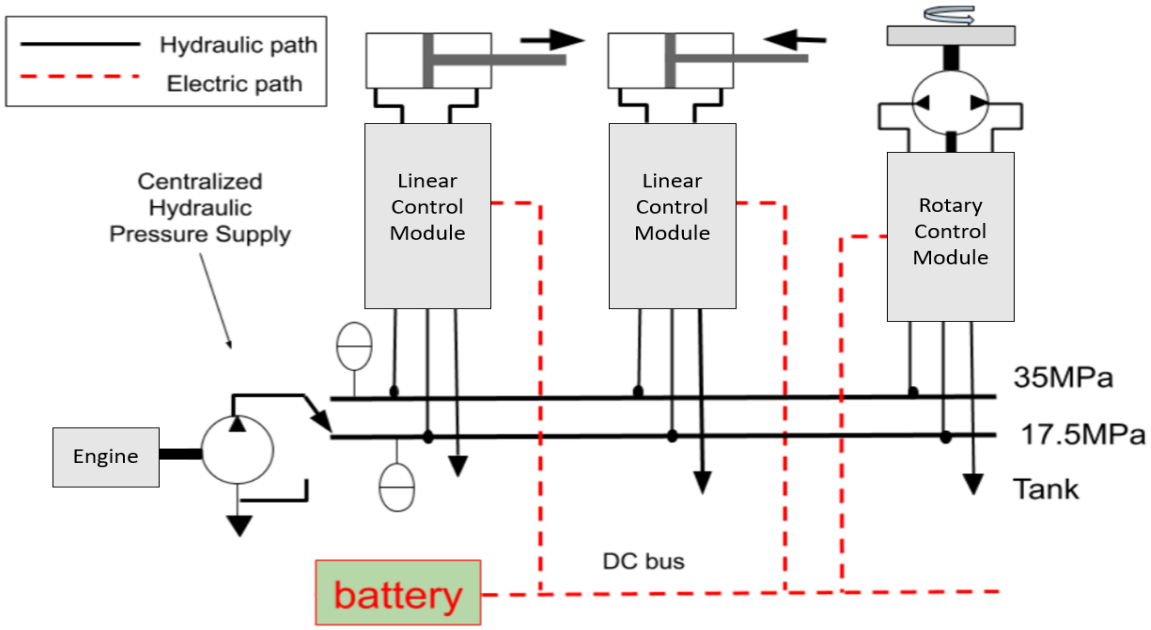

FIGURE 1.1: HHEA GENERAL SYSTEM LEVEL ARCHITECTURE [4]

The difference between the STEAM and HHEA architecture is the method of actuator control. STEAM utilizes traditional throttling valves while the HHEA uses hydraulic-electric control modules (HECM) [3]. An HECM is a hydraulic pump/motor that is coupled to an electric motor/generator; this researched focused on directly integrating the components instead of using a shaft connection. Actuator control is achieved by adjusting the speed of the electric motor which varies the flow rate created by the hydraulic pump/motor [2, 4].

The proposed integration of the electric motor and hydraulic pump is different from the modular approach typically used to shaft couple the two machines, as is done in Electro-Hydraulic Actuators (EHAs). Removing the shaft reduces the number of components (no shaft, no duplicate bearings, no seal, etc.) and allows direct oil cooling of the electric machine. This direct cooling allows the current density of the electric machine to increase which increases the power density of the electrical system. This, along with the direct coupling, increases the power density of the unit when compared to an equivalent shaft coupled machine. The final method for maximizing the power density is increasing the rotation speed of the integrated unit which reduces the required displacement [2, 5].

A high power density is a primary goal of the HECM architecture because of its proposed application to mobile hydraulics. Consider an excavator, the boom, stick, and bucket are three actuators that require precise control. To achieve this, the HECM should be as close as possible to

the actuators to avoid unwanted line and system dynamics, thus improving the controllability. The boom, stick, and bucket actuators are often at a distance far from the center of rotation making any mass added at their location greatly impact the rotational inertia of the system. The more compact the HECM system, the closer the unit can physically be to the actuator it is controlling, while minimizing any unwanted effects.

Another goal of the integration is efficiency. The pressure rails limit the pressure differential across the pump to a small portion of the actuator pressure. For the hydraulic machine, the reduced pressure differential limits losses associated with leakage. For the electrical machine, the low pressure differential and high rotational speed results in a low torque requirement. Lowering the torque reduces current based losses and limits the chance of overheating; two valuable features when designing electrical machines [2].

The push to increase power density and efficiency are two of the design criteria that drive the architecture decision for the pump of the HECM. Some other design criteria include: four quadrant operation, direct integration, and the potential to reach high speeds. A radial ball piston design was the chosen embodiment [5][1]. As shown in Figure 1.2, this pump/motor is a radial piston architecture, but balls are used instead of cylindrical pistons. The balls translate within the cylinder to perform the pumping and suction strokes and roll on the cam to keep the friction low at that surface. The architecture is an inside impinged pump/motor that uses a pintle to set the valve timing [6]. The rolling balls reduce the losses at the cam, especially compared with hydrodynamic bearings at high speed. A roller-follower could be attached to a cylindrical piston but using a ball piston decreases the radial size, creating a more compact unit. One of the concerns of the radial ball piston pump is the sealing between the ball and the cylinder. The clearance seal between the ball and cylinder is a line contact which can result in significant leakage. However, as mentioned before, the pressure rails of the HHEA architecture reduce the pressure differential and the subsequent leakage.

[1] Appendix A shares the process and the results that led to selecting the radial ball piston architecture.

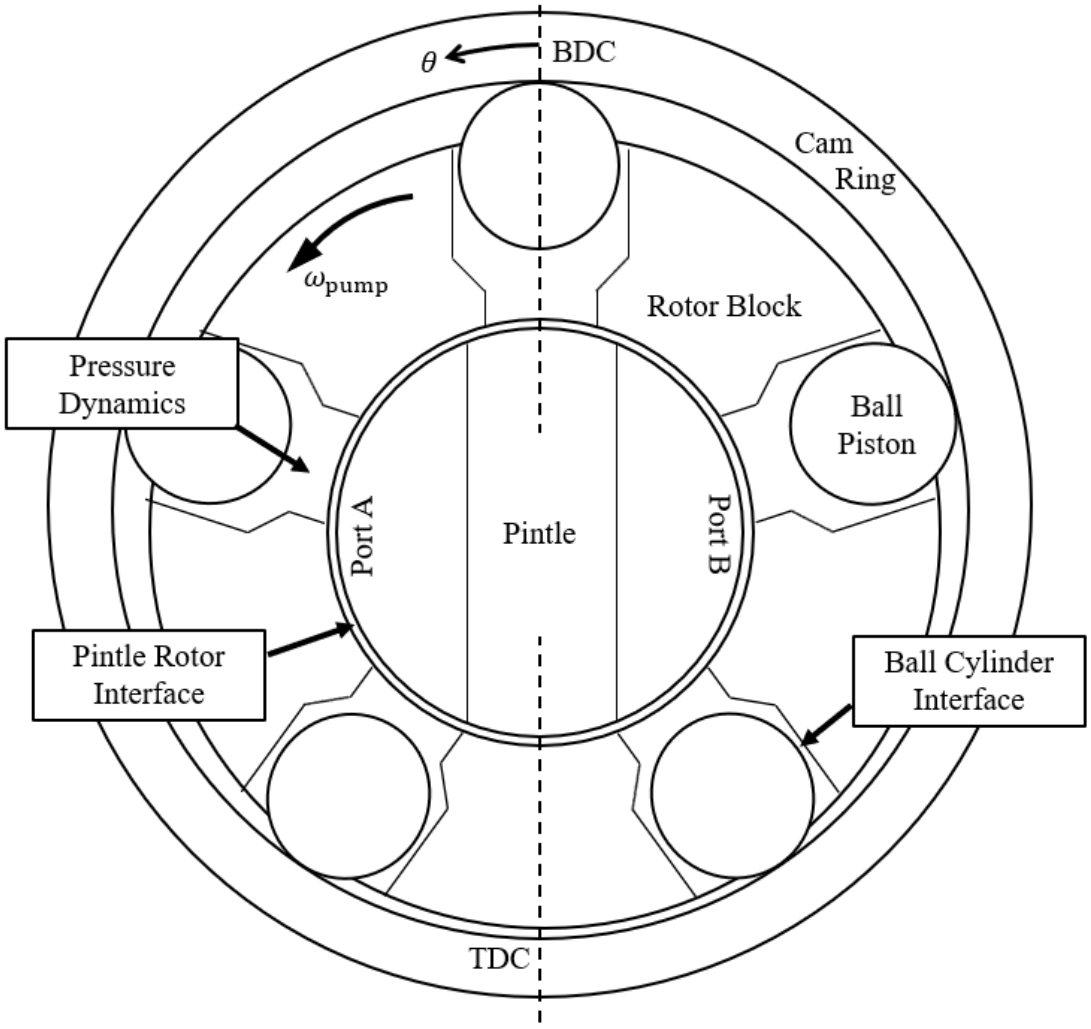

FIGURE 1.2: RADIAL BALL PISTON ARCHITECTURE

The radial ball piston pump is driven by an axial flux permanent magnet electric motor. The axial flux architecture was selected over the more common radial flux design because of the complementary scaling with the radial ball piston. The radial ball piston pump grows predominately in the radial direction and scales almost equivalently to the axial flux design. Radial flux electric machines optimally grow more axially when compared to their axial flux design counterparts. This difference in scaling allowed the axial flux design to offer superior packaging, reducing mass and rotational inertia [7].

The radial ball piston unit and axial flux permanent magnet machine are integrated through the rotating features. A cross section of the HECM is shown in Figure 1.3. The electric machine is a single-stator single-rotor design that uses permanent magnets. Typically, the permanent magnet

rotor (PM rotor) is integrated with the hydraulic rotor block. The rotor block is supported by the pintle and bearings. A pintle is stationary shaft which includes fluid lines and ports to the hydraulic cylinders. There are several design considerations when integrating the two systems. The hydraulic unit must fit within the electric machine stator, the bearings support the radial load from the hydraulic unit and an axial load from the single rotor electric machine, and the air gap (space between magnets and stator) needs to be held within a tight tolerance. Another major feature to design is the oil cooling paths from the hydraulic unit through the electric machine [8].

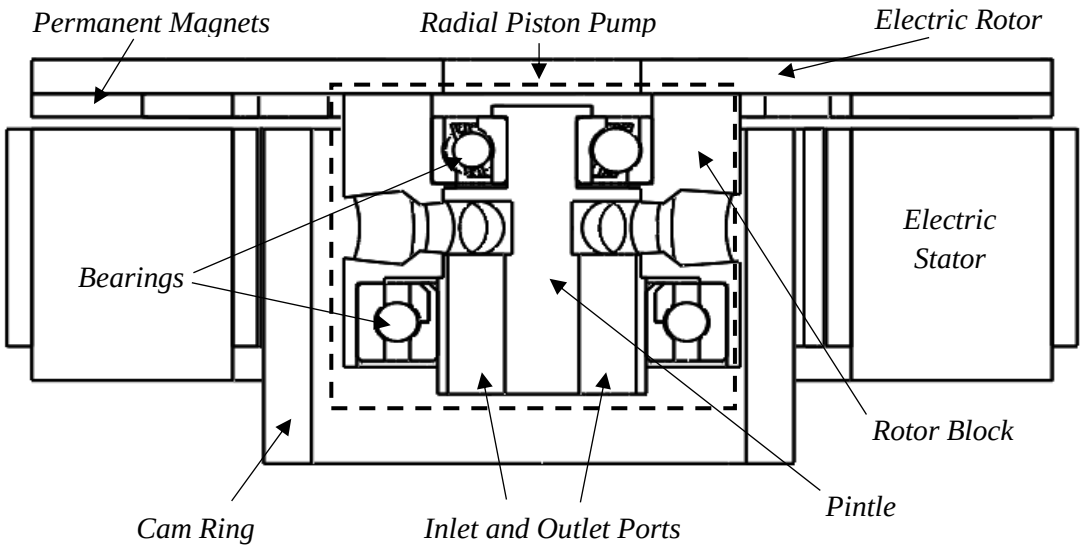

FIGURE 1.3: HECM CROSS SECTION SHOWING THE INTEGRATED ELECTRIC MOTOR AND HYDRAULIC PUMP[2]

1.2 Literature Review

The work presented in this thesis extends previous efforts for directly integrating hydraulic pumps with electric motors. While this technology and electro-hydraulic actuators (EHAs) have a common application, coupling electric motors and hydraulic pumps, EHAs have not seen a significant thrust towards component integration. Instead, direct integration is currently pursued by academic researchers and niche industry applications that focus on developing a more efficient hybridization of hydraulic and electrical systems. The other field that this thesis contributes to is

[2] Figure created by Md Minal Nahin

the modeling of radial ball piston pumps/motors. This architecture is not new to the hydraulic community, with Eaton having a radial ball piston pump in the market since the 80s [9, 10]. However, the architecture is less common in applications than radial cylindrical piston, axial piston, and gear pumps. This also means that there has been limited research done on the radial ball piston architecture. Lastly, this thesis is concerned with the performance of high speed hydraulic machines, which is dominated by EHAs for aerospace. The techniques that aerospace has used to overcome the challenges of reaching high speeds are a useful guide when designing the HECM hydraulic unit. This literature review will examine the current state of electrical motor and hydraulic pump direct integration, radial ball piston modeling, and high speed hydraulic units.

1.2.1 Electric-Hydraulic Integration

The direct integration of hydraulic and electrical machines is currently being pursued by companies and academic institutions. The push towards electrification and the complimentary benefits of hydraulic and electrical systems has made their integration an attractive possibility. Research is still active regarding the best hydraulic architecture (gear pump, piston pump, vane pump, etc.) and application for the integrated system. It is likely that several different applications will benefit from the direct integration of electro-hydraulic machines and each of these may require different component architectures.

Kerstech is a company that is focused on hybridizing the drive trains of electric vehicles that have frequent stop and start events. The targeted applications include city buses, forklifts, and refuse trucks. The general concept is to utilize the electric machine for high speed events and the hydraulic system for low speed events. This allows the electric machine to operate where it is most efficient, high speed and low torque, and the hydraulics to do the same, low speed and high torque. According to KersTech's website, "This preserves battery energy to extend driving range by up to 45%, depending on the vehicle's drive cycle, or enables the use of smaller batteries for equivalent range [Kerstech][11]." The company also highlights that the longevity of the battery is improved when hydraulics handle high torque events, reducing maintenance costs. This principle of using hydraulics and electrics while each are in their most efficient operating regime is shown in Figure 1.4. The integrated hydraulic-electric machine is Kerstech's patented TwinTorq motor. An example of the TwinTorq behavior applied to a city bus is shown in Figure 1.5 [12].

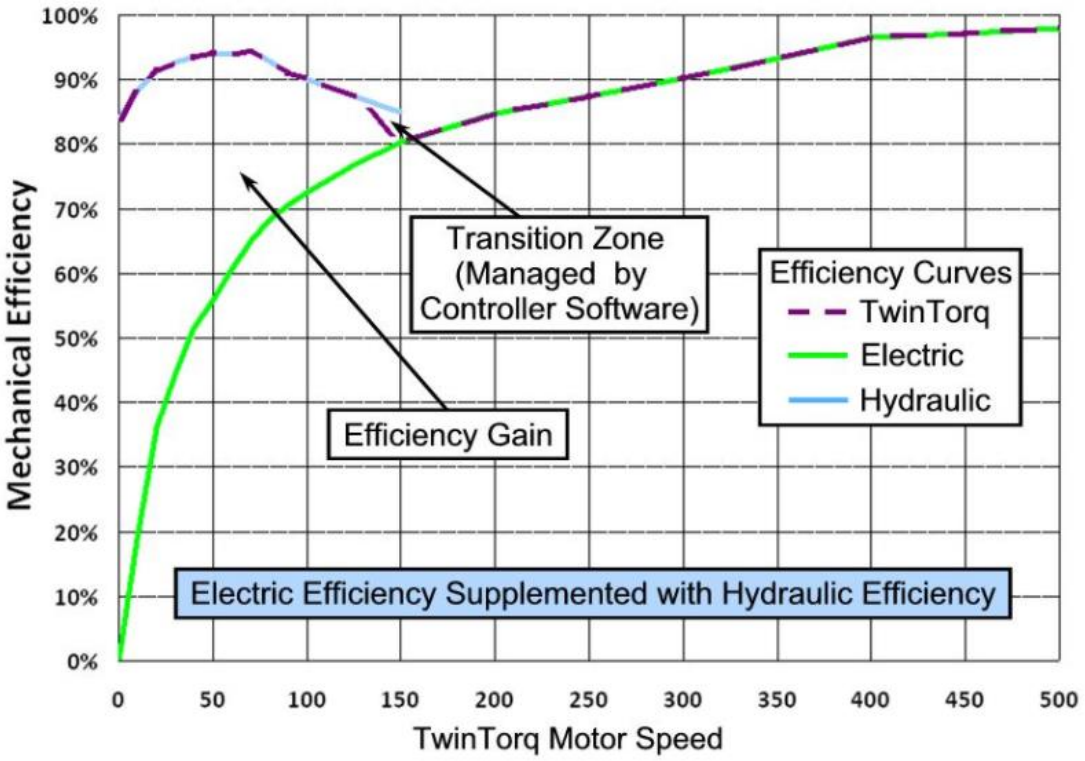

FIGURE 1.4: KERSTECH TWINTORQ EFFICIENCY CURVE [13]

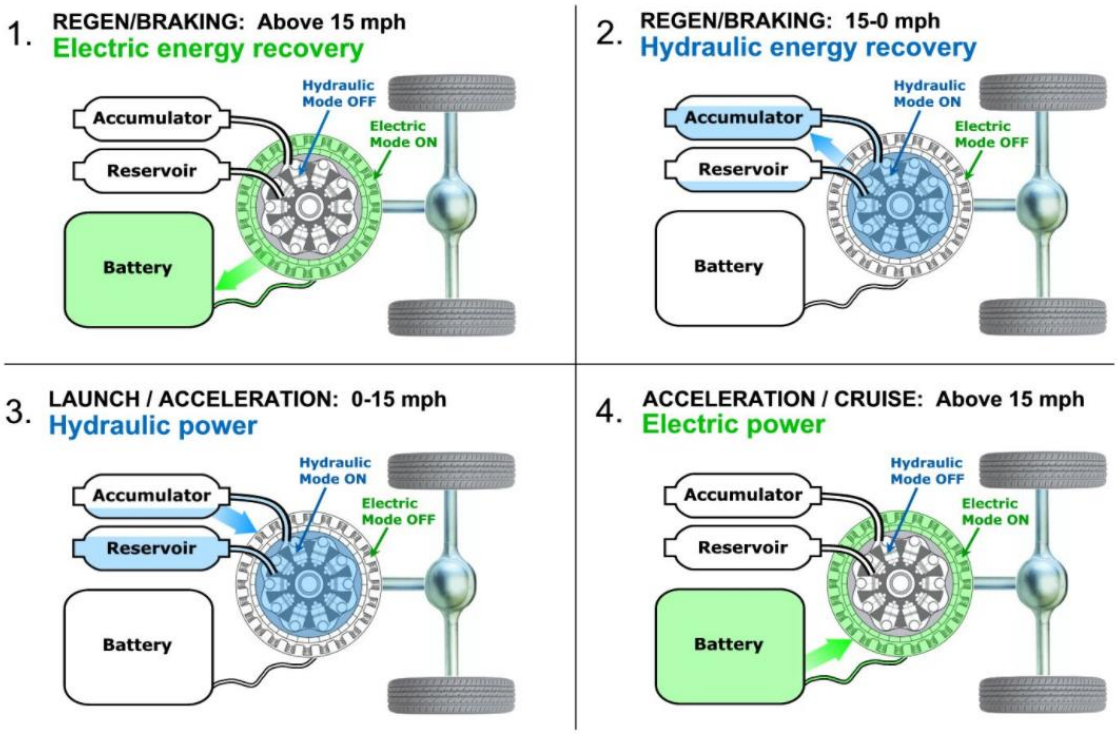

FIGURE 1.5: EXAMPLE TWINTORQ OPERATION [13]

The TwinTorq motor is a highly integrated system with minimal footprint which is important because Kerstech is marketing the product for mobile applications. The other benefit of the compact TwinTorq design is that the architecture is axially short, like a pancake, creating a low center of gravity, which is another important feature for mobile drivetrains. The system uses an electric ring motor with a multilobe radial piston pump. This allows for a highly integrated design as shown in Figure 1.6, with a legend for the numerical labels provided in Table 1.1. The TwinTorq motor is designed to be an all-in-one motor and generator for drivetrains that seamlessly switches between utilizing hydraulic and electrical power to drive the mechanical drive train [12].

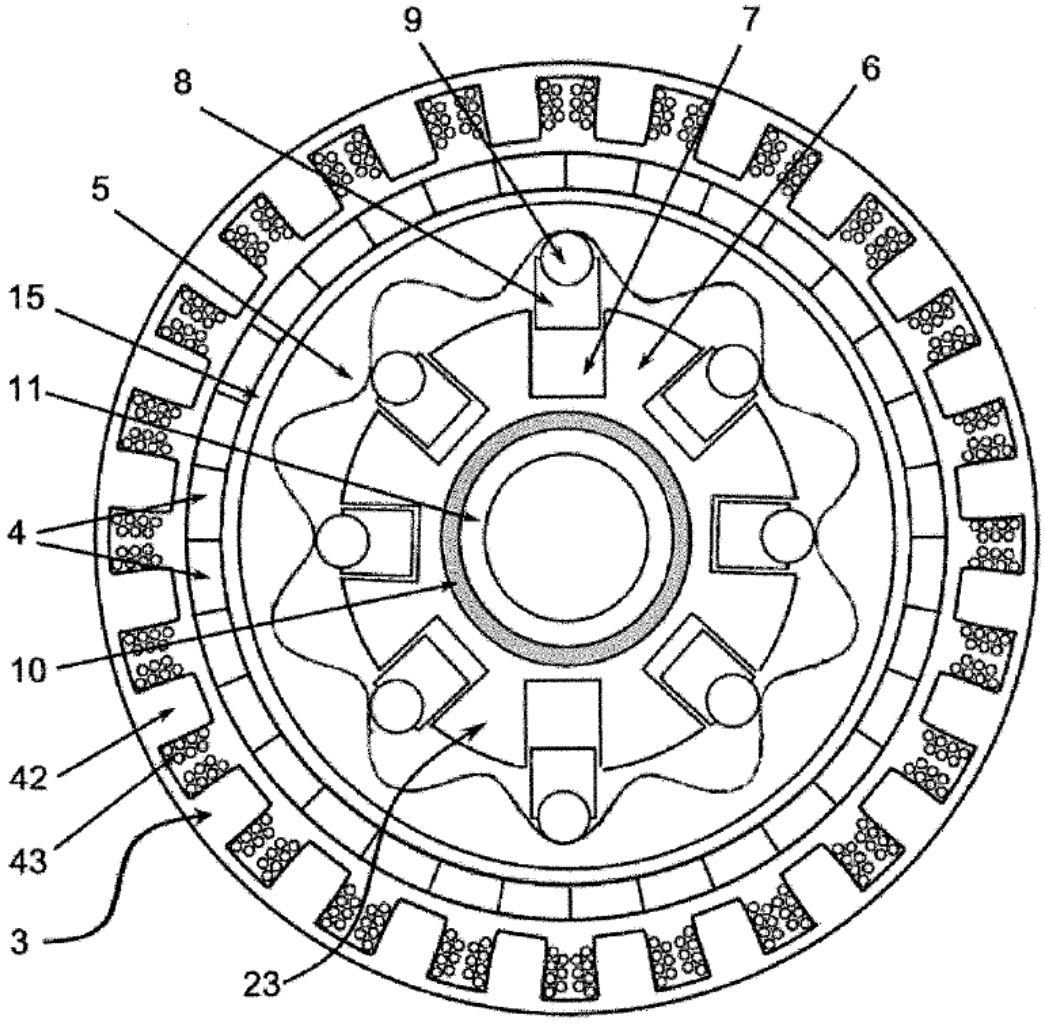

FIGURE 1.6: TWINTORQ MOTOR PLANE CROSS SECTION [12]

TABLE 1.1: TWINTORQ PATENT LABELS [12]

Number in Drawing	Name	Number in Drawing	Name
1	Stator Structure	10	Bearings
2	Rotor Structure	11	Motor Shaft
3	Stator Assembly	15	Back Iron Ring
4	Permanent Magnets	21	Stator Assembly
5	Cam Ring	22	Rotor Assembly
6	Hydraulic Motor Hub	23	Hydraulic Motor Hub Assembly
7	Cylinders	42	Stator Core
8	Pistons	43	Coil Windings
9	Roller		

Voith, a multinational company from Germany, also has an integrated hydraulic-electric product. Their EPAI takes an internal gear pump and places it inside an asynchronous electrical motor, as shown in Figure 1.7 [14]. The application for the unit is less specific than the TwinTorq motor since the EPAI is a hydraulic power unit which is designed to generate hydraulic power for use in other applications.

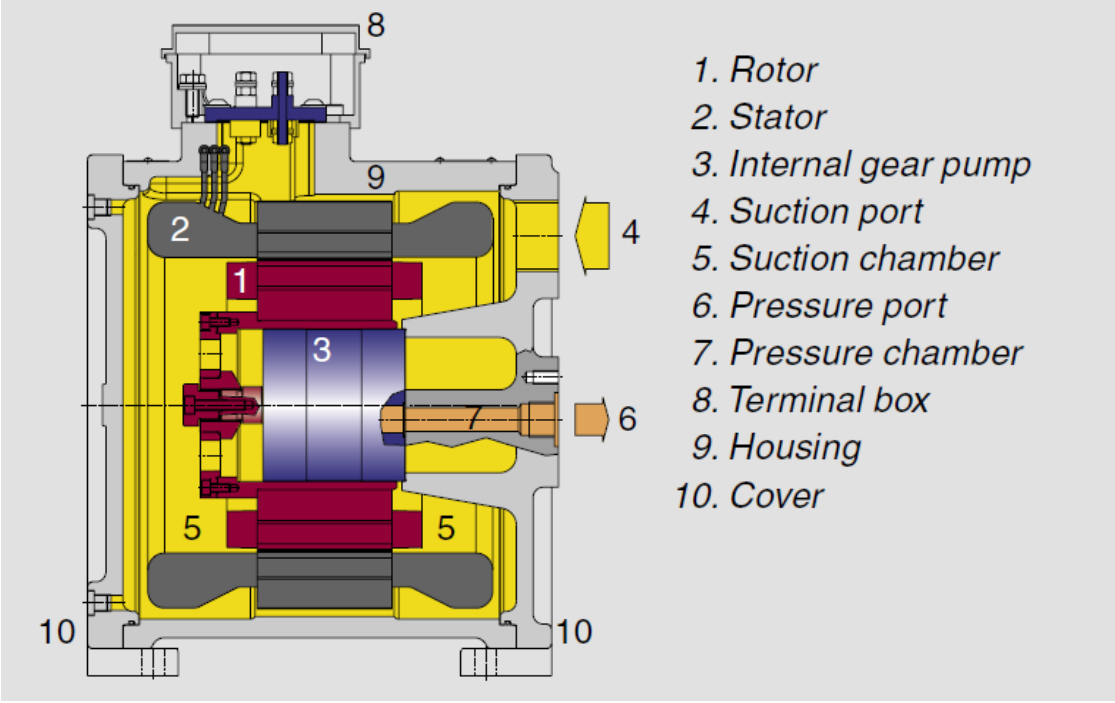

FIGURE 1.7: VOITH EPAI INTEGRATED HYDRAULIC PUMP AND ELECTRIC MOTOR [14]

One aspect of the Voith design that takes advantage of the integrated system is that the case surrounding the motor and hydraulic pump is used as the low pressure port. Oil enters at location 4 in the figure, which floods the case and cools the electrical system before being drawn into the pump. Voith also mentions several other benefits of the integrated design. The biggest advantage is the compactness of the unit which can be half the size of a conventional setup. This size improvement is partly because no mechanical shaft is required to transmit the force from the electric machine to the hydraulic one. Removing the shaft creates a design that does not have dynamic seals which decreases leakage to the unit's surroundings. The integrated unit also produces low noise levels that are significantly less than conventional electric motor/hydraulic pump systems. Voith also claims the service life expectancy is improved because of the reduction of wear parts [14].

The advantages mentioned by Voith are also quoted in research done by Gamez-Montero et al. on the GeroMAG concept. The GeroMag was conceived as a solution to increasingly stringent environmental standards which desire hydraulic systems with reduced noise and no leakage. Therefore, Gamez-Montero et al. directly integrated a gerotor hydraulic pump within an electric motor to remove the shaft and dynamic seal. The pump was designed to work as a variable flow device for low rotational speeds [15].

The architecture is shown below in Figure 1.8. The concept allows for a compact package, but early prototype efforts did not demonstrate efficient performance. The authors stated that their primary goal was to produce good volumetric efficiency which was demonstrated at higher speeds. Unfortunately, the mechanical efficiency suffered because the tight clearances required to limit leakage increased friction losses. Overall, the authors showed that directly integrating hydraulics and electrics could be done and reducing noise levels and external leakage was possible [15].

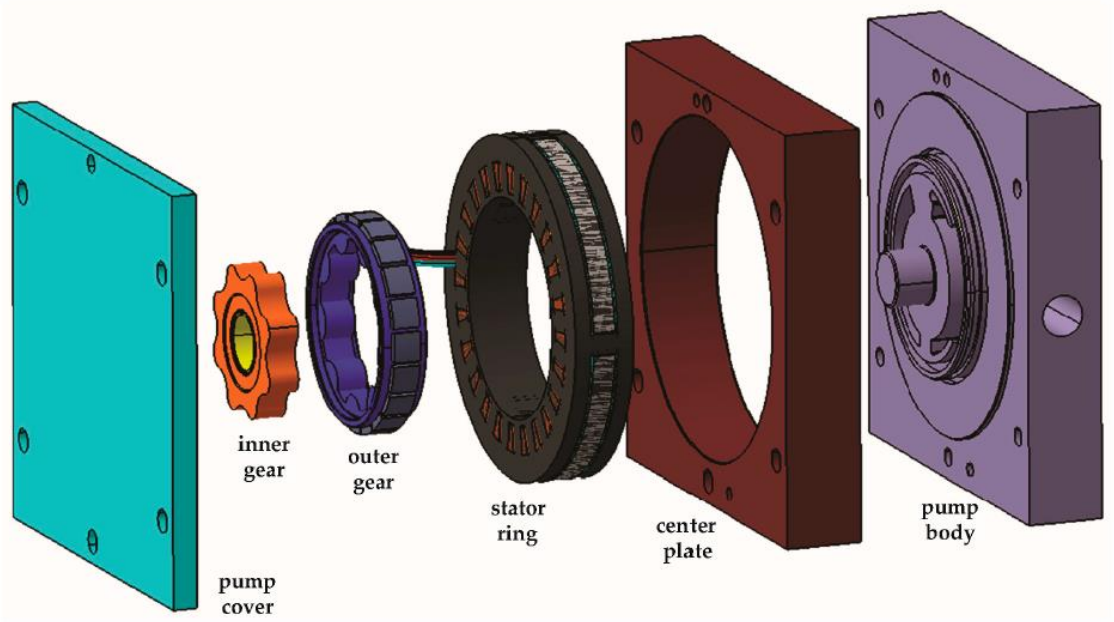

FIGURE 1.8: GEROMAG EXPLODED CAD VIEW [15]

Another group that studied electric hydraulic integration was from the University of Wroclaw. Their proposed application was similar to the HECM; it involved a fixed displacement hydraulic pump integrated with an electric motor to perform actuator control. However, demonstrating acceptable dynamic performance using electric motor speed control was the only goal of the group. Their solution was a double-acting vane pump that was integrated inside a brushless direct current (BLDC) electric motor that operated in a single quadrant (hydraulic pump that rotates in one direction) [16]. Considering the design in Figure 1.9, there are several O-ring seals (the black squares in the left cross section) used to prevent the fluid from leaving the hydraulic chamber and reaching the electric machine. This contrasts with the Voith group that used the oil to cool the electric machine. It is known that oil cooling is more effective than air cooling for electric machines and that higher power densities can be achieved by using a direct oil cooling method. The group also did not push the rotational speed of the system and stayed below 3,500 rpm. Despite not utilizing these possible advantages, the University of Wroclaw still found their design to be 40 percent more compact than the conventional system. The researchers also concluded that the variable speed drive achieve satisfactory dynamic performance [16].

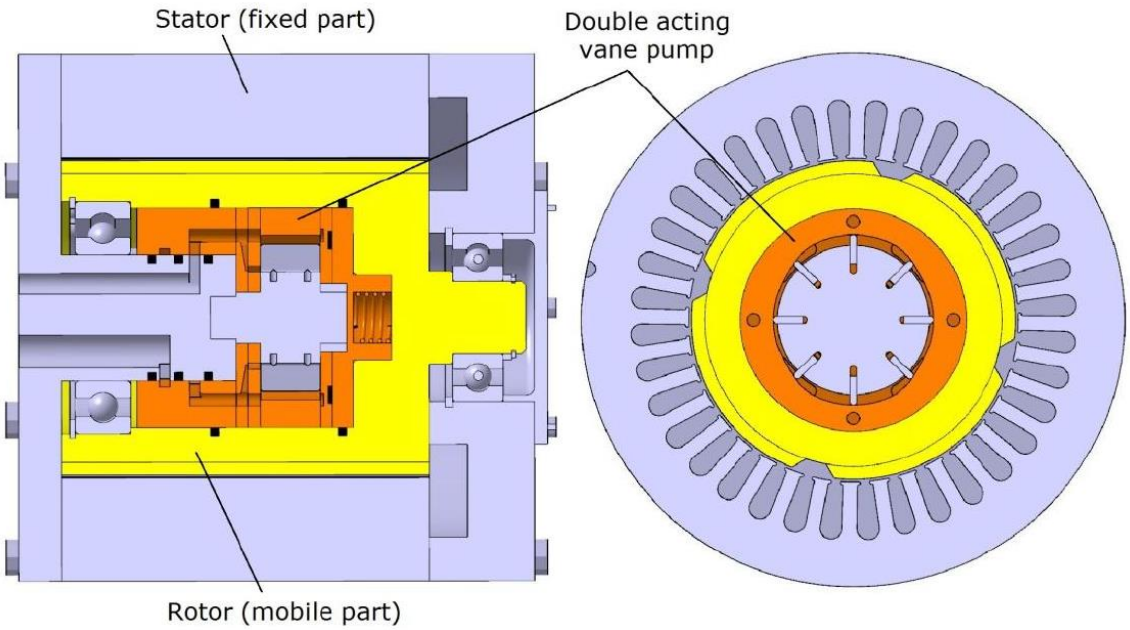

FIGURE 1.9: DOUBLE VANE PUMP INTEGRATED WITHIN BLDC ELECTRIC MOTOR [16]

The topologies discussed thus far have been rotary machines. Research has also been conducted looking at the feasibility of linear electric-hydraulic machines like the one shown in Figure 1.10. The linear machine was found to be the preferred architecture for low power (fractional kW) hydraulic pumping applications due to poor efficiency and power density of the rotary counterpart at that power level [17, 18]. To achieve high power density and electrical efficiency, the linear machines prefer to operate at frequencies up to 300 Hz [17]. The main challenge when trying to achieve these high frequencies is getting enough hydraulic fluid into the pumping chambers; often, specially design check valves are required [17, 19]. Another design technique that is used to improve efficiency is the addition of mechanical springs to allow energy recovery and improve performance. Research thus far has experimentally validated system efficiencies at 80 percent and optimizations have shown the potential for 85 percent overall efficiency [17], [19 – 21].

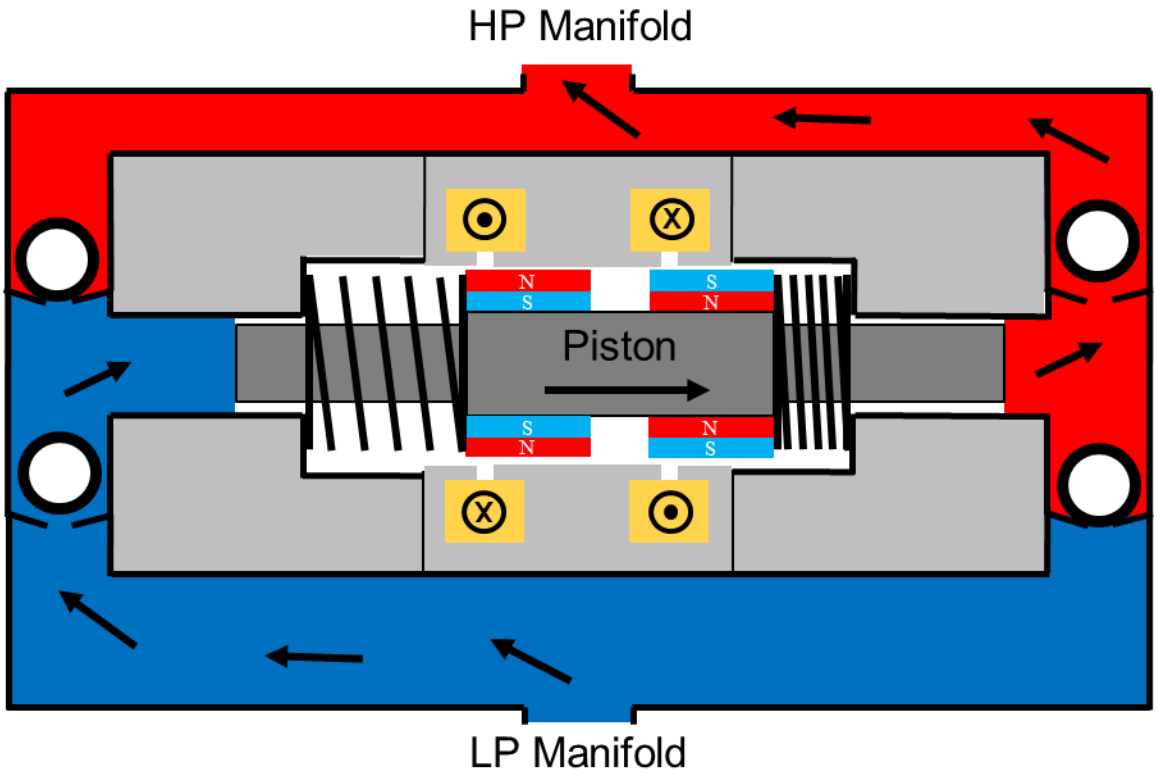

FIGURE 1.10: LINEAR ELECTRIC-HYDRAULIC CONVERSION MACHINE [20]

The work done to directly integrate hydraulic pumps with electric motors is still in its infancy but has shown several potential benefits, such as compactness, reduced noise, reduced external leakage, and improved dynamic control. The applications that have been explored include hydraulic power units of various size, a hybrid motor for electric vehicles, and a flow control unit. Each proposed integration thus far has utilized a different hydraulic architecture: vane, gerotor, internal gear, and radial piston. However, each design has used a radial flux machine with three of the four mentioned above being permanent magnet machines. Only one of the designs highlighted the ability to directly cool the electric machine and none of the designs pushed the speeds of the system. As mentioned in the background, Section 1.1, the HECM being studied will utilize a radial ball piston pump with an oil cooled axial flux electric motor. The next section reviews the previous modeling work associated with the radial ball piston architecture.

1.2.2 Radial Ball Piston Architecture

The radial ball piston architecture is a commercially available pump that has found success in light duty hydrostatic transmissions [9]. The architecture benefits from its simplicity; the ball

pistons function as the pumping element and rolling element on the cam. This creates a highly robust and compact design. The biggest challenge with the architecture is its limited pressure capabilities, which reduces its number of feasible applications. Leakage losses dominate at high pressure operating conditions because the ball piston seal is inherently less effective than the seal achieved with a cylindrical piston, Figure 1.11. Possibly because of this limited market exposure, the modeling and research surrounding ball piston pumps is less developed than axial piston, radial cylindrical piston, gear pumps, and other architectures.

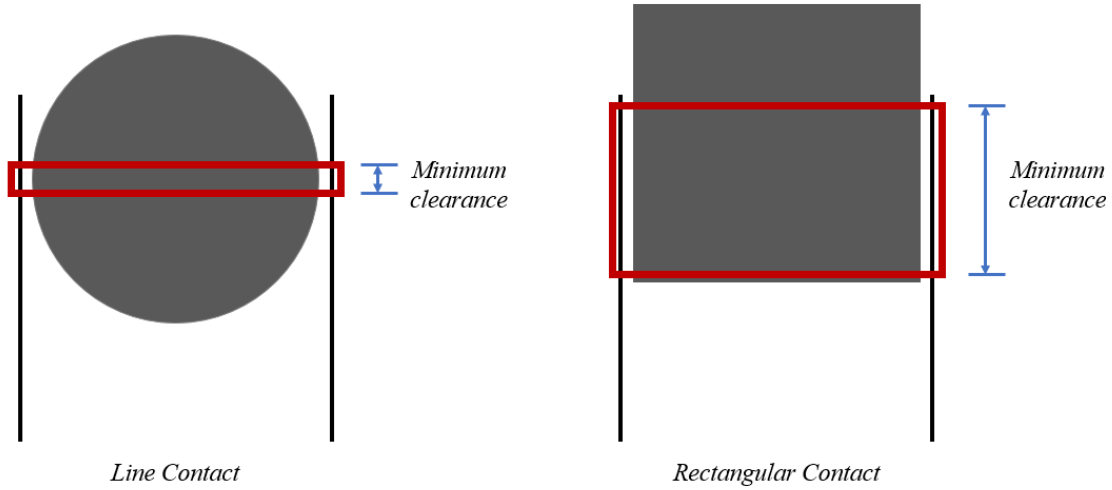

FIGURE 1.11: COMPARISON OF BALL PISTON AND CYLINDRICAL PISTON SEALING CONTACTS

Some of the earliest modeling work related to radial ball piston pumps was a dissertation titled "Study of Losses in a Ball Piston Pump" by Fereydoon Jamzadeh, awarded by the Mechanical Engineering Department at the University of Wisconsin-Madison in 1983. The dissertation focused on modeling the piston-cylinder interface and the fluid mechanics that occurred around the ball under steady state conditions [10].

Jamzadeh developed equations for the pressure, shear, and leakage that occurs around the ball for two distinct cases. The first was at zero speed when the ball simply acts as a seal preventing leakage. In this static situation, two equilibrium positions exist and were analyzed, the ball being centered and the ball being against a cylinder wall. The other case analyzed a rotating ball piston. To solve this situation, an iterative approach was used to determine the quasi-static location of the ball in the cylinder. The three situations that were considered are shown in Figure 1.12 [10].

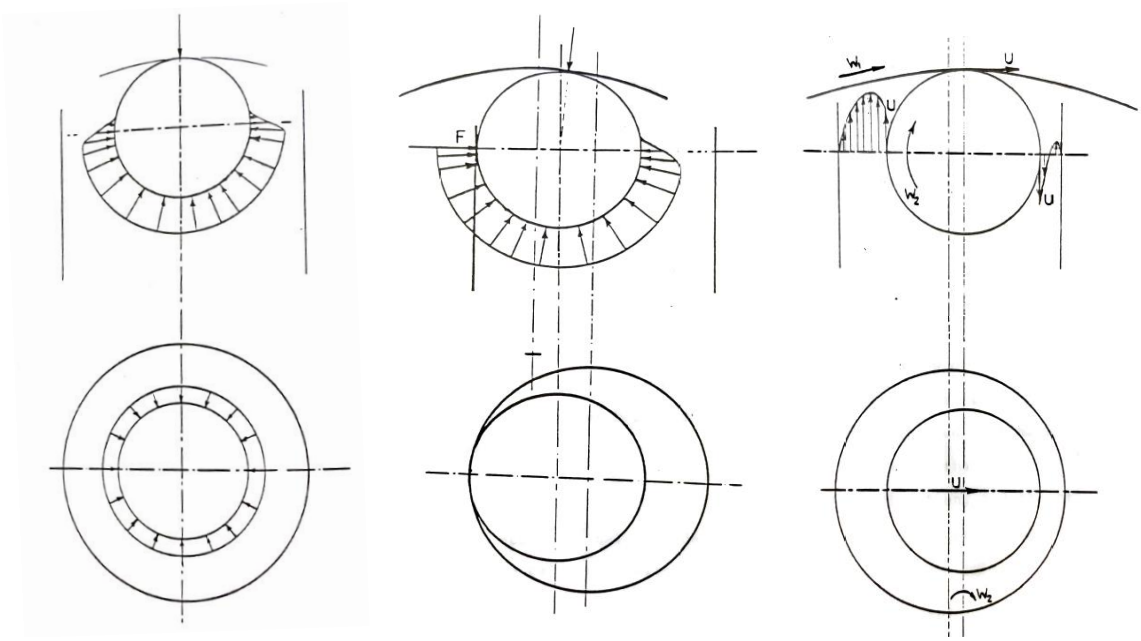

Static Centered *Static Offset* *Steady Rotation*

FIGURE 1.12: DIFFERENT PHYSICAL SITUATIONS MODELED BY JAMZADEH [10]

Experimental work was also done by Jamzadeh to validate the models he developed. Figure 1.13 shows the custom built setup that Jamzadeh used to test his models. The setup is comprised of three main features which are highlighted: a cam ring, a pressurized cylinder, and two ball pistons. The pressurized cylinder replaces the cylinder block of a typical radial ball piston pump. These cylinders were stationary and remained pressurized during the entirety of the tests. Jamzadeh machined four cylinders to different inner diameters which created four diametral clearances when coupled with the ball pistons: 4.6, 8.0, 9.2, and 12.2 microns. The setup also measured the leakage during the test runs to experimental validate his model predictions. To validate the rotating ball model, the cam ring was attached to a dynamometer that would spin the cam ring at a selected speed and measure the torque. The spinning cam provided the relative motion necessary to rotate the ball [10].

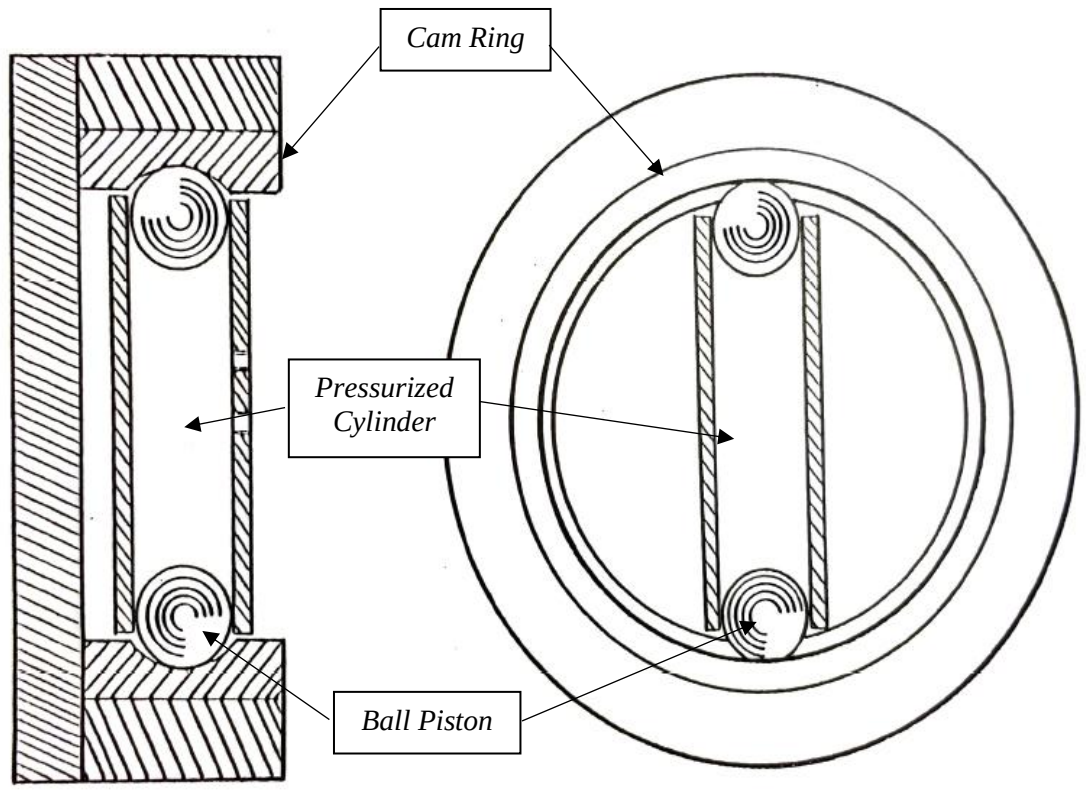

FIGURE 1.13: EXPERIMENTAL SETUP USED TO VALIDATE JAMZEDEH'S MODELS [10]

An important distinction between the experimental setup and an actual ball piston pump is that the cam ring was not in an eccentric position. Therefore, spinning the cam ring only created ball piston rotation and not translation. Without eccentricity no changes in pressure occurred within the cylinder and the cam surface was perfectly normal to the axis of the piston, resulting in no pressure angle on the ball. Another difference between was that most pumps use a flooded case which could not be simulated using this setup [10].

The results that Jamzadeh presented showed good agreement – correct trend and relative magnitude – for the leakage predictions of his model. The model did underpredict the leakage slightly for the non-rotating ball which was attributed to uncertainty in the temperature of the oil. As expected, the leakage increased with larger pressure or larger clearance [10].

The study of the rotating ball was more complex, and the predictions were less accurate. The leakage predictions were underpredicted, but still showed acceptable agreement in magnitude and trend. Increasing pressure, clearance, or speed resulted in increased leakage. Torque predictions

were made for the rotating ball and these also showed the correct trend, however, only 50 percent of the experimental torque was predicted by the model [10].

Jamzadah highlighted several uncertainties and assumptions within his simulation that could contribute to the inaccurate predictions. First, the isoviscous assumption was likely invalid. The ball piston moved to an eccentric position within the cylinder during the experiment which resulted in heat (shear losses) added to the oil that varied spatially. Not only were there different amounts of heat added to the oil, but the eccentric ball position created unequal fluid volumes. This would result in viscosity that varied around the ball. The oil temperature would vary with time as well. The second assumption that was likely invalid was the uniform cylinder expansion. Jamzadeh assumed that the fluid always remained in the hydrodynamic lubrication regime and ignored any localized deformation or elastohydrodynamic effects. This was likely an inaccurate assumption because the ball shifts very close to one wall. The last issue was the alignment between the ball centerline and the race centerline. If these were not perfectly aligned, there would be a side load on the ball piston forcing it into one of the walls perpendicular to its direction of rotation. The misalignment could be extremely small and still create interference because of the micron clearances [10].

The primary contribution of Jamzadeh's thesis was his theoretical modeling approach. His work showed that analytical models could accurately predict losses at the ball-cylinder interface despite multiple simplifying assumptions. His approach was necessary in 1983 because computers did not have the computational power to run more complex simulations. Similar models of radial ball piston pumps have been developed to study the contact stresses, kinematics, and lubrication characteristics of water as a working fluid [22 – 25]. This modeling strategy, of simplifying the fluid mechanics to develop analytical solutions, has been adopted for mineral oil [26, 27] with success and was extended to include more complicated phenomena by this thesis in order to develop a design optimization framework.

Today, the state-of-the-art approach to simulating the physics around the ball piston is 2D computational fluid mechanics coupled with FEA for the solid deformation. This strategy is more accurate but requires longer computation times [28]. Jing et al. from the Beijing Institute of Technology used this numerical approach to study the lubrication characteristics of pumps by creating models for the ball-cylinder, ball-cam ring, and pintle-rotor interfaces, as shown in Figure 1.14. Their work was presented in three separate papers with each paper focusing on a different interface [29 – 31].

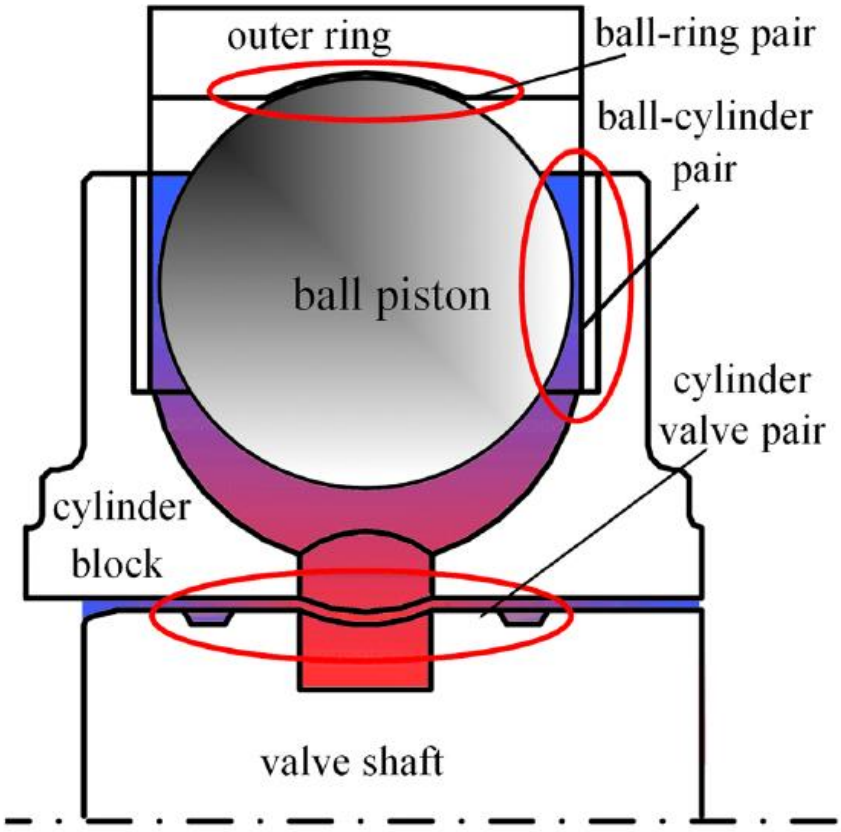

FIGURE 1.14: MAIN FRICTION INTERFACES WITHIN A BALL PISTON PUMP

The Beijing Institute performed an experimental test of the input torque required by a radial ball piston pump. The simulation included models for the three interfaces shown in Figure 1.14 and the results matched the experiments well. There were some discrepancies between the simulation and experimental torque; however, one challenge of pump level testing is that individual loss mechanisms cannot be validated. Instead, the total losses are validated, and the hope is that the individual loss contributions will be approximately correct. This makes it difficult to identify the root cause of discrepancies between the experiments and the simulation [30].

The Beijing Institute only presented information on modeling the mechanical losses (torque) which ignores the other major pump loss contributor, leakage. A model of the leakage losses would have to be built for them to predict the overall efficiency of a given design. The models developed are a great analysis tool though, allowing the performance of a machine to be understood at different operating conditions without running experiments. However, the computational complexity which provides this accuracy also increases the computation time to a point that makes the model infeasible to use for design optimization.

1.2.3 Electric Hydraulic Actuators

This thesis also contributes to the progression of high speed hydraulic pumps, which today is dominated by Electro-Hydraulic Actuators (EHAs). Typical hydraulic pumps and motors do not reach speeds above 5,000 rpm, with 3,600 rpm as a common maximum; however, aerospace EHAs often reach 10,000-20,000 rpm. These speeds are required in aerospace applications because keeping the overall mass low is critical. Another feature of an EHA that helps keep mass low is that it is a distributed hydraulic system. Instead of one main pump with hydraulic lines running to actuators, EHAs are fully self-contained and only need electrical wiring to provide power. This feature also improves the maintainability of the system because broken EHAs can easily be swapped out [32]. An EHA is shown in Figure 1.15 and is made up of four major components. An electric motor, a hydraulic pump, a hydraulic reservoir, and a hydraulic actuator.

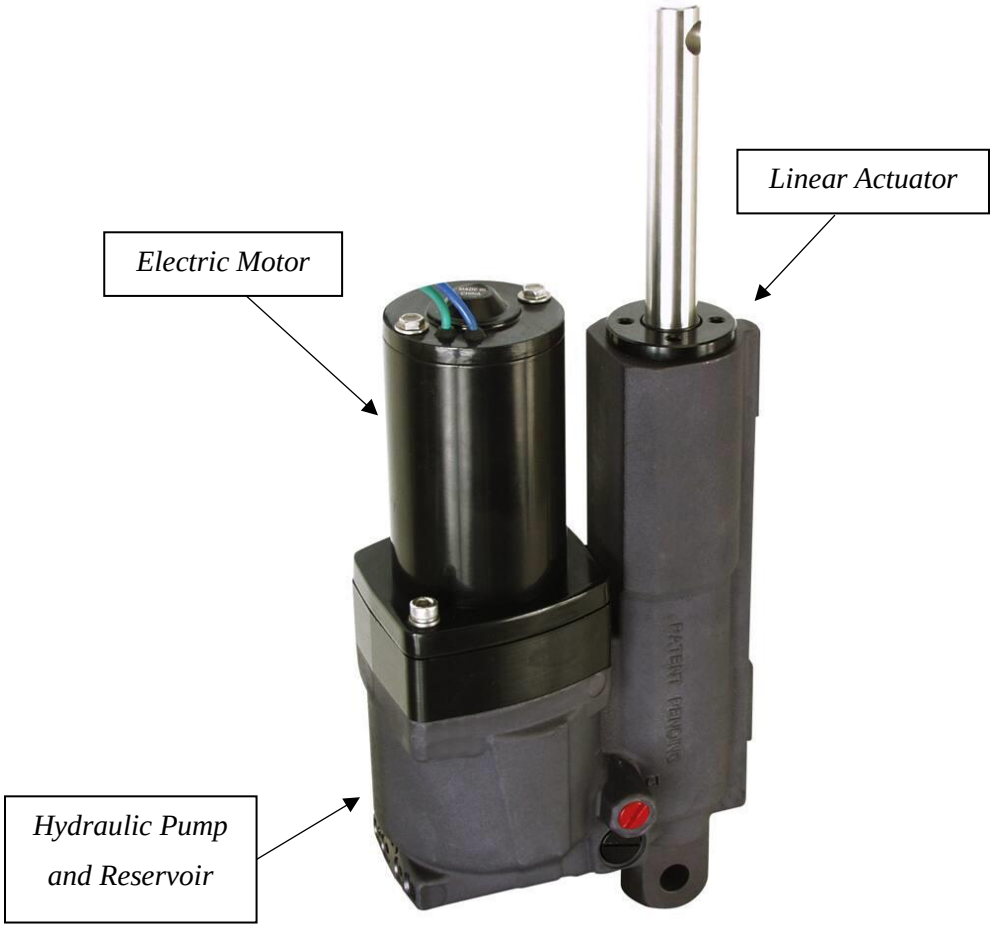

FIGURE 1.15: EXAMPLE EHA [33]

The electric motor is connected via a shaft to the hydraulic pump, which creates the flow required to control the actuator. This design has the advantage of using pre-existing modular components, but redundancies arise because of the two shafts. A review of EHAs for aerospace applications was done by Chao et al. [32] who explored the main difficulties when pushing hydraulic units to high speeds. The primary challenges discussed for EHAs were cavitation, flow and pressure ripples, tilting of the rotating group, and excessive temperatures [32]. Fortunately for the HECM, the tilting of the rotating group is not an issue because of the decision to use a radial piston architecture instead of an axial one. Also, the excessive temperature and heat generation is a concern in EHAs because of their self-contained nature. The HECM is part of a larger hydraulic system allowing conventional cooling techniques to be utilized.

However, the other issues, cavitation, flow ripples, and pressure ripples, do need to be considered. Cavitation is when the localized pressure of the oil drops below the vapor pressure resulting in small bubbles forming within the oil. When the pressure increases again, the bubbles collapse (burst) and release enough energy to damage surfaces within the pump. This damage reduces the life and efficiency of the pump [34]. The HECM architecture always operates between pressurized rails that are above atmospheric pressure, eliminating cavitation concerns [35 – 39].

The other issue with high speed operation is the pressure and flow ripple which tends to increase with speed [40 – 43]. It has been found that reverse flow is the largest contributor to the dynamic flow and pressure ripples [44 – 46]. Fortunately, good valve timing can reduce or even eliminate this phenomenon [32]. Therefore, optimizing the valve timing is considered the best method for reducing both the pressure and flow ripples. This is the approach that will be taken within this thesis.

1.3 Overview

This thesis is concerned with the design of an integrated hydraulic-electric machine that is compact and efficient. It focuses on the development, validation, and utilization of a radial ball piston pump/motor model. The model will be designed to be both fast and accurate. Experimental tests were performed to validate the model and ensure confidence in its results. The validated model was then utilized in a design optimization framework to develop a four quadrant radial ball piston unit capable of high speed operation.

Chapter 2 deals with the development of a radial ball piston model. It focuses on determining the losses and efficiency of the unit at different operating conditions. The model begins by determining the pressure dynamics within the cylinder which allows the valve timing to be

evaluated. This information provides a baseline for the efficiency of the unit before mechanical and volumetric losses at the interfaces are included. The thesis presents detailed models for the ball-cylinder and pintle-rotor interfaces. As mentioned previously, the model is used for design optimization and therefore needs to be relatively fast and accurate. The computational speed constraint drove the decision to use an approach similar to the one used by Jamzadeh (Section 1.2.2), but the accuracy constraint led to the use of empirical elastohydrodynamic lubrication (EHL) relationships for the ball-cylinder pair. The pintle-rotor interface utilizes journal bearing theory which was adapted from Hamrock [47]. The interface losses are then incorporated into an efficiency prediction for both pumping and motoring operating cases.

Chapter 3 presents experimental work that was done to validate the model. The chapter describes the Eaton radial ball piston pump that was tested. Several experimental circuits are presented and their use in the validation process is explained. Sensitivity studies are used to show the impact of different physical parameters on the simulation results. Experimental data is then shown alongside simulation data to establish the accuracy of the model.

Chapter 4 considers the optimization of the radial ball piston pump. The chapter presents a simplified model and explains why that model is used to optimize the size of the machine. A genetic algorithm framework lays out the optimization parameters and the geometric constraints that are considered to ensure a valid geometry. Next, the objective function is defined along with a description of the process used to select the operating conditions. The chapter then describes the one-dimensional optimization that is used to determine the clearance between the ball and cylinder. Lastly, the results of the optimization are shown, and the finalized design is analyzed to demonstrate the overall hydraulic machine performance.

The final chapter gives a summary of the presented model, validation, and optimization results. It discusses the implications of this work and the value it creates. Finally, it concludes by suggesting future work and further areas of study.

2 Radial Ball Piston Model

2.1 Introduction

The desire to electrify hydraulics has necessitated the need for a compact, energy efficient hydraulic pump/motor unit that can operate in four quadrants. As discussed in Section 1.1, the radial ball piston design was selected as the most promising architecture given its application within the Hybrid Hydraulic Electric Architecture (HHEA). Unfortunately, there has been limited work on radial ball piston units in academia and no information exists for designing one for high speed applications. In order to generate a design that meets all the operating requirements, an optimization framework is needed. Utilizing models for design optimizations requires a tradeoff between computational speed and accuracy. Speed is required because thousands of designs need to be analyzed, and the knowledge gained from previous simulations needs to be leveraged to continuously improve performance. Perfect accuracy is not required, but the model needs to predict the correct trends and relative losses to drive the optimization in the correct direction. The following chapter presents a radial ball piston model that accomplishes these goals.

2.1.1 Literature Review

Research in hydraulic pump modeling has been revolutionized by the development of modern computers. Many complicated and interconnected phenomena occur within hydraulic units, particularly at sealing surfaces where an understanding of tribology is required. Today, numerical techniques are often used to predict the behavior at these critical interfaces [29 – 31, 47]. This method makes few simplifying assumptions, resulting in extremely accurate predictions. However, the lack of assumptions creates a slow model that is not capable of performing design optimization. A high degree of accuracy can be maintained, and the computation speed improved by selecting realistic assumptions; this was the approach used in early tribology work done throughout the 1970s [47] and in the work by Jamzedeh on the radial ball piston pump in 1983 [10]. This is the approach utilized within this chapter.

The fluid mechanics at hydraulic pump interfaces fit within lubrication theory and are therefore governed by Reynold's equation [47]. Reynold's equation applies the conservation of mass and momentum to fluid volumes where pressure and viscous forces dominate. This occurs in lubrication theory, which is when the length scale of one dimension is significantly smaller than the others. For the radial ball piston unit, the ball-cylinder and pintle-rotor interfaces both meet the criteria since the clearance length scale (microns) is dwarfed by the size of the ball and rotor (centimeters).

Even though the Reynold's equation simplifies fluid flow by ignoring inertial effects, it is still too complicated in most situations to be solved analytically without further assumptions.

The ball-cylinder interface model makes several assumptions to make an analytical solution possible. This was an approach originally proposed by Jamzedeh [10] which has been expanded upon within this thesis to included more complicated behavior. These assumptions are described within the modeling section of the chapter; however, the model assumptions are only valid when the ball is within the hydrodynamic lubrication regime, which is characterized by a full fluid film between the two surfaces and moderate (megapascal) localized pressures. During certain operating conditions, the ball piston is forced into the cylinder wall and hydrodynamic lubrication transitions into the elastohydrodynamic lubrication (EHL) regime. EHL is characterized by gigapascal localized pressures that deform the solids and increase viscosity. The EHL effects are accounted for using piezo-viscous relationships and empirical models as proposed by Hamrock [47].

The pintle-rotor interface does not transition into the EHL regime at the pressures and speeds analyzed throughout this thesis. The pintle acts as a journal bearing for the rotor block making journal bearing theory applicable [47]. All the assumptions used by Hamrock to simplify the fluid mechanics and develop an analytical expression are still valid for the pintle-rotor interface; however, the pintle contains pressure ports which complicates the selection of boundary conditions within the model.

2.1.2 Overview

The chapter begins by describing the cylinder pressure dynamics and the approach used to determine the valve timing. After this, the losses at the pintle-rotor and ball-cylinder interface are considered. The forces acting on the rotor block are considered and the journal bearing behavior of the pintle is analyzed quasi-statically. A simple heat transfer model is also developed to account for the impact of temperature on the viscosity, thus improving the leakage and shear predictions. The ball-cylinder model describes the geometry, kinematics, and dynamics of the ball before a detailed breakdown of the fluid mechanics is presented. The heat transfer model is applied to the new geometry to improve predictions. An empirical EHL model is then presented to account for the limitations of the original fluid mechanic assumptions. The chapter concludes by highlighting interesting model predictions and analyzing various results.

2.2 Methods

The radial ball piston model is broken down into three main sections: pressure dynamics, ball-cylinder interface, and pintle-rotor interface. Figure 2.1 shows each section within the architecture. These pieces account for most of the losses within the hydraulic unit. The figure includes two losses that are not included within the model, the ball-cam interface and churning losses. The ball-cam interface does not need to be modeled because it is assumed that the ball always rolls on the cam ring. The churning losses were determined experimentally, creating an empirical model.

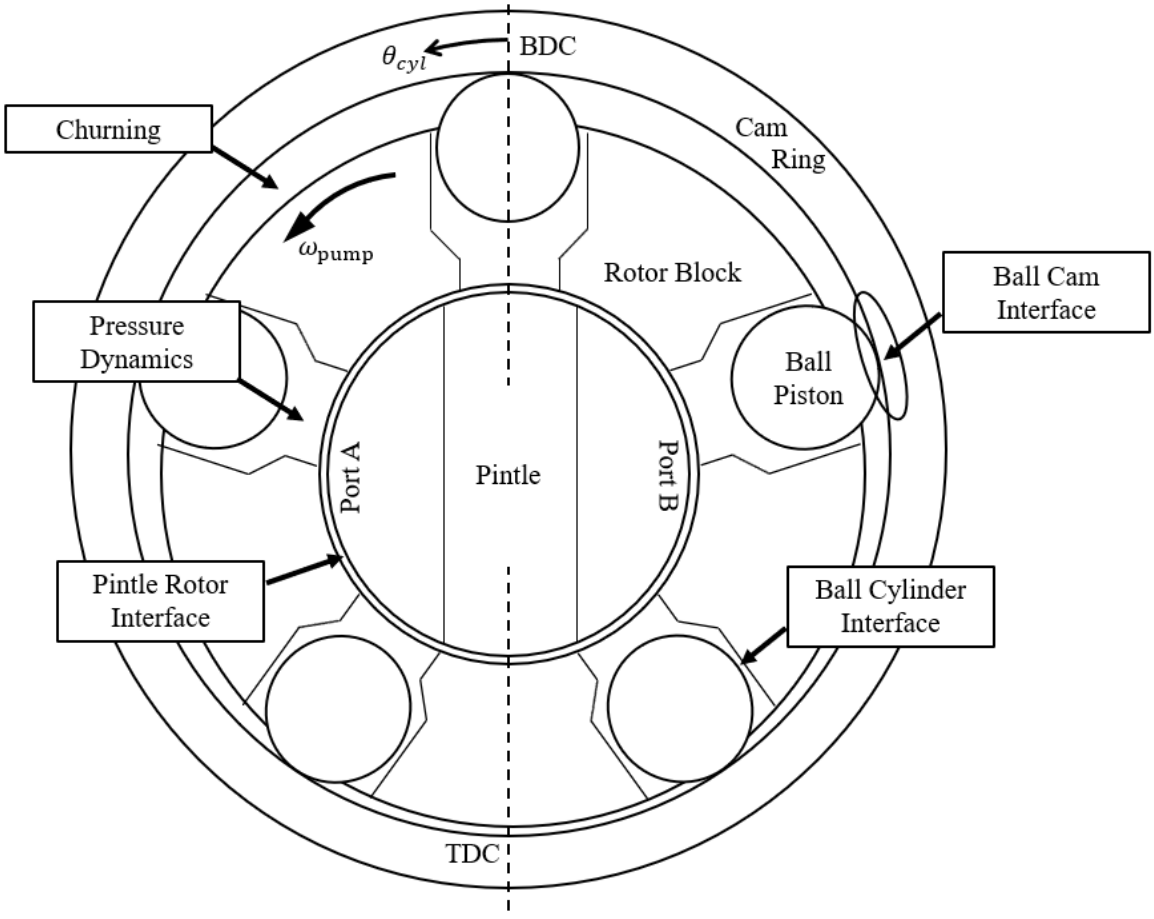

FIGURE 2.1: RADIAL BALL PISTON ARCHITECTURE OVERVIEW

2.2.1 Pressure Dynamics

The cylinder volume being analyzed is dependent on the position of the piston, which is approximately a sinusoidal profile due to the eccentric cam ring. Referring to Figure 2.1, the rotation angle of a cylinder, θ_{cyl}, is zero at bottom dead center (BDC) and rotates counterclockwise

to top dead center (TDC) at θ_{cyl} equals π radians. The ball position is shown at these two rotation angles in Figure 2.2; the figure also defines the dead volume, V_{dead}, which is the unswept fluid volume within the cylinder.

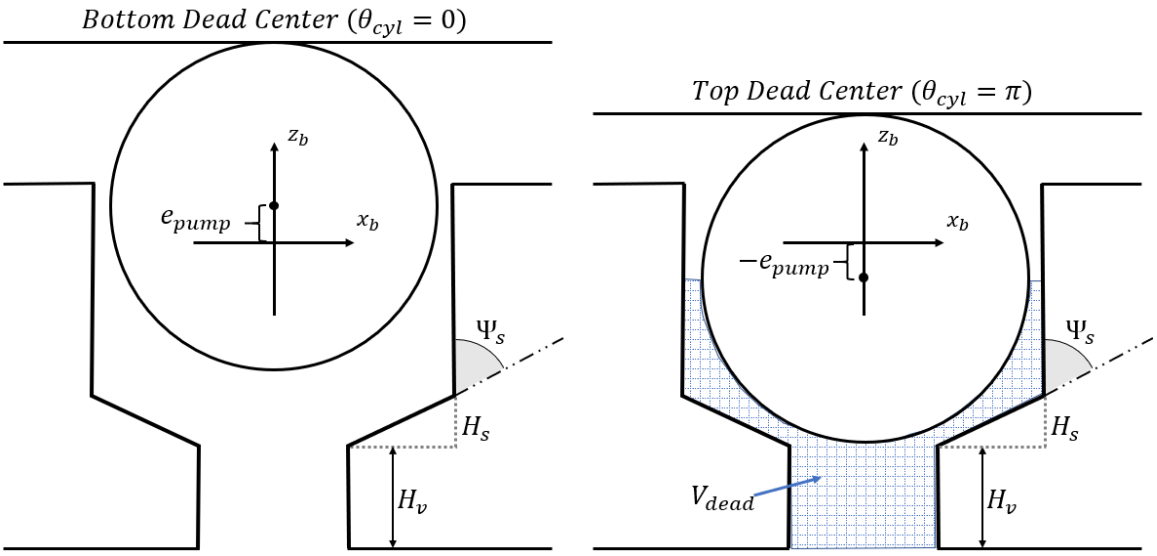

FIGURE 2.2: CYLINDER POSITION AND GEOMETRY

Using the geometry and local reference frame of Figure 2.2, the kinematics of the ball piston can be described.

$$z_b = e_{pump} \cos \theta_{cyl} \tag{2.1}$$

$$\dot{z}_b = -e_{pump} \omega_{pump} \sin \theta_{cyl} \tag{2.2}$$

where z_{ball} is the position of the ball and $\dot{z}_{ball}$ is the velocity of the ball. Knowledge of the piston position allows the volume to be determine for any pump angle, eq. (2.3).

$$V_{cyl} = \pi r_b^2 \left(e_{pump} + e_{pump} \cos \theta_{cyl}\right) + V_{dead} \tag{2.3}$$

where r_b is the radius of the ball piston. Equation (2.4) gives the change in volume with respect to time.

$$\frac{dV_{cyl}}{dt} = \frac{dV_{cyl}}{d\theta_{cyl}} \cdot \frac{d\theta_{cyl}}{dt} = -\pi r_b^2 e_{pump} \omega_{pump} \sin \theta_{cyl} \tag{2.4}$$

The definition of bulk modulus is used to calculate the change in cylinder pressure, eq. (2.5).

$$\frac{dp_{cyl}}{dt} = \frac{\beta}{V_{cyl}}\left(Q_A + Q_B - \frac{dV_{cyl}}{dt}\right) \tag{2.5}$$

where β is the bulk modulus, and Q_A and Q_B are the flowrates from ports A and B to the cylinder. Any leakage into or out of the cylinder will impact the pressure dynamics, but this effect is minimal, and the losses can be captured accurately through post processing. The bulk modulus of the fluid is a function of pressure with the relationship determined using eq. (2.6) [11]. This model considers the amount of entrained air in the oil and the subsequent impact on the compressibility.

$$\beta = \beta_o\left[\frac{R + \left(\frac{p}{p_o} + 1\right)^{\frac{1}{\gamma}} e^{-\frac{p}{\beta_o}}}{\frac{R}{\gamma}\frac{\beta_o}{p + p_o} + \left(\frac{p}{p_o} + 1\right)^{\frac{1}{\gamma}} e^{-\frac{p}{\beta_o}}}\right] \tag{2.6}$$

where β_o is the bulk modulus at atmospheric pressure, R is the percent of entrained air within the fluid, p is the cylinder pressure, p_o is the atmospheric pressure, and γ is the ratio of specific heats for air. The flow rates Q_A and Q_B are modeled using the orifice equation.

$$Q_A = sign\left(p_A - p_{cyl}\right) \cdot C_d A_A \sqrt{\left|\frac{2}{\rho}\left(p_A - p_{cyl}\right)\right|} \tag{2.7}$$

$$Q_B = sign\left(p_B - p_{cyl}\right) \cdot C_d A_B \sqrt{\left|\frac{2}{\rho}\left(p_B - p_{cyl}\right)\right|} \tag{2.8}$$

where A_A and A_B are the orifice areas for port A and B respectfully, C_d is the coefficient of discharge, and ρ is the density of the oil. The orifice areas are functions of the rotation angle, and the area profile for an entire rotation is referred to as the valve timing. The valve timing is considered a critical design feature for hydraulic pumps/motors. Figure 2.3 is a cross section view of the pintle and the two machined ports. The angles θ_{A_o}, θ_{A_c}, θ_{B_o}, and θ_{B_c} are the opening and closing angles for ports A and B as measured from bottom dead center (BDC). The angle θ_{cyl} measures the rotational position of the cylinder valve being considered.

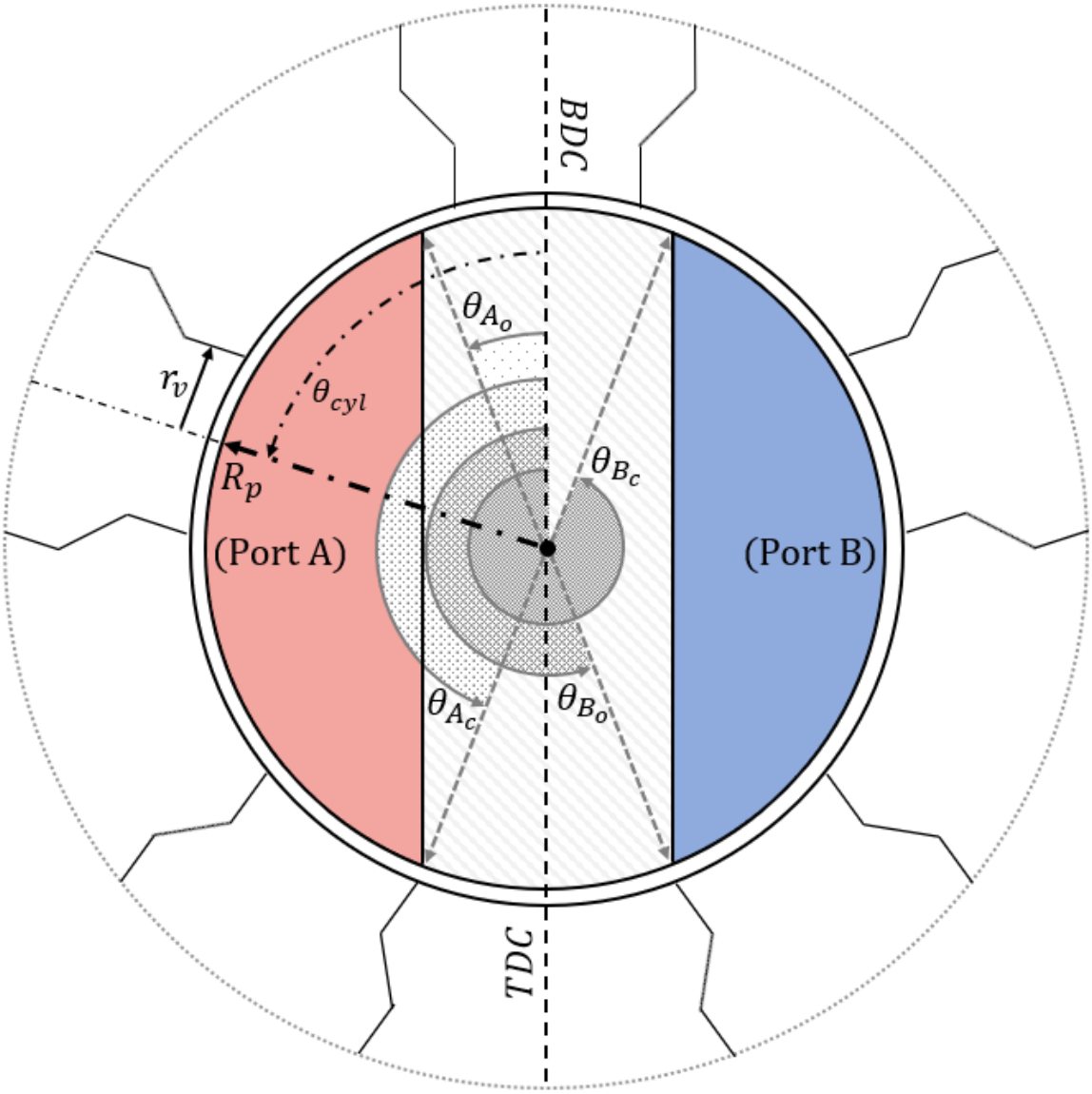

FIGURE 2.3: PINTLE GEOMETRY AND VALVE TIMING ANGLES

The pintle geometry and valve timing can also be viewed by unwrapping the pintle into a rectangle as shown in Figure 2.4. A single cylinder is shown for simplicity and because the pressure dynamics are analyzed once, but in reality, the total number of pistons would be evenly spaced across the unwrapped pintle. Port ramps are shown in Figure 2.4 at the end of each rectangular port, these create a more gradual transition near top and bottom dead center[3]. The counterclockwise

[3] Valve timings can also include silencing grooves (small slits) at the ends of the ports to improve transitions.

rotation of the pump corresponds to the cylinder valve moving left to right across the unwrapped pintle. As the valve moves, its circular cross section overlaps with ports A and B by varying amounts.

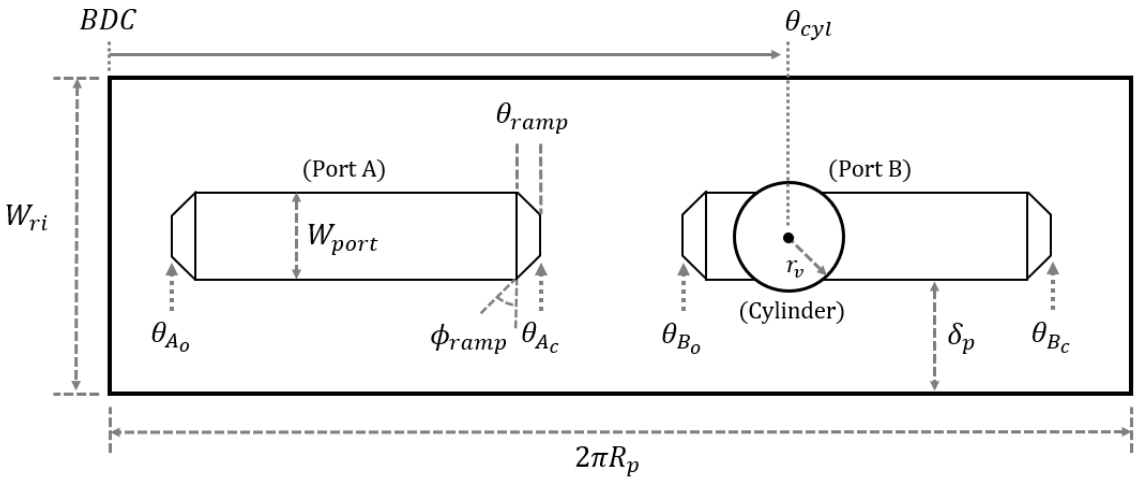

FIGURE 2.4: GEOMETRIC FEATURES OF UNWRAPPED PINTLE FOR VALVE TIMING

The area profile can be calculated using analytical integrals that describe the intersection of the valve's circular cross section with the ports of the pintle. The total valve area is broken into three components: opening port ramp, main port, and closing port ramp. The equations that describe these intersecting areas are defined in Appendix B. An example valve timing (area profile) is shown in Figure 2.5 with the intersection area of the port ramps and main port separated.

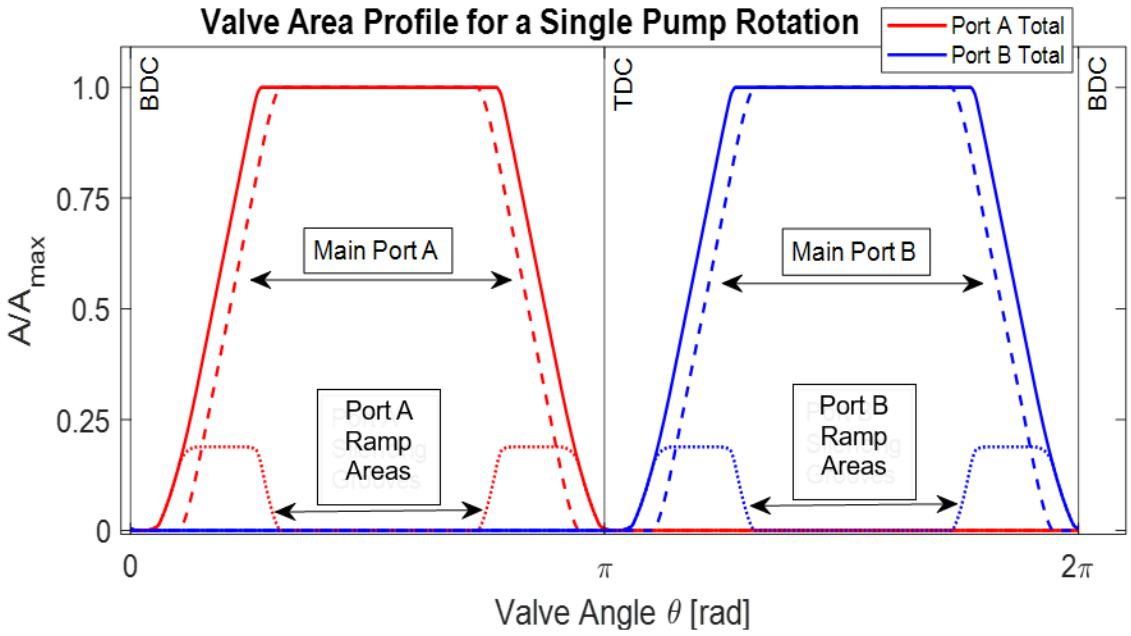

FIGURE 2.5: VALVE ORIFICE AREA

2.2.2 Pintle-Rotor Interface

The pintle not only determines the valve timing as discussed in the previous section, but it also acts as a journal bearing for the rotor. The interface has a complicated pressure distribution acting between the surfaces that creates an unbalanced force on the rotor. A piece-wise pressure distribution is established to predict the dynamics and journal bearing theory is used to determine the rotor's eccentricity around the pintle. Knowing the eccentricity allows the leakage and shearing losses to be accurately calculated at the interface. This modeling section begins by approximating the rotor expansion, so the clearance is known. The static pressure distributions are analyzed to determine the net force on the rotor, and then, a quasi-static journal bearing approach is used to calculate the eccentricity. Finally, the losses at the interface are found, and the model used to predict the change in oil temperature is presented.

2.2.2.1 Pintle Expansion

The expansion of the inside radius of the rotor can be described using a thick walled pressure vessel assumption. This expansion is critical to the rest of the pintle-rotor analysis since the clearance impacts the fluid mechanics, dynamics, kinematics, and heat transfer. Figure 2.6 shows the pressure distribution acting on the rotor block. To simplify the calculations, the piston bores are

ignored, and the rotor is treated as a solid ring. This will underpredict the expansion, but the model is still considered acceptable.

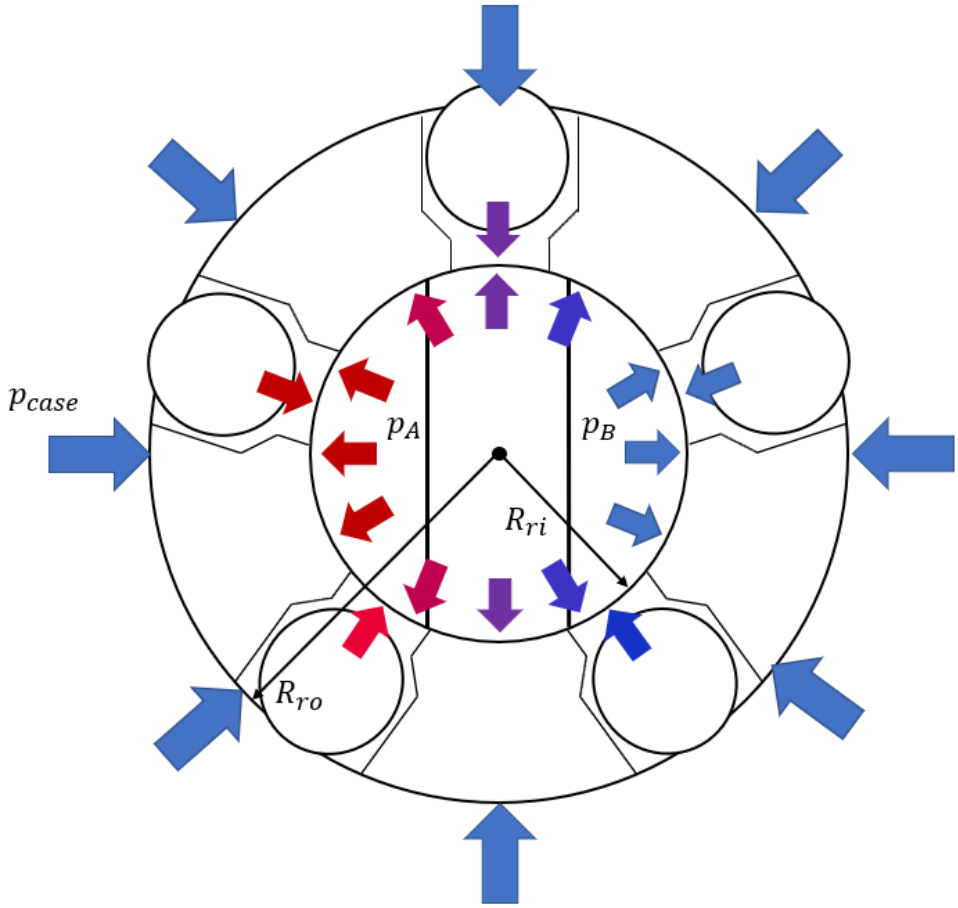

FIGURE 2.6: PRESSURE DISTRIBUTION ACTING ON THE ROTOR BLOCK

The governing equation for the change in radius of a thick walled pressure vessel with only internal pressure is defined in eq. (2.9).

$$\Delta R = \frac{R_{ri}^3(1-\nu)p_i + (1+\nu)p_i R_{ri} R_{ro}^2}{E\left(R_{ro}^2 - R_{ri}^2\right)} \tag{2.9}$$

where p_i is the average pressure at the internal radius, E is the elastic modulus, and ν is Poisson's ratio. Simplifying the expression yields eq. (2.10).

$$\Delta R = \frac{p_i R_{ri}}{E} \frac{\left(R_{ri}^2 - R_{ri}^2\nu + R_{ro}^2 + R_{ro}^2\nu\right)}{R_{ro}^2 - R_{ri}^2}$$

$$\Delta R = \frac{p_i R_{ri}}{E}\left(\nu + \frac{R_{ro}^2 + R_{ri}^2}{R_{ro}^2 - R_{ri}^2}\right) \tag{2.10}$$

The clearance between the pintle and rotor is then calculated.

$$H_p = (R_{ri} + \Delta R) - R_p \tag{2.11}$$

2.2.2.2 Rotor Dynamics – Cylinder Pressures

As shown in Figure 2.6, the cylinders, port A, and port B apply pressure to the rotor block. The force created by these distributions is unbalanced and shifts the rotor into an eccentric position around the pintle, changing the gap height between the two features. The eccentricity coupled with the relative motion between the two surfaces causes the pintle to behave like a journal bearing and support the resultant load. Figure 2.7 depicts this situation. Note that the clearance is greatly exaggerated.

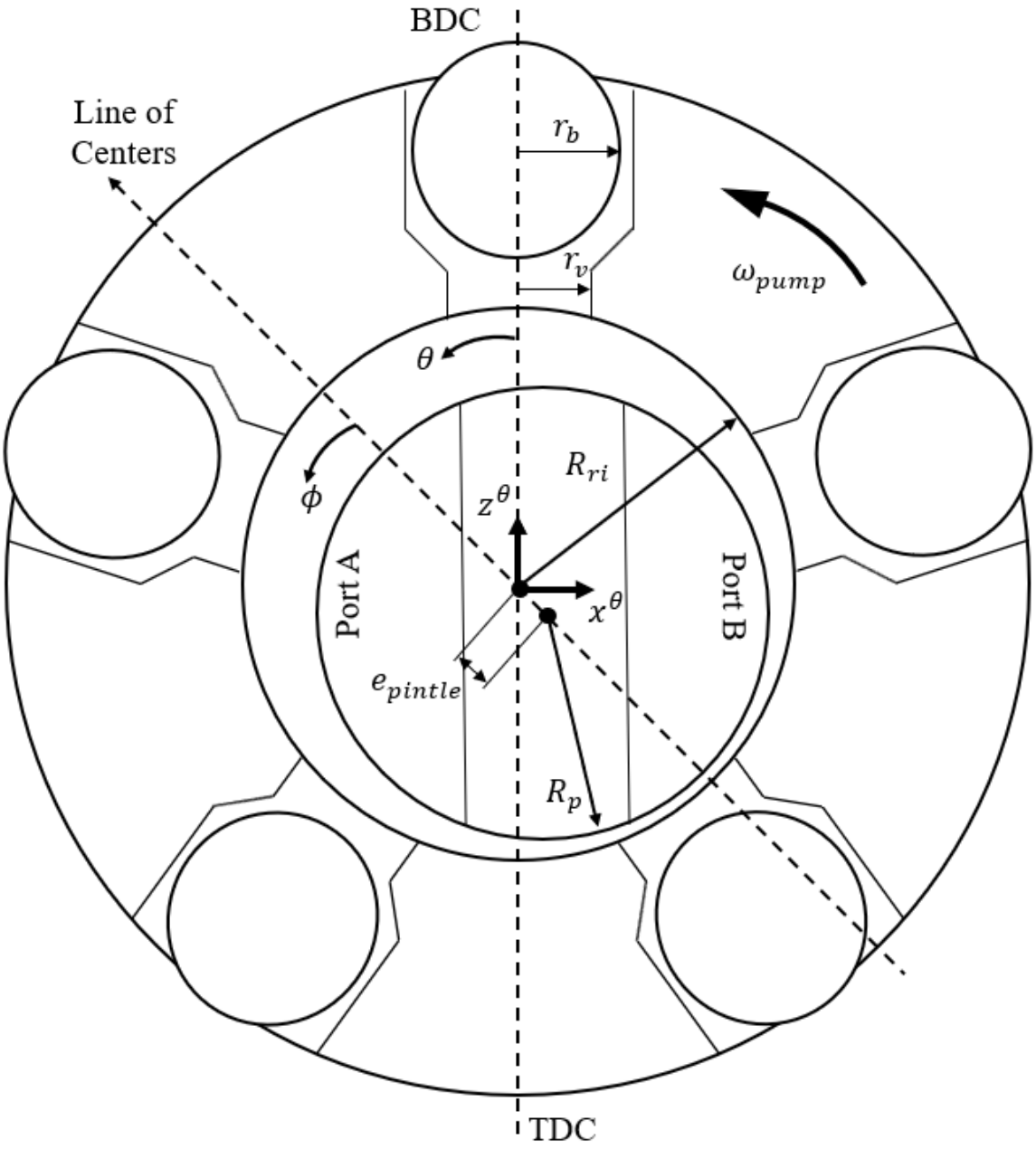

FIGURE 2.7: PINTLE-ROTOR INTERFACE GEOMETRY AND COORDINATES

The pressure found for a single cylinder is shifted based on the number of pistons allowing the dynamics of the rotor block to be analyzed. Each cylinder applies force into the rotor, and the net

force in the x^θ and z^θ directions is given by eq. (2.12) and (2.13)[4]. As seen in Figure 2.7, x^θ is perpendicular and z^θ is parallel to the line through BDC and TDC respectfully.

$$F_{cyl}^{x^\theta} = \sum_{i=1}^{n} -\pi r_b^2 \left(p_{cyl_i} - p_{case}\right) \sin\theta_{cyl_i} \tag{2.12}$$

$$F_{cyl}^{z^\theta} = \sum_{i=1}^{n} \pi r_b^2 \left(p_{cyl_i} - p_{case}\right) \cos\theta_{cyl_i} \tag{2.13}$$

where n is the number of ball pistons, p_{cyl_i} is the pressure in the i^{th} cylinder, and θ_{cyl_i} is the angle of the i^{th} cylinder from BDC.

2.2.2.3 Rotor Dynamics – Piecewise Pressure Distribution

To calculate the resultant force acting on the rotor, a piecewise solution to the pressure distribution between the pintle and the rotor is developed. Figure 2.8 shows the pintle geometry used for the force balance calculations and the name for the pressure distribution in each region of the interface. Note that the geometry of the valve timing has been simplified. The relative motion between the pintle and rotor for counterclockwise rotor rotation is also shown in the figure and defined by eq. (2.14). The pressure distributions are assumed to be symmetric about the midline of the pintle, $1/2\, W_{ri}$, and the pressure above and below W_{ri} is P_{case}. Another assumption is that the pressure distribution resulting from the rotation of the rotor can be decoupled from the distribution caused by the pressure sources at port A and B. Because the pressure sources are static, the net force produced by them will be independent of time.

$$U_{rotor} = R_p \omega_{pump} \tag{2.14}$$

[4] Physically, the area of the rotor that the cylinder pressures act on is $n(\pi r_b^2 - \pi r_v^2)$ and the area of the rotor that the pintle pressure acts is $2\pi R_p W_{ri} - n\pi r_v^2$, see Figure 2.6 - Figure 2.8 for geometric definitions. The pressures acting on the valve cross sections, $n\pi r_v^2$, are equal and opposite, thus canceling each other. Therefore, in the model, πr_b^2 is the area for the cylinder pressures and $2\pi R_p W_{ri}$ is the area at the inside of the rotor.

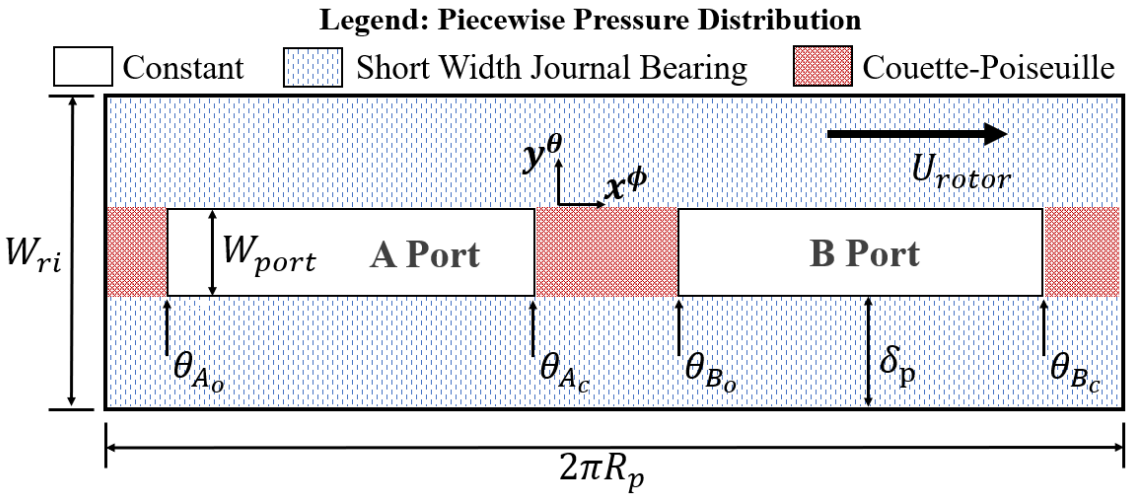

FIGURE 2.8: PINTLE-ROTOR INTERFACE PRESSURE DISTRIBUTIONS

2.2.2.4 Rotor Dynamics – Couette Poiseuille Distribution

The constant pressures at port A and B are given as p_A and p_B respectively. The pressure distribution occurring between port A and B assumes a Couette-Poiseuille flow profile. This implies unidirectional flow with a pressure differential and relative velocity acting in one dimension. Under these assumptions, the Navier-Stokes equation reduces to eq. (2.15) and the pressure distribution is given by eq. (2.16) and (2.17).

$$\frac{d^2u}{dz^2} = \frac{1}{\mu R_p}\frac{dp}{d\theta} \tag{2.15}$$

$$p_{A-B}(\theta) = \frac{p_A - p_B}{\theta_{A_c} - \theta_{B_o}}\left(\theta - \theta_{A_c}\right) + p_A \tag{2.16}$$

$$p_{B-A}(\theta) = \frac{p_B - p_A}{\theta_{B_c} - \left(\theta_{A_o} + 2\pi\right)}\left(\theta - \theta_{B_c}\right) + p_B \tag{2.17}$$

2.2.2.5 Rotor Dynamics – Short Width Journal Bearing Distribution

The next pressure distribution analyzed is outside of the ports where the short width journal bearing assumptions are applied. The geometry for these regions uses the coordinates defined in Figure 2.7 and Figure 2.8. In Figure 2.7, the line of centers goes through the center of the pintle and the center of the rotor, and ϕ is defined as positive in the direction of rotation. The difference between the pintle and rotor radii has been greatly exaggerated with the actual radial clearance is

in the micron range. From these figures, several variables are defined. Cylindrical to cartesian position.

$$x^{\phi} = R_p \phi \tag{2.18}$$

The nominal radial clearance.

$$H_p = (R_{ri} + \Delta R) - R_p \tag{2.19}$$

The eccentricity ratio.

$$\epsilon = \frac{e_{pintle}}{H_p} \tag{2.20}$$

The gap height at any point.

$$H_\epsilon = H_p(1 + \epsilon \cos \phi) \tag{2.21}$$

The governing equation for the short width journal bearing starts with Reynold's Equation, then, using a series of assumptions, Hamrock [47] arrives at eq. (2.22) for a steadily loaded short width journal bearing.

$$\frac{\partial}{\partial y^\theta}\left(H_\epsilon^3 \frac{\partial p}{\partial y^\theta}\right) = 6\mu\omega_{pump} \frac{\partial H_\epsilon}{\partial \phi} \tag{2.22}$$

Integrating the equation twice with respect to y^θ yields eq. (2.23).

$$p(\phi, y^\theta) = \frac{3\mu\omega_{pump}}{H_\epsilon^3} \frac{\partial H_\epsilon}{\partial \phi} {y^\theta}^2 + \frac{C_1}{H_\epsilon^3} y^\theta + C_2 \tag{2.23}$$

where C_1 and C_2 are constants of integration. Notice that this integration only works if the rotor is aligned parallel to the pintle so that H_ϵ is not a function of y^θ. The boundary conditions $p = p_o$ at $y^\theta = 0$ and $p = p_{case}$ at $y^\theta = \delta_{\mathrm{p}}$ are selected, where p_o is the piecewise function defined in eq. (2.24).

$$p_o(\theta) = \begin{cases} p_A & \theta_{A_o} < \theta < \theta_{A_c} \\ \dfrac{p_A - p_B}{\theta_{A_c} - \theta_{B_o}}\left(\theta - \theta_{A_c}\right) + p_A & \theta_{A_c} < \theta < \theta_{B_o} \\ p_B & \theta_{B_o} < \theta < \theta_{B_c} \\ \dfrac{p_B - p_A}{\theta_{B_c} - \left(\theta_{A_o} + 2\pi\right)}\left(\theta - \theta_{B_c}\right) + p_B & \theta_{B_c} < \theta < \left(\theta_{A_o} + 2\pi\right) \end{cases} \tag{2.24}$$

Notice that θ is used instead of ϕ in the definition of p_o because the line of centers is not known, and it is assumed that the static pressure distributions do not depend on the eccentricity. Applying the boundary conditions to eq. (2.23) allows the constants of integration to be determined.

$$C_1 = -3\mu\delta_p\omega_{pump}\frac{\partial H_\epsilon}{\partial \phi} - \frac{H_\epsilon^3(p_o - p_{case})}{\delta_p} \tag{2.25}$$

$$C_2 = p_o \tag{2.26}$$

Substituting these into the expressions yields the short-width journal bearing pressure distribution.

$$p\left(\phi, y^\theta\right) = \frac{3\mu\omega_{pump}}{H_\epsilon^3}\frac{\partial H_\epsilon}{\partial \phi}\left({y^\theta}^2 - \delta_p y^\theta\right) + p_o\left(1 - \frac{y^\theta}{\delta_p}\right) + \frac{y^\theta}{\delta_p}p_{case} \tag{2.27}$$

2.2.2.6 Rotor Dynamics – Static Pressure Distributions

Now that the pressure distributions between the pintle and the rotor are defined, the net radial force from the static pressure distributions is determined. The forces produced by the pressure ports are given in eq. (2.28) and (2.29).

$$F_{port_m}^{x^\theta} = -p_m H_{port} R_p \int_{\theta_{m_o}}^{\theta_{m_c}} \sin\theta \, d\theta \tag{2.28}$$

$$F_{port_m}^{z^\theta} = p_m H_{port} R_p \int_{\theta_{m_o}}^{\theta_{m_c}} \sin\theta \, d\theta \tag{2.29}$$

where m denotes the port of interest, A or B. The force generated by the static portion of the short-width journal bearing distribution, eq. (2.27), is defined in eq. (2.30) and (2.32), simplifying the expressions leads to eq. (2.31) and (2.33).

x component:

$$F_{p_o}^{x^\theta} = -2\int_0^{\delta_p}\int_0^{2\pi}\left[p_o\left(1-\frac{y^\theta}{\delta_p}\right)+\frac{y^\theta}{\delta_p}p_{case}\right]R_p\sin\theta\,d\theta dy^\theta \tag{2.30}$$

$$F_{p_o}^{x^\theta} = -2R_p\int_0^{2\pi}\left[p_o\left(y^\theta-\frac{{y^\theta}^2}{2\delta_p}\right)+\frac{{y^\theta}^2}{2\delta_p}p_{case}\Big|_{y^\theta=0}^{y^\theta=\delta_p}\right]\sin\theta\,d\theta$$

$$F_{p_o}^{x^\theta} = -\delta_p R_p\int_0^{2\pi}(p_o-p_{case})\sin\theta\,d\theta \tag{2.31}$$

z component:

$$F_{p_o}^{z^\theta} = 2\int_0^{\delta_p}\int_0^{2\pi}\left[p_o\left(1-\frac{y^\theta}{\delta_p}\right)+\frac{y^\theta}{\delta_p}p_{case}\right]R_p\cos\theta\,d\theta dy^\theta \tag{2.32}$$

$$F_{p_o}^{z^\theta} = 2R_p\int_0^{2\pi}\left[p_o\left(y^\theta-\frac{{y^\theta}^2}{2\delta_p}\right)+\frac{{y^\theta}^2}{2\delta_p}p_{case}\Big|_{y^\theta=0}^{y^\theta=\delta_p}\right]\cos\theta\,d\theta$$

$$F_{p_o}^{z^\theta} = \delta_p R_p\int_0^{2\pi}(p_o-p_{case})\cos\theta\,d\theta \tag{2.33}$$

Solving the integrals in eq. (2.31) and (2.33) requires accounting for the piece-wise nature of p_o, expanding the integrals.

$$\begin{aligned}F_{p_o}^{x^\theta} = -\delta_p R_p\Bigg[&\int_{\theta_{A_o}}^{\theta_{A_c}}(p_A-p_{case})\sin\theta\,d\theta\\&+\int_{\theta_{A_c}}^{\theta_{B_o}}\left(\frac{p_A-p_B}{\theta_{A_c}-\theta_{B_o}}(\theta-\theta_{A_c})+p_A-p_{case}\right)\sin\theta\,d\theta\\&+\int_{\theta_{B_o}}^{\theta_{B_c}}(p_B-p_{case})\sin\theta\,d\theta\\&+\int_{\theta_{B_c}}^{2\pi+\theta_{A_o}}\left(\frac{p_B-p_A}{\theta_{B_c}-(\theta_{A_o}+2\pi)}(\theta-\theta_{B_c})+p_B-p_{case}\right)\sin\theta\,d\theta\Bigg]\end{aligned} \tag{2.34}$$

$$F_{p_o}^{z^\theta} = \delta_p R_p \left[\int_{\theta_{A_o}}^{\theta_{A_c}} (p_A - p_{case}) \cos\theta \, d\theta \right.$$
$$+ \int_{\theta_{A_c}}^{\theta_{B_o}} \left(\frac{p_A - p_B}{\theta_{A_c} - \theta_{B_o}} (\theta - \theta_{A_c}) + p_A - p_{case} \right) \cos\theta \, d\theta$$
$$+ \int_{\theta_{B_o}}^{\theta_{B_c}} (p_B - p_{case}) \cos\theta \, d\theta \qquad (2.35)$$
$$\left. + \int_{\theta_{B_c}}^{2\pi+\theta_{A_o}} \left(\frac{p_B - p_A}{\theta_{B_c} - (\theta_{A_o} + 2\pi)} (\theta - \theta_{B_c}) + p_B - p_{case} \right) \cos\theta \, d\theta \right]$$

Solving the integrals in eq. (2.34) and (2.35) for the constant pressures (ports) is straightforward. When transitioning between the ports, p_o is a linear distribution, and it can be written generally as $p_o = \alpha(\theta - \gamma) + \beta$ between θ_1 and θ_2, where α, γ, and β are constants. The sine and cosine integrals are evaluated according to eq. (2.36) and (2.37) respectfully.

$$\int_{\theta_1}^{\theta_2} [\alpha(\theta - \gamma) + \beta] \sin\theta \, d\theta = [\beta \cos\theta - \alpha(\gamma \cos\theta + \sin\theta - \theta \cos\theta)]_{\theta_1}^{\theta_2} \qquad (2.36)$$

$$\int_{\theta_1}^{\theta_2} [\alpha(\theta - \gamma) + \beta] \cos\theta \, d\theta = [\beta \sin\theta + \alpha(\cos\theta + \theta \sin\theta - \gamma \sin\theta)]_{\theta_1}^{\theta_2} \qquad (2.37)$$

The forces from the Couette-Poiseuille regions are given in eq. (2.38) - (2.41). These have the same linear pressure distributions as the short-width journal bearing and can be solved using the previously defined integrals.

$$F_{A-B}^{x^\theta} = -H_{port} R_p \int_{\theta_{A_c}}^{\theta_{B_o}} \left(\frac{p_A - p_B}{\theta_{A_c} - \theta_{B_o}} (\theta - \theta_{A_c}) + p_A \right) \sin\theta \, d\theta \qquad (2.38)$$

$$F_{A-B}^{z^\theta} = H_{port} R_p \int_{\theta_{A_c}}^{\theta_{B_o}} \left(\frac{p_A - p_B}{\theta_{A_c} - \theta_{B_o}} (\theta - \theta_{A_c}) + p_A \right) \cos\theta \, d\theta \qquad (2.39)$$

$$F_{B-A}^{x^\theta} = -H_{port} R_p \int_{\theta_{B_c}}^{2\pi+\theta_{A_o}} \left(\frac{p_B - p_A}{\theta_{B_c} - (\theta_{A_o} + 2\pi)} (\theta - \theta_{B_c}) + p_B \right) \sin\theta \, d\theta \qquad (2.40)$$

$$F_{B-A}^{z^\theta} = H_{port} R_p \int_{\theta_{B_c}}^{2\pi+\theta_{A_o}} \left(\frac{p_B - p_A}{\theta_{B_c} - \left(\theta_{A_o} + 2\pi\right)} \left(\theta - \theta_{B_c}\right) + p_B \right) \cos\theta \, d\theta \tag{2.41}$$

Once the forces from the static pressures are known, eq. (2.42) and (2.43) calculate the net force on the rotor caused by the static pressure distributions between the pintle and rotor. Equations (2.44) and (2.45) give the magnitude, F_R, and direction, Φ_R, of the net radial force generated by the static pressure sources and the pumping cylinders.

$$F_{pintle}^{x^\theta} = F_{port_A}^{x^\theta} + F_{port_B}^{x^\theta} + F_{p_o}^{x^\theta} + F_{A-B}^{x^\theta} + F_{B-A}^{x^\theta} \tag{2.42}$$

$$F_{pintle}^{z^\theta} = F_{port_A}^{z^\theta} + F_{port_B}^{z^\theta} + F_{p_o}^{z^\theta} + F_{A-B}^{z^\theta} + F_{B-A}^{z^\theta} \tag{2.43}$$

$$F_R = \sqrt{\left(F_{cyl}^{x^\theta} - F_{Pintle}^{x^\theta}\right)^2 - \left(F_{cyl}^{z^\theta} - F_{Pintle}^{z^\theta}\right)^2} \tag{2.44}$$

$$\Phi_R = \tan^{-1}\left(\frac{F_{cyl}^{x^\theta} - F_{Pintle}^{x^\theta}}{F_{cyl}^{z^\theta} - F_{Pintle}^{z^\theta}} \right) \tag{2.45}$$

2.2.2.7 Rotor Dynamics – Journal Bearing Eccentricity

A quasi-static assumption is used, implying that the resultant force, F_R, is balanced by the change in eccentricity of the rotor and the pressure that this creates. The eccentricity dependent pressure force is a subset of eq. (2.27) and is explicitly stated in eq. (2.46).

$$p_\epsilon\left(\phi, y^\theta\right) = \frac{3\mu\omega_{pump}}{H_\epsilon^3} \frac{\partial H_\epsilon}{\partial \phi} \left({y^\theta}^2 - \delta_p y^\theta \right) \tag{2.46}$$

Using the definition of H_ϵ from eq. (2.21), taking its derivative, and substituting.

$$p_\epsilon = \frac{3\mu\omega_{pump}\epsilon(\delta_p y^\theta - {y^\theta}^2)}{H_p^2} \left[\frac{\sin\phi}{(1+\epsilon\cos\phi)^3} \right] \tag{2.47}$$

A Half-Sommerfeld condition is assumed which means eq. (2.47) applies for $0 \leq \phi < \pi$ and $p_\epsilon = 0$ for $\pi \leq \phi < 2\pi$. This condition removes the unrealistic negative pressure from the distribution that would arise in a Full-Sommerfeld solution, but this is at the expense of mass

conservation. In this analytical model, the Half-Sommerfeld was considered the best tradeoff between increasing complexity and accuracy. This problem is well documented in Hamrock [47].

Using the technique presented by Hamrock [47], the load components the bearing supports parallel, w^z, and perpendicular, w^x, to the line of centers are calculated according to eq. (2.48) - (2.51).

$$w^x = 2\int_0^{\pi}\int_0^{\delta_p} p_\epsilon R_p \sin\phi \, dy^\theta d\phi \tag{2.48}$$

$$w^x = \frac{\mu R_p \delta_p^3 \omega_{pump}}{2H_p^2}\left[\frac{\pi\epsilon}{(1-\epsilon^2)^{\frac{3}{2}}}\right] \tag{2.49}$$

$$w^z = -2\int_0^{\pi}\int_0^{\delta_p} p_\epsilon R_p \cos\phi \, dy d\phi \tag{2.50}$$

$$w^z = \frac{2\mu R_p \delta_p^3 \omega_{pump}}{H_p^2}\left[\frac{\epsilon^2}{(1-\epsilon^2)^2}\right] \tag{2.51}$$

Now that the perpendicular and parallel load carrying capacity of the eccentric rotor is known, the total load carrying capacity can be calculated.

$$w_R = \sqrt{(w^x)^2 + (w^z)^2} = \frac{\mu R_p \delta_p^3 \omega_{pump}}{2H_p^2}\frac{\epsilon}{(1-\epsilon^2)^2}\sqrt{16\epsilon^2 + \pi^2(1-\epsilon^2)} \tag{2.52}$$

Because it is assumed that $w_R = F_R$, the eccentricity is the only unknown. Therefore, eq. (2.52) can be rearranged as a polynomial of ϵ.

$$\epsilon^8 - 4\epsilon^6 + \frac{6\Lambda + \pi^2 - 16}{\Lambda}\epsilon^4 - \frac{4\Lambda + \pi^2}{\Lambda}\epsilon^2 + 1 = 0 \tag{2.53}$$

where $\Lambda = \left(\frac{2F_R H_p^2}{\mu R_p \delta_p^3 \omega_{pump}}\right)^2$

The roots of ϵ can be found numerically, and then, keeping only the non-imaginary root between zero and one provides the physically significant eccentricity ratio. Once the eccentricity ratio is known, the only other parameter that needs to be determined is the attitude angle, Φ_A, which

is the angle the force vector needs to be rotated in the direction of motion to reach the line of centers. Its value is given by eq. (2.54) and its geometric relationship to the other forces is shown in Figure 2.9.

$$\Phi_A = \tan^{-1}\frac{w^x}{w^z} = \tan^{-1}\frac{\pi\sqrt{1-\epsilon^2}}{4\epsilon} \tag{2.54}$$

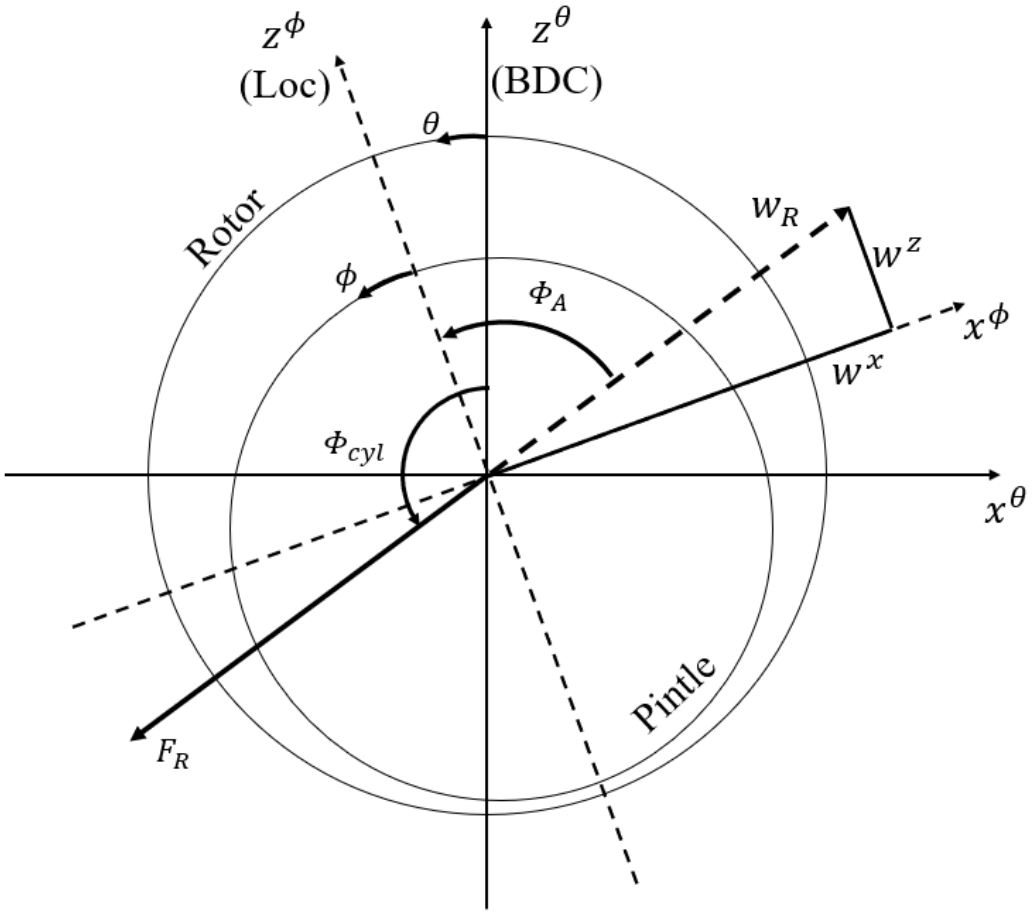

FIGURE 2.9: ECCENTRIC ROTOR GEOMETRY AND FORCE COMPONENTS

From Figure 2.9, the relationship between θ and ϕ can be written according to eq. (2.55).

$$\theta_\phi = \Phi_{cyl} + \pi + \Phi_A \tag{2.55}$$

With this relationship, the gap height can be written in terms of θ.

$$H_\epsilon^\theta = H_p\left[1 + \epsilon\cos\left(\theta - \theta_\phi\right)\right] \tag{2.56}$$

2.2.2.8 Pintle-Rotor Losses

Now that the gap height is known in terms of θ, the leakage and shear at the pintle-rotor interface can be calculated. From Navier-Stokes, the equations for the leakage and shear in the θ and y^{θ} directions per unit width are given according to eq. (2.57) - (2.60).

$$q_{\theta} = -\frac{(H_{\epsilon}^{\theta})^3}{12\mu R_p}\frac{\partial p}{\partial \theta} + \frac{H_{\epsilon}^{\theta} R_p \omega_{pump}}{2} \tag{2.57}$$

$$q_{y} = -\frac{(H_{\epsilon}^{\theta})^3}{12\mu R_p}\frac{\partial p}{\partial y^{\theta}} \tag{2.58}$$

$$\tau_{\theta} = -\frac{H_{\epsilon}^{\theta}}{2R_p}\frac{\partial p}{\partial \theta} + \mu\frac{U_{rotor}}{H_{\epsilon}^{\theta}} \tag{2.59}$$

$$\tau_{y} = -\frac{H_{\epsilon}^{\theta}}{2}\frac{\partial p}{\partial y} \tag{2.60}$$

It is assumed that no losses occur at the constant pressure ports because leakage does not apply within the port and the gap height is considered infinite implying there is no shear. The losses from the Couette-Poiseuille are only in the θ direction with leakage and shear occurring between the ports. Lastly, the short-width journal bearing region experiences leakage in the y^{θ} direction and torque in the θ direction from shear. These integrals are solved for each region numerically in each timestep.

2.2.2.9 Pintle-Rotor Interface Heat Transfer

An important physical parameter when calculating the losses between the pintle and rotor is the viscosity which is temperature dependent. Therefore, a heat transfer model was built to predict the temperature of the oil in the thin gap between the pintle and rotor. The general geometry and control volume boundary are shown in Figure 2.10.

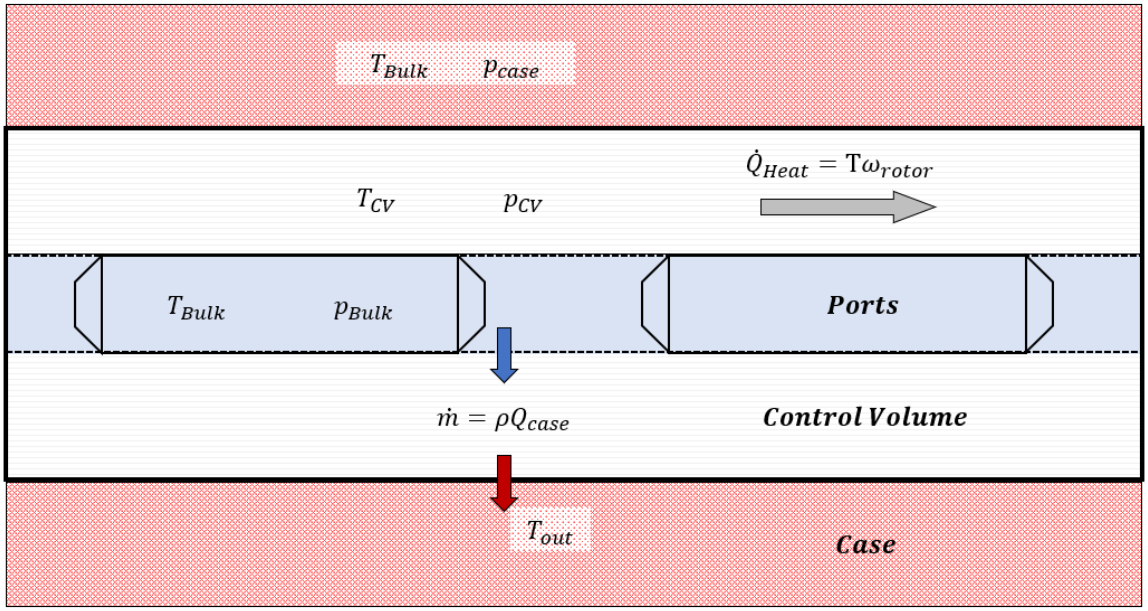

FIGURE 2.10: CONTROL VOLUME DEFINITION FOR HEAT TRANSFER AT THE PINTLE-ROTOR INTERFACE

The model is formed from the first law of thermodynamics where the change in energy in the control volume (E_{cv}) is equal to the change in incoming energy minus the change in outgoing energy ($\dot{E}_{in} - \dot{E}_{out}$).

$$\frac{dE_{cv}}{dt} = \dot{E}_{in} - \dot{E}_{out} \tag{2.61}$$

Also from the first law of thermodynamics, $\dot{E}_{in}$ and $\dot{E}_{out}$ can be rewritten.

$$\frac{dE_{cv}}{dt} = T\omega + \dot{m}_{in}\left(c_p T_{bulk} + \frac{1}{\rho}p_{bulk} + \frac{KE}{\dot{m}_{in}} + \frac{PE}{\dot{m}_{in}}\right) - \dot{m}_{out}\left(c_p T_{out} + \frac{1}{\rho}p_{out} + \frac{KE}{\dot{m}_{out}} + \frac{PE}{\dot{m}_{out}}\right) \tag{2.62}$$

The assumptions are made that there is no significant change in kinetic or potential energy, that the outgoing pressure is case, and that the fluid is incompressible in the thin gap. This last assumption implies that $\dot{m}_{in} = \dot{m}_{out} = \dot{m}$. Using these assumptions, eq. (2.62) simplifies to eq. (2.63).

$$\frac{dE_{cv}}{dt} = T\omega + \dot{m}\left(c_p(T_{bulk} - T_{out}) + \frac{1}{\rho}(p_{bulk} - p_{case})\right) \tag{2.63}$$

The energy in the gap is described according to the first law of thermodynamics.

$$E_{cv} = m_{cv}c_pT_{cv} + V_{cv}p_{cv} + KE_{cv} + PE_{cv} \tag{2.64}$$

where m_{cv} is the mass, V_{cv} is the volume, p_{cv} is the mean pressure, KE_{cv} is the kinetic energy, and PE_{cv} is the potential energy. Taking the derivative.

$$\frac{dE_{cv}}{dt} = \frac{d\left(m_{cv}c_pT_{cv}\right)}{dt} + \frac{d(V_{cv}p_{cv})}{dt} + \frac{d(KE)}{dt} + \frac{d(PE)}{dt} \tag{2.65}$$

$$\frac{dE_{cv}}{dt} = c_p\left[T_{cv}\frac{dm_{cv}}{dt} + m_{cv}\frac{dT_{cv}}{dt}\right] + p_{cv}\frac{dV_{cv}}{dt} + V_{cv}\frac{dp_{cv}}{dt} \tag{2.66}$$

Plugging eq. (2.66) into eq. (2.63) and solving for the time derivative of temperature yields eq. (2.68).

$$\begin{aligned} c_pT_{cv}\frac{dm_{cv}}{dt} + c_pm_{cv}\frac{dT_{cv}}{dt} + p_{cv}\frac{dV_{cv}}{dt} + V_{cv}\frac{dp_{cv}}{dt} \\ = \mathrm{T}\omega + \dot{m}\left(c_p(T_{bulk} - T_{out}) + \frac{1}{\rho}(p_{bulk} - p_{case})\right) \end{aligned} \tag{2.67}$$

$$\begin{aligned} \frac{dT_{cv}}{dt} = \frac{1}{c_pm_{cv}}\left[\mathrm{T}\omega + \dot{m}\left(c_p(T_{bulk} - T_{out}) + \frac{1}{\rho}(p_{bulk} - p_{case})\right) - p_{cv}\frac{dV_{cv}}{dt}\right. \\ \left. - V_{cv}\frac{dp_{cv}}{dt} - c_pT_{cv}\frac{dm_{cv}}{dt}\right] \end{aligned} \tag{2.68}$$

Equation (2.68) applies to any control volume where there is no heat generation, no significant change in kinetic or potential energy, and the inlet and outlet flow rates are equal. The following assumptions are made to apply the equation to the pintle-rotor interface.

1. There is one control volume that uses average properties. This is effectively assuming the rotation of the rotor thoroughly mixes the oil.
2. The top and bottom of the control volume seen in Figure 2.10 are symmetric.
3. Torque and leakage between ports is not considered in the heat transfer model. Ports A & B are considered temperature sources of sufficient thermal mass to maintain a constant temperature, T_{bulk}.

The variables in eq. (2.68) are defined as follows. First, the torque can be found according to eq. (2.59) and (2.60). The mass flow rate is from the center of the pintle to the case.

$$\dot{m} = \rho Q_{leak} \tag{2.69}$$

where Q_{leak} is found according to eq. (2.58). The volume and mass of the fluid within the control volume are given by eq. (2.70) and (2.71) respectfully.

$$V_{cv} = 2\delta_p \pi \left(R_{ri}^2 - R_p^2\right) \tag{2.70}$$

$$m_{cv} = \rho V_{cv} \tag{2.71}$$

The volume does not change with time, so the derivatives of eq. (2.70) and (2.71) are both zero. Next, a linear temperature distribution is assumed through the control volume in the direction of leakage. This means that the temperature out of the control volume can be written in terms of the temperature in the control volume.

$$T_{cv} = \frac{1}{2}(T_{out} + T_{bulk}) \Rightarrow T_{out} = 2T_{cv} - T_{bulk} \tag{2.72}$$

The pressure in the control volume, p_{cv}, can be found numerically by averaging the pressure distribution given in eq. (2.27). The derivative of the control volume pressure with respect to time, $d(p_{cv})/dt$ is found numerically. Lastly, the bulk pressure, p_{bulk}, is found using the weighted average of the pressure ports and the Couette-Poiseuille pressure distributions.

These variable definitions are applied within each timestep of the simulation. The differential equation, (2.68), is solved by assuming an initial temperature and numerically integrating through time. This temperature is then used to calculate the fluid viscosity before the rotor position is found using the method presented in Sections 2.2.2.2 - 2.2.2.7. The full procedure for analyzing the pintle-rotor interface is presented in Figure 2.11.

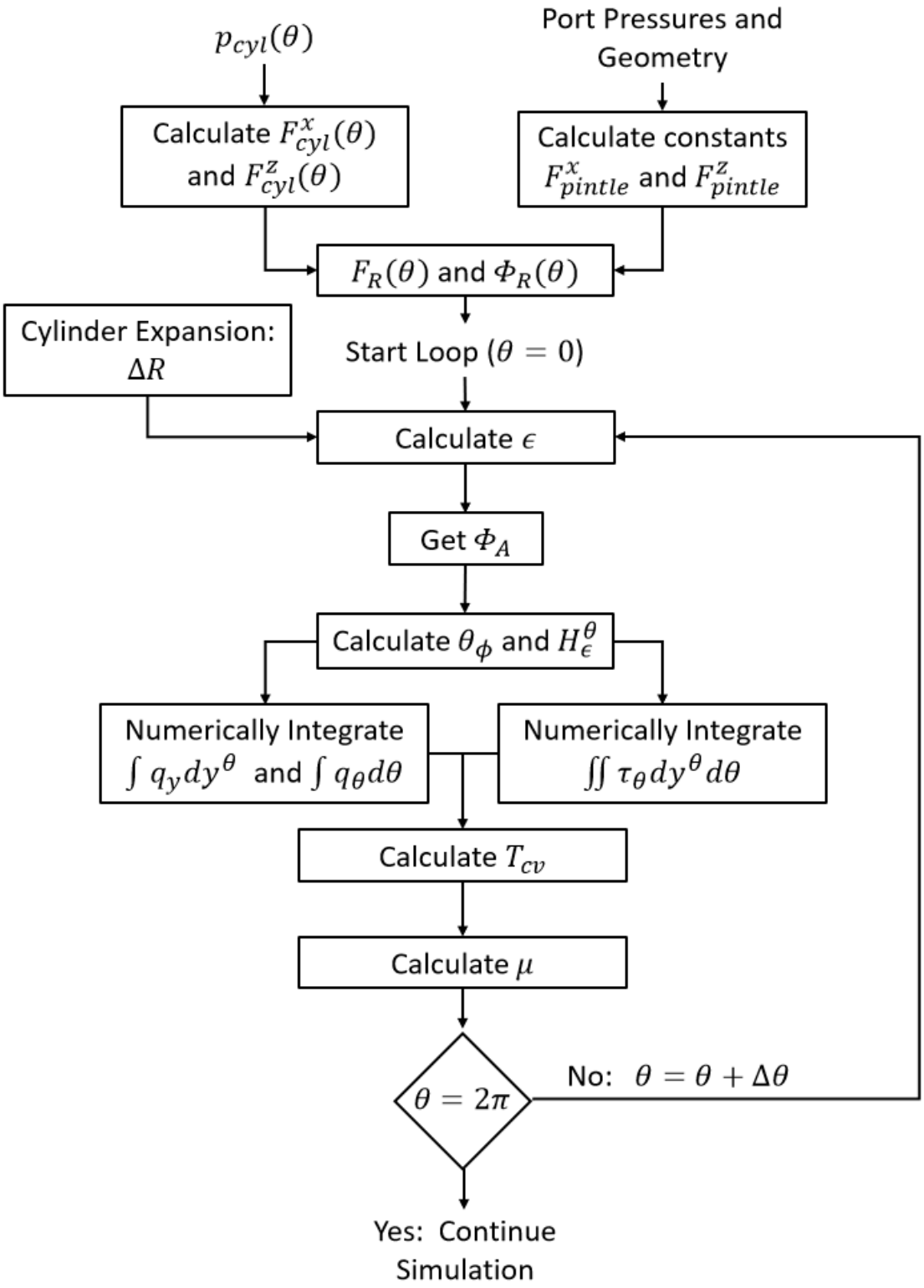

FIGURE 2.11: PINTLE-ROTOR INTERFACE CODE DIAGRAM

2.2.3 Ball-Cylinder Interface

The next interface that is modeled is between the ball piston and the cylinder wall. The model begins by assuming that the pump rotates at a constant speed, and therefore, the ball piston kinematics can be defined. Next, the dynamics needed to achieve the kinematics are analyzed and the position of the ball within the cylinder is modeled. The ball position along with the cylinder expansion model is used to determine the clearance at each point around the ball. After the clearance is known, the hydrodynamic fluid mechanics model is presented to find the pressure, shear, and leakage at the ball piston. Next, this information is used within the heat transfer model to determine the oil temperature. The section concludes by discussing the limitations of the hydrodynamic lubrication assumption and presenting an empirical elastohydrodynamic model that is used when the original assumptions are not valid.

2.2.3.1 Ball-Cylinder Interface Kinematics

The geometry of the radial ball unit is defined in Figure 2.12. It shows the pump eccentricity between the cam ring and rotor block. A single ball piston and cylinder wall are shown for simplicity. The pressure angle, ϕ_{pump}, denotes the angle between the normal force and the linear velocity of the piston; note that the direction of the velocity is towards the center of the rotor, O_R, and the normal force direction is towards the center of the cam, O_C. From the law of sines, the pressure angle is given in eq. (2.73).

$$\phi_{pump} = \sin^{-1}\left(\frac{e_{pump}}{R_o}\sin\theta\right) \tag{2.73}$$

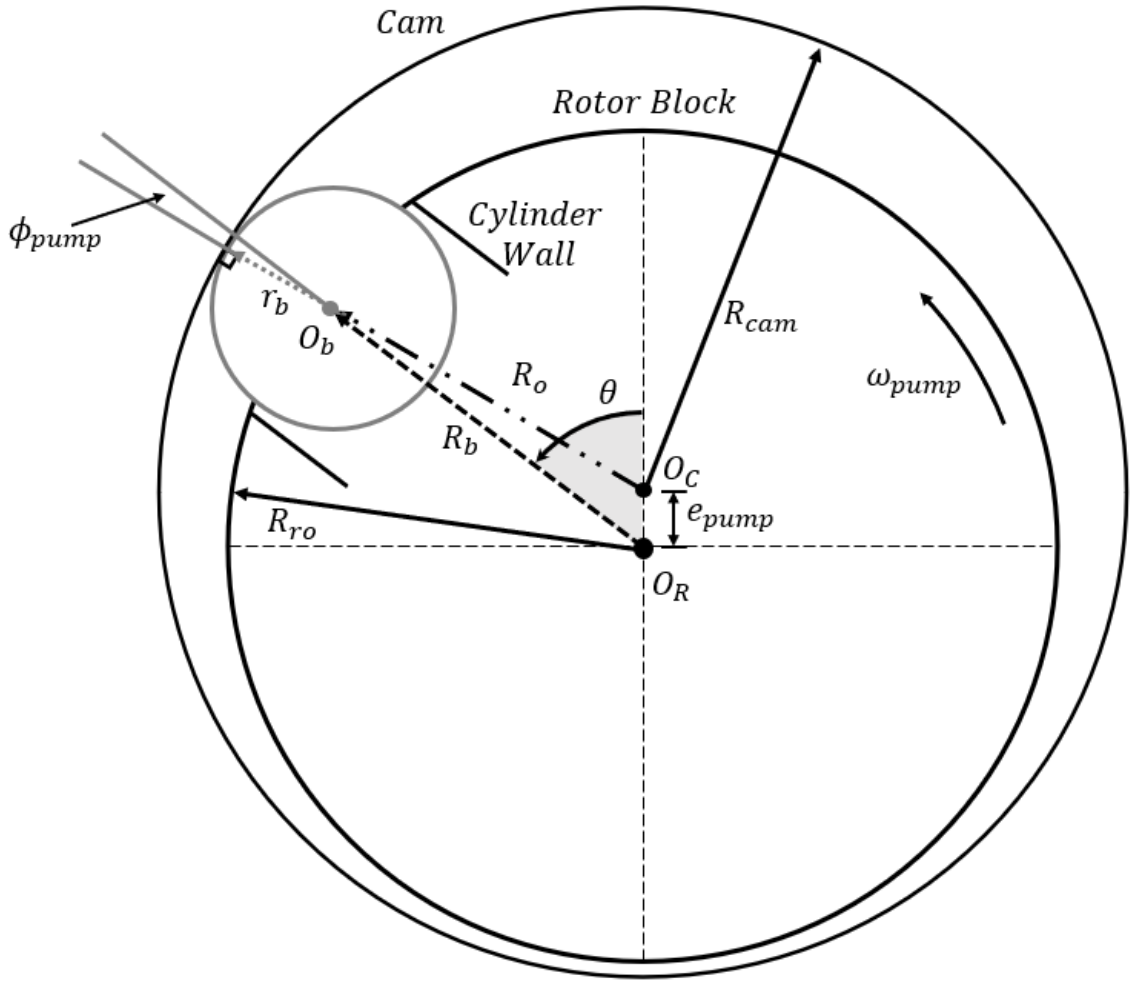

FIGURE 2.12: BALL PISTON KINEMATICS

To calculate the kinematics of the ball piston, a reference frame needs to be selected. From Figure 2.12, polar coordinates are used with origin at O_R, θ sets the angular position, and R_b sets the radial position of the ball piston. Within this reference frame, the angular velocity is constant, ω_{pump}. The radial position is found using the law of cosines, eq. (2.74).

$$R_o^2 = R_b^2 + e_{pump}^2 - 2R_b e_{pump}\cos\theta$$

$$0 = R_b^2 - R_b\left(2e_{pump}\cos\theta\right) + \left(e_{pump}^2 - R_o^2\right)$$

$$R_b = \frac{1}{2}\left(2e_{pump}\cos\theta \pm \sqrt{4e_{pump}^2\cos^2\theta - 4\left(e_{pump}^2 - R_o^2\right)}\right)$$

$$R_b = e_{pump}\cos\theta + \sqrt{R_o^2 + e_{pump}^2(\cos^2\theta - 1)} \tag{2.74}$$

where $R_o = R_{cam} - r_b$. Next, because a constant angular velocity of ω_{pump} is known in advance, angular kinematics can be used to determine the ball piston acceleration in the r and θ directions with unit vectors $\hat{e}_r$ and $\hat{e}_\theta$ respectfully. Equation (2.75) and (2.76) give the known kinematic relationships for polar coordinates [49].

$$\vec{v} = \dot{r}\hat{e}_r + r\dot{\theta}\hat{e}_\theta \tag{2.75}$$

$$\vec{a} = \left(\ddot{r} - r\dot{\theta}^2\right)\hat{e}_r + \left(r\ddot{\theta} + 2\dot{r}\dot{\theta}\right)\hat{e}_\theta \tag{2.76}$$

Using the physical situation shown in Figure 2.12, the expressions (2.77) - (2.81) are known.

$$\dot{\theta} = \omega_{pump} \tag{2.77}$$

$$\ddot{\theta} = 0 \tag{2.78}$$

Utilizing the fact that $R_o^2 \gg e_{pump}^2$, eq. (2.74) can be simplified.

$$r = R_b \approx R_o + e_{pump}\cos\theta \tag{2.79}$$

$$\dot{r} = \dot{R}_b \approx -e_{pump}\omega_{pump}\sin\theta \tag{2.80}$$

$$\ddot{r} = \ddot{R}_b \approx -e_{pump}\omega_{pump}^2\cos\theta \tag{2.81}$$

Substituting eq. (2.77) - (2.81) into eq. (2.76).

$$\begin{aligned}\vec{a} = &\left[-e_{pump}\omega_{pump}^2\cos\theta - \left(R_o + e_{pump}\cos\theta\right)\omega_{pump}^2\right]\hat{e}_r \\ &+ \left[-2e_{pump}\omega_{pump}^2\sin\theta\right]\hat{e}_\theta\end{aligned} \tag{2.82}$$

2.2.3.2 Ball-Cylinder Interface Dynamics

The kinematic analysis is necessary to determine the forces acting on the ball piston; these are shown in Figure 2.13. The normal force, F_N acts towards the center of the cam, O_c, while the

traction force, F_T, acts perpendicular to the normal. Also shown are the pressure distribution, $p(\vartheta, \varphi)$, and the shear distribution, $\tau(\vartheta, \varphi)$[5].

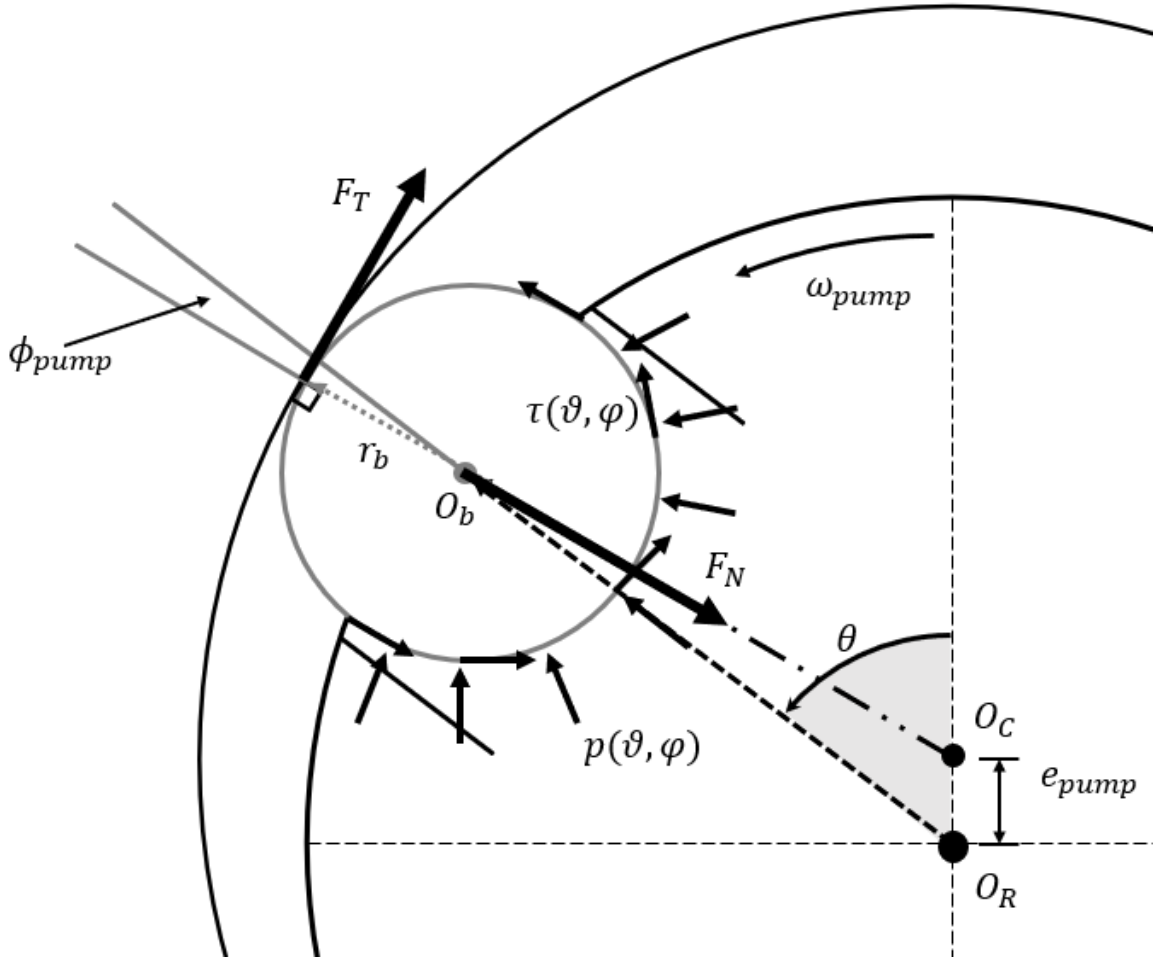

FIGURE 2.13: BALL PISTON DYNAMICS

The traction force can be found using a moment balance.

$$\sum M_{O_b} = F_T r_b + F_\tau r_b = 0$$

$$F_T = -F_\tau \tag{2.83}$$

[5] ϑ and φ are spherical coordinates that define positions on the ball piston's surface.

where F_τ is the force from the shear distribution. The normal force can be calculated using the acceleration from eq. (2.82) in the r direction, Newton's second law gives eq. (2.84).

$$F_{N_{\hat{r}}} = m_b\left(-2e_{pump}\omega_{pump}^2\cos\theta - R_o\omega_{pump}^2\right) - F_{p_{\hat{r}}} - F_{\tau_{\hat{r}}} - F_{T_{\hat{r}}} \tag{2.84}$$

where F_p is the force from the pressure distribution. Finally, the force balance can be solved in the θ direction using the acceleration from eq. (2.82).

$$m_b\left(-2e_{pump}\omega_{pump}^2\sin\theta + a_{\hat{\theta}}\right) = F_{p_{\hat{\theta}}} + F_{\tau_{\hat{\theta}}} + F_{T\hat{\theta}} + F_{N_{\hat{\theta}}} \tag{2.85}$$

where $a_{\hat{\theta}}$ is the ball's acceleration within the cylinder and is the only unknown. Solving for this acceleration.

$$a_{\hat{\theta}} = \frac{1}{m_b}\left(F_{p_{\hat{\theta}}} + F_{\tau_{\hat{\theta}}} + F_{T\hat{\theta}} + F_{N_{\hat{\theta}}}\right) + 2e_{pump}\omega_{pump}^2\sin\theta \tag{2.86}$$

$a_{\hat{\theta}}$ accounts for the fact that the ball can freely move within the cylinder; however, the possible movement is on the order of magnitude of microns making the constant angular velocity assumption still valid. The small angular deviation also means that a local reference frame at the ball piston can be represented in cartesian coordinates. The local reference frame is shown with the dynamics in Figure 2.14 with z_b always in the r direction and x_b always in the θ direction. Note that the clearance between the ball and the cylinder wall is greatly exaggerated. The ball kinematics in this local coordinate frame can then be solved, where e_{b_k} defines the ball eccentricity of the ball during the k^{th} timestep.

$$\ddot{e}_{b_k} = -a_{\hat{\theta}\,k} \tag{2.87}$$

$$\dot{e}_{b_k} = \dot{e}_{b\,k-1} + e_{b_k}\Delta t \tag{2.88}$$

$$e_{b_k} = e_{b_{k-1}} + \dot{e}_{b_k}\Delta t + \frac{1}{2}\ddot{e}_{b_k}\Delta t^2 \tag{2.89}$$

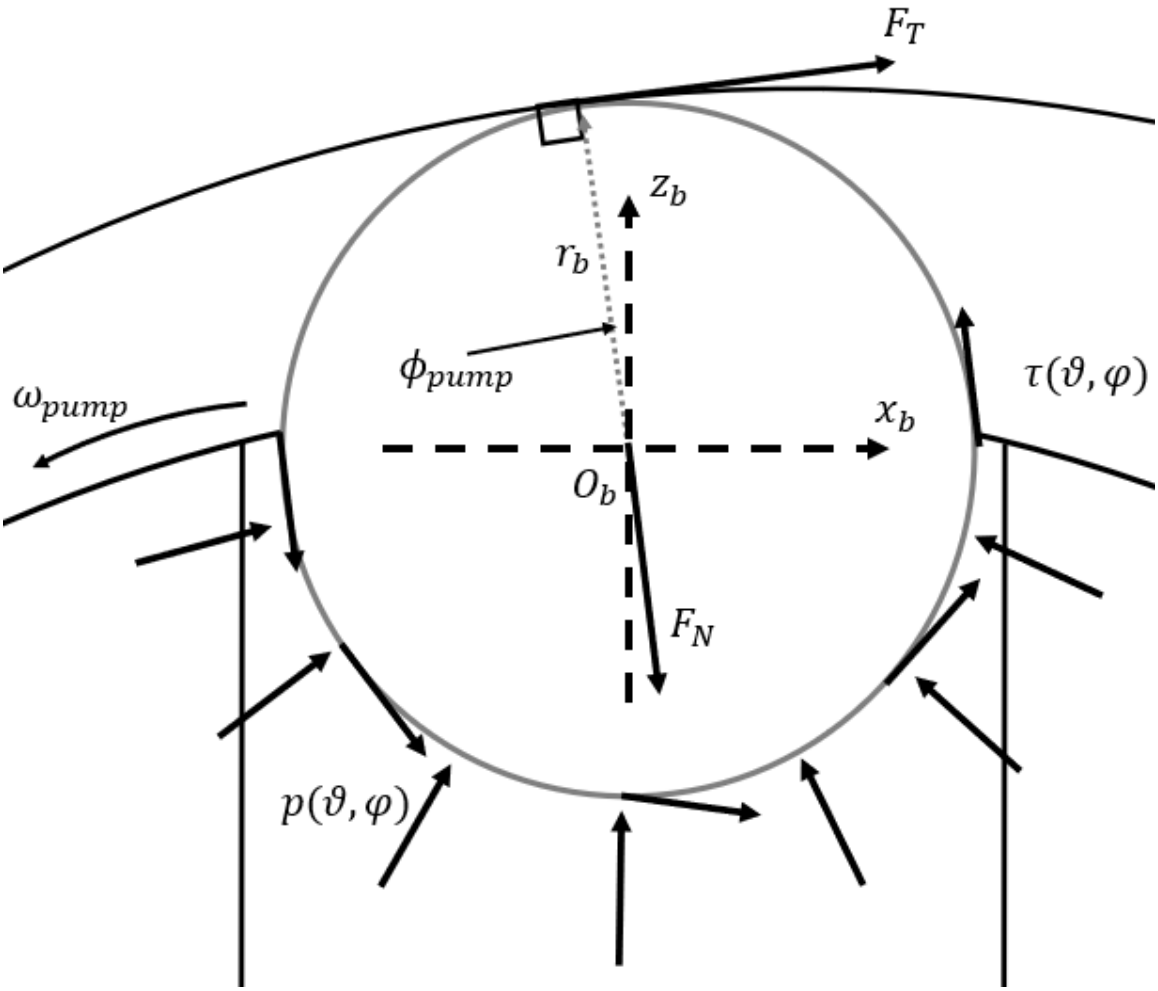

FIGURE 2.14: LOCAL BALL PISTON REFERENCE FRAME AND DYNAMICS

The moment and force balances can be solved if the pressure and shear distributions are known. The following sections walk through the fluid mechanics at the ball-cylinder interface.

2.2.3.3 Cylinder Expansion

First, to calculate the fluid mechanics at the ball-cylinder interface, the clearance between the ball piston and the cylinder wall must be known. The initial clearance can be measured, but the pressure during operation will elastically deform the cylinder. Therefore, a rough model of the cylinder expansion was created to approximate the change in clearance between the two surfaces. The geometry is shown in Figure 2.15.

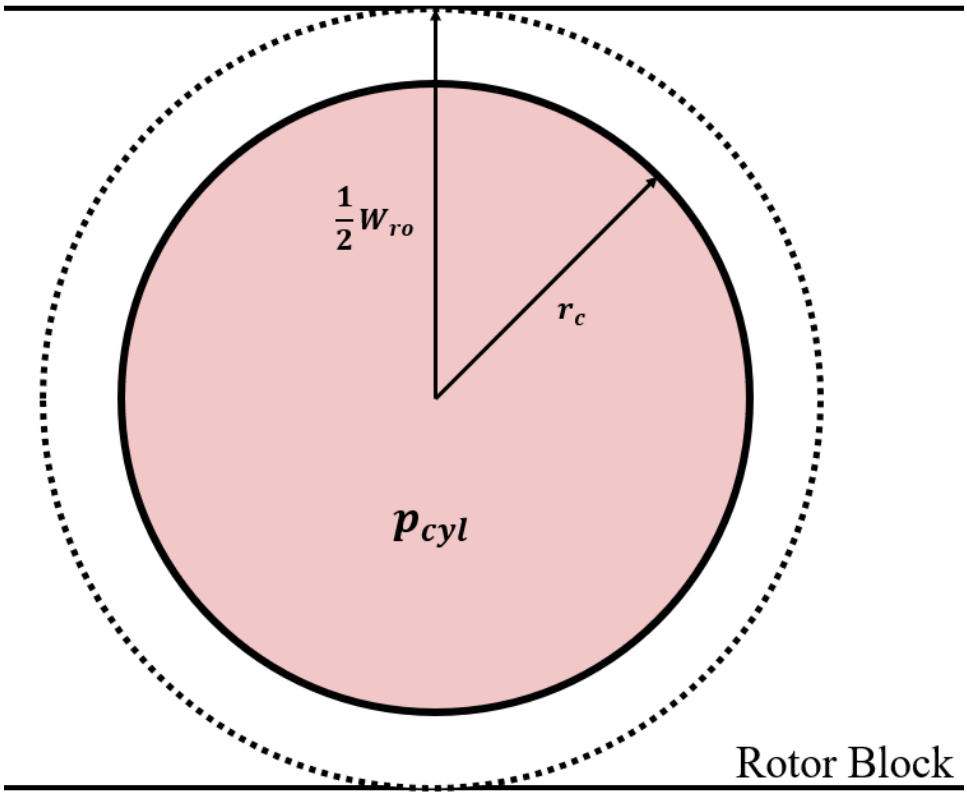

FIGURE 2.15: BALL-CYLINDER PRESSURE VESSEL GEOMETRY

The expansion was modeled using a thick walled pressure vessel assumption with only internal pressure. Note that this change in radius and the clearance will be a function of time because the cylinder pressure changes throughout operation.

$$\Delta r_c = \frac{p_{cyl} r_c}{E}\left(\nu + \frac{\left(\frac{1}{2}W_{ro}\right)^2 + r_c^2}{\left(\frac{1}{2}W_{ro}\right)^2 - r_c^2}\right) \tag{2.90}$$

where E is the elastic modulus, and ν is Poisson's ratio. The radial clearance between the parts is given in eq. (2.91).

$$h_o = r_c + \Delta r_c - r_b \tag{2.91}$$

The change in radius calculated by eq. (2.90) overpredicts the expansion because $\frac{1}{2}W_{ro}$ is the thinnest value of the wall. However, this provides a conservative estimate for the power loss since the leakage is more sensitive to the clearance than the shear rate.

2.2.3.4 Ball-Cylinder Interface Fluid Mechanics

Work by Jamzedeh [10] calculated the ball's eccentric position in the cylinder based on a static operating pressure and determined the equilibrium position of the ball. Jamzedeh did not consider the cylinder pressure dynamics or the side load arising from the cam pressure angle. The following model predicts the fluid mechanics at the ball piston throughout operation. Figure 2.16 and Figure 2.17 show the geometry of the ball-cylinder.

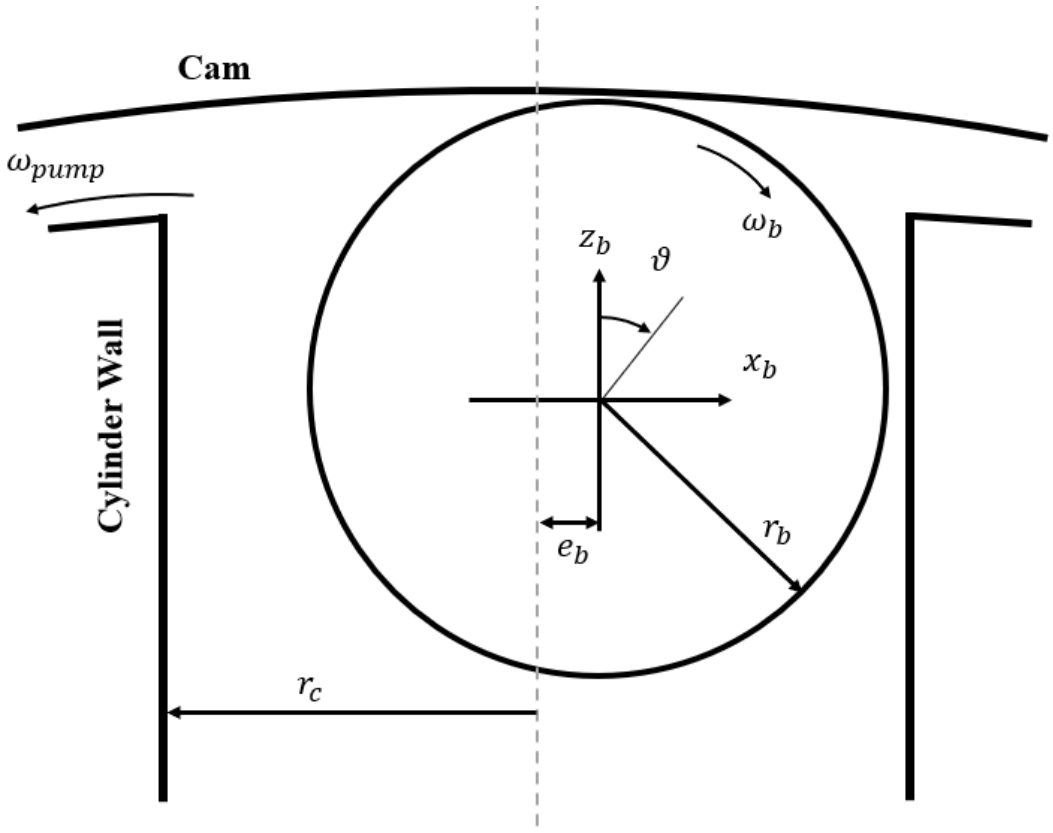

FIGURE 2.16: BALL PISTON X-Z CROSS SECTION

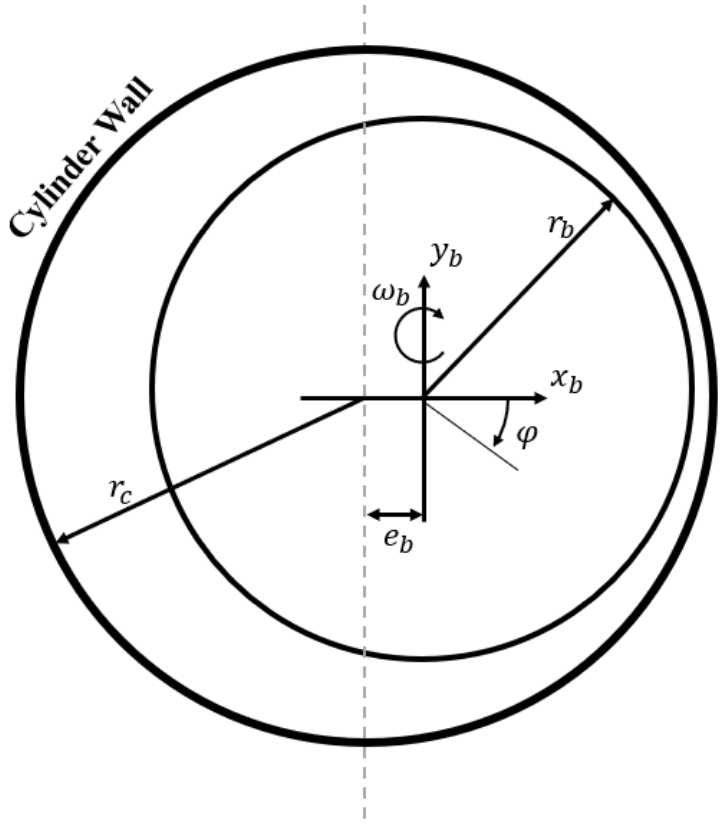

FIGURE 2.17: BALL PISTON X-Y CROSS SECTION

The clearance is greatly exaggerated in the figures with the actual difference between r_b and r_c being in the micron range. Jamzedeh showed that for this geometry the distance between the ball piston and the cylinder at any location can be found using eq. (2.92) [10].

$$h = h_o + r_b - r_b \sin\vartheta - e_b \cos\varphi \tag{2.92}$$

where h_o is defined in eq. (2.91). The change in nominal radial clearance, h_o, is considered approximately constant, so the ball eccentricity is the only part of eq. (2.92) that changes with time. Equation (2.93) gives the time derivative of the gap height.

$$\frac{dh}{dt} = -\dot{e}_b \cos\varphi \tag{2.93}$$

The extremely thin gap between the ball and cylinder means that lubrication theory is applicable, and Reynold's equation governs the fluid mechanics. The full Reynold's equation can be written using the cartesian coordinates defined in Figure 2.16 and Figure 2.17.

$$\frac{\partial}{\partial z_b}\left(-\frac{h^3}{12\mu}\frac{\partial p}{\partial z_b}+(U_1+U_2)\frac{h}{2}\right)+\frac{\partial}{\partial y_b}\left(-\frac{h^3}{12\mu}\frac{\partial p}{\partial y_b}+(V_1+V_2)\frac{h}{2}\right)+\frac{dh}{dt}=0 \quad (2.94)$$

Using the geometry defined in Figure 2.16 and applying eq. (2.94) to the thin gap (where $z_b \approx 0$), then there is no significant velocity or pressure differential in the y_b direction. Applying this assumption.

$$\frac{\partial}{\partial z_b}\left(-\frac{h^3}{12\mu}\frac{\partial p}{\partial z_b}+(U_1+U_2)\frac{h}{2}\right)+\frac{dh}{dt}=0 \quad (2.95)$$

Converting from Cartesian to spherical coordinates can be done using the following relationships.

$$x_b = r_b \sin\vartheta \cos\varphi \quad (2.96)$$

$$y_b = r_b \sin\vartheta \sin\varphi \quad (2.97)$$

$$z_b = r_b \cos\vartheta \quad (2.98)$$

Writing Reynold's equation with spherical coordinates.

$$\frac{-1}{r_b \sin\vartheta}\frac{\partial}{\partial\vartheta}\left(-\frac{h^3}{12\mu}\frac{-1}{r_b \sin\vartheta}\frac{\partial p}{\partial\vartheta}+(U_1+U_2)\frac{h}{2}\right)+\frac{dh}{dt}=0 \quad (2.99)$$

where ϑ is the polar angle and φ is the azimuthal angle. Using spherical coordinates, the tangential velocity at each point on the ball surface can be determined.

$$U_b = r_b\omega_b\sqrt{\cos^2\vartheta+\sin^2\vartheta\cos^2\varphi}+e_{pump}\omega_{pump}\sin\theta_{cyl} \quad (2.100)$$

Equation (2.100) is simplified because only the thin gap region is considered.

$$U_b = r_b\omega_b\cos\varphi+e_{pump}\omega_{pump}\sin\theta_{cyl} \qquad (\vartheta \approx \pi/2) \quad (2.101)$$

Rearranging the equations and integrating by ϑ.

$$\frac{h^3}{12\mu r_b \sin\vartheta}\frac{\partial p}{\partial\vartheta}+U_b\frac{h}{2}+r_b\cos\vartheta\frac{dh}{dt}=C_o \quad (2.102)$$

Substituting the expression for $\frac{dh}{dt}$, eq. (2.93), and letting $C_1 = 12r_bC_o$.

$$\frac{\partial p}{\partial \vartheta} = C_1 \frac{\mu \sin \vartheta}{h^3} + 12 r_b^2 \dot{e}_b \cos \varphi \frac{\mu \cos \vartheta \sin \vartheta}{h^3} - 6 r_b U_b \frac{\mu \sin \vartheta}{h^2} \tag{2.103}$$

To determine the pressure at each point around the ball, two boundary conditions are needed so that eq. (2.103) can be integrated:

$$\vartheta = 0 \quad \rightarrow \quad p = p_{case}$$
$$\vartheta = \pi \quad \rightarrow \quad p = p_{cyl}$$

μ and h both are functions of ϑ so integrating the equation is done numerically.

$$\int_{p_{case}}^{p_{cyl}} dp = C_1 \int_0^{\pi} \frac{\mu \sin \vartheta}{h^3} d\vartheta + 12 r_b^2 \dot{e}_b \cos \varphi \int_0^{\pi} \frac{\mu \cos \vartheta \sin \vartheta}{h^3} d\vartheta - 6 r_b U_b \int_0^{\pi} \frac{\mu \sin \vartheta}{h^2} d\vartheta \tag{2.104}$$

The integrals are definite and can be evaluated. Equations (2.105) - (2.108) define their values to form an expression for the constant C_1.

$$\Delta p = p_{cyl} - p_{case} \tag{2.105}$$

$$S_1 = \int_0^{\pi} \frac{\mu \cos \vartheta \sin \vartheta}{h^3} d\vartheta \tag{2.106}$$

$$S_2 = \int_0^{\pi} \frac{\mu \sin \vartheta}{h^2} d\vartheta \tag{2.107}$$

$$S_3 = \int_0^{\pi} \frac{\mu \sin \vartheta}{h^3} d\vartheta \tag{2.108}$$

$$C_1 = \left(\Delta p - 12 r_b^2 \dot{e}_b \cos \varphi \, S_1 + 6 r_b U_b S_2 \right) \frac{1}{S_3} \tag{2.109}$$

Substituting these equations into eq. (2.103) gives an expression for the change in pressure.

$$\frac{\partial p}{\partial \vartheta} = \frac{\Delta p \mu \sin\vartheta}{S_3 h^3} - 12 r_b^2 \dot{e}_b \cos\varphi \frac{\mu \sin\vartheta}{h^3}\left(\frac{S_1}{S_3} - \cos\vartheta\right) + 6 r_b U_b \frac{\mu \sin\vartheta}{h^3}\left(\frac{S_2}{S_3} - h\right) \tag{2.110}$$

But $\vartheta \approx \pi/2$ so $\cos\vartheta \approx 0$.

$$\frac{\partial p}{\partial \vartheta} = \frac{\Delta p \mu \sin\vartheta}{S_3 h^3} - 12 r_b^2 \dot{e}_b \cos\varphi \frac{\mu \sin\vartheta}{h^3}\frac{S_1}{S_3} + 6 r_b U_b \frac{\mu \sin\vartheta}{h^3}\left(\frac{S_2}{S_3} - h\right) \tag{2.111}$$

Next, to find the pressure at any point of the ball, integration is done again, but this time from 0 to an arbitrary polar angle, ϑ.

$$\int_{p_{case}}^{p(\vartheta)} dp = C_1 \int_0^{\vartheta} \frac{\mu \sin\vartheta}{h^3} d\vartheta + 12 r_b^2 \dot{e}_b \cos\varphi \int_0^{\vartheta} \frac{\mu \cos\vartheta \sin\vartheta}{h^3} d\vartheta - 6 r_b U_b \int_0^{\vartheta} \frac{\mu \sin\vartheta}{h^2} d\vartheta \tag{2.112}$$

Defining the integrals.

$$R_1 = \int_0^{\vartheta} \frac{\mu \cos\vartheta \sin\vartheta}{h^3} d\vartheta \tag{2.113}$$

$$R_2 = \int_0^{\vartheta} \frac{\mu \sin\vartheta}{h^2} d\vartheta \tag{2.114}$$

$$R_3 = \int_0^{\vartheta} \frac{\mu \sin\vartheta}{h^3} d\vartheta \tag{2.115}$$

The expression for the pressure at any point of the ball is given by eq. (2.116).

$$p(\vartheta) = p_{case} + \Delta p \frac{R_3}{S_3} - 12 r_b^2 \dot{e}_b \cos\varphi \left(S_1 \frac{R_3}{S_3} - R_1\right) + 6 r_b U_b \left(S_2 \frac{R_3}{S_3} - R_2\right) \tag{2.116}$$

Equation (2.116) shows that the pressure distribution contains three separate physical contributions. A pressure differential term:

$$p_p(\vartheta) = p_{case} + \Delta p \frac{R_3}{S_3}$$

A normal squeeze term:

$$p_n(\vartheta) = -12r_b^2\dot{e}_b\cos\varphi\left(S_1\frac{R_3}{S_3} - R_1\right)$$

And a velocity, or Couette term:

$$p_c(\vartheta) = 6r_bU_b\left(S_2\frac{R_3}{S_3} - R_2\right)$$

Once the pressure distribution is known, the leakage and shear that occur at the ball piston can be determined. It is assumed that in the gap, there is not significant leakage circumferentially around the ball so only the polar direction (cylinder to case) is considered. The general expression for the leakage in the ϑ direction is given in eq. (2.117).

$$Q_\vartheta = \frac{h^3}{12\mu r_b\sin\vartheta}\frac{\partial p}{\partial\vartheta} + \frac{U_1+U_2}{2}h \tag{2.117}$$

Substituting the expression found for $\partial p/\partial\vartheta$.

$$Q_\vartheta = \frac{\Delta p}{12r_bS_3} - r_b\dot{e}_b\cos\varphi\frac{S_1}{S_3} + \frac{U_b}{2}\frac{S_2}{S_3} \tag{2.118}$$

The same process can be done for the shear distribution on the ball where the general form is given in eq. (2.119).

$$\tau_{ball}(\vartheta) = -\frac{h}{2r_b\sin\vartheta}\frac{\partial p}{\partial\vartheta} + \mu\frac{U_1-U_2}{h} \tag{2.119}$$

Again, substituting the expression found for $\partial p/\partial\vartheta$.

$$\tau_{ball}(\vartheta) = -\frac{\mu}{h^2}\left[\frac{\Delta p}{2r_bS_3} - 6r_b\dot{e}_b\cos\varphi\frac{S_1}{S_3} + 4U_b\left(\frac{3S_2}{4S_3} - h\right)\right] \tag{2.120}$$

The shear on the ball creates a resistive torque acting on the ball piston that must be overcome to keep the ball from skidding.

$$\mathrm{T}_{ball} = \int_0^{2\pi}\int_{\vartheta_1}^{\vartheta_2}\tau_{ball}(\vartheta,\varphi)\cdot r_b^3\sin\vartheta\sqrt{\cos^2\vartheta + \sin^2\vartheta\cos^2\varphi}\cdot sign(\cos\varphi)d\vartheta d\varphi \tag{2.121}$$

The $sign(\cos\varphi)$ term is necessary to determine the direction of the torque. A positive T_{ball} implies that it is assisting the ball in rotating. The square root term gives the correct distance from the axis of rotation to the point on the ball surface.

An important note is that the fluid mechanics derivation applies to a given azimuthal angle, φ, and that to determine the pressure, shear, and leakage distributions around the ball, each azimuthal angle must be analyzed.

2.2.3.5 Ball-Cylinder Interface Heat Transfer

Just like the pintle-rotor interface discussed in section 2.2.2.9, the fluid mechanics at the ball-cylinder interface are highly dependent on the viscosity, which means that a heat transfer model is necessary to accurately predict the interface behavior. Figure 2.18 shows the general geometry for the heat transfer model around the ball.

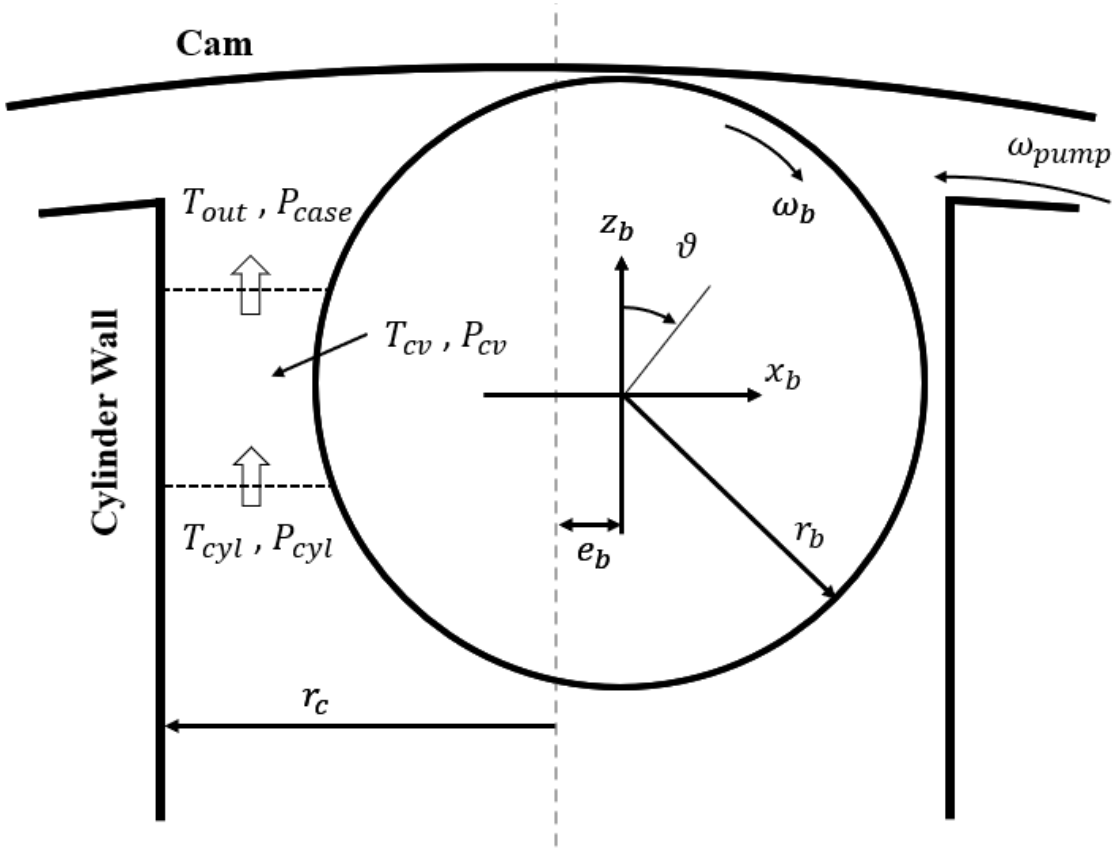

FIGURE 2.18: GENERAL BALL CYLINDER HEAT TRASFER CONTROL VOLUME

The governing equation, (2.122), applies the first law of thermodynamics to a control volume assuming the kinetic and potential energy are negligible. However, a single control volume can no longer be selected as the temperature will vary spatially around the ball.

$$\frac{dE_{cv}}{dt} = \mathrm{T}\omega + \dot{m}_{in}\left(c_p T_{bulk} + \frac{1}{\rho}p_{bulk}\right) - \dot{m}_{out}\left(c_p T_{out} + \frac{1}{\rho}p_{out}\right) \tag{2.122}$$

The following assumptions are made to apply the equation to the ball-cylinder interface.

1. No leakage in the azimuthal direction means multiple control volumes are needed to determine the temperature change circumferentially around the ball, see Figure 2.19.
2. Leakage from cylinder to case implies the fluid is thoroughly mixed for a given circumferential position allowing the temperature to not vary with changing ϑ.
3. The movement of the ball piston changes the amount of mass within a control volume; therefore, the inlet and outlet mass flow rate are not equal.
4. The cylinder and case are considered temperature sources of sufficient thermal mass to maintain a constant temperature, T_{bulk}.

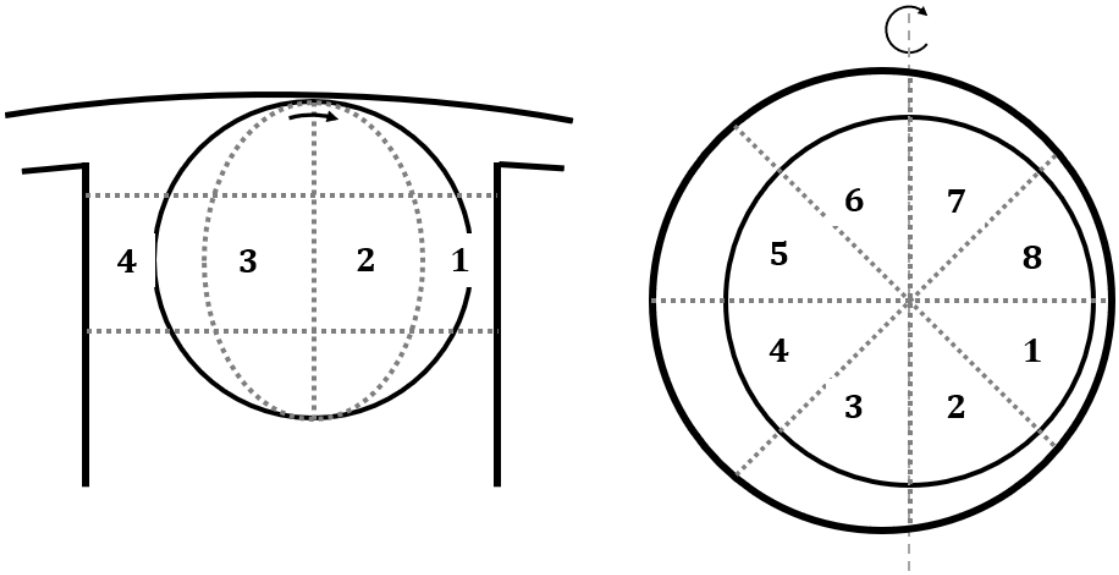

FIGURE 2.19: EXAMPLE CONTROL VOLUME DISTRIBUTION

The energy in the gap is described according to the first law of thermodynamics.

$$E_{cv} = m_{cv}c_p T_{cv} + V_{cv}p_{cv} + KE_{cv} + PE_{cv} \tag{2.123}$$

where m_{cv} is the mass, V_{cv} is the volume, p_{cv} is the mean pressure, KE_{cv} is the kinetic energy, and PE_{cv} is the potential energy. Taking the derivative.

$$\frac{dE_{cv}}{dt} = \frac{d\left(m_{cv}c_pT_{cv}\right)}{dt} + \frac{d(V_{cv}p_{cv})}{dt} + \frac{d(KE)}{dt} + \frac{d(PE)}{dt} \tag{2.124}$$

$$\frac{dE_{cv}}{dt} = c_p\left[T_{cv}\frac{dm_{cv}}{dt} + m_{cv}\frac{dT_{cv}}{dt}\right] + p_{cv}\frac{dV_{cv}}{dt} + V_{cv}\frac{dp_{cv}}{dt} \tag{2.125}$$

Plugging eq. (2.125) into eq. (2.122) and solving for the time derivative of temperature yields eq. (2.127).

$$\begin{aligned} c_pT_{cv}\frac{dm_{cv}}{dt} + c_pm_{cv}\frac{dT_{cv}}{dt} + p_{cv}\frac{dV_{cv}}{dt} + V_{cv}\frac{dp_{cv}}{dt} \\ = \mathrm{T}\omega + \dot{m}_{in}\left(c_pT_{bulk} + \frac{1}{\rho}p_{bulk}\right) - \dot{m}_{out}\left(c_pT_{out} + \frac{1}{\rho}p_{out}\right) \end{aligned} \tag{2.126}$$

$$\begin{aligned} \frac{dT_{cv}}{dt} = \frac{1}{c_pm_{cv}}\Big[\mathrm{T}\omega + \dot{m}_{in}\left(c_pT_{bulk} + \frac{1}{\rho}p_{bulk}\right) - \dot{m}_{out}\left(c_pT_{out} + \frac{1}{\rho}p_{out}\right) \\ - p_{cv}\frac{dV_{cv}}{dt} - V_{cv}\frac{dp_{cv}}{dt} - c_pT_{cv}\frac{dm_{cv}}{dt}\Big] \end{aligned} \tag{2.127}$$

Equation (2.127) is the governing equation for each control volume. The control volumes can be defined by specifying the bounds in the ϑ and φ directions. The polar direction is a single control volume, but the heat transfer analysis is limited to the thin gap ($\pm\pi/12$ from the minimum gap). Therefore, the control volume bounds in the polar direction are:

$$\vartheta_{cv} = \left[\frac{5\pi}{12} \quad \frac{7\pi}{12}\right] \tag{2.128}$$

The control volume bounds in the azimuthal direction are:

$$\varphi_{cv} = [\varphi_{cv_1} \quad \varphi_{cv_2} \quad \varphi_{cv_3} \dots \varphi_{cv_{N_{cv}+1}}] \tag{2.129}$$

where

$$\varphi_{cv_k} = \frac{2\pi(k-1)}{N_{cv}} \qquad \text{with } k = 1 \dots N_{cv} + 1 \tag{2.130}$$

Note that this means $\varphi_{cv_1} = 0$ and $\varphi_{cv_{N_{cv}+1}} = 2\pi$.

The variables in eq. (2.127) are defined as follows. The torque in the k^{th} control volume.

$$\mathrm{T}_{cv_k} = \int_{\varphi_k}^{\varphi_{k+1}} \int_{\vartheta_1}^{\vartheta_2} \tau_{ball}(\vartheta, \varphi) \cdot r_b^3 \sin\vartheta \sqrt{\cos^2\vartheta + \sin^2\vartheta \cos^2\varphi} \cdot sign(\cos\varphi) d\vartheta d\varphi \quad (2.131)$$

The volume for the k^{th} control volume.

$$V_{cv_k} = \int_{\varphi_k}^{\varphi_{k+1}} \int_{\vartheta_1}^{\vartheta_2} h \sin\vartheta \, r_b^2 d\vartheta d\varphi \quad (2.132)$$

$$V_{cv_k} = \int_{\varphi_k}^{\varphi_{k+1}} \int_{\vartheta_1}^{\vartheta_2} (h_o + r_b - r_b \sin\vartheta - e_b \cos\varphi) \sin\vartheta \, r_b^2 d\vartheta d\varphi \quad (2.133)$$

$$\begin{aligned} V_{cv_k} = r_b^2 \Big\{ (\varphi_{k+1} - \varphi_k) \Big[(h_o + r_b)(\cos\vartheta_1 - \cos\vartheta_2) - \frac{r_b}{2}(\vartheta_2 - \vartheta_1) \\ + \frac{r_b}{4}(\sin 2\vartheta_2 - \sin 2\vartheta_1) \Big] \\ - e_b(\cos\vartheta_1 - \cos\vartheta_2)(\sin\varphi_{k+1} - \sin\varphi_k) \Big\} \end{aligned} \quad (2.134)$$

Once the volume is known the mass of the fluid within the control volume is found according to eq. (2.135).

$$m_{cv_k} = \rho V_{cv_k} \quad (2.135)$$

Taking the derivative of the control volume with respect to time.

$$\frac{dV_{cv_k}}{dt} = -r_b^2 \dot{e}_b (\cos\vartheta_1 - \cos\vartheta_2)(\sin\varphi_{k+1} - \sin\varphi_k) \quad (2.136)$$

Once the time derivative of the volume is known, the change in mass is found.

$$\frac{dm_{cv_k}}{dt} = \rho \frac{dV_{cv_k}}{dt} \quad (2.137)$$

The leakage in the k^{th} control volume needs to be known to determine the inlet and outlet mass flow rates.

$$Q_{cv_k} = \int_{\varphi_k}^{\varphi_{k+1}} Q_\vartheta r d\varphi \quad (2.138)$$

where Q_ϑ is found according to eq. (2.118) from the fluid mechanics. This leakage corresponds to the flow rate passed the minimum clearance as shown in Figure 2.20. Using the figure, the expressions for the flow rate in and out of the control volume can be determined.

$$\dot{m}_{in_k} = \frac{1}{2}\frac{dm_{cv_k}}{dt} + \rho Q_{cv_k} \tag{2.139}$$

$$\dot{m}_{out_k} = \rho Q_{cv_k} - \frac{1}{2}\frac{dm_{cv_k}}{dt} \tag{2.140}$$

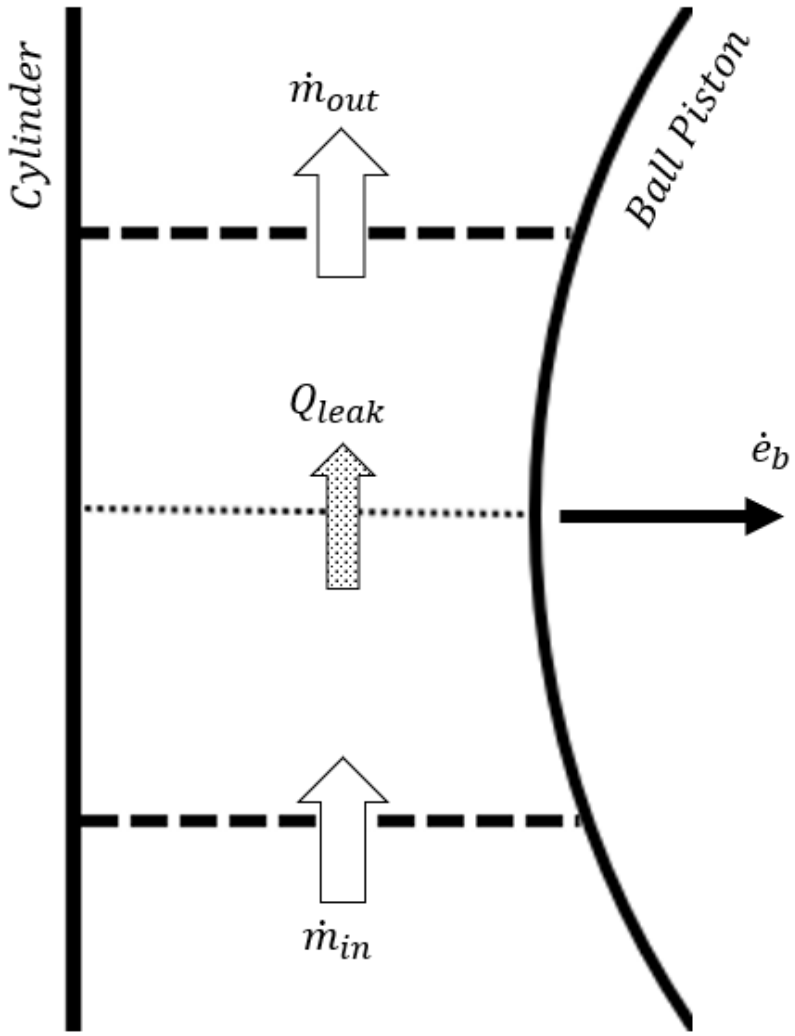

FIGURE 2.20: CONTROL VOLUME MASS FLOW RATES

Next, a linear temperature distribution is assumed through the control volume in the direction of leakage. This means that the temperature out of the control volume can be written in terms of the temperature in the control volume.

$$T_{cv_k} = \frac{1}{2}(T_{out_k} + T_{bulk}) \Rightarrow T_{out_k} = 2T_{cv_k} - T_{bulk} \tag{2.141}$$

The pressure in the control volume, p_{cv_k}, can be found numerically by averaging the pressure distribution given in eq. (2.116). The derivative of the control volume pressure with respect to time, $d(p_{cv_k})/dt$ is then found numerically. Lastly, the bulk pressure, p_{bulk}, is simply the cylinder pressure, p_{cyl}.

Once the temperature in the control volume is known, the viscosity can be calculated. Walther's equation is used to describe the relationship between the temperature and viscosity.

$$\log_{10}(\log_{10}(\nu_k + 0.7)) = A - B\log_{10} T_{cv_k} \tag{2.142}$$

where ν_k is the kinematic viscosity in the k^{th} control volume. The dynamic viscosity is calculated using eq. (2.143).

$$\mu_k = \rho\nu_k \tag{2.143}$$

To solve the differential equation presented in eq. (2.127) the integration through time is done numerically. An initial temperature is assumed, and the cylinder pressure and time data has already been solved. Figure 2.21 shows the code chart for the ball-cylinder interface.

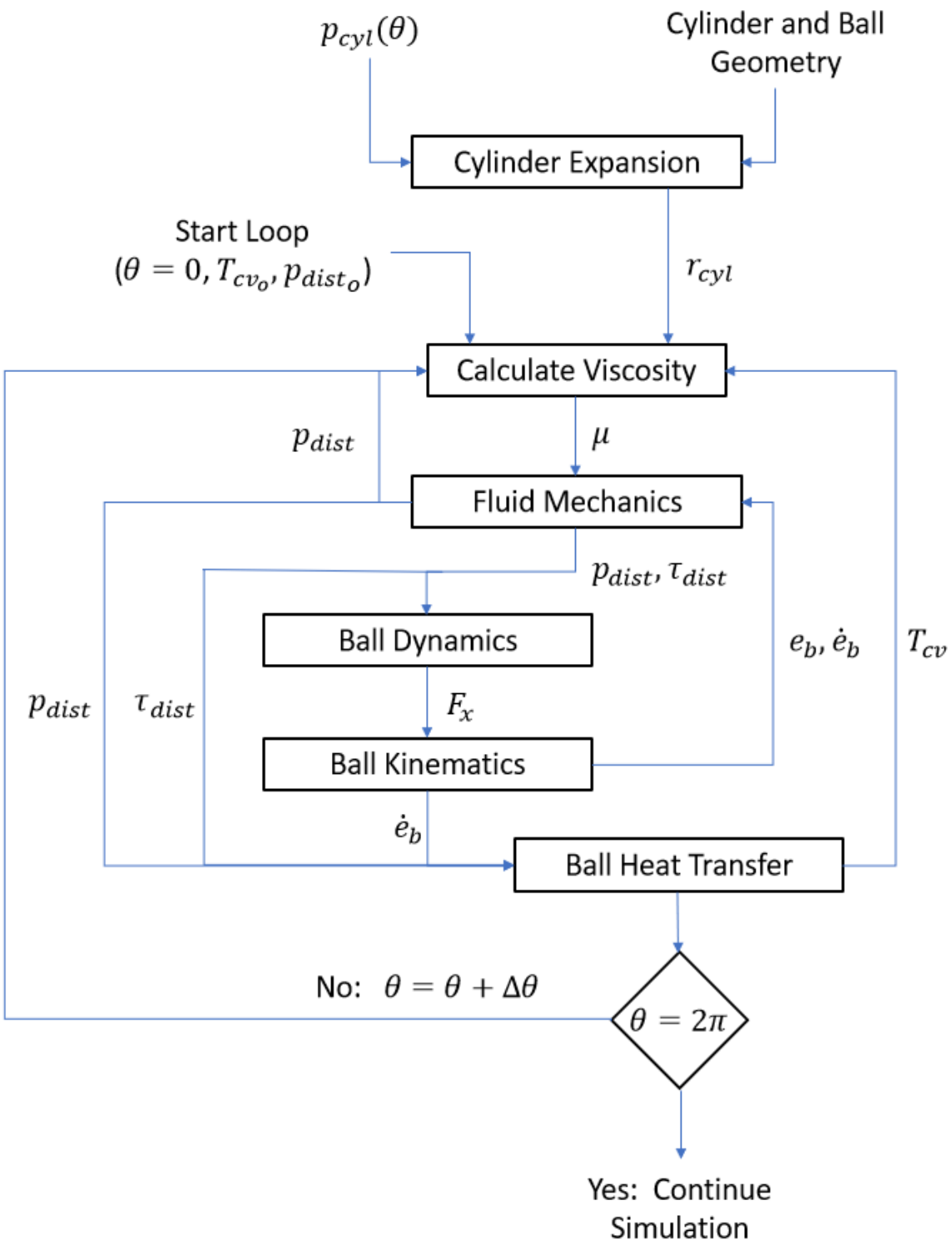

FIGURE 2.21: BALL-CYLINDER INTERFACE CODE DIAGRAM

2.2.3.6 Model Limitations and Elastohydrodynamic Lubrication

The ball-cylinder fluid mechanics presented in the previous section are valid through most of the simulation, but when the ball becomes too close to the cylinder wall, modifications are required to maintain a physically realistic situation. The model presented above assumes that the ball is in the hydrodynamic lubrication regime, but as the ball nears the wall, the physics are described using elastohydrodynamic lubrication theory, or EHL.

The main feature of EHL is the high localized pressure spikes that occur due to the minimal clearance between the two surfaces. The localized pressure is very similar to Hertzian contact pressure that describes dry contacts. It is not uncommon for pressure values to reach the GPa range. Two important physical phenomena happen due to this pressure spike, localized deformation of the surfaces and localized increasing of viscosity. The viscosity-pressure (piezo-viscous) relationship used is given in eq. (2.144):

$$\mu = \mu_o \exp(\alpha_p p) \tag{2.144}$$

where α_p is a coefficient typically in the 15-30 GPa^{-1} range. A representative situation showing the localized deformation is presented in Figure 2.22 with the gap height to length greatly exaggerated. In the figure, the dotted lines show the undeformed surfaces of the two solids, which also are exaggerated to aid in understanding.

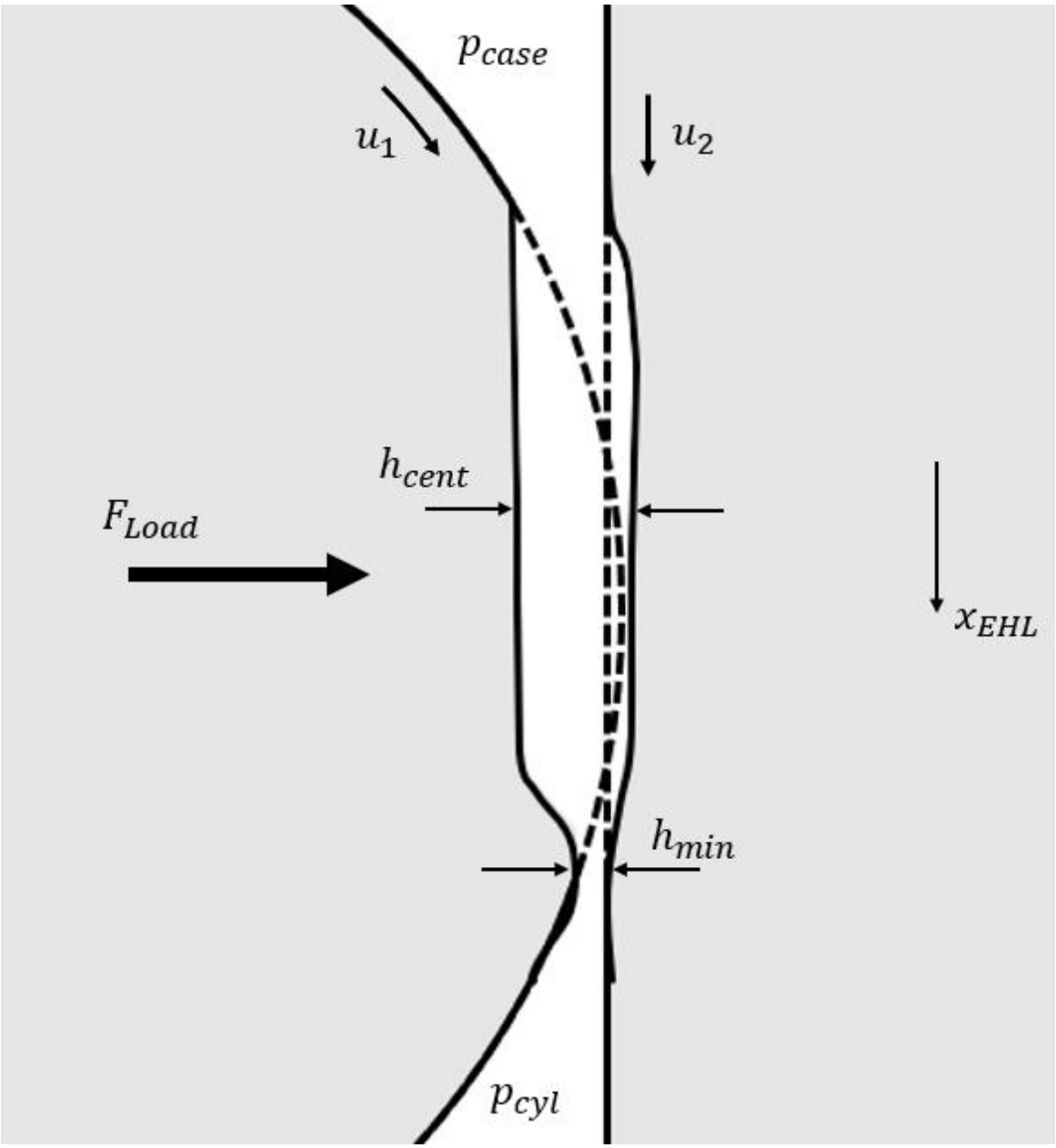

FIGURE 2.22: ELASTOHYDRODYNAMIC LUBRICATION EXAMPLE GEOMETRIC FEATURES

To rigorously solve an EHL problem requires simultaneously solving the fluid mechanics, localized deformation, and a load balance. Calculating accurate solutions involves nontrivial computation time and sufficient knowledge of numerical techniques to succeed. However, empirical models do exist, and these were leveraged when the model detected that the ball had

entered the EHL regime. The empirical models as presented by Hamrock and Dowson [47] are shown in eq. (2.145) and (2.146).

$$\frac{h_{min}}{R_x} = 3.63U^{0.68}G^{0.49}W^{-0.073}(1 - \exp(-0.68k)) \tag{2.145}$$

$$\frac{h_{cent}}{R_x} = 2.69U^{0.67}G^{0.53}W^{-0.067}(1 - 0.61\exp(-0.73k)) \tag{2.146}$$

where k is the ellipticity parameter:

$$k \approx 1.0339\left(\frac{R_y}{R_x}\right)^{0.636} \tag{2.147}$$

W is the dimensionless load parameter:

$$W = \frac{F_{Load}}{E'R_x^2} \tag{2.148}$$

U is the dimensionless speed parameter:

$$U = \frac{\mu_o u_o}{E'R_x} \tag{2.149}$$

G is the dimensionless materials parameter:

$$G = \alpha_p E' \tag{2.150}$$

The rest of the variables needed for these definitions are given below. R_x and R_y are the effective radii of the interface.

$$\frac{1}{R_x} = \frac{1}{R_{x_1}} + \frac{1}{R_{x_2}} \qquad \& \qquad \frac{1}{R_y} = \frac{1}{R_{y_1}} + \frac{1}{R_{y_2}} \tag{2.151}$$

where $R_{\hat{e}_i}$ is the radius of curvature in the $\hat{e}$-direction for surface i. The effective elasticity, E'.

$$\frac{1}{E'} = \frac{1}{2}\left(\frac{1-\nu_1^2}{E_1} + \frac{1-\nu_2^2}{E_2}\right) \tag{2.152}$$

where ν_i and E_i are Poisson's ratio and the modulus of elasticity for surface i. The mean velocity at the interface, u_o.

$$u_o = \frac{1}{2}(u_1 + u_2) \tag{2.153}$$

where u_1 and u_2 are the velocities of surfaces 1 and 2 in the x-direction. See Figure 2.22 for reference. μ_o is the inlet viscosity. And α_p is the same value that was used in eq. (2.144). The value of F_{Load}, eq. (2.154), comes from the previous timestep and is a subset of the dynamic equations presented earlier in eq. (2.85).

$$F_{load} = F_{\tau_{\hat{\theta}}} + F_{T\hat{\theta}} + F_{N_{\hat{\theta}}} + m_b\left(2e_{pump}\omega_{pump}^2 \sin\theta\right) \tag{2.154}$$

The empirical models for the minimum and central film thickness provide a physically realistic limit to the ball position. Now that a limit has been placed on the clearance, that bound needs to be implemented in the ball position kinematics. Based on the geometry in Figure 2.22, it is seen that h_{cent} and h_{min} correspond to multiple points between the ball and the cylinder, which is a characteristic of EHL. In fact, the surfaces within the contact region typically deform in such a way that the gap height stays relatively constant. Therefore, if the contact region is known, the local deformation can be considered.

The EHL contact region is approximated using contact mechanics and the Hertzian contact ellipse. The geometry of the situation is shown in Figure 2.23. The ellipticity parameter from eq. (2.147) is related to the semi-major axis, a, and semi-minor axis, b, by definition.

$$k = \frac{a}{b} \tag{2.155}$$

where a is calculated from contact mechanics.

$$a = \left(\frac{6k^2\xi F_{Load}R}{\pi E'}\right)^{1/3} \tag{2.156}$$

where ξ is the second elliptic integral.

$$\xi = \int_0^{\pi/2} \sqrt{1 - (1 - k^{-2})\sin\chi}\, d\chi \tag{2.157}$$

After a is calculated, b is found using the ellipticity parameter.

$$b = a/k \tag{2.158}$$

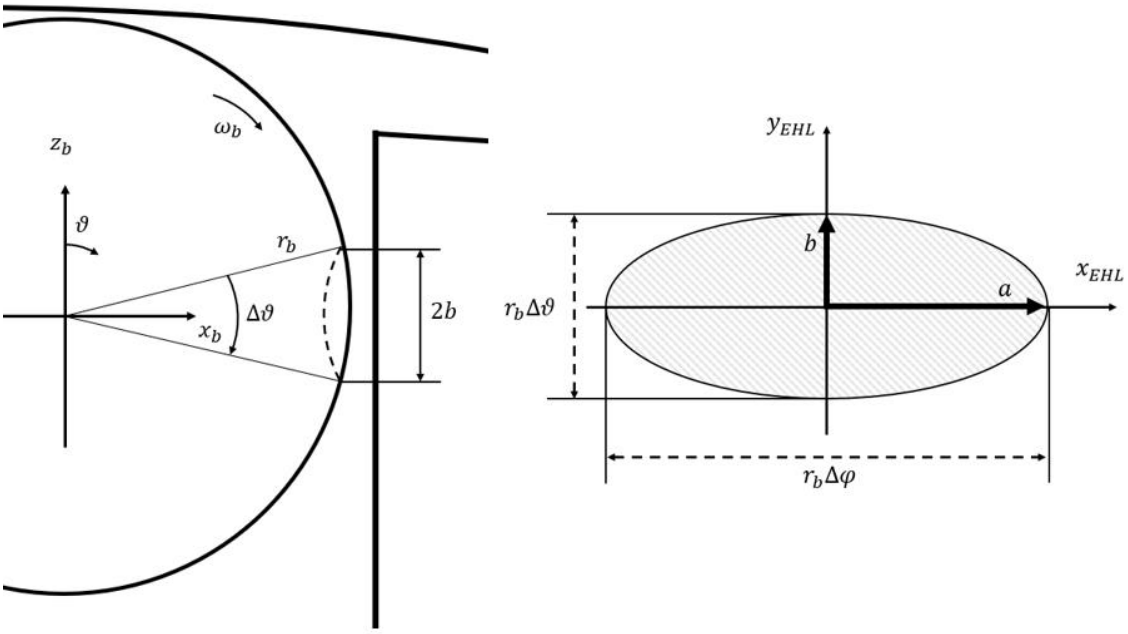

FIGURE 2.23: GEOMETRIC RELATIONSHIP BETWEEN BALL PISTON COORDINATES AND THE HERTZIAN CONTACT ELLIPSE

Once a and b are known, the process for determining the localized deformation can begin. An iteration is done over the discretized ball surface to determine if the point is within the contact ellipse. The inequality in eq. (2.159) will be true for any points within the contact ellipse.

$$\left(\frac{r_b \sin\vartheta_l \sin\varphi_k}{a}\right)^2 + \left(\frac{r_b \cos\vartheta_l}{b}\right)^2 < 1 \tag{2.159}$$

The amount of deflection for a point that satisfies the inequality is using eq. (2.160)

$$h_{d_{kl}} = h_{EHL} - \left(h_{o_t} + r_b - r_b \sin\vartheta_l + e_{b_t} \cos\varphi_k\right) \tag{2.160}$$

where $h_{EHL} = \frac{1}{4}h_{min} + \frac{3}{4}h_{cent}$. In actual EHL, the surface deflection is not one value, so the coefficients of $1/4$ and $3/4$ were selected arbitrarily to approximate the situation. Because the ball is moving dynamically in the simulation, there is the potential for its minimum clearance of a point to be greater than h_{EHL}. In this case, eq. (2.160) will have negative values. Negative deflections are removed before calculating the fluid mechanics.

Another possible numeric pitfall is if the ball dynamically moves too close to the wall and a point outside the contact ellipse is less than h_{EHL}. In this case the ball position needs to be corrected

so that no point on the ball is closer than h_{EHL}. The correction factor, e_b', is found according eq. (2.161).

$$e_b' = \min\left(\min\left(h_{o_t} + r_b - r_b \sin\vartheta - e_{b_{t-1}} \cos\varphi + h_d\right)\right) - h_{EHL} \quad : e_b' < 0 \qquad (2.161)$$

Equation (2.161) finds the minimum gap height when the deflection is considered and compares it to h_{EHL}. If the ball is not close to the wall, then e_b' will be set to zero due to the limits on its value. If the ball was too close to the cylinder and a point outside of the contact zone was less than h_{EHL}, e_b' would shift the ball center to correct the gap height. Combining the correction factor, eq. (2.161), with the localized deformation, eq. (2.160), gives the final gap height around the ball.

$$h = h_{o_t} + r_b - r_b \sin\vartheta - (e_{b_{t-1}} + e_b') \cos\varphi + h_d \qquad (2.162)$$

A code diagram for the EHL behavior is shown in Figure 2.24. The EHL section is modular allowing the user to determine if EHL behavior should be considered during the simulation. If EHL is modeled, it is implemented between the "Calculate Viscosity" and "Fluid Mechanics" blocks of Figure 2.21.

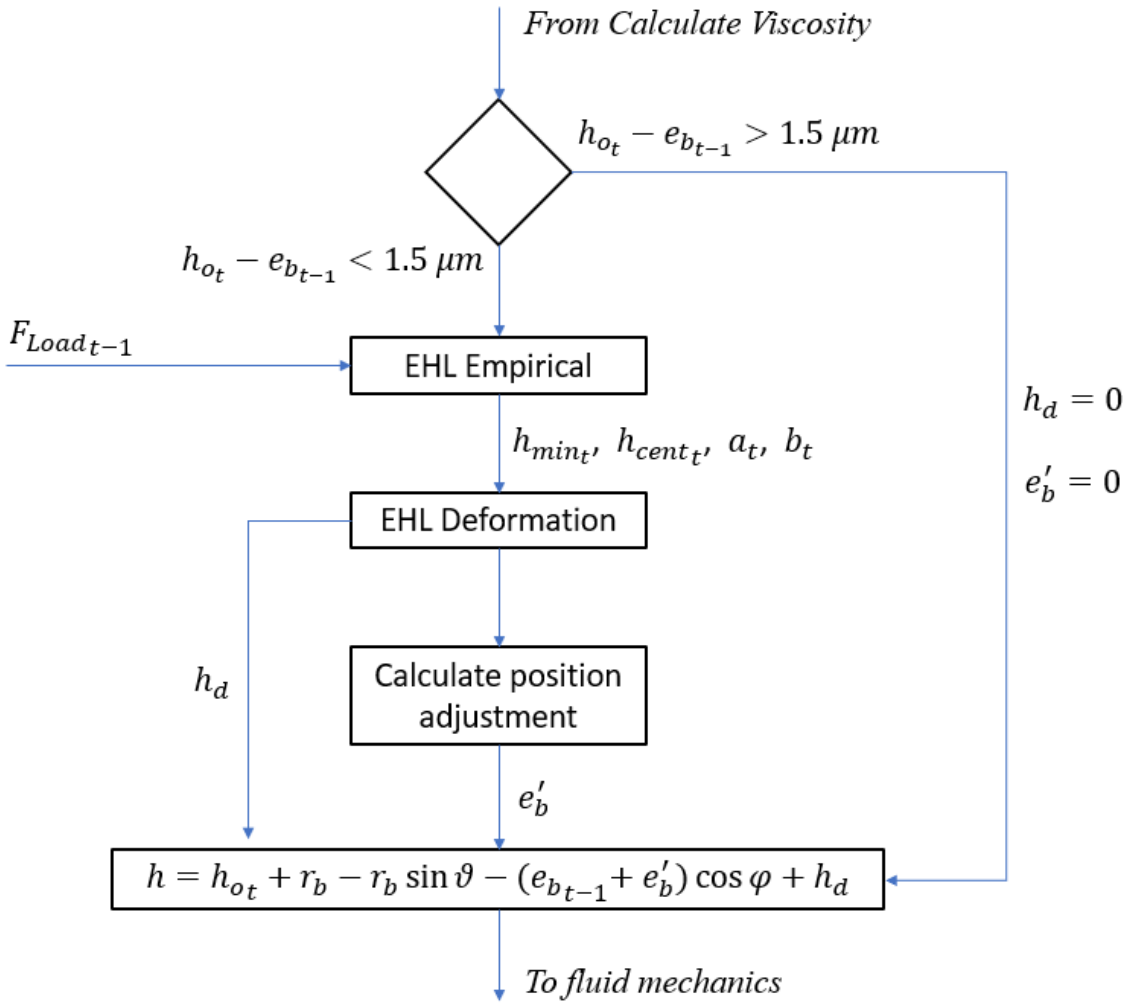

FIGURE 2.24: EHL CODE DIAGRAM

2.2.4 Unmodeled Losses

The pintle-rotor and ball-cylinder interfaces are the most critical interfaces to consider when modeling the energy losses in a radial ball piston unit. However, other, less critical energy losses that are not modeled need to be considered. Notable among these losses are the churning losses, the bearing losses, and the unmodeled ball-cam interface. In this work, these losses are determined empirically from experiment results.

2.3 Results and Discussion

The following section highlights trends and insights that the model provides. It will be broken into two subsections; the first considers the pressure dynamics and valve timing, while the second

considers energy losses at the interfaces. A set of initial parameters that was used to produce these results is given in Table 2.1, these parameters were then optimized in Section 4.3.2.

TABLE 2.1: MODEL PARAMETERS

Parameter	Value	Unit	Description
n	5	[unitless]	Number of pistons
R_{ro}	35	[mm]	Outside radius of the rotor block
R_p	14	[mm]	Outside radius of the pintle
δ_p	10	[mm]	Distance from the pintle ports to case
r_v	5	[mm]	Radius of the valve opening
r_b	9	[mm]	Radius of the ball piston
β_o	1.65	[GPa]	Bulk modulus of the oil at atmospheric pressure
ρ_o	876	$[\mathrm{kg/m^3}]$	Density of the oil
T_o	310	[K]	Temperature of the oil
c_p	1960	$[\mathrm{J/(kg \cdot K)}]$	Specific heat of the oil
R	0.005	[unitless]	Entrained air of the oil

To improve coherence between results, all the results will correspond to two operating conditions, which are shown in Table 2.2. Note that the geometry and performance for this section has not been optimized but is meant to show model utility. Optimized parameters and performance will also be shared in Chapter 4. Figure 2.25 shows the architecture with the key interfaces highlighted.

TABLE 2.2: SIMULATION OPERATING CONDITIONS

Operation	Speed	Port A Pressure	Port B Pressure
Pump	5000 RPM	8.10 MPa	2.45 MPa
Motor	5000 RPM	2.45 MPa	8.10 MPa

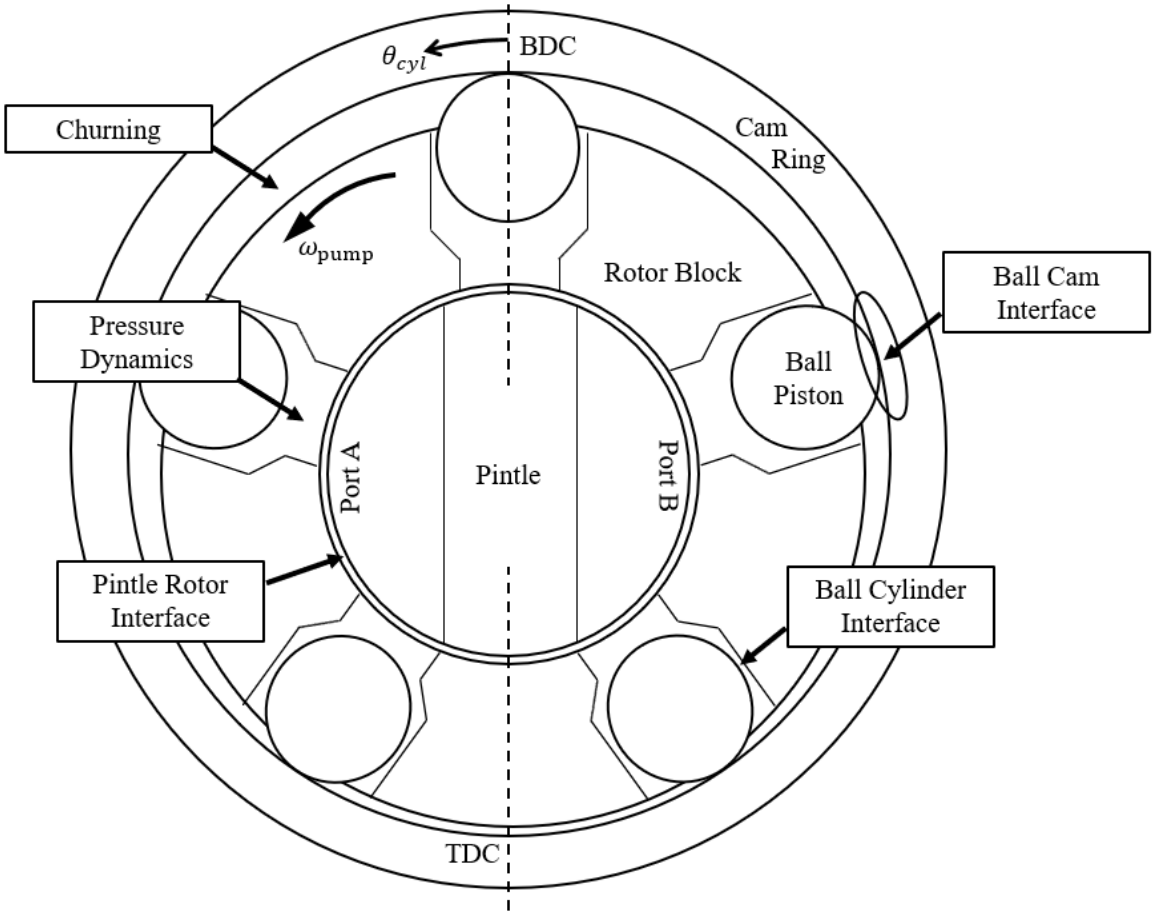

FIGURE 2.25: RADIAL BALL PISTON MODEL SECTIONS

2.3.1 Hydraulic Performance – Cylinder Pressure Dynamics

The cylinder pressure dynamics are fundamental when attempting to capture the performance of the pump or motor. Figure 2.26 shows the pressure in a single cylinder during one full pump and motoring cycle, BDC and TDC are located at 0 and 6 milliseconds respectively. These points in the cylinder cycle, where the piston changes direction and the cylinder switches between ports, are the most interesting portions of the pressure dynamics.

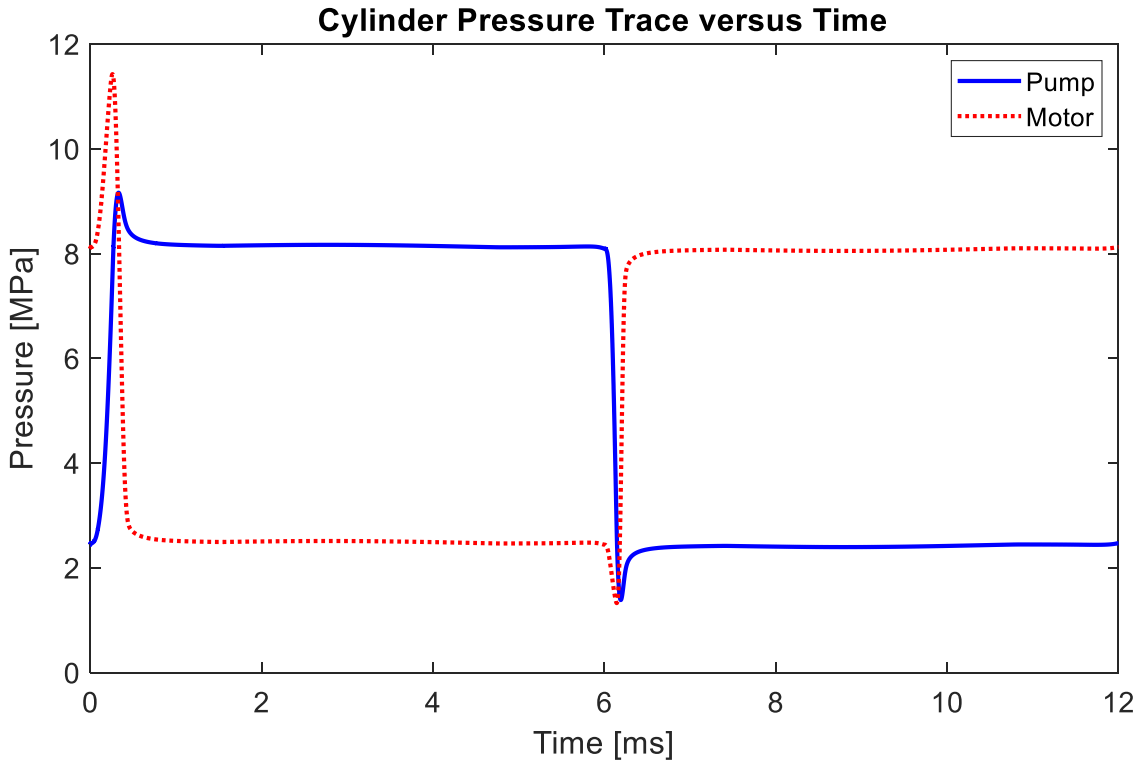

FIGURE 2.26: CYLINDER PRESSURE DYNAMICS

Consider the pressure dynamics in the pumping case, there is pressure overshoot following BDC because the cylinder volume is decreasing faster than the fluid can leave the cylinder. For the same reason, there is a pressure undershoot right after TDC in the pumping cycle. These pressure spikes create small amounts of reverse flow (negative values) for both ports in the pumping case, which can be seen in the flow rate plots of Figure 2.27.

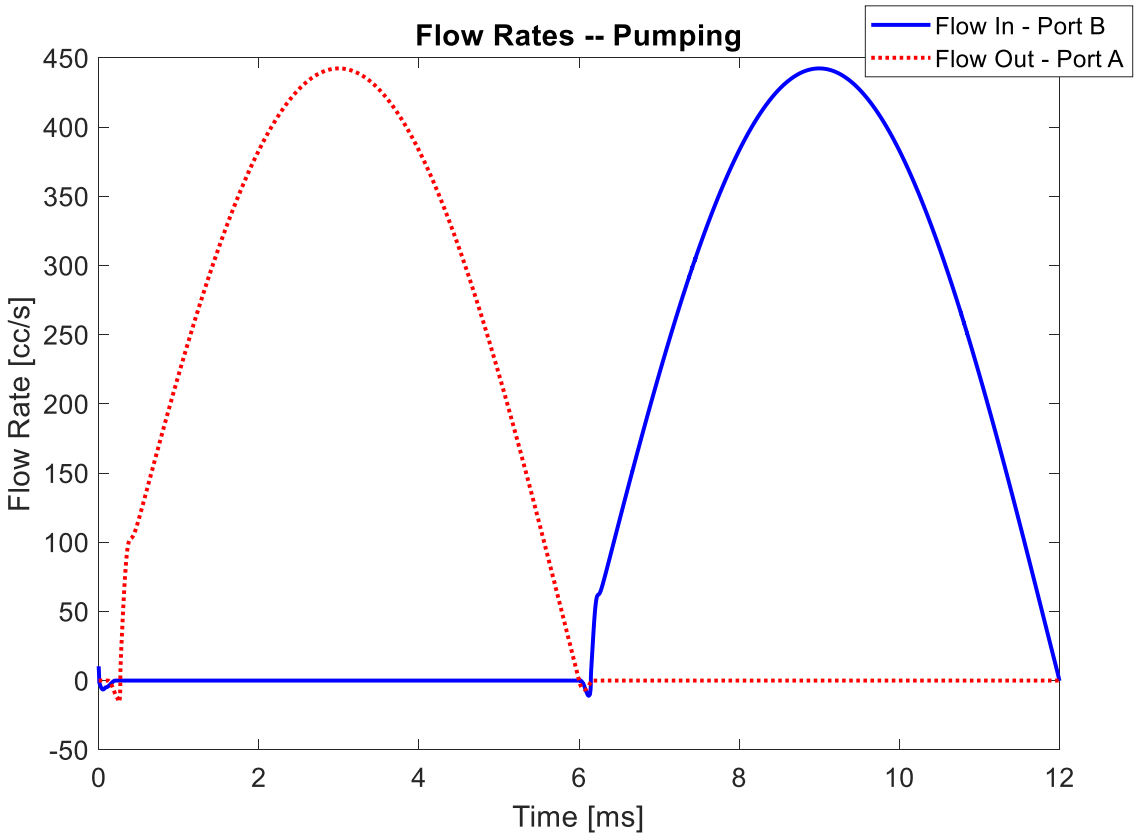

FIGURE 2.27: PUMP FLOW RATES

In the motoring case (see Figure 2.26) there is a large spike in pressure following BDC. This sharp rise in pressure happens because the cylinder is still connected to high pressure while the volume begins to decrease. Next, the cylinder, still at high pressure, reaches the low pressure port and a rush of flow from the cylinder to the port occurs. This behavior can be seen in the port A flow rate of Figure 2.28, with a similar phenomenon occurring in the flow of port B due to the pressure drop immediately after TDC.

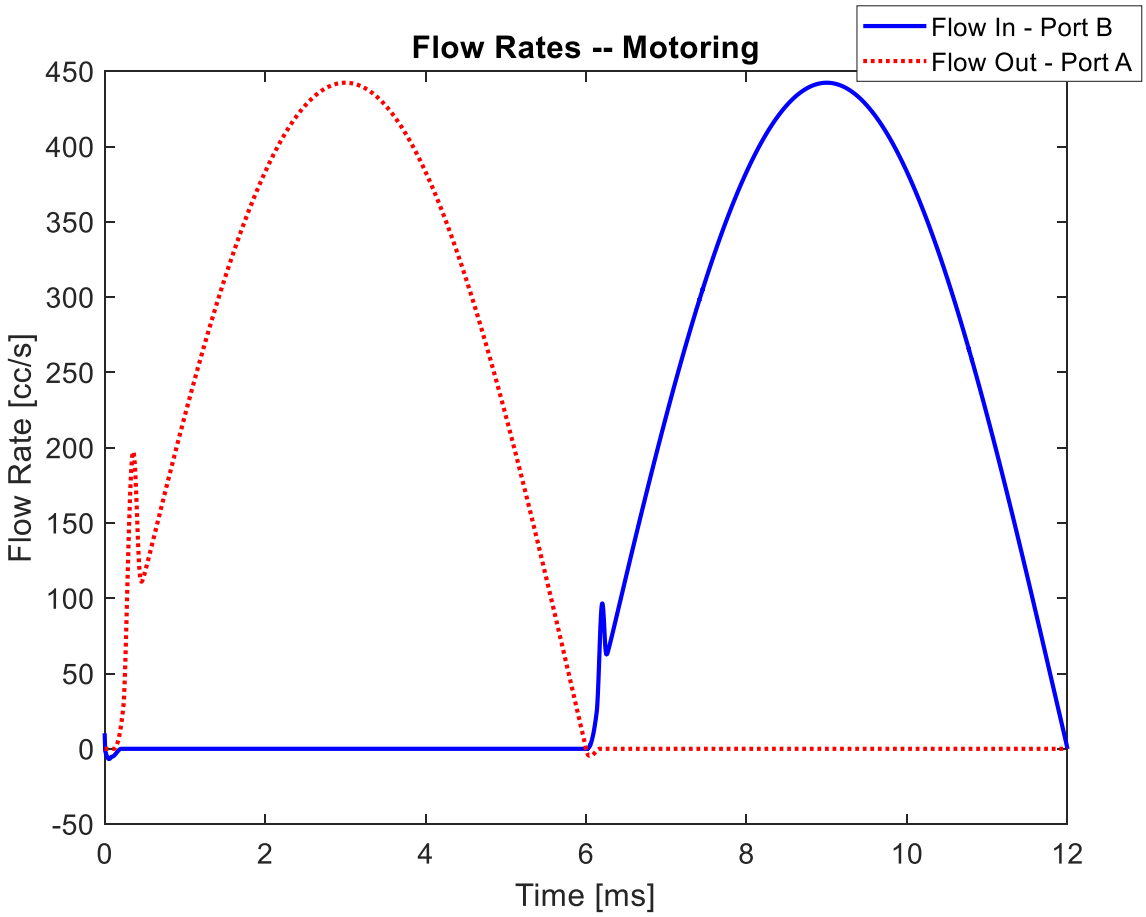

FIGURE 2.28: MOTOR FLOW RATES

Another way of analyzing the pressure dynamics is considering the P-V diagram for the cylinder as shown in Figure 2.29. The figure shows the transitions around BDC and TDC very well, providing insight into how quickly the pressure rises and falls with very little change in cylinder volume. Understanding why the pressure spikes during motoring becomes evident when looking at the P-V diagram. From the motoring start position, the pressure increases rapidly as the volume decreases. Then the cylinder connects to the low pressure port, and at that point, just after BDC, the pressure drops rapidly to the port pressure. This process is easy to notice because the lines cross at the transitions of the P-V diagram.

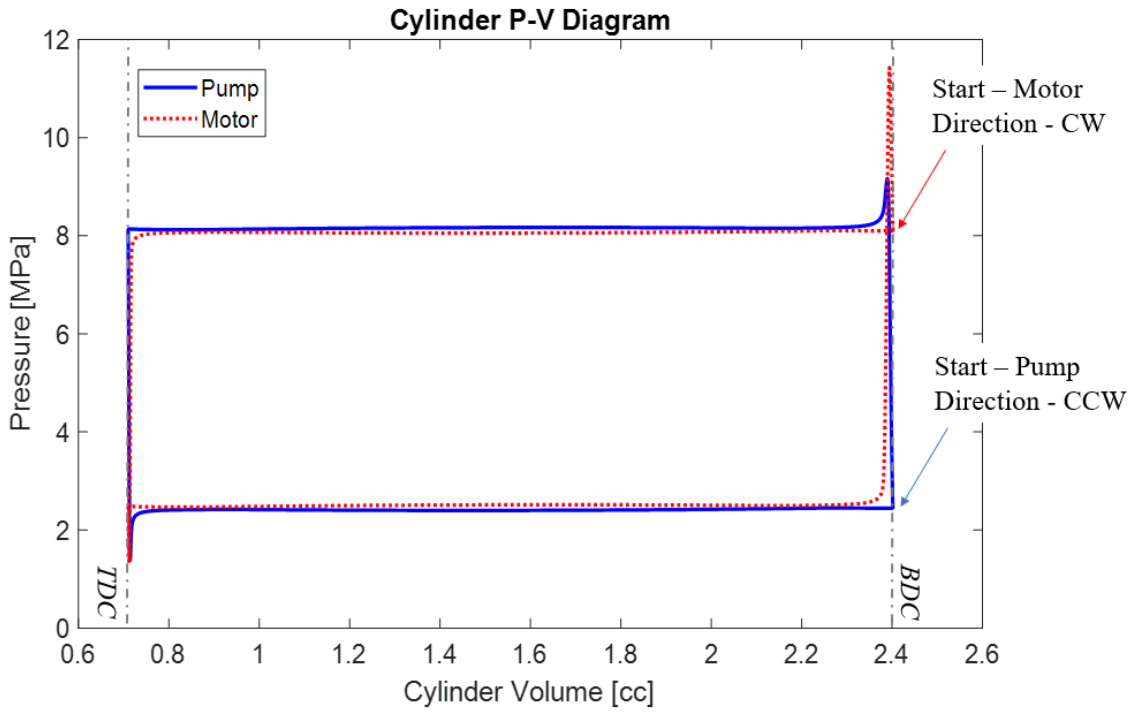

FIGURE 2.29: CYLINDER P-V DIAGRAM

The pressure dynamics are sensitive to the valve timing, which determines when the cylinder is connected to each port. The optimal of the valve timing is dependent on port pressures, rotation speed, and rotation direction, which makes designing the timing difficult if the hydraulic pump/motor operates across a wide range of conditions. To determine the quality of the valve timing, throttling losses can be calculated to see how much power is lost throughout the cycle. Throttling losses can be found using eq. (2.163).

$$\mathcal{P}_t = Q \cdot (\Delta p) \tag{2.163}$$

where Q is the flow rate across the valve, and Δp is the pressure drop across the valve. The throttling loss for the pump and motor case can be seen in Figure 2.30. From the figure, the valve timing is better for pumping then motoring with much smaller losses during the transitions.

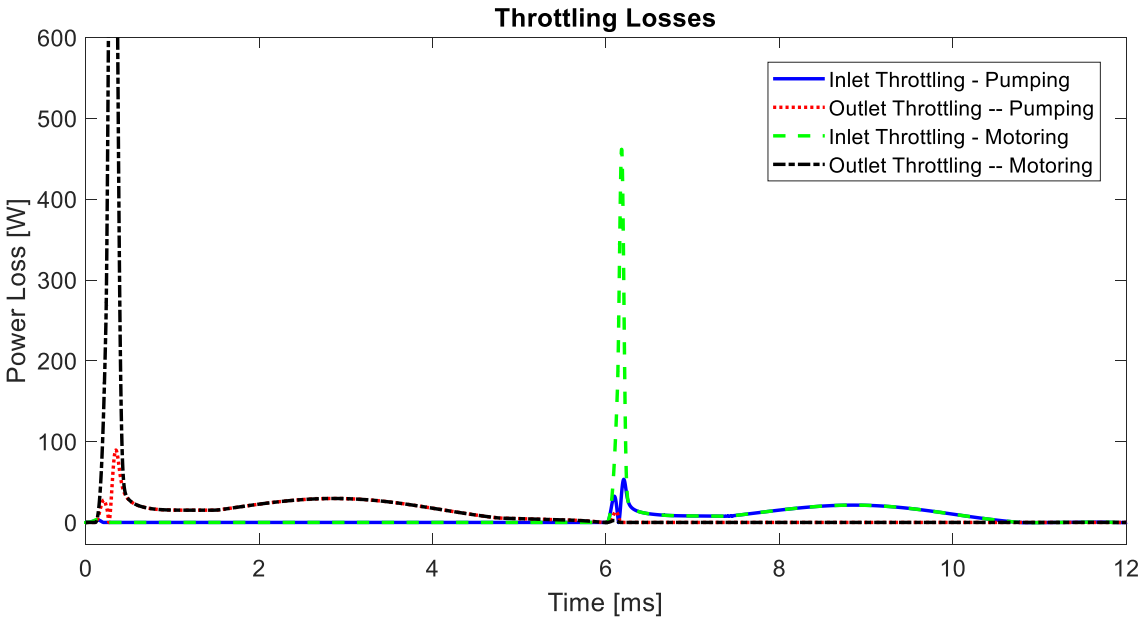

FIGURE 2.30: PUMP AND MOTOR THROTTLING LOSSES

The pressure dynamics can be used to predict the flow ripple and torque ripple of the pump and motor respectively. The output flow ripple of the pump can be found by summing the output flow of each cylinder. To determine the torque ripple of the motor, eq. (2.164) is used.

$$\mathrm{T}_{Out} = \frac{1}{\omega_p} \sum_{i=1}^{n_{pistons}} \pi r_b^2 \left(p_{cyl_i} - p_{case}\right) \cdot \varepsilon_p \omega_p \sin\theta_{cyl_i} \tag{2.164}$$

The flow ripple and torque ripple are shown in Figure 2.31 and Figure 2.32 respectively. This shows the dynamic behavior of the output of the hydraulics. Generally, it is desirable to minimize torque and flow ripple in hydraulics to reduce vibrations and noise. Minimizing ripple is even more important when the system is being used for control purposes to avoid jerky behavior.

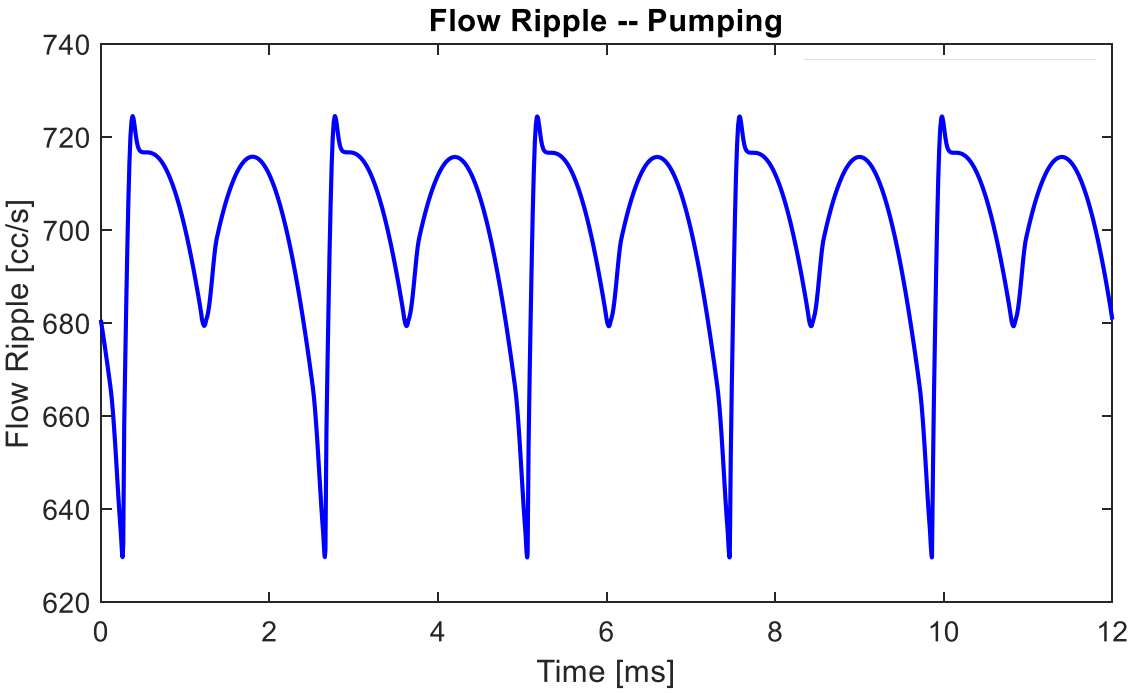

FIGURE 2.31: PUMP OUTPUT FLOW RIPPLE

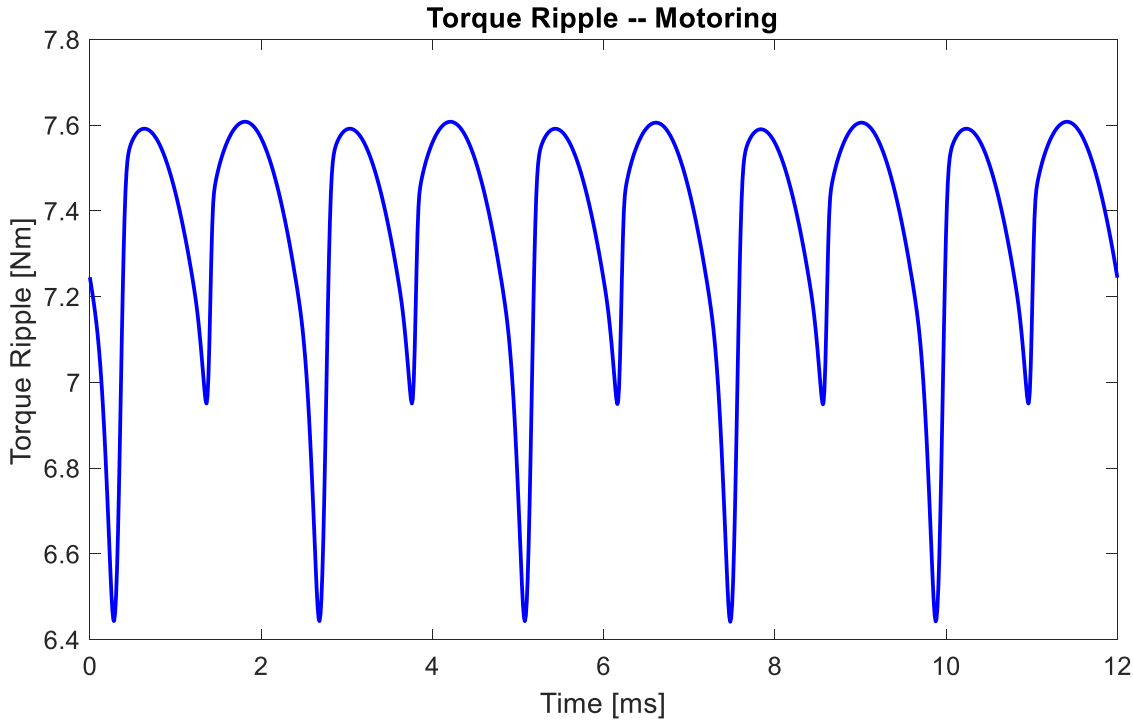

FIGURE 2.32: MOTOR OUTPUT TORQUE RIPPLE

2.3.2 Hydraulic Inefficiencies – Interface Losses

The pressure dynamics provide information on the general hydraulic performance but does not capture most of the energy losses within the pump/motor. Referencing Figure 2.33, most of the losses come from the pintle-rotor and ball-cylinder interfaces because these have relative motion and small clearances. In both cases, there is a tradeoff between the viscous shearing and the leakage, making them interesting interfaces to model, study, and design. The ball-cam interface is not modeled so it is assumed that the ball remains rolling on the cam surface. The churning losses are also not modeled but capture experimentally. The losses are examined for the pumping operating condition from Table 2.2.

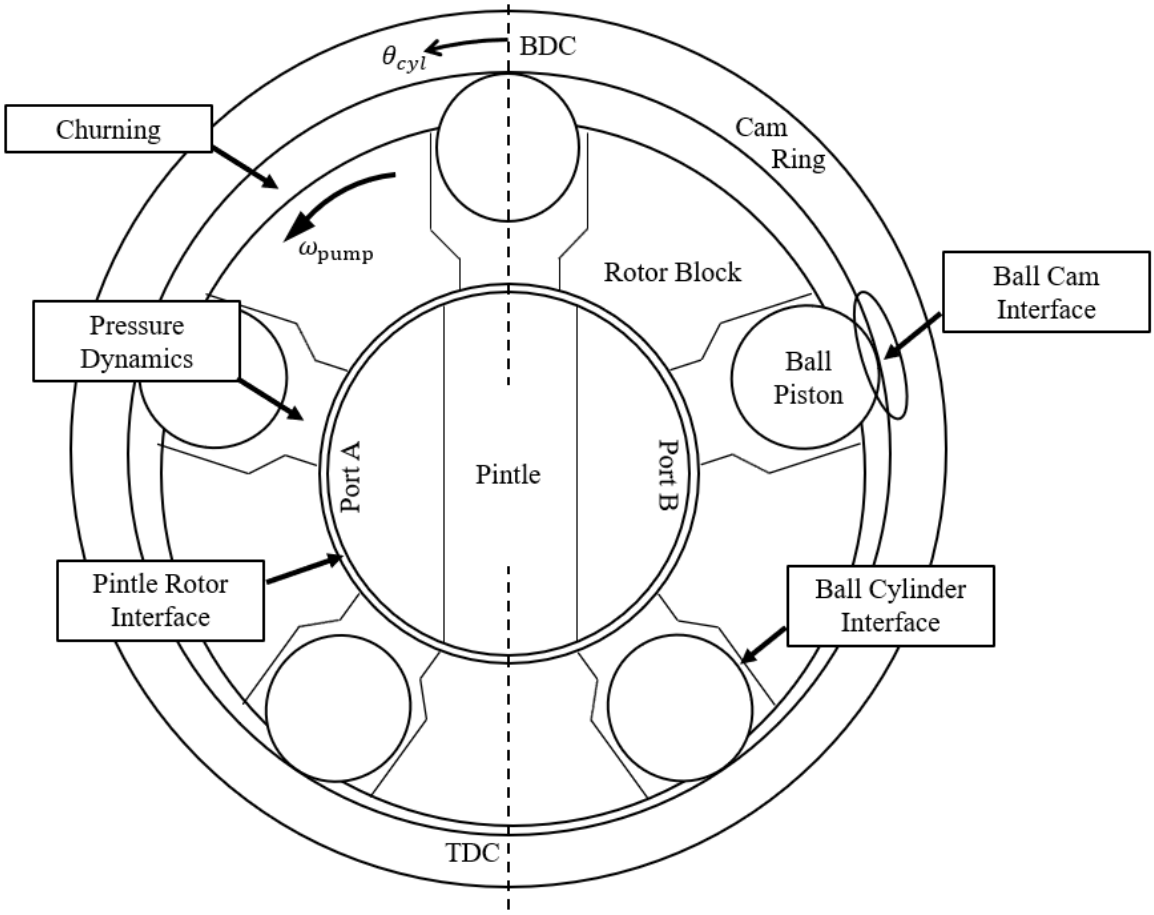

FIGURE 2.33: RADIAL BALL PISTON MODEL SECTIONS

2.3.2.1 Pintle-Rotor Losses

The pintle-rotor interface is solved quasi-statically for each timestep making it easier to analyze since the kinematics do not have to be considered. For review, the geometry of the rotor is shown in Figure 2.34. A detailed description is provided in Section 2.2.2.

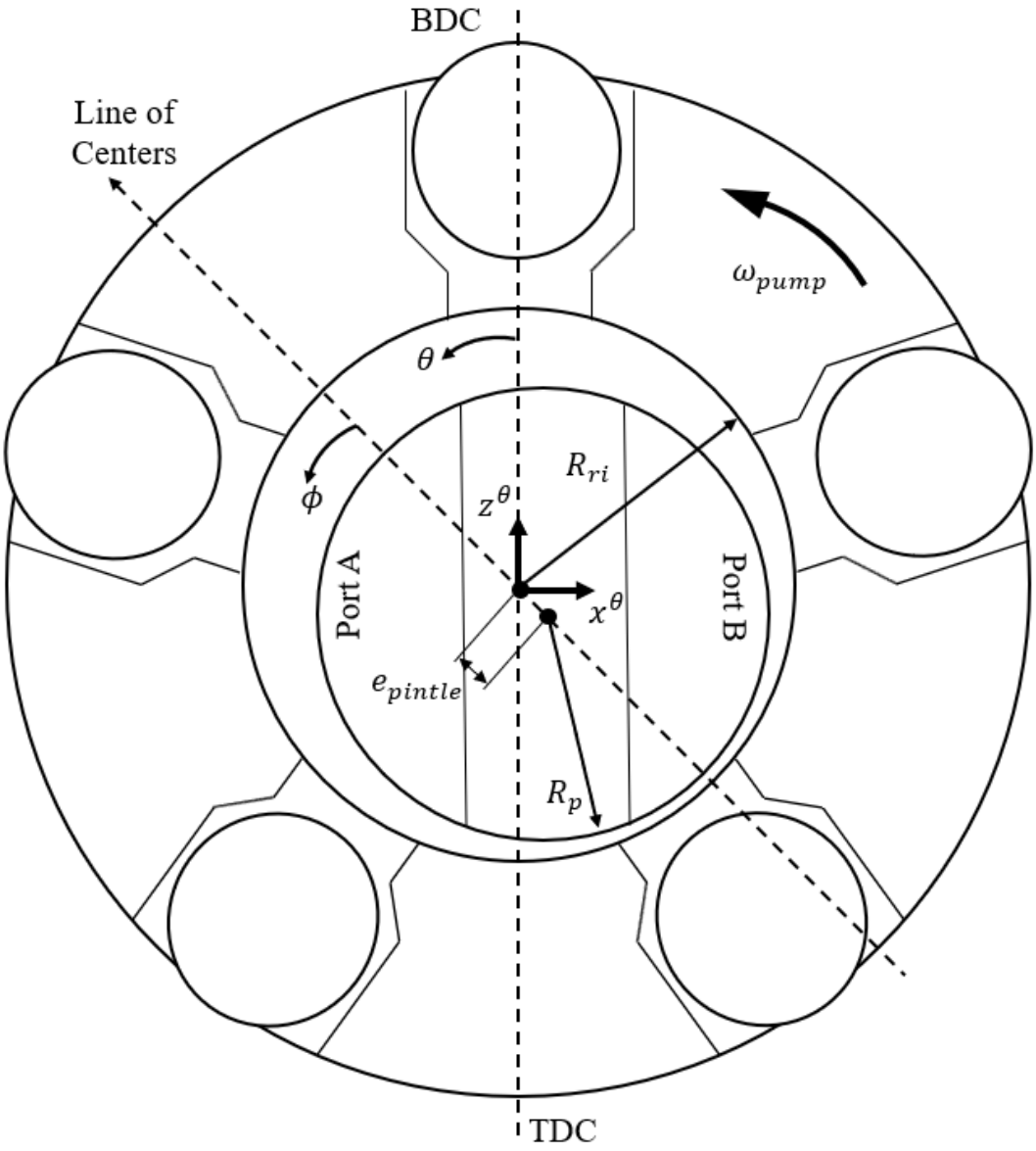

FIGURE 2.34: PINTLE-ROTOR GEOMETRY

The dynamics of the pintle-rotor interface are shown in Figure 2.35. The forces acting on the rotor are periodic, with a frequency equal to the number of pistons times the pump's angular speed. Therefore, the figure shows one cycle of the forces, in this case, a fifth of a revolution. The force

results use the geometry shown in Figure 2.34 with high pressure at port A. In the x^{θ} direction, the force is dominated by the pressure difference between the ports, so the net force is relatively constant and always to the left (negative) direction. The port pressures are balanced in the z^{θ} direction causing the cylinder positions to determine the net force's direction. When a cylinder has high pressure just after BDC, the net force is downward (negative), and when a cylinder has high pressure just before TDC, the net force is upward (positive).

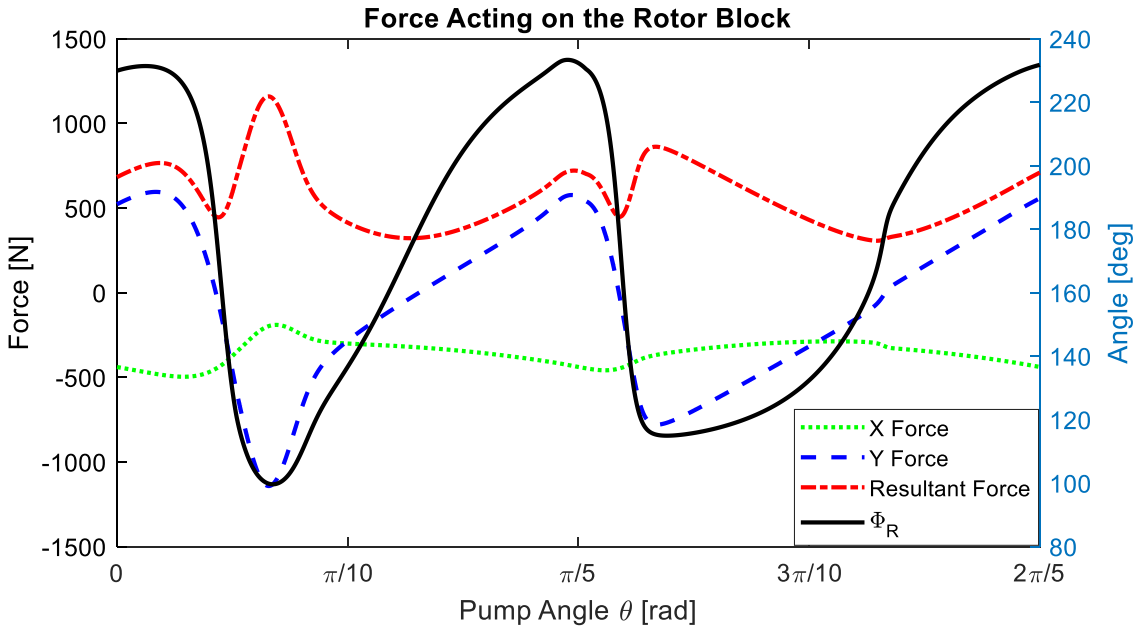

FIGURE 2.35: NET FORCE ACTING ON THE ROTOR TO BE COUNTERED BY THE JOURNAL BEARING BEHAVIOR

The resultant force showed in Figure 2.35 is balanced by the rotor moving to an eccentric position. The geometry of this situation is shown in Figure 2.36. The load holding components w^{x} and w^{z} act perpendicular and parallel to the line of centers. The resulting eccentricity ratio and attitude angle that are needed to balance the resultant force are shown in Figure 2.37. Again, a fifth of a revolution is shown due to the periodic nature. Because the rotor force is balanced in each timestep, the eccentricity ratio changes in phase with the resultant force's magnitude and the attitude angle adjusts based on the direction of the resultant force, Φ_R. To check the quasi-static assumption, the inertial force of the rotor block was examined. The inertial term was approximately a tenth of the resultant force, making the quasi-static assumption valid for this operating condition. If the operating speed was increased, the rotor inertia would have to be taken into consideration.

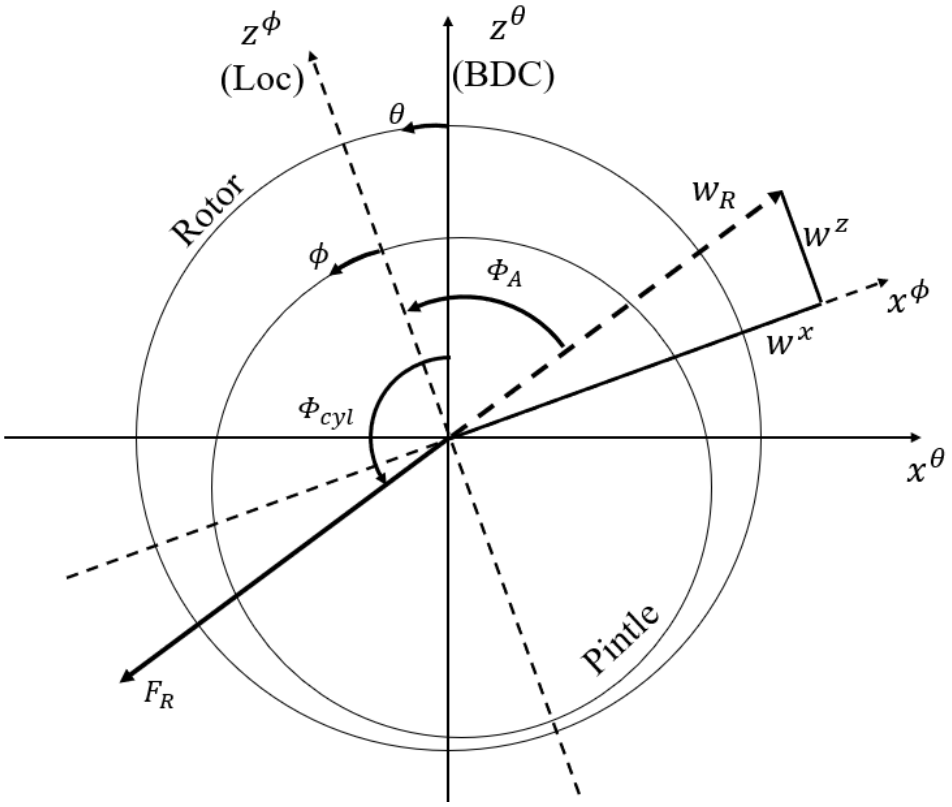

FIGURE 2.36: ECCENTRIC ROTOR GEOMETRY AND FORCE COMPONENTS

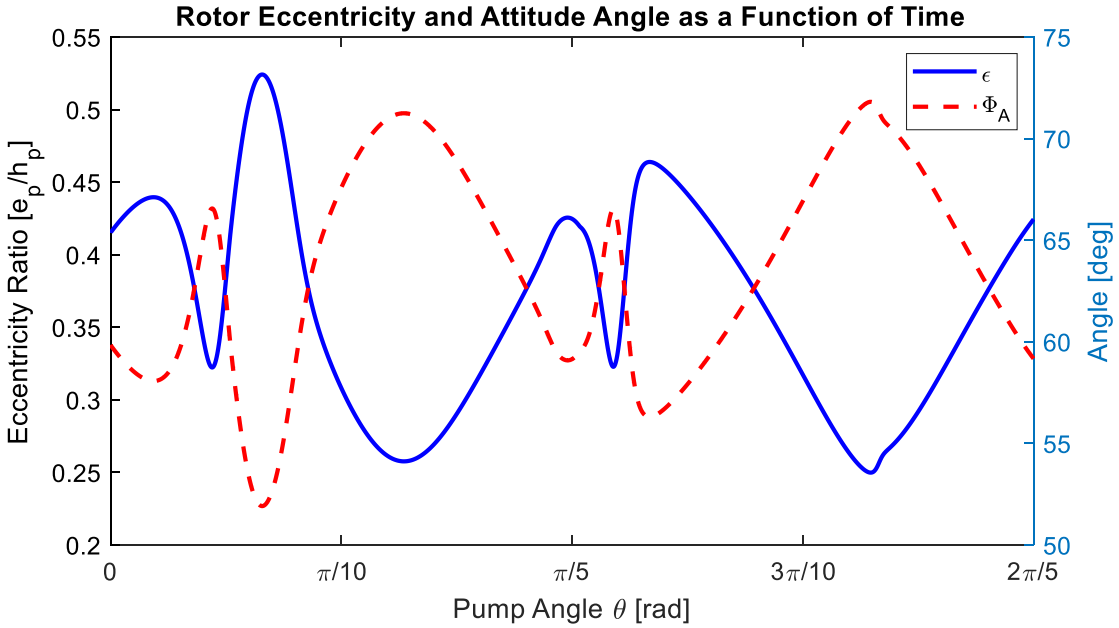

FIGURE 2.37: ROTOR ECCENTRICITY AND ATTITUDE ANGLE TO COUNTER UNBALANCED FORCES

Next, the losses at the pintle with and without eccentricity are compared. Figure 2.38 and Figure 2.39 show the torque and leakage at the pintle-rotor interface, again for the first fifth of a revolution. The eccentricity impacts both the leakage and torque. The leakage increases significantly, roughly doubling, when the eccentricity is taken into consideration. The torque is slightly affected, dropping about 15 percent once the eccentricity is considered. Also, the torque is considered negative because it acts against the pump block rotation. As derived, the pintle eccentricity model requires care if it is applied to high speed operating conditions where the quasi-static loading assumption would become invalid. A detailed discussion of when this assumption is appropriate can be found in Hamrock [47].

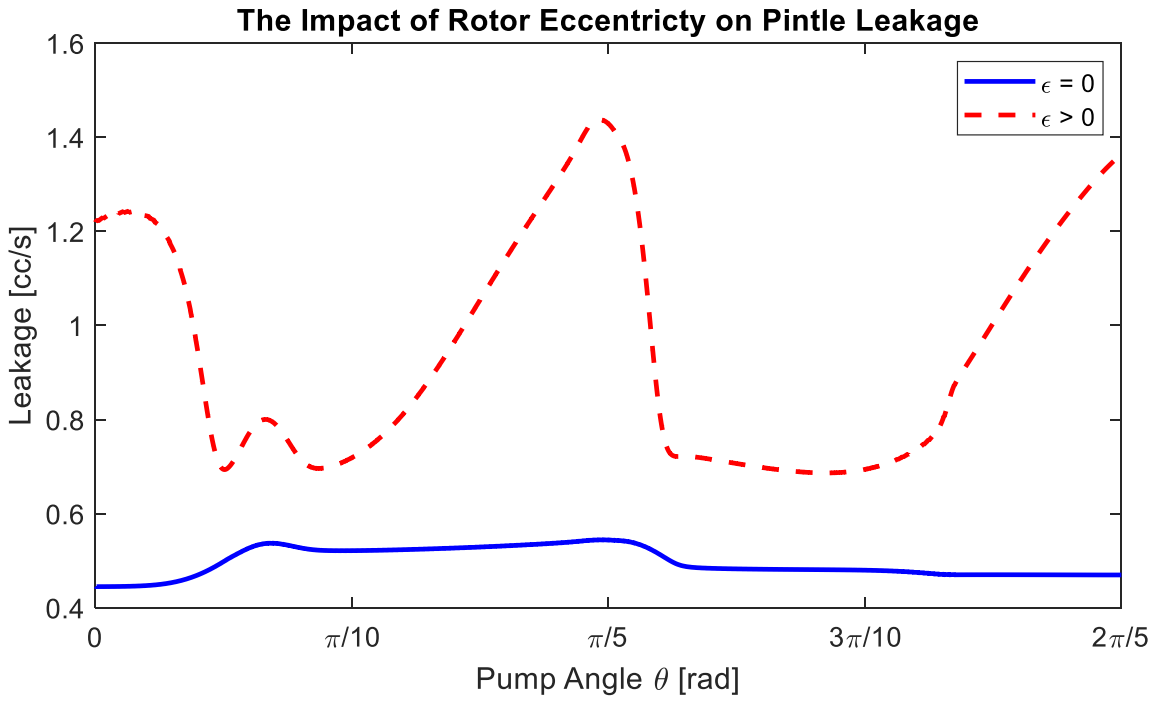

FIGURE 2.38: COMPARISON OF THE LEAKAGE AT THE PINTLE-ROTOR INTERFACE

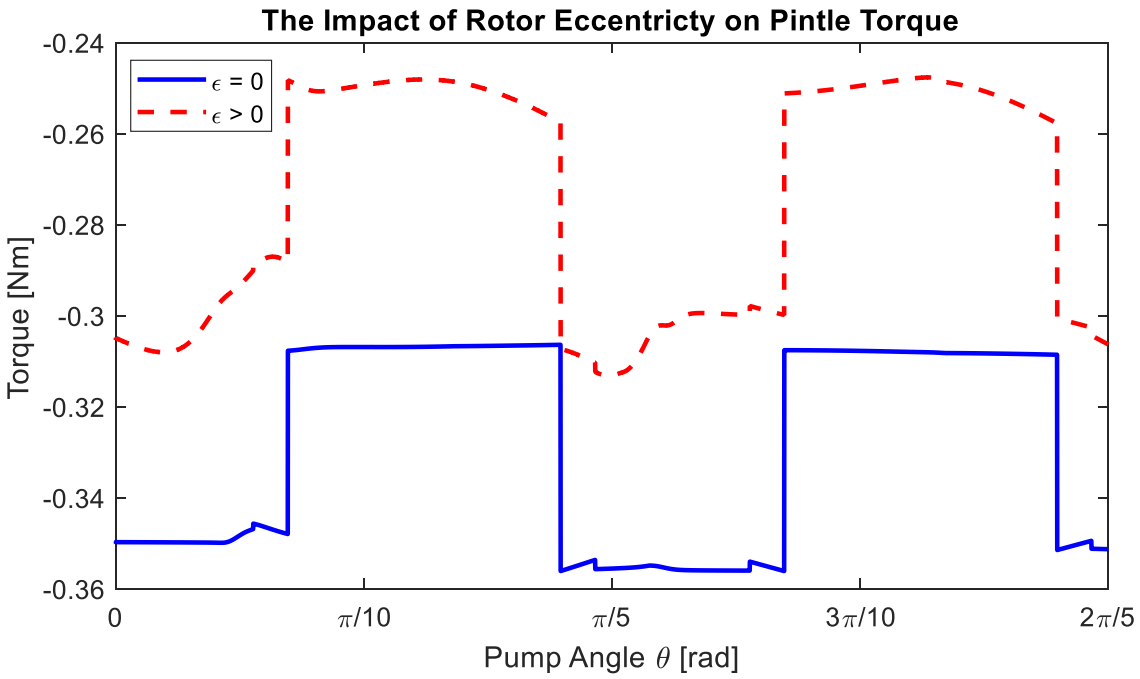

FIGURE 2.39: COMPARISON OF THE TORQUE AT THE PINTLE-ROTOR INTERFACE

2.3.2.2 Ball-Cylinder Interface Losses

Solving for the ball position in the cylinder yields the result shown in Figure 2.40 for the full dynamic model and one without heat transfer and EHL. At the start of the cycle, the ball moves quickly from a centered position towards the right wall (grey dashed line), which corresponds to the start of the pump's discharge stroke. As the pump switches from discharge to suction, around π radians, the ball moves back towards the center, but does not get as close to the other wall as it did during discharge. This happens because the normal force, along with the pressure angle, creates a side load on the ball that drives it towards the wall. The pressure is higher during the discharge stroke and thus a higher normal force is experienced. These trends are independent of whether the model considers heat transfer and EHL behavior.

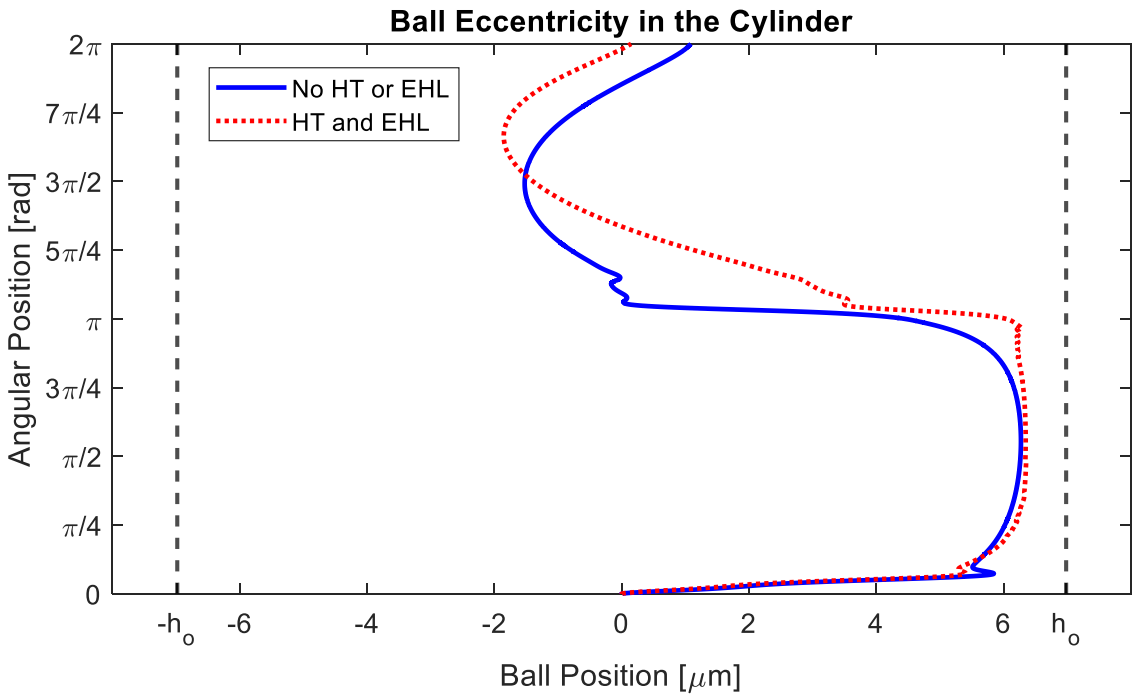

FIGURE 2.40: BALL PISTON ECCENTRICITY

Comparing the results of the heat transfer and EHL versus the no heat transfer and EHL model shows that the two results are similar, particularly at the start of the discharge stroke. The heat transfer and EHL model takes longer to leave the side of the wall, as the elevated temperatures in the heat transfer model decrease the Couette contribution to the pressure distribution. In general, the model with heat transfer and EHL appears to have more damping near the cylinder wall then its isothermal counterpart. The real value of the model that includes EHL is its robustness. When heat transfer and EHL are not considered, the model is sensitive to the assumed viscosity and operating condition. Without EHL, the model has no mechanism for preventing the ball from hitting the cylinder wall, particularly at low speeds where hydrodynamic lubrication is less reliable.

The entirety of the ball piston kinematics are shown in Figure 2.41 to compare the heat transfer and EHL model to one without those features. An interesting result is that the EHL model has more numerical noise, which is a direct consequence of the stiff behavior of the differential equation that governs the physics. The EHL's exponential piezo-viscous relationship is physically realistic but does create a complicated system of equations requiring very small timesteps to prevent numerical noise. Fortunately, the numerical noise from the EHL quickly dissipates and does not impact the ball position which is a critical value when calculating losses. Despite the numerical noise, the EHL model comes with a major advantage, it provides a physically realistic method for bounding the

ball position during low speed, high pressure operating conditions. Figure 2.42 shows what happens during a low speed, high pressure operating condition when EHL affects are not considered. The ball position predicted by the model without EHL crosses the cylinder wall creating an unrealistic situation (upper right). This happens because the hydrodynamic lubrication is not capable of maintaining a fluid film at this operating condition. There is still some numerical noise that occurs in the EHL model (lower right), but it at least maintains physical coherence. Note that the zoomed out plot (left) is for the model without EHL considered, the image is intended to show the realistic position bound created by the EHL model.

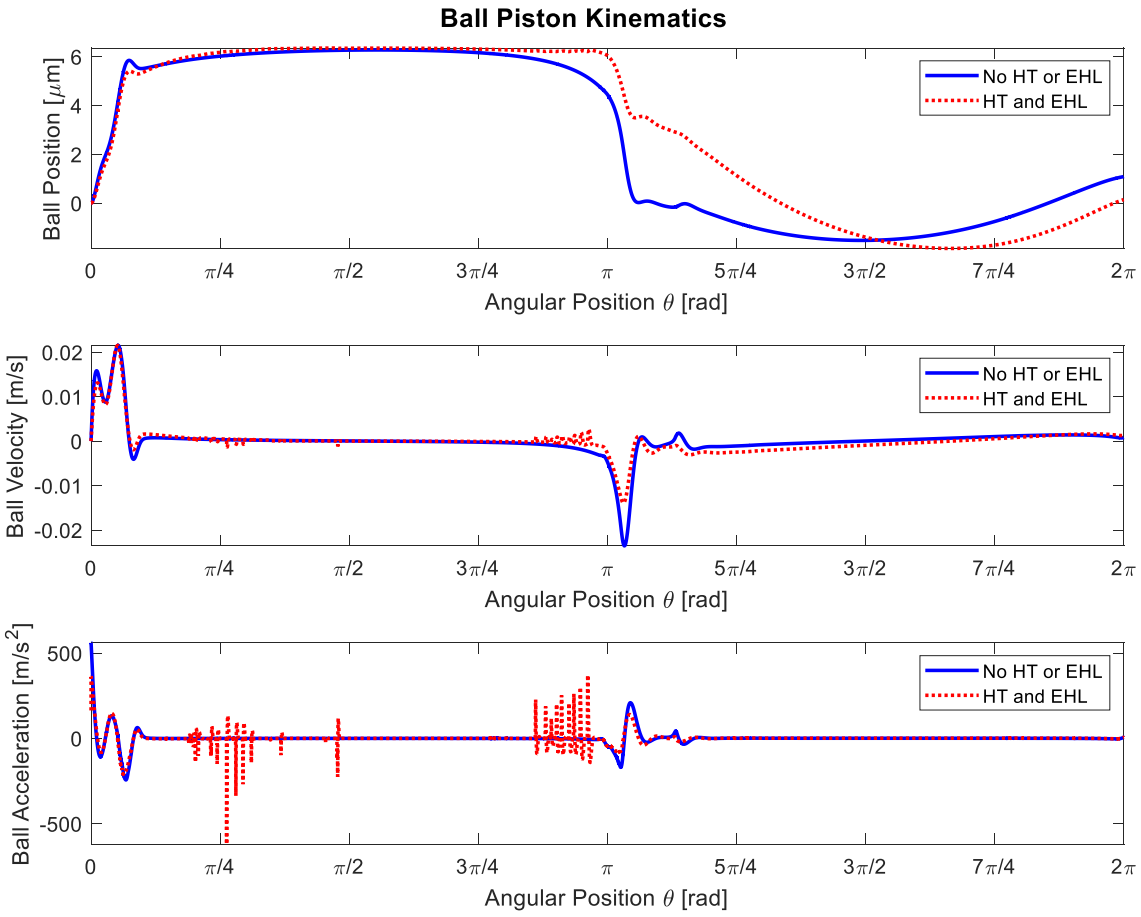

FIGURE 2.41: BALL PISTON KINEMATICS

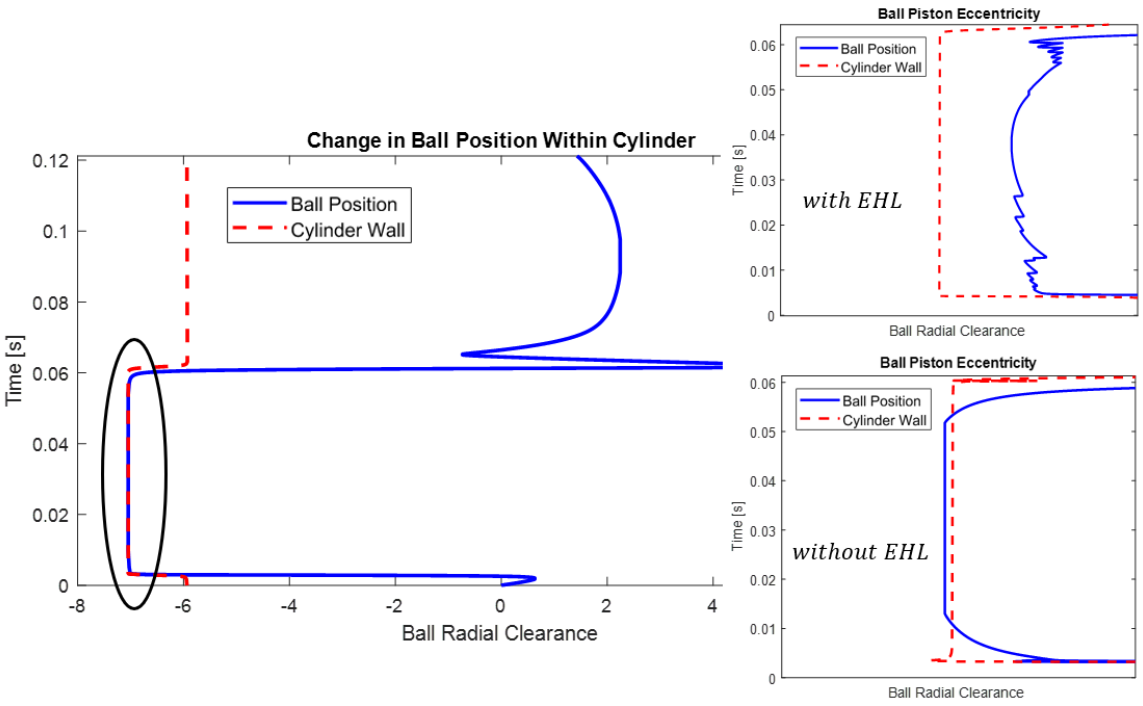

FIGURE 2.42: BALL ECCENTRICITY WITHOUT EHL (BOTTOM) VERSUS EHL (TOP) – 500 RPM 3.45 MPA

The position of the ball changes dramatically during a pump revolution, which impacts the shear and leakage predictions at the ball-cylinder interface. Figure 2.43 and Figure 2.44 show the difference in the leakage and torque predictions for a ball that stays centered in the cylinder and one that is free to move based on the dynamics. In both cases there is an increase in losses when the ball piston is very close to one side of the cylinder, but the effect is significantly more pronounced in the torque prediction. To make a fair comparison, the dynamic model used does not include heat transfer or EHL because the centered model did not consider heat transfer.

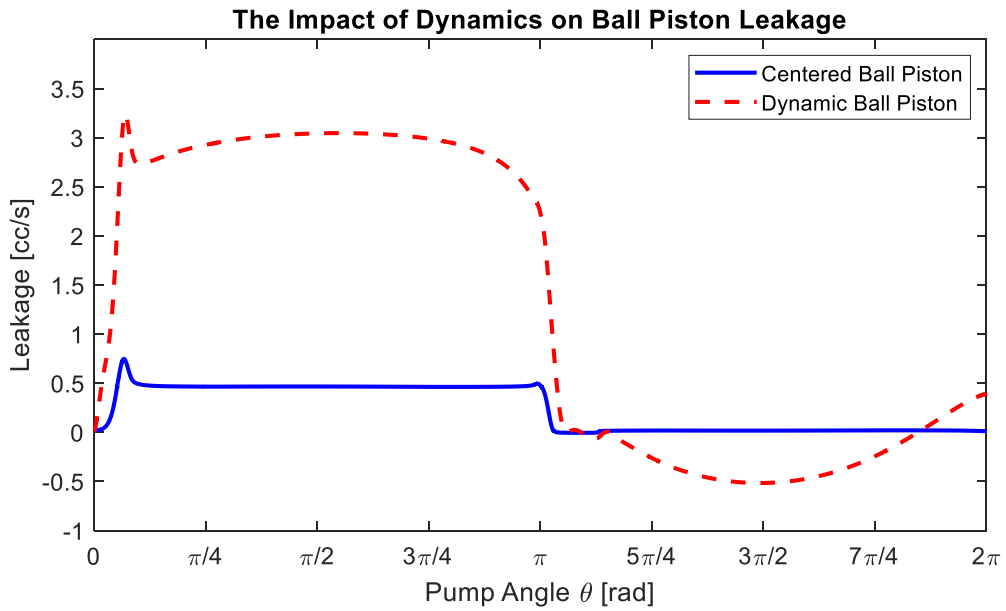

FIGURE 2.43: BALL PISTON LEAKAGE COMPARISON

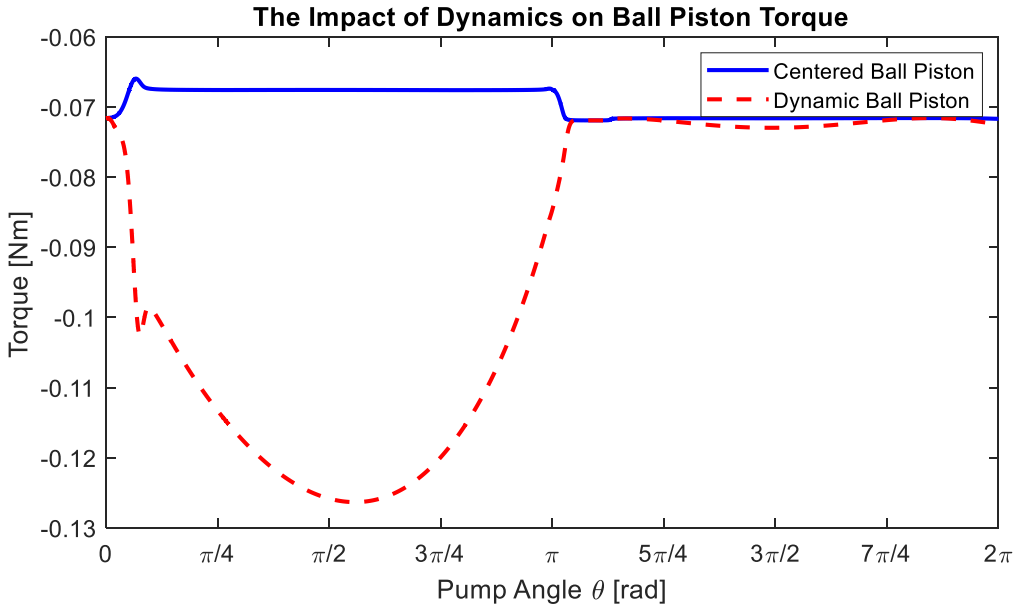

FIGURE 2.44: BALL PISTON TORQUE COMPARISON

These results show that the ball dynamics cannot be ignored when trying to determine the losses, especially the torque, at the ball-cylinder interface. The next question is whether the heat transfer model is required to capture the full extent of the losses. The thermal control volumes used for the results are shown in Figure 2.45 for reference and the temperatures around the ball are shown

in Figure 2.46. The figure is broken into two subplots, showing the right side of the ball piston and the left. In each half there are four evenly spaced control volumes. Note that the right side of the ball is where the piston approaches the cylinder wall during the high pressure discharge. Many interesting features can be seen from Figure 2.46. First, the oil temperature can vary widely during the cycle, particularly when the ball moves to one side of the cylinder and the control volume size decreases resulting in less thermal mass. Even though the temperature increases and decreases in each control volume, it never drops below the bulk temperature of 310 K. Due to the symmetry of the analysis, control volumes 1 and 8, 2 and 7, 3 and 6, and 4 and 5 should be equivalent. This is indeed the case according to the thermal model.

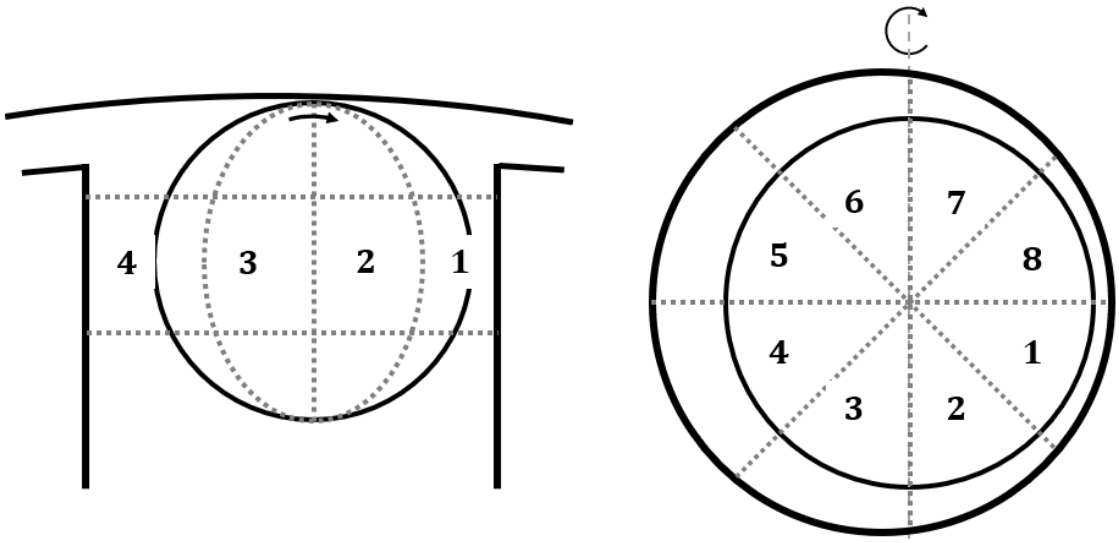

FIGURE 2.45: THERMAL MODEL CONTROL VOLUMES

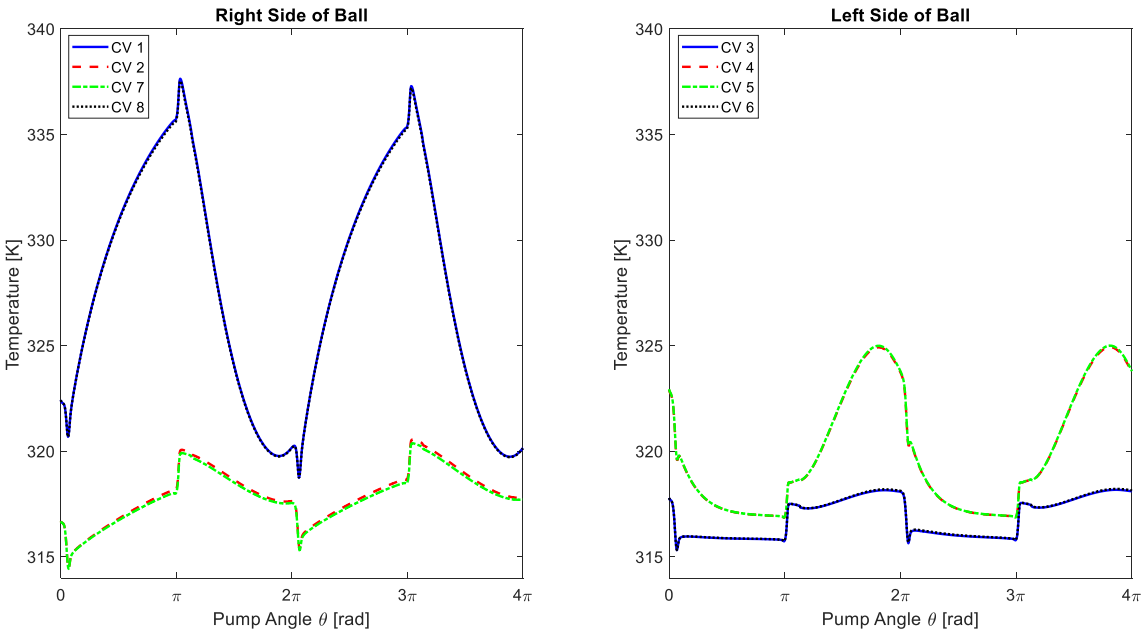

FIGURE 2.46: CONTROL VOLUME TEMPERATURES AROUND THE BALL PISTON

According to the model, the temperature around the ball piston changes significantly during operation. However, Figure 2.47 and Figure 2.48 show that the losses do not change significantly whether heat transfer is considered or not. The total losses do not change much, but the loss mechanism does. As expected, the higher oil temperatures in the heat transfer model results in less shearing loss but more leakage loss. The overall losses calculated by the heat transfer model do not tend to increase at high pressures because the ball does not stay centered. Most of the temperature rise occurs at the thinnest gaps where the height limits the leakage; also, EHL behavior occurs preventing the viscosity from dropping too low. The shearing losses do experience some of the noise that was seen in the kinematics, but the average value through the noise is approximately correct making it insignificant to the model.

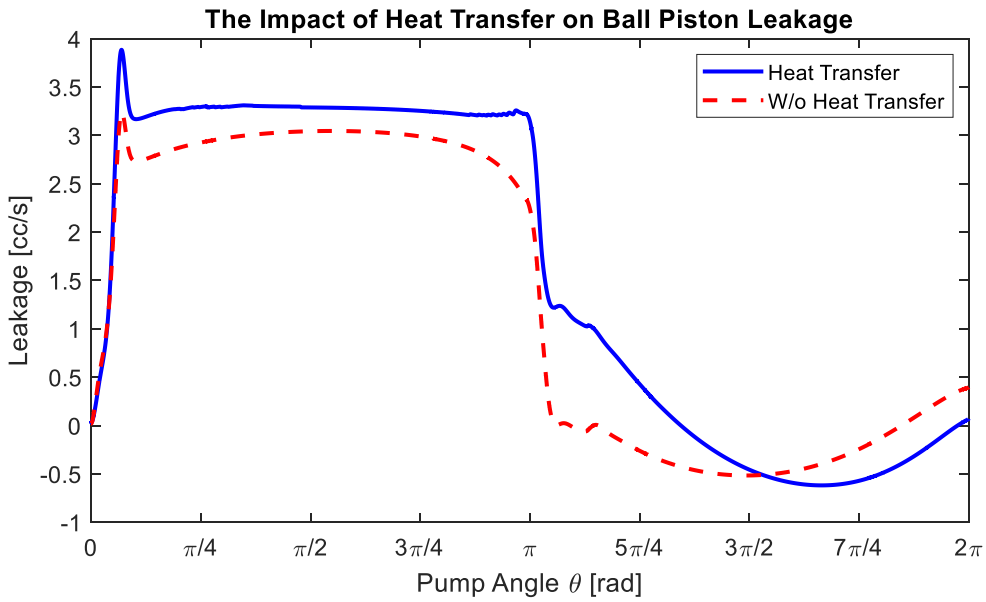

FIGURE 2.47: HEAT TRANSFER AND BALL PISTON LEAKAGE

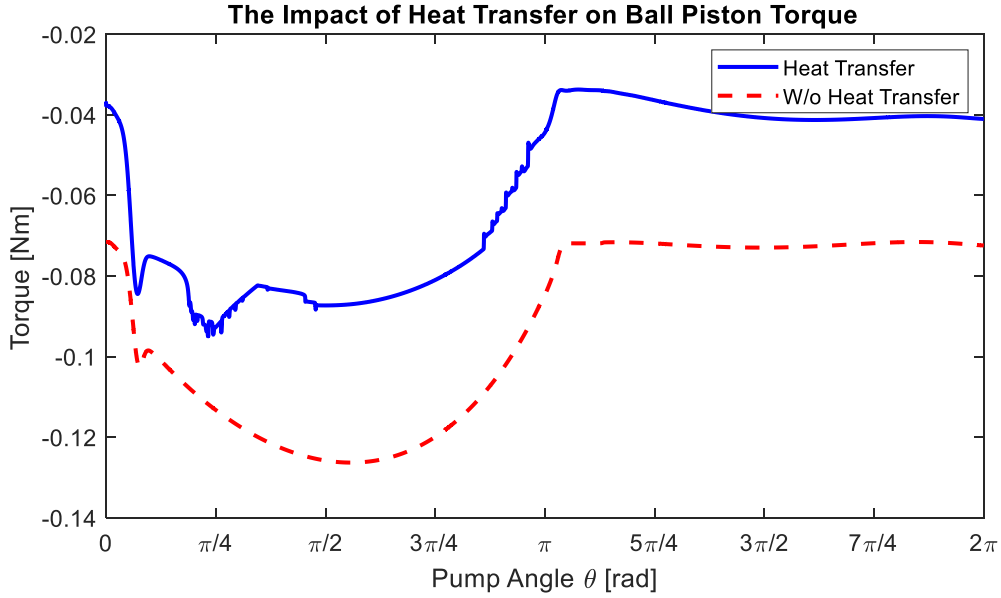

FIGURE 2.48: HEAT TRANSFER AND BALL PISTON TORQUE

Both dynamic models increase the predicted losses and improve the accuracy of the simulation. Figure 2.49 shows the power loss amount for one cylinder using the full dynamic model. From the figure, the ball piston losses are the most significant contribution and will be multiplied by the number of pistons making it a crucial interface. For reference these losses are relative to a pump output power of 3,955 Watts, or roughly 790 Watts per cylinder. The simulation results shown are

based on an unoptimized design that is being developed for experimental validation. The model requires 1 hour to run on the Minnesota Supercomputer with 1 core and 52gb of memory. This time is longer for slower operating conditions and shorter for faster ones.

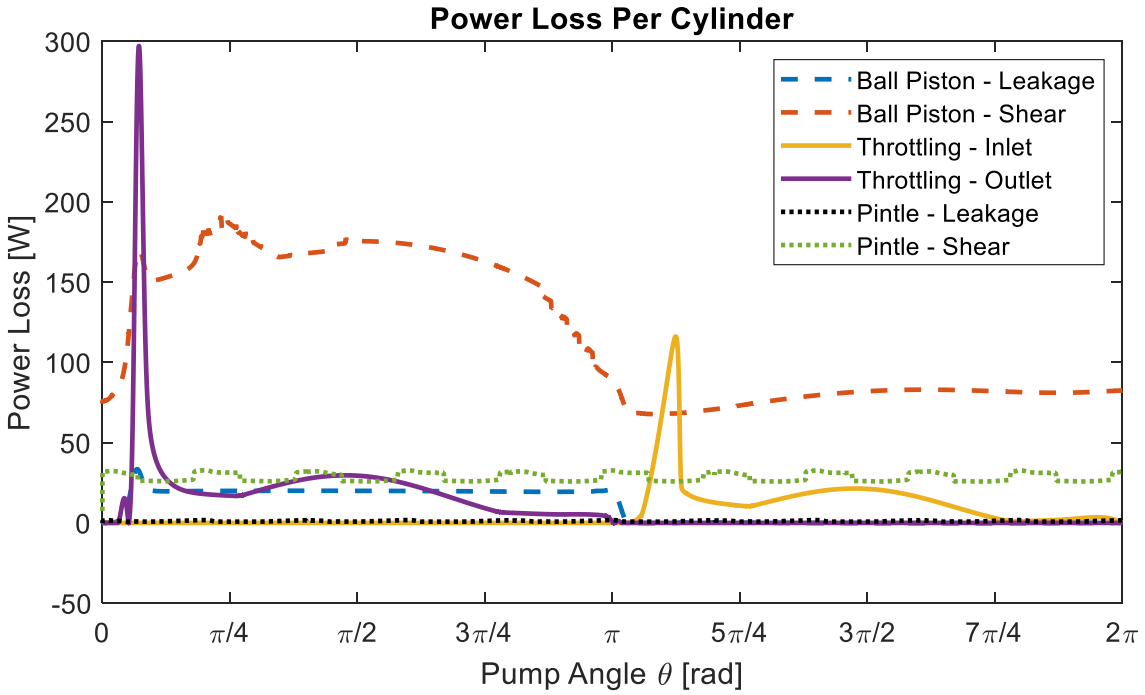

FIGURE 2.49: FULL MODEL CYLINDER POWER LOSS DURING PUMPING OPERATION

2.4 Conclusion

This chapter demonstrated that a radial ball piston pump/motor model can be developed that encapsulates all the necessary physics while maintaining computational efficiency. The model provides physically realistic behavior for the pressure dynamics, pintle-rotor interface, and the ball-cylinder interface. The model can predict the overall efficiency of the unit, as well as the individual loss mechanisms.

Analytical techniques were used as often as possible to improve the computational efficiency. For example, analytical expressions were used for the valve area profile in the pressure dynamics solver to improve the speed of evaluation. The pintle-rotor interface assumed a piece-wise pressure distribution that was analytic and captured the fundamental dynamics. The interface also implemented a short-width journal bearing model [47] to determine the rotor position and improve the accuracy of the loss predictions without sacrificing speed. The ball-cylinder interface assumed hydrodynamic lubrication to make it as simple as possible without losing realistic behavior, and

empirical models were utilized for elastohydrodynamic behavior whenever the original assumptions were violated. Both the pintle-rotor and ball-cylinder interfaces involved simple heat transfer models to avoid having to use an unrealistic isothermal assumption.

These model features predict interface torques, leakage losses, and throttling performance, but the validity of these results is unknown. Their trends and magnitudes appear physically realistic, but without experimental confirmation, confidence in the model is not verifiable. Therefore, the next chapter examines an off-the-shelf radial ball piston pump and compares experimental data that was collected to simulations.

3 Experimental Results and Model Validation

3.1 Introduction

The radial ball piston model developed in Chapter 2 describes many of the phenomena that occur within the unit. The qualitative trends and results appear reasonable, but without experimental results, the quantitative accuracy of the model predictions is uncertain. Therefore, the simulation needs to be compared to experimental data to provide confidence in its predictions. This is especially important because the model will be utilized in an optimization framework driving design decisions. If the model accuracy is poor, then it could miss optimal solutions and generate an inefficient design. Another reason why validating the model is important is to determine possible limitations. Assumptions had to be made during the modeling section (Chapter 2) to maintain fast computation speed. This created a model that is inherently less accurate than computationally intensive CFD and FEA simulations. By validating the model against experiments, limitations can be identified if they exist.

3.1.1 Overview

The chapter begins by describing the off-the-shelf radial ball piston pump that was used for the experiments. It then describes the experimental setups and processes that were used to ensure accurate and repeatable data, such as calibrations and repeatability measurements done across several weeks. The chapter breaks down the various hydraulic circuits that were implemented and the benefits of each one. It describes how the total efficiency, leakage, and ball torque were all captured using the various circuits. The role of system temperature is also described through measurement and sensitivity studies. Sensitivity studies are leveraged throughout the results to understand how uncertainties within the experimental setups can impact the model performance. The chapter concludes by quantifying the accuracy of the simulation predictions and analyzing various qualitative trends.

3.2 Methods

3.2.1 Radial Ball Piston Pump

The radial ball piston model was validated using Eaton's Light Duty Hydrostatic 720-001 radial ball piston pump. The pump is a bi-directional variable displacement unit with a maximum speed of 3600 rpm. Its recommended applications include industrial settings and mobile equipment,

especially tasks that require variable displacement in both directions, such as hydrostatic transmissions [9]. The peak flow rate through the unit is 27.4 Lpm at 8.62 MPa continuous pressure, making it capable of 4 kW at a corner operating power. An image of the pump from Eaton's data sheet can be seen in Figure 3.1.

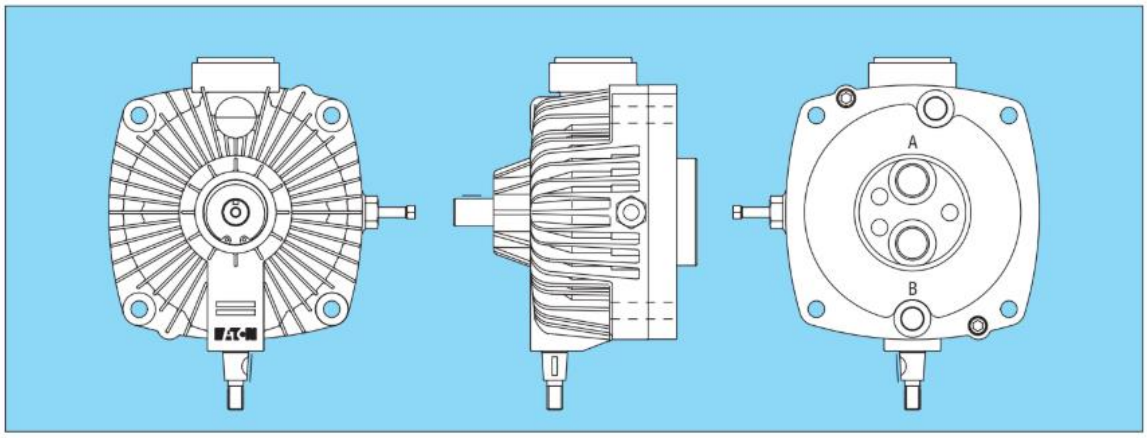

FIGURE 3.1: EATON RADIAL BALL PISTON MODEL 7 PUMP [9]

Other features of the pump can be seen in Figure 3.2, which shows the internal fluid passages in a schematic. From the schematic, port A and port B function as inlet and outlet ports depending on the pump displacement and input shaft rotation direction. Ports C and D are case drains, and port E is a fluid expansion reservoir. Other components shown in the schematic are the check valves and dump valve. The check valves allow fluid from the case to be drawn to the input port if the inlet pressure drops, thus avoiding cavitation. The dump valve manually opens the check valves, allowing the pump to freely rotate, which is useful within its application as part of a hydrostatic transmission.

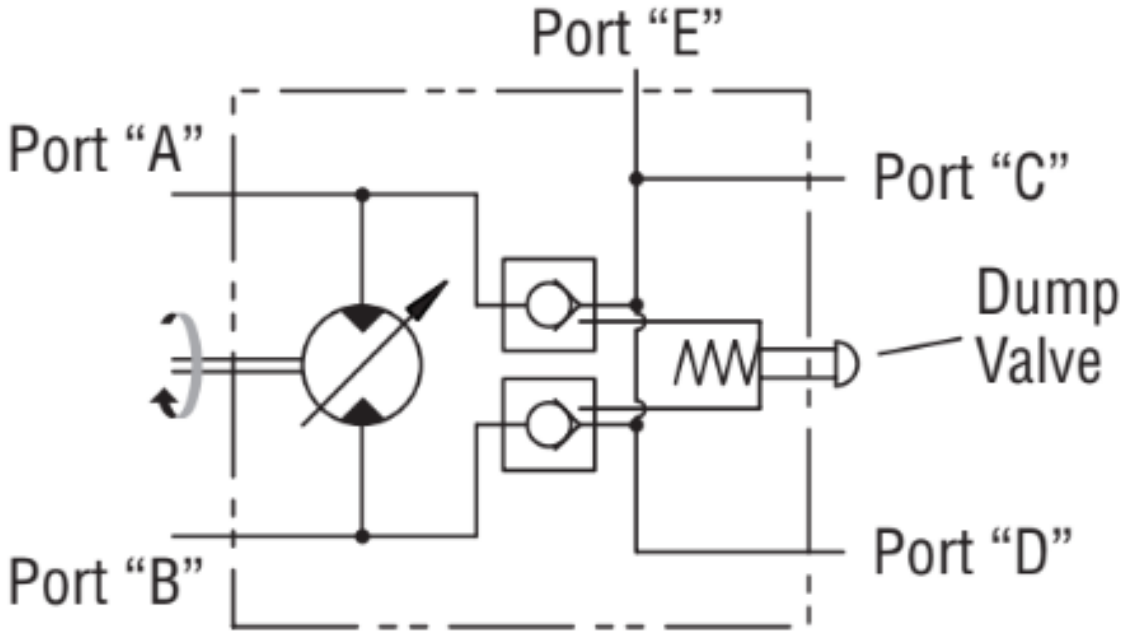

FIGURE 3.2: RADIAL BALL PISTON INTERNAL SCHEMATIC [9]

The parameters required for the simulation of the pump were determined based on drawings and direct measurements. The ball-cylinder clearance was measured during assembly using air gauges to get micrometer precision. The pintle-rotor clearance was measured to micron precision with a micrometer and bore gauge. The other values were incorporated into the model using part drawings provided by the manufacturer. These drawings included specifications for the overall size, valve timing angles, valve areas, and dead volumes.

3.2.2 Experimental Setup and Data Collection

3.2.2.1 System Efficiency

After acquiring the pump geometric parameters, the values were inputted into the model to simulate the specific pump that was being tested. The pump came assembled and was incorporated into *Circuit A*; the experimental test shown in Figure 3.3. The setup tests the overall efficiency of the pump and was utilized as the baseline experiment. The following discussion regarding the hardware and sensors for this experimental setup also apply to the other setups presented later in this section.

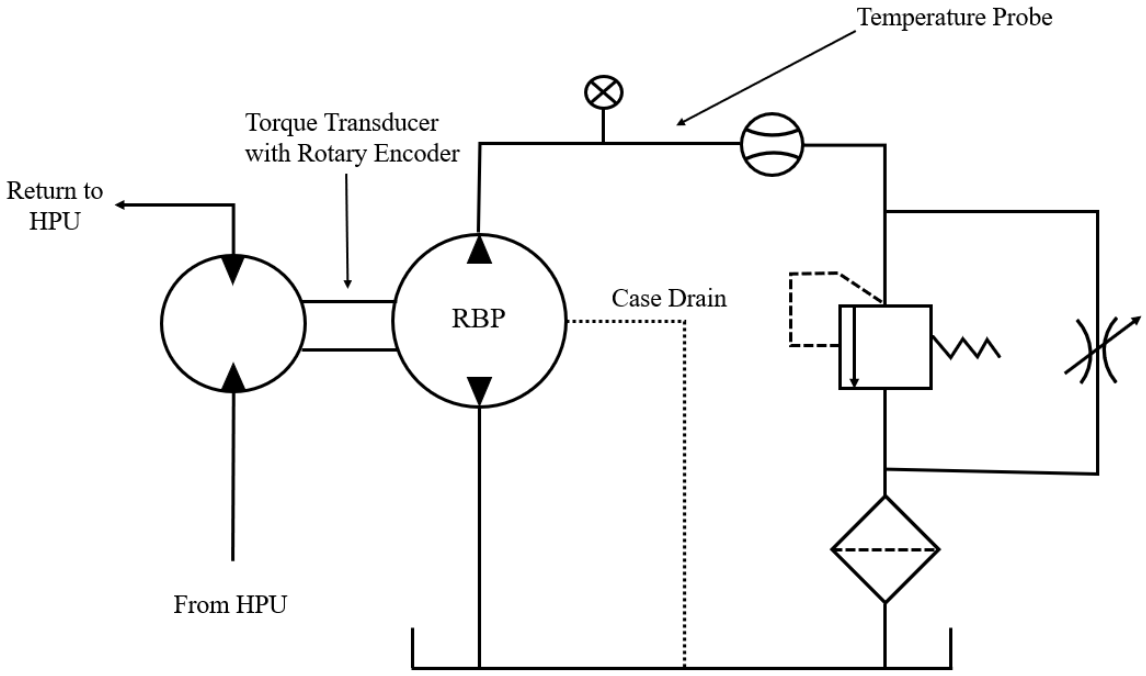

FIGURE 3.3: EFFICIENCY EXPERIMENTAL TEST SETUP (*CIRCUIT A*)

The motor driving the radial ball piston pump was a Rexroth bent-axis motor (A6VM 28 EP1 / 63W-VAB010A). The motor was bi-directional and used a proportional solenoid valve along with a hard stop to control the displacement. The bent-axis motor was driven hydraulically by a hydraulic power unit within a separate circuit.

The input torque and angular velocity were acquired from a Futek Torque Sensor – model TRS605 50 Nm – with nonlinearity $\pm 0.2\%$, hysteresis $\pm 0.1\%$, and non-repeatability of $\pm 0.2\%$ of the rated output. The torque sensor also comes with a 2 x 360 encoder to measure leading and trailing counts, this allows the rotation speed and direction to be measured experimentally. The output flow rate was measured using an AW Lake Gear Meter model JV#-30KG that has a resolution of 1.7 cc/pulse and $\pm 0.5\%$ accuracy with changes in viscosity. The outlet pressure was measured with an Ashcroft model T2 3000 psi pressure transducer with $\pm 0.25\%$ accuracy considering non-linearity, hysteresis, and non-repeatability. This is a resolution of 0.052 MPa. The pressure at the inlet port was assumed to be atmosphere.

The flow rate and rotational speed used counts to measure the experimental values, therefore, no calibration was required. However, calibration was needed for the pressure and torque transducers. A dead weight tester was used to calibration the pressure transducer and the results are shown in Figure 3.4 below. The calibration of the torque transducer was performed by coupling the

transducer's shaft to a pulley and then hanging known masses on the outer radius of the pulley. The calibration for the torque transducer was done in both the counter-clockwise and clockwise directions with the data shown in Figure 3.5.

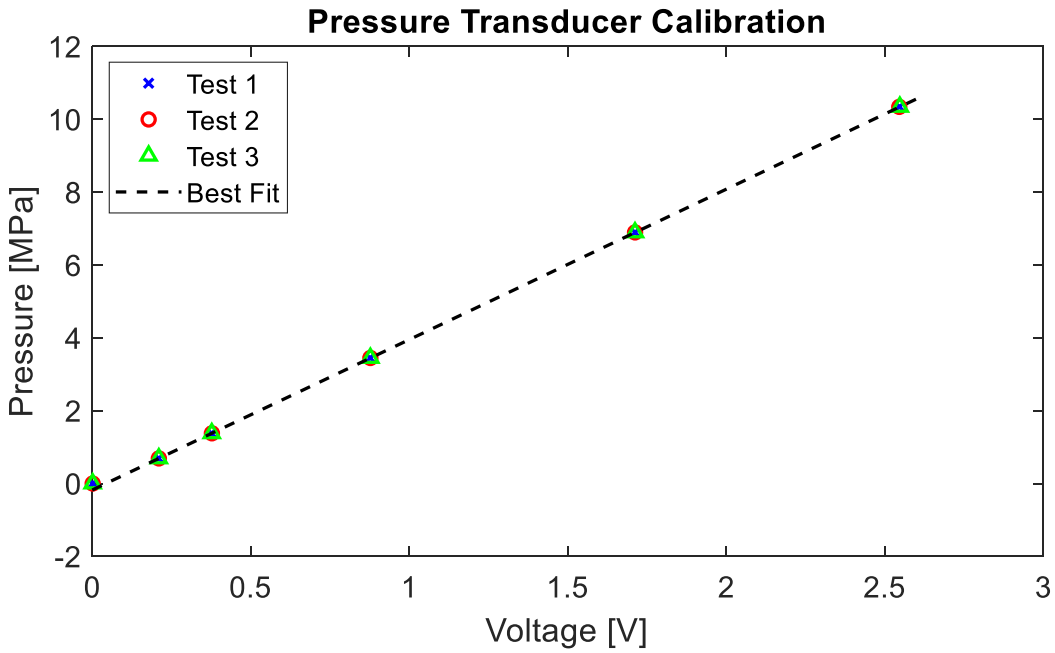

FIGURE 3.4: PRESSURE TRANSDUCER CALIBRATION DATA

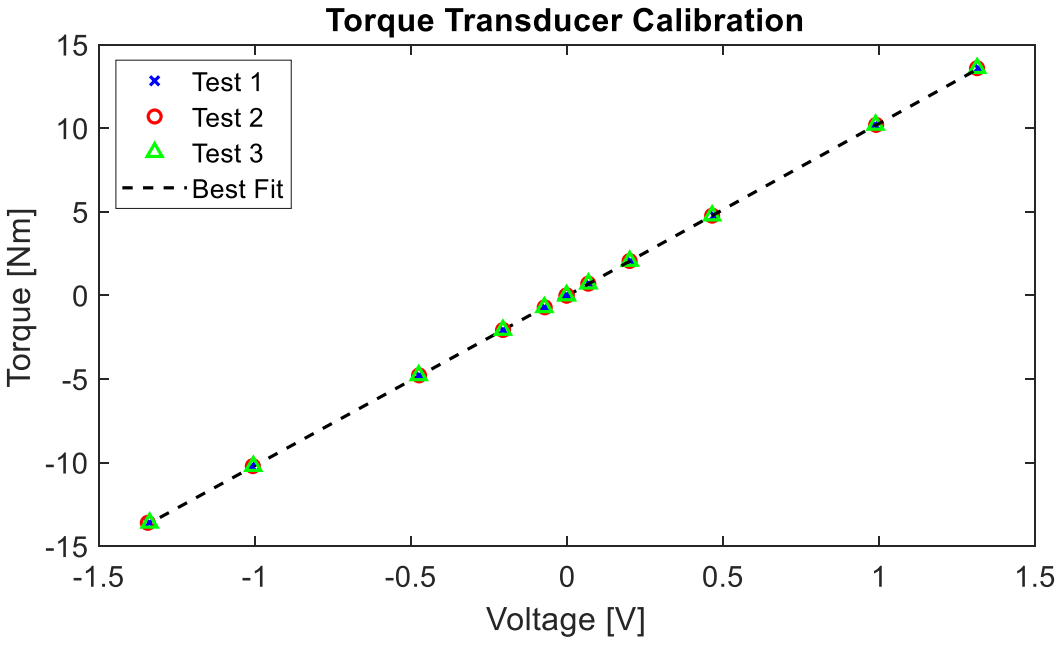

FIGURE 3.5: TORQUE TRANSDUCER CALIBRATION DATA

From *Circuit A* (Figure 3.3), the output flow rate and input torque were measured using the aforementioned flow meter and torque transducer. This information allowed the experimental efficiency to be calculated according to eq. (3.1).

$$\eta = \int_0^{t_{end}} \frac{\Delta p Q_{out}}{\mathrm{T}_{input}\omega_{input}} dt \tag{3.1}$$

To compare the simulation to the experiments, the pressure differential across the pump and the input angular velocity were measured, and these values were entered into the simulation as known operating conditions. The oil temperature from the experiment was also inputted to determine the oil viscosity. The simulation then predicts the output flow rate and required input torque. These predictions were compared against the measured outlet flow rate and input torque. This technique allows for the model to be validated at the system level making predictions that are useful when considering an overall pump design.

3.2.2.2 Leakage Measurement

The goal of the model is to predict the pump efficiency, however, there are both volumetric and mechanical losses to consider. It is important that both losses are understood when moving into the design stage of the project. There is also compressible energy that is carried by the high pressure hydraulic oil, but this term was ignored due to the relatively low operating pressures of this unit.

Leakage is a major contributor of volumetric losses and is particularly important to predict when designing the integrated hydraulic-electric unit. The leakage from the pump determines the mass flow rate across the electric machine for cooling; an essential parameter when determining the power density that the machine can safely reach.

A second experimental setup, *Circuit B*, was implemented to validate the leakage predictions of the model. As shown in Figure 3.2 and discussed in section 3.2.1, the Eaton pump was designed with check valves from the case back to the pump inlet to ensure that inlet cavitation does not occur. If the inlet pressure ever becomes lower than the case pressure, which is often one atmosphere, then the check valve opens, and additional flow is pulled from the case to inlet. However, this means that a significant portion of the pump's leakage is often being recirculated within the body of the pump. Therefore, a charge pump was added to the inlet of the Eaton pump to ensure that the inlet stayed above case pressure and no leakage recirculated within the case. The charge pressure was set to 0.34 MPa during the experiments by adjusting the needle valve in parallel with the charge ump outlet. This setup is shown in Figure 3.6.

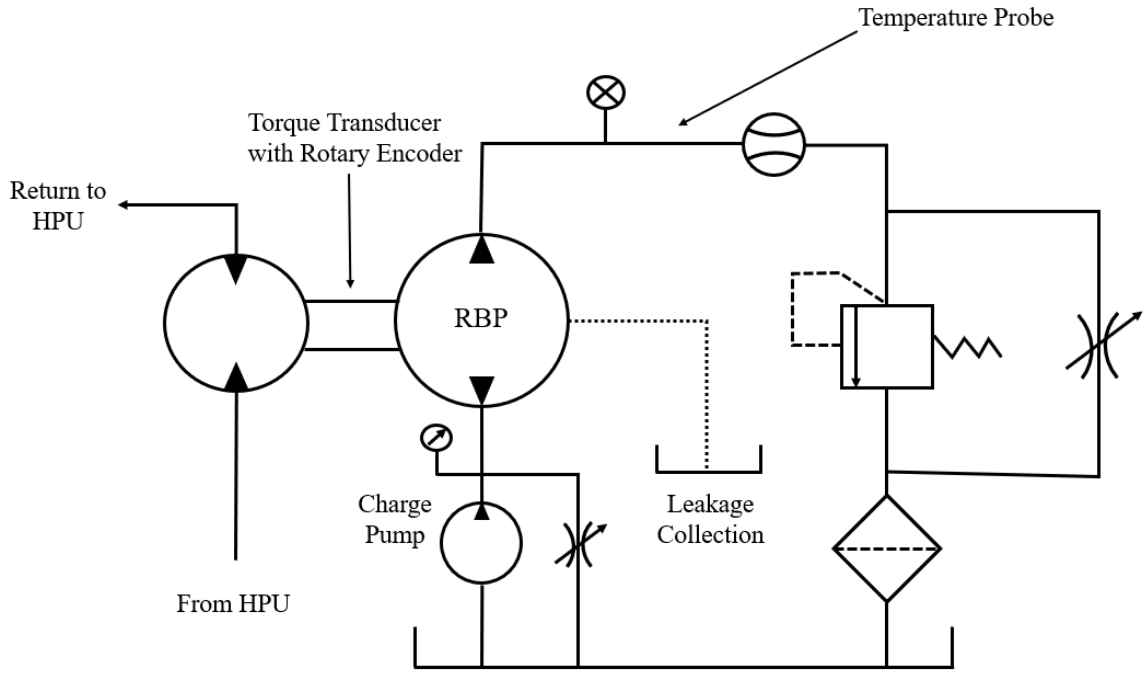

FIGURE 3.6: LEAKAGE EXPERIMENTAL TEST SETUP (*CIRCUIT B*)

Figure 3.6 shows the radial ball piston pump case-drain emptying back to a separate atmospheric pressure reservoir, which was a beaker for this experiment. The beaker collected the leakage from the pump for a fixed input speed and outlet pressure. The mass of the beaker was measured before and after the leakage was collected, and then, using the oil's density, the volume of the oil was determined. Thermal effects on the oil density were considered when calculating the volume. This volume was averaged over a 20 or 30 second period to determine the leakage flow rate.

3.2.2.3 Unmodeled Torque Estimation

Mechanical losses consist of any friction or throttling that occurs within the pump and are the second category of inefficiencies in hydraulic power units. These losses manifest themselves as a resistive torque that needs to be overcome. The required input torque follows eq. (3.2) in the general case.

$$\mathrm{T}_{input} = \frac{\Delta p D}{2\pi} + \mathrm{T}_{loss} \tag{3.2}$$

where $\Delta pD/2\pi$ is the required torque for an ideal machine and T_{loss} can be broken down further according to eq. (3.3).

$$T_{loss} = T_{ball} + T_{pintle} + T_{cam} + T_{churn} + T_{bearing} + T_{seal} \quad (3.3)$$

where T_{ball} is the torque at the ball-cylinder interfaces, T_{pintle} is the torque at the pintle-rotor interface, T_{cam} is the torque created on the ball-cam interface, T_{churn} is the torque from churning fluid in the flooded case, $T_{bearing}$ and T_{seal} are the torques created at the shaft by the bearing and seal respectfully. From the modeling chapter, T_{ball} and T_{pintle} are significant contributors to the torque and are the losses that are modeled. T_{cam} is assumed to be approximately zero because the ball is assumed to remain rolling on the cam, resulting in little power loss at that interface. The churning, bearing, and seal losses were all unmodeled.

It was desired to isolate the torque losses, which, according to eq. (3.2), can be done by setting the pressure differential to zero. Therefore, an experimental setup was constructed that connected the inlet and the outlet port together. This setup is shown in Figure 3.7 and will be referred to as *Circuit C*. Note that the displacement could also be set to zero, but this is done via a manual adjustment while the pump is running. Without a locking feature on the displacement, it was decided that creating zero pressure differential would be more repeatable then tuning the displacement for each run.

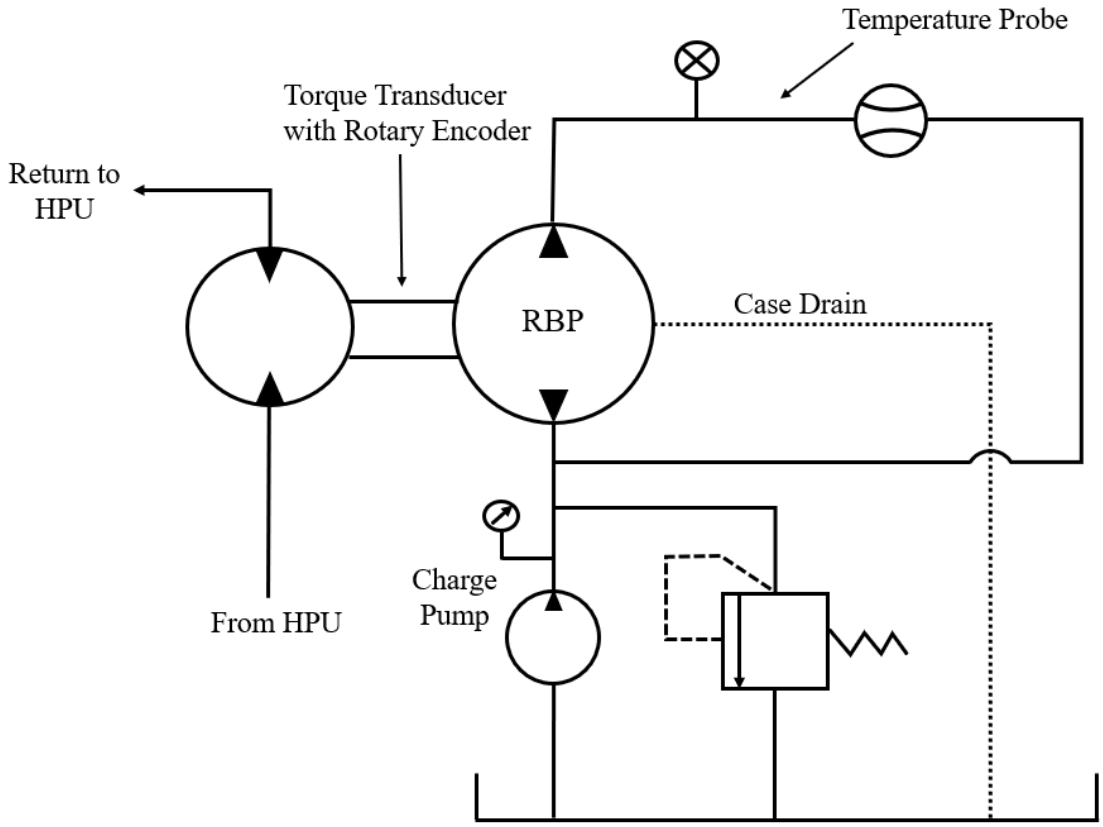

FIGURE 3.7: ZERO PRESSURE DIFFERENTIAL EXPERIMENTAL TEST SETUP (*CIRCUIT C*)

The input torque for these experiments were measured and because the pressure differential is approximately zero, the required input torque should be solely to losses. *Circuit C* offers another advantage as well. Most of the leakage is driven by a pressure differential from the pump to the case, if the pump's inlet and outlet are both connected to tank pressure then there is minimal leakage due to pressure differentials. This allows the magnitude of the other volumetric losses to be estimated.

The final setup, *Circuit D*, was designed to experimentally determine the churning, bearing, and seal losses. The experiment involved disassembling the pump, removing the ball pistons, and then reassembling the unit. The circuit rotated the pump without ball pistons so no pumping could be done, and eq. (3.3) simplified to eq. (3.4).

$$T_{loss} = T_{pintle} + T_{churn} + T_{bearing} + T_{seal} \tag{3.4}$$

T_{loss} was measured experimentally and T_{pintle} was found using the simulation predictions. Therefore, an estimate for $T_{churn} + T_{bearing} + T_{seal}$ could be found and utilized to approximate the unmodeled losses.

3.2.3 Test Procedures

The tests were run by setting the pressure differential and input speed of the pump. A combination of a pressure relief valve and a needle valve bypass were used to adjust the pressure differential. A rough value for the pressure was set using an analog gauge that provided visual feedback of the setting. Once the value was approximately correct, an oscilloscope recording data from a pressure transducer was used to fine-tune the setting. The inlet pressure was assumed to be at atmospheric pressure for *Circuit A*. A second pressure gauge was used to visually record the inlet pressure for *Circuits B* and *C*.

Setting the input speed was cumbersome because it involved tuning different experimental system parameters. The hydraulic power unit's (HPU) flow rate could be changed secondarily by adjusting the output pressure of the unit. This had to be done because the HPU was pressure controlled and had no flow control feedback or capability. Therefore, to get better control of the pressure at the HPU, a needle valve was added between the HPU and the Rexroth bent-axis motor. By adjusting the pressure setting and the needle valve, the flow and thus the speed of the motor could be controlled. The speed was set iteratively along with the pressure in the radial ball piston circuit because as the pressure increased, the HPU flow rate would be impacted by the increased torque at the Rexroth motor. The takeaway from this process was that setting the pressure differential and speed input was difficult to repeat precisely. The desired pressure and speed settings for the experiments are shown in Table 3.1.

TABLE 3.1: PRESSURE DIFFERENTIAL AND SPEED FOR EXPERIMENTAL TESTING

Experimental Operating Conditions					
Pressures [MPa]	1.03	3.45	5.17	6.89	8.27
Speeds [rpm]	500	1000	1500	2000	

Despite the inputs being difficult to precisely repeat, several tests were run at each operating condition to check the repeatability of the measurements. The standard amount was three tests at each operating condition to provide a robust procedure. These three tests were not done in order, instead the tests for a given day were randomized to improve confidence that the ordering was not

impacting measurements. Also, the repeatability was checked across multiple days to ensure that there were not significant changes due to time. Three examples are given below in Figure 3.8 - Figure 3.10. The results show that the setup is repeatable with the trends between speed and flow rate, and pressure and torque being linear as expected. The deviations from the linearity for the flow rate is explainable by considering the temperature differences and pressure differences between runs. The same phenomena hold true when considering the differences in torque values, but these are harder to notice because the range of input pressure differentials is higher than input speeds.

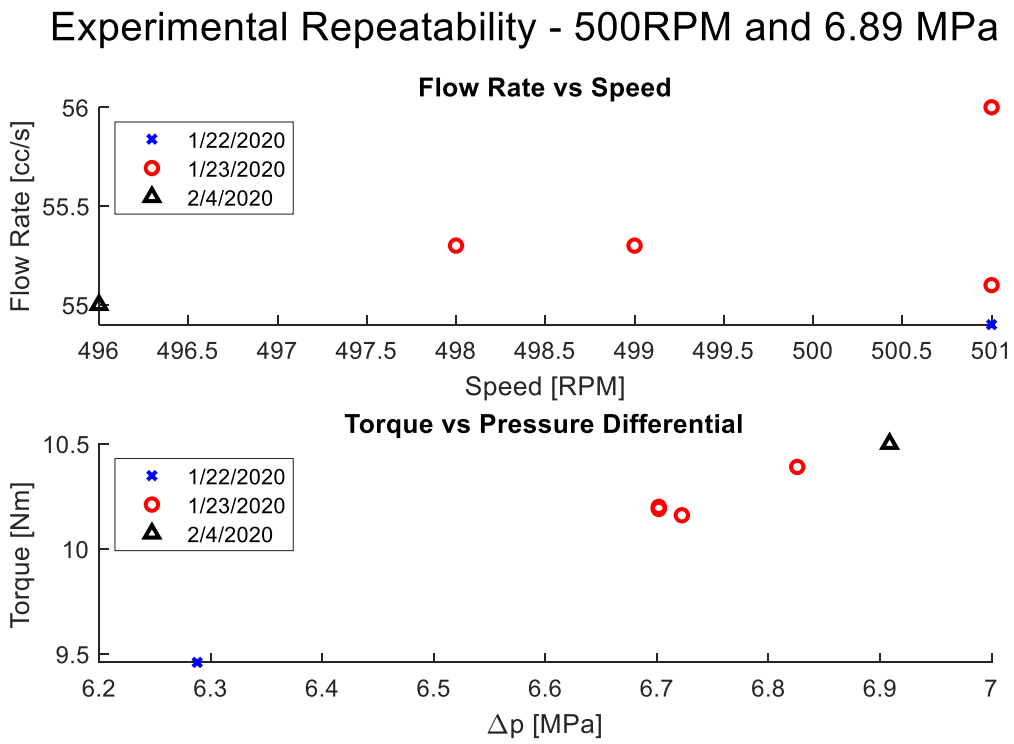

FIGURE 3.8: MEASUREMENT SETUP REPEATABILITY – 500 RPM AND 6.89 MPA

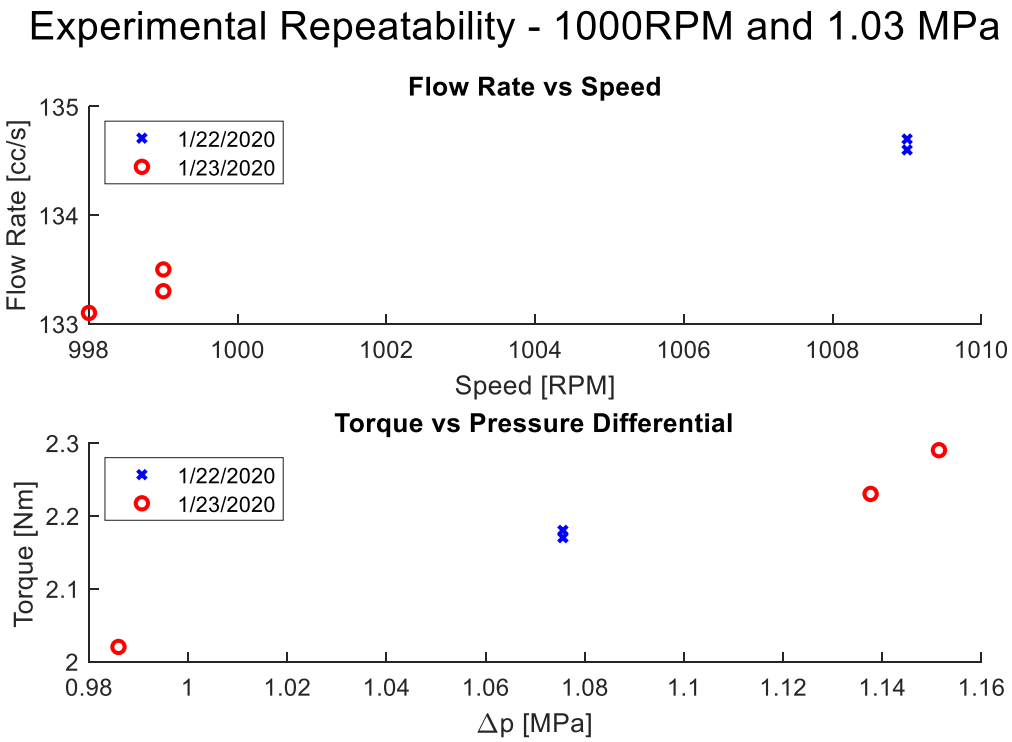

FIGURE 3.9: MEASUREMENT SETUP REPEATABILITY – 1000 RPM AND 1.03 MPA

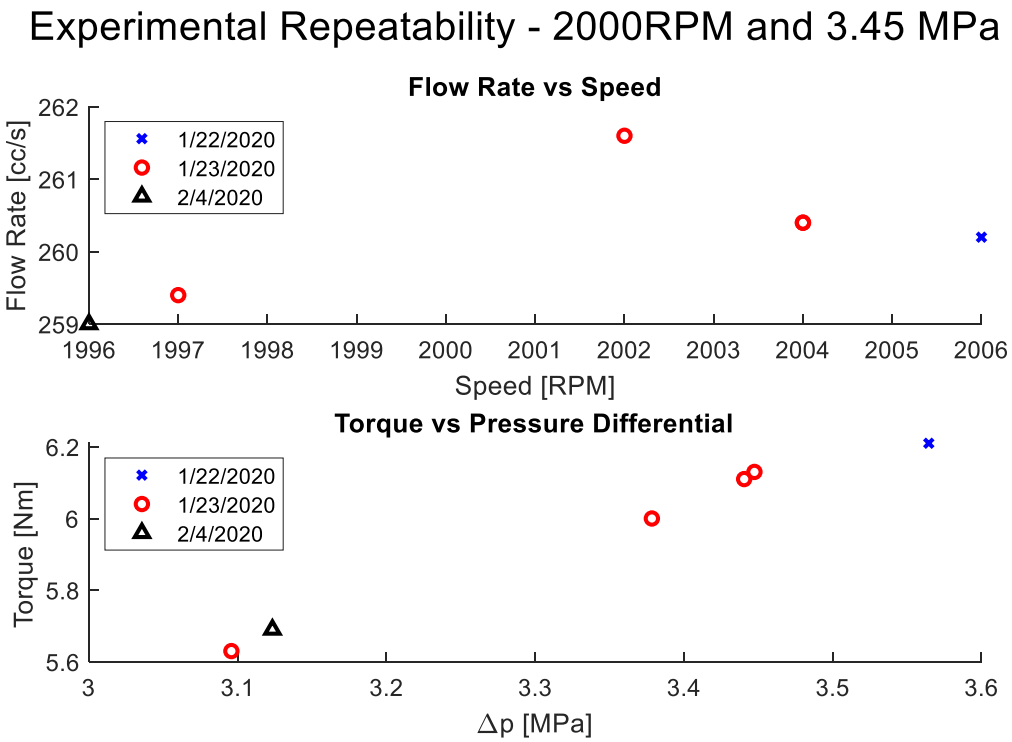

FIGURE 3.10: MEASUREMENT SETUP REPEATABILITY – 2000 RPM AND 3.45 MPA

3.2.4 Thermal Considerations

As mentioned in the repeatability discussion, the end of section 3.2.3, the temperature of the fluid impacted the results. This is largely due to the temperature dependence of viscosity. As the temperature increases, the viscosity of the oil decreases, resulting in more leakage and reduced torque, assuming a full lubrication film is maintained. The load carrying capacity of the fluid drops with decreasing viscosity as well, so higher temperatures make it more likely that metal to metal contact will occur. For these reasons, it is very important to know the experimental oil temperature to match with simulation.

A thermocouple was used at the outlet of the pump to ensure the temperature was consistent between runs. The hydraulic circuit was run without collecting data until the outlet oil temperature reached approximately 311 K. Data was typically collected for runs when the temperature was between 311 – 313.7 K which improved the repeatability of the experiments. The temperature was recorded manually for each run.

This temperature was measured using a temperature probe near the outlet of the hydraulic unit for *Circuit A*, *B*, and *C* (Figure 3.3, Figure 3.6, and Figure 3.7 respectively). When the ball pistons were removed and no pumping was performed, *Circuit D*, then the temperature was measured using an IR thermometer. Comparisons were done that showed the temperature probe and the IR thermometer were consistent with each other.

Lastly, the electronic circuit was on for 30 minutes before data was collected. This allowed the circuit to reach a steady state temperature and avoid any thermal drift in the electronics.

3.2.5 Sensitivity Studies

The last method used when validating the model was parameter sensitivity studies. This technique served two purposes: explaining the variation between simulation and experiment and providing insight into the relative importance of different parameters. The studies were done within the pressure dynamic portion of the model. This section of the model uses eq. (3.5) to determine the pressure in the cylinder throughout the pump revolution. For a detailed description, see section 2.2.1.

$$\frac{dp_{cyl}}{dt} = \frac{\beta}{V_{cyl}}\left(Q_A + Q_B - \frac{dV_{cyl}}{dt}\right) \tag{3.5}$$

The studies were done by varying the parameters and recording the flow rate and throttling losses. Note that the power loss from throttling was converted into a torque by dividing by the rotation speed. The parameters that were studied are as follows:

1. Entrained air (air content dissolved in oil). This parameter was varied from 0.3 percent to 5 percent. Entrained air of 5 percent is considered high for hydraulic systems; however, the analyzed results are from the leakage experiment where oil was constantly having to be added back into the reservoir causing air to be regularly added to the system. This also implies that the entrained air may not be constant across all the runs.
2. Dead volume. This parameter was varied by ± 25 percent of the value from the technical drawings.
3. Valve timing. This parameter was varied by $\pm 5\pi/180$ radians of the value from the technical drawings. Due to the machining of the pintle, it is expected that the largest uncertainty is the valve timing's relationship with bottom and top dead center. Therefore, all timing angles were shifted by the same offset.
4. Pump eccentricity. The value was varied from 85 percent to 100 percent of the value given from the technical drawings. The variable displacement mechanism made it impossible to measure the actual eccentricity during operation. Also, the method for setting the cam displacement experienced greater deflection at higher pressures and uncertainty arose at higher speeds to the increased vibration.

3.3 Results and Discussion

3.3.1 Introduction

This section compares the results of the model described in Chapter 2 with the data produced from the experiments described in this chapter. The experimental data used throughout this section is from *Circuit B* (Figure 3.6) because the exact leakage amount was known. If data comes from a different experimental setup, it will be noted upon presentation. The results are also compared with the flow rate and torque from an ideal pump as defined in eq. (3.6) and (3.7).

$$Q_{idl} = \frac{\omega D}{2\pi} \tag{3.6}$$

$$\mathrm{T}_{idl} = \frac{\Delta p D}{2\pi} \tag{3.7}$$

Quantitative representation of the model accuracy is also presented throughout this chapter using boxplots; therefore, a brief description of interpreting boxplots is discussed here. Boxplots break data into quartiles, Q1 is the smallest 25 percent of the data, Q2 is data from 25 percent to 50 percent, Q3 is from 50 percent to 75 percent, and Q4 is from 75 percent to 100 percent (the largest 25 percent). The box within figures represents Q2 and Q3, and is called the interquartile range (IQC). The red line within the IQC is the median value of the data. Q1 and Q4 are shown as "whiskers" below and above the IQC respectfully. Some graphs have a red plus sign outside of the whiskers. These represent outliers and, by defintion, are not included within any quartile. Outliers are found according to eq. (3.8) and (3.9).

$$outlier^{-} < Q2 - 1.5 \times IQC \tag{3.8}$$

$$outlier^{+} > Q3 + 1.5 \times IQC \tag{3.9}$$

where the IQC is calculated using eq. (3.10).

$$IQC = \max(Q3) - \min(Q2) \tag{3.10}$$

The results of this chapter are presented in three sections: baseline parameters, parameter sensitivity, adjusted parameters. Within these sections, the volumetric and mechanical efficiency predictions are studied.

3.3.2 Empirical Coefficients

Before the experimental results and the simulation could be compared, empirical relationships needed to be developed for the unmodeled physics of the pump. Referencing section 3.2.2.3, the unmodeled torque created by the churning, bearing, and seal were determined experimentally. This was done by rotating the pump without ball piston, *Circuit D*. This experimental data included the torque created at the pintle-rotor interface; therefore, to avoid double counting, the pintle-rotor torque was simulated and subtracted from the experimental results. The simulation was done based on four operating speeds: 500 rpm, 1000 rpm, 1500 rpm, and 2000 rpm.

Again, this was done by removing the pistons from the pump and rotating it. This experimental data included the torque created at the pintle-rotor interface. Therefore, to avoid double counting, the pintle-rotor torque was simulated and subtracted from the experimental results. Note that this simulation was done based on four operating speeds: 500 rpm, 1000 rpm, 1500 rpm, and 2000 rpm. The results are shown in Figure 3.11.

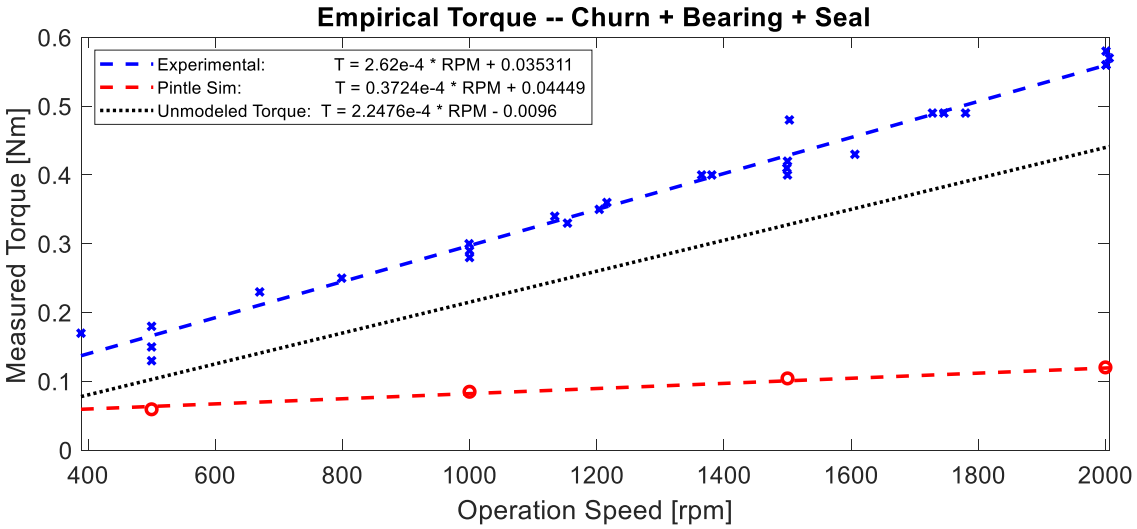

FIGURE 3.11: EMPIRICAL TORQUE VALUES FOR UNMODELED LOSSES

A linear regression was used to determine the lines of best fit. It was determined that the linear fit accurately represented the data shown and the empirical model was only used for interpolation. Without extrapolating the model to higher speeds, it is acceptable to ignore the quadratic behavior of the churning losses. The resulting experimental torque and simulated pintle torque are given in eq. (3.11) and (3.12).

$$\mathrm{T}_{empirical} = 0.000262 \times RPM + 0.03511 \tag{3.11}$$

$$\mathrm{T}_{pint_{sim}} = 0.00003724 \times RPM + 0.04449 \tag{3.12}$$

Subtracting (3.12) from (3.11) gives the unmodeled torque that can be used when comparing results.

$$\mathrm{T}_{churn+bearing+seal} = \mathrm{T}_{unmodeled} = 0.00022476 \times RPM - 0.0096 \tag{3.13}$$

These methods worked well for characterizing the unmodeled torque, however, there are some situations where it should be used with caution. From eq, (3.13), there exists a low speed limit where the prediction breaks down. The hydrodynamic film breaks down at low speeds and the lubrication regime will transition on the Stribeck curve [50]. However, since the equation is never used below 400 rpm, it is expected be valid throughout its use cases.

The more difficult question is whether pressure plays a significant role in the unmodeled torque predictions. The lack of pistons forced all the experimental data to be collected under a no load

operating condition. The churning losses are fundamentally viscous drag and are theoretically only speed dependent. The bearing torque is proportional to the normal force at the shaft. This could be pressure dependent since the single lobe cam creates an unbalanced force on the rotor block, but it is unclear how much of that force is reacted by the pintle-rotor journal bearing and how much is countered by a moment at the bearings. In the model, it is assumed that the journal bearing reacts the entirety of the force, which results in no pressure dependence at the bearing and seal. Even if the bearing does experience a changing load, the torque amount is expected to be negligible compared to the viscous drag.

3.3.3 Simulation with Baseline Parameters

The parameters that were originally selected for the simulation are shown in Table 3.2. These were considered good baseline values to begin the experimental and simulation comparison.

TABLE 3.2: BASELINE PARAMETER VALUES

Parameter	**Value**
Temperature	$\approx 311\ K$ (Experimental Value)
Clearance	Nominal Value
Entrained Air	0.5%
Eccentricity	Nominal Value

3.3.3.1 Volumetric Efficiency

The volumetric efficiency compares the flow rate produced by the pump with the flow rate predicted by the model simulations. Leakage and compressibility are two mechanisms for inefficiencies to arise in the output flow rate. The first, leakage, is the loss of useful flow due to clearances and can be directly measured experimentally. Inefficiencies in compressibility are predicted within the pressure dynamics and are dependent on factors such as oil stiffness, valve timing, and dead volume. A comparison of the experimental, simulated, and ideal flow rates is shown in Figure 3.12. The predictions from the simulation follow the experimental trends; however, the model does a poor job predicting the magnitude of the losses. It is evident that the simulation's predictions are closer to the ideal case than to the experimental data. The inaccuracy appears to be intensified at high pressure.

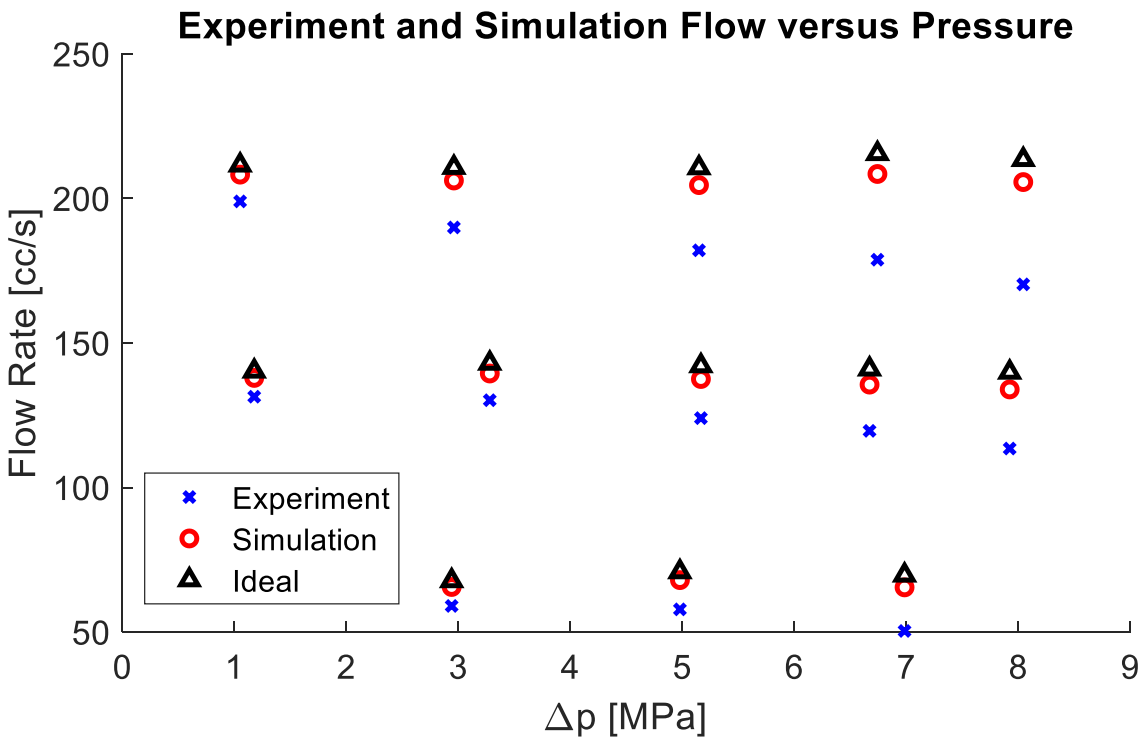

FIGURE 3.12: SIMULATION VOLUMETRIC FLOW RATE PREDICTIONS

The boxplot in Figure 3.13 quantifies the trends seen in Figure 3.12. using two measurements of error. The first is referred to as the accuracy of the simulation and is found according to eq. (3.14).

$$Q^{\%} = \frac{Q_{sim} - Q_{exp}}{Q_{exp}} \times 100 \tag{3.14}$$

Note that the accuracy is positive if the simulation overpredicts the flow rate and is negative if the simulation underpredicts the flow. The second type of error is referred to as the loss error throughout the chapter and is found using eq. (3.15).

$$Q^{\%}_{loss} = \frac{Q_{sim} - Q_{exp}}{Q_{idl} - Q_{exp}} \times 100 \tag{3.15}$$

The loss error quantifies the relationship between the experimental, ideal, and simulated data. If $Q^{\%}_{loss} = 0\%$ then the simulated data equals the experimental case, and if $Q^{\%}_{loss} = 100\%$ then the simulated data equals the ideal values. With these definitions in mind, Figure 3.13 shows that the accuracy and loss error become worse with increasing pressure. There does not appear to be a

strong correlation between speed and the errors since the median speed, 1000 rpm, has the best accuracy. Also clear from the figure is that the accuracy is reasonable, between 5 percent and 30 percent, but the loss predictions are poor. The average loss error is about 75 percent or only 25 percent better than using the idealized model.

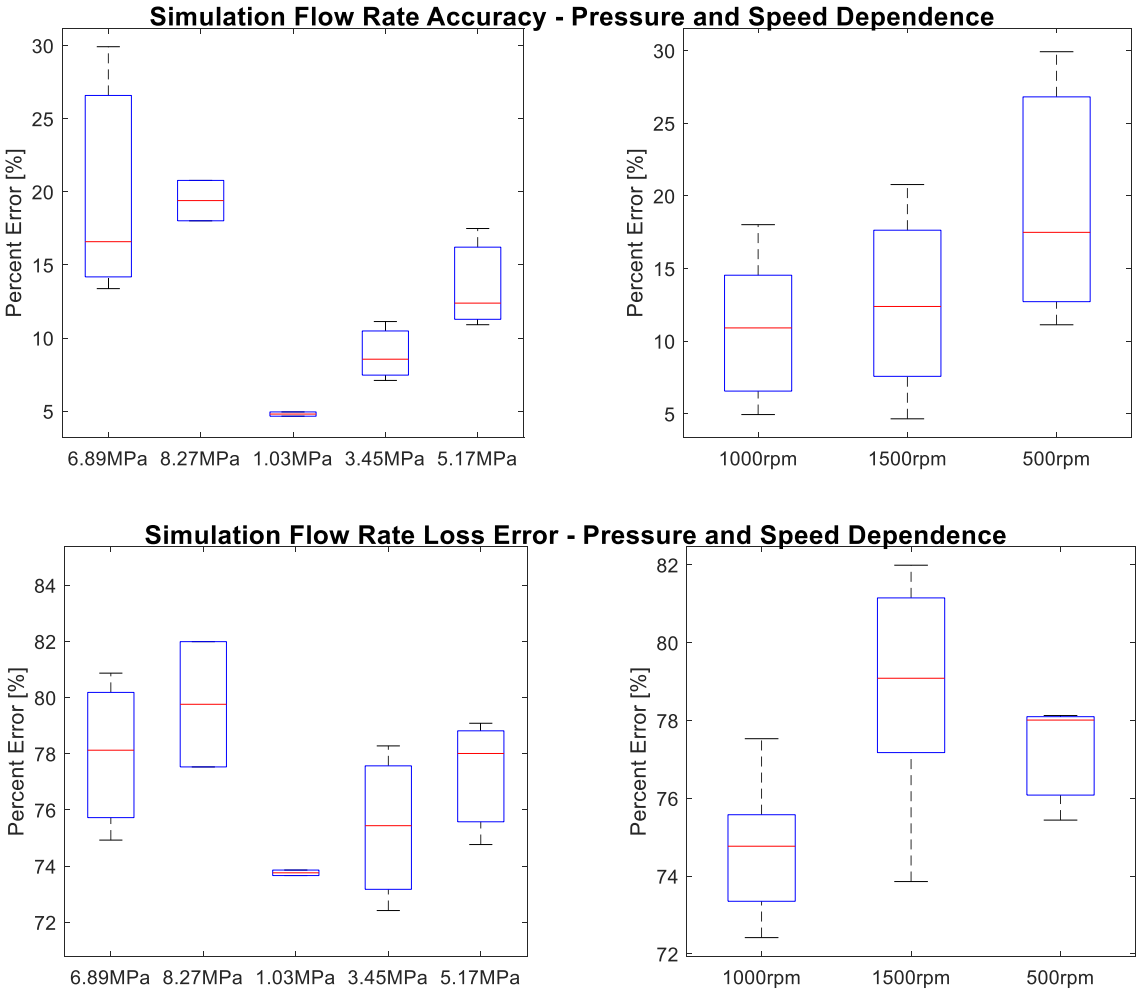

FIGURE 3.13: SIMULATION ERROR FOR FLOW RATE PREDICTIONS

Next, the leakage is compared to analyze the volumetric predictions of the model in more detail. Figure 3.14 shows that the leakage is underpredicted; however, the relationships between neighboring points is predicted correctly by the model. Using the values around 3 MPa as an example, the smallest, middle, and largest simulation values correspond to the smallest, middle, and largest experimental values. The magnitude and slope of the predictions is too low causing the discrepancy to increase at high pressures.

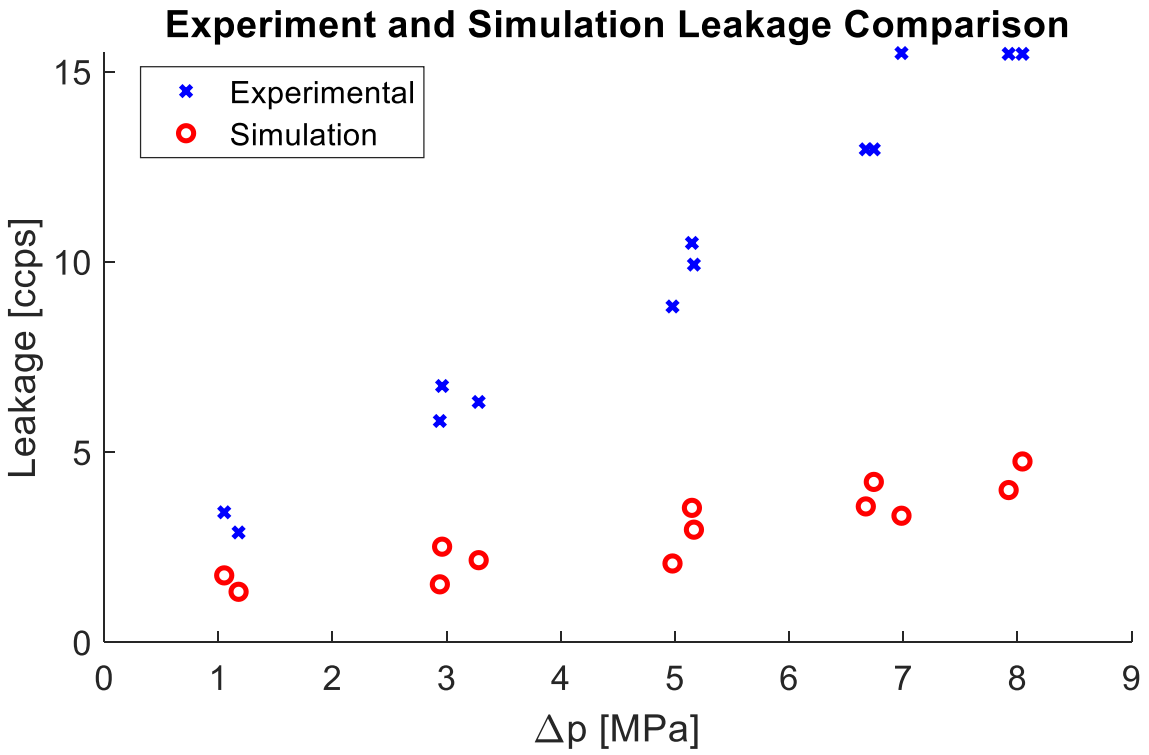

FIGURE 3.14: BASELINE SIMULATION LEAKAGE COMPARISON

3.3.3.2 Mechanical Efficiency

In hydraulic pumps, the mechanical efficiency accounts for losses from friction and throttling which require additional input torque to overcome. The simulation predicts these losses and Figure 3.15 shows the model's agreement with experiment. Overall, the predictions are relatively good, but trends in the data are not obvious. Qualitatively the predictions behave as expected with the simulated result somewhere between the ideal and experimental value.

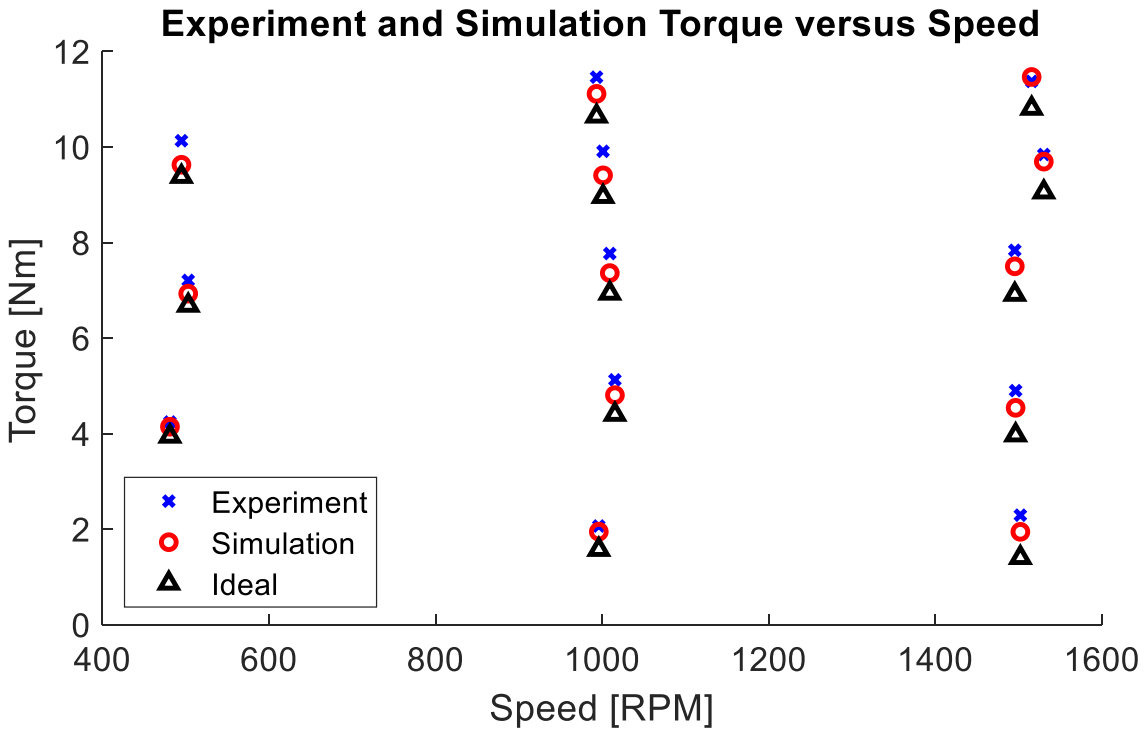

FIGURE 3.15: SIMULATION TORQUE PREDICTIONS

The trends are easier to determine using the quantitative information in the boxplots of Figure 3.16. The torque accuracy and torque loss error are given in eq. (3.16) and (3.17) respectfully.

$$\mathrm{T}^{\%} = \frac{\mathrm{T}_{sim} - \mathrm{T}_{exp}}{\mathrm{T}_{exp}} \times 100 \tag{3.16}$$

$$\mathrm{T}^{\%}_{loss} = \frac{\mathrm{T}_{exp} - \mathrm{T}_{sim}}{\mathrm{T}_{exp} - \mathrm{T}_{idl}} \times 100 \tag{3.17}$$

The accuracy is typically less than zero, denoting that the simulation is underpredicting losses. The loss error positive, with $\mathrm{T}^{\%}_{loss} = 0\%$ occurring when the simulation matches experiment and $\mathrm{T}^{\%}_{loss} = 100\%$ corresponding to the simulation matching the idealized case. Referring to Figure 3.16 and eq. (3.16) and (3.17), the accuracy increases with pressure, which is expected because a greater percentage of the torque is due to the pressure differential instead of the losses. The loss error does not have a consistent trend with the pressure differential, but it does seem to improve with speed. One explanation is that at higher speeds the ball piston stays closer to the hydrodynamic

lubrication regime. Another takeaway is that the torque loss prediction varies significantly between runs, spanning 75 percent to 0 percent torque error loss.

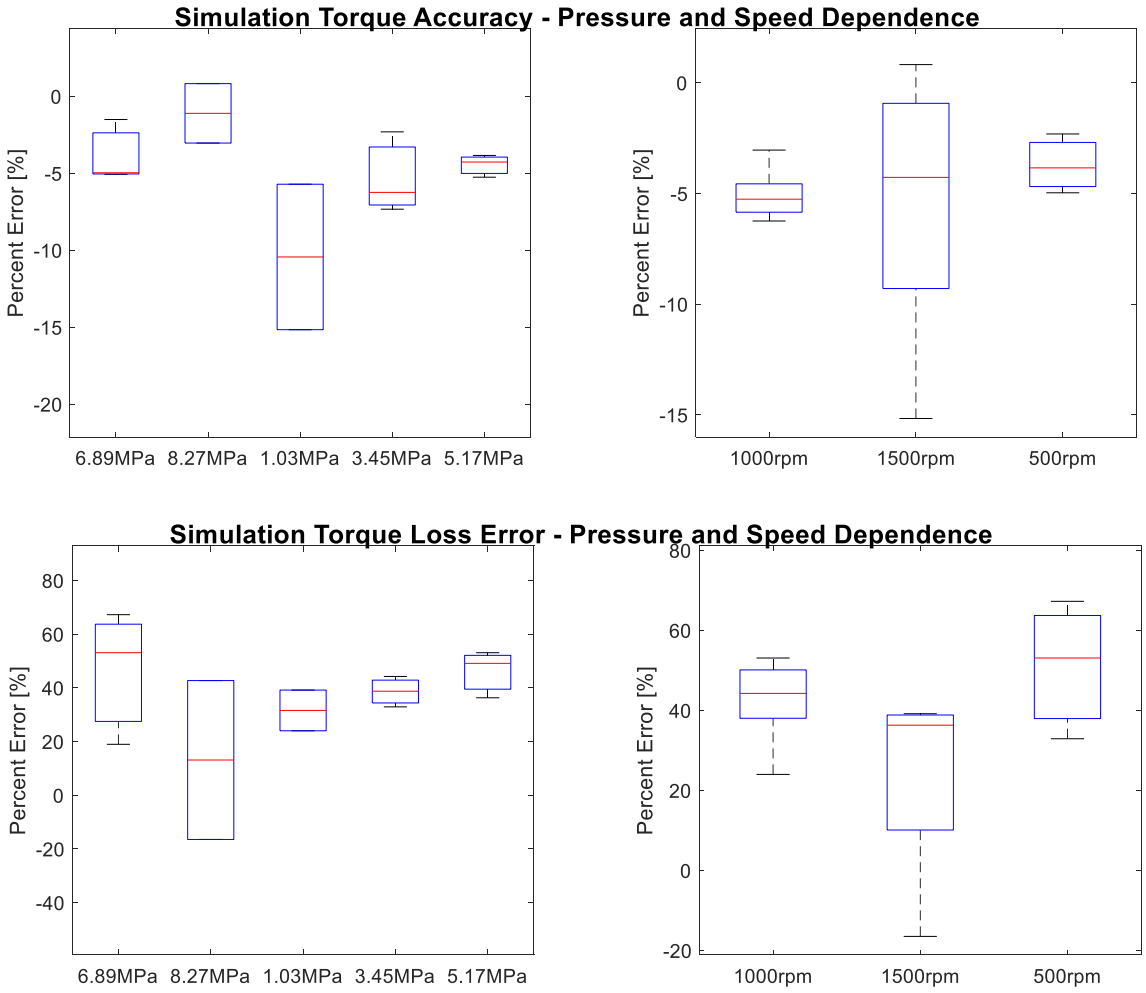

FIGURE 3.16: SIMULATION ERROR FOR TORQUE PREDICTIONS

3.3.3.3 Total Efficiency

The total efficiency for the hydraulic pump is defined as the ratio of output power to input power and is found using eq. (3.18).

$$\eta = \int_0^{t_{end}} \frac{\Delta p Q_{out}}{\mathrm{T}_{input}\omega_{input}} dt \tag{3.18}$$

where Δp and ω_{input} are the pressure differential and pump rotation speed respectively, these values come from the experimental operation conditions. Q_{output} is the flow rate and T_{input} is the torque; these values come from experiments or simulation depending on which is being analyzed.

The definition in eq. (3.18) shows that an increase in output flow or a decrease in input torque will increase the efficiency. Therefore, based on the results from sections 3.3.3.1 and 3.3.3.2, which showed the flow rate was overpredicted and the torque was underpredicted, it is expected that the simulation overpredicts the efficiency. This result is demonstrated in Figure 3.17. The figure shows good agreement between the simulation and experiment for the trend. The efficiency increases and then levels off for the simulation like the experiments, the only difference, like the previous sections, is the magnitude of the values. Another feature that the simulation predicts is the relationship between points. This means if one experiment is more efficient than another, the simulation captures this relationship 69 percent of the time (9 out of 13 data points).

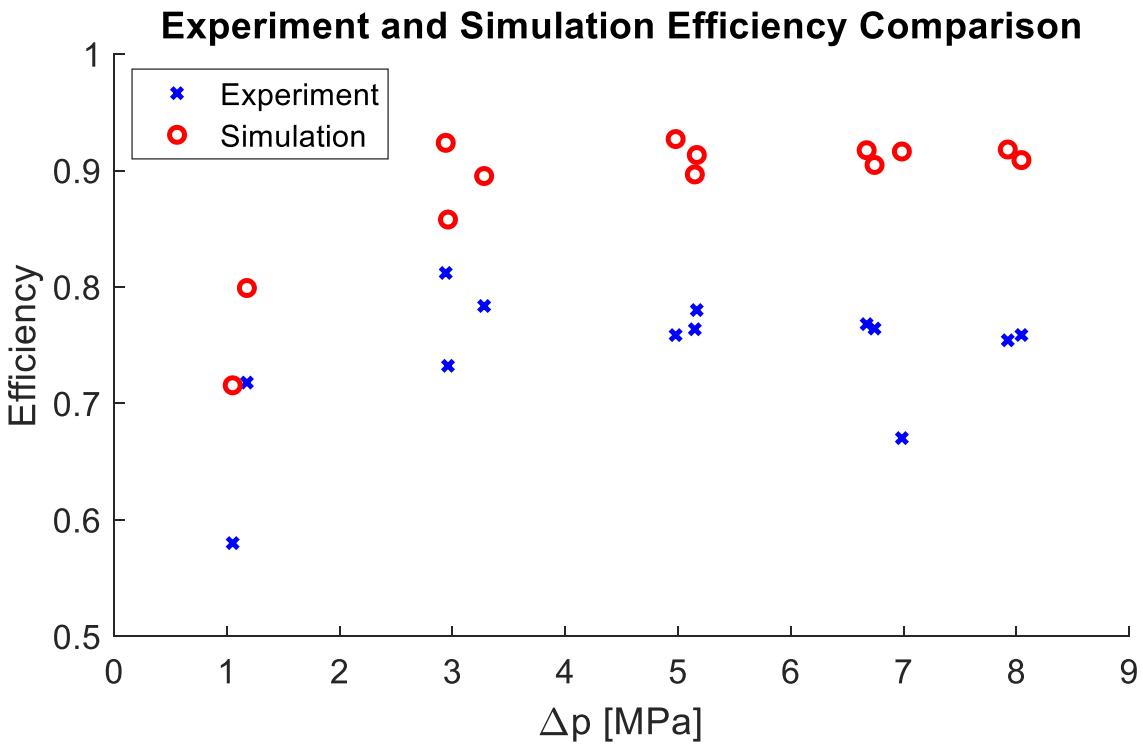

FIGURE 3.17: SIMULATION EFFICIENCY PREDICTIONS

3.3.4 Parameter Sensitivity Studies

The results presented using the baseline parameters, section 3.3.3, did not predict the magnitude of the losses accurately. However, there were several variables that could not be measured

effectively during the experiments creating a lack of confidence in the model's predictions. This section considers the parameters with the most uncertainty and potential to impact the model results.

3.3.4.1 Effect of Thermal Conditions on Performance

As stated in section 3.2.4, the temperature was measured using a probe placed in the hydraulic circuit. The value measured at this probe was typically 311 K, but no measurement was taken in the pump or near the thin gap regions. These regions could have localized heating of the oil and surrounding material given that most of the heat is generated there. The thermal model presented in section 2.2.2.9 and 2.2.3.5, does not consider heat transfer to or with the surroundings; instead this phenomenon is lumped with the bulk oil temperature. Therefore, to determine the impact of localized heating near the thin gaps, the bulk oil temperature was varied.

The temperature was increased from the port's measured bulk temperature by 44 K. This is a nontrivial temperature increase, but detailed FEA analysis and experimental data of an axial piston pump has shown that the temperature of the piston and cylinder can increase by 10 – 20 K compared to the oil temperature at the ports. The operating conditions tested had viscous power loss at the piston-cylinder interface similar to the experimental work for the radial ball piston [48]. Also, the piston-cylinder in an axial piston pump is a conformal surface which distributes the viscous losses relatively evenly, but the ball-cylinder interface is a nonconformal contact that concentrates these losses. It is not uncommon for nonconformal contacts to have high localized heating in a phenomenon known as flash temperature [51, 52].

Figure 3.18 shows that as the temperature increases so does the leakage, with the effect becoming more noticeable at higher pressures. Therefore, it is possible to fit the leakage data by increasing the temperature to 355 K. However, this requires the localized surface and oil temperatures near the ball piston and pintle to be significantly higher that what was measured later in the circuit. This is possible, but without developing a more accurate heat transfer model it is hard to evaluate the validity of this idea.

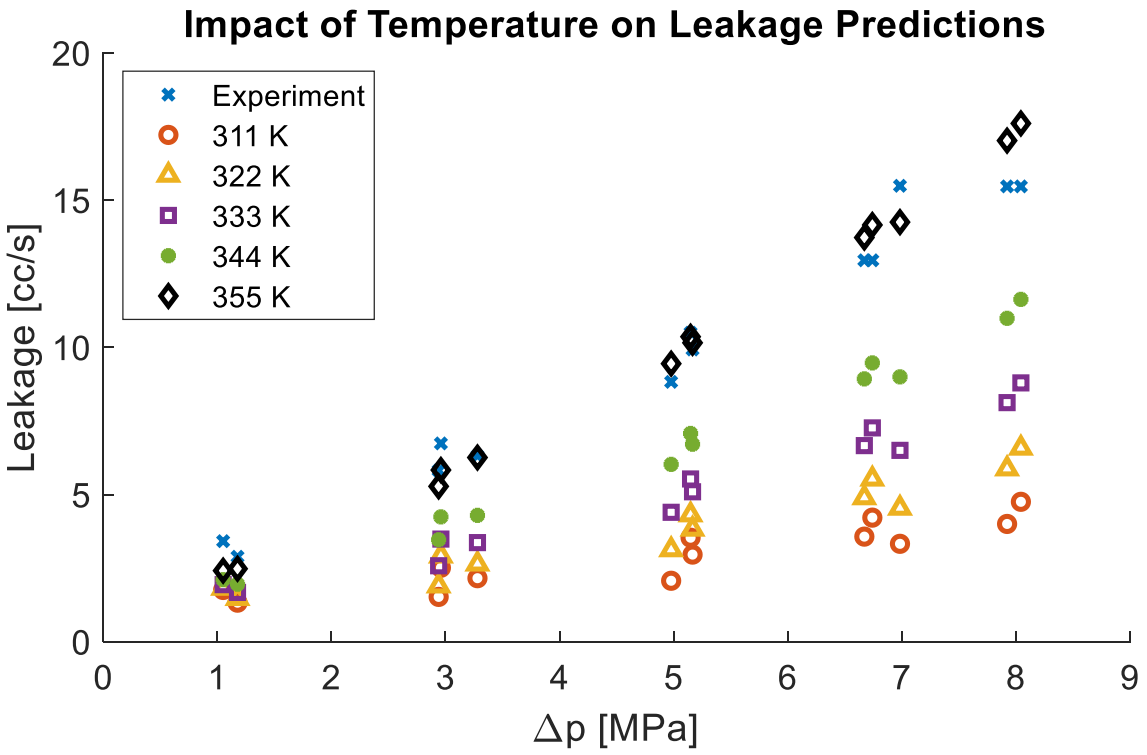

FIGURE 3.18: TEMPERATURE DEPENDENCE OF THE LEAKAGE

The temperature has a significant impact on the leakage from the pump; therefore, the overall flow rate should show a strong correlation with the temperature as well. Figure 3.19 shows that the higher the temperature the smaller the error in the flow rate with the median loss error reducing from 77 percent to 40 percent (right). One insight is that 20 to 70 percent of the overall losses are accounted for at 355 K, when the simulation and experimental leakage are almost equal. This implies that compressibility losses are also underpredicted by the model and that the operating condition has a major impact on the primary loss mechanism. This is expected because of the leakage's dependence on both temperature and pressure. As shown in Figure 3.18, the increasing temperature does little to the leakage at low pressures, but significantly impacts the amount when the pressure is high.

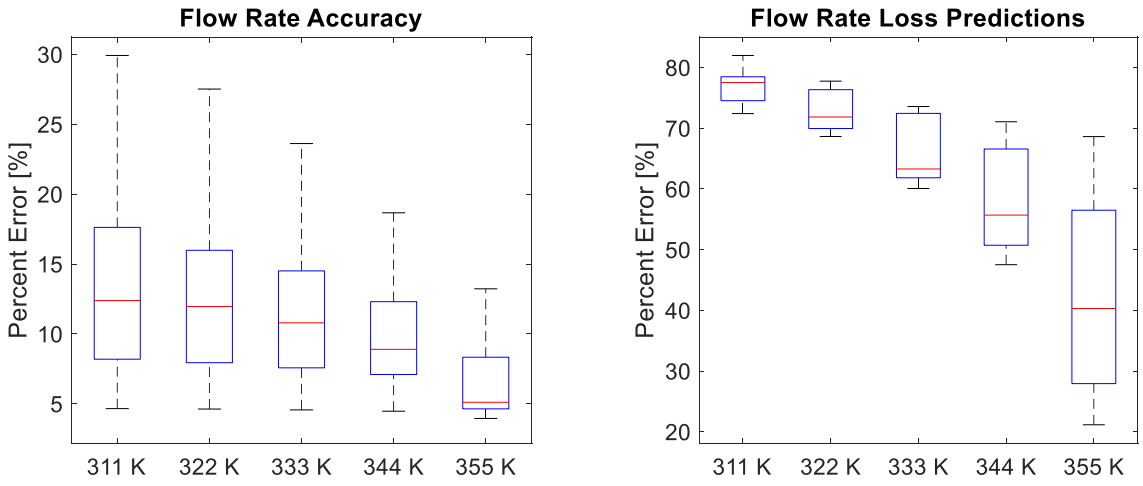

FIGURE 3.19: FLOW RATE SENSITIVITY TO TEMPERATURE

Increasing the temperature is known to decrease the viscosity of the fluid which is why leakage increased when looking at volumetric efficiency. Assuming hydrodynamic lubrication is maintained, this decrease in viscosity is expected to decrease the viscous drag at interfaces and therefore, decrease the torque loss. This will cause the model predictions to become worse with increasing temperature. This trend is seen in Figure 3.20. The overall accuracy is not sensitive to temperature with the accuracy dropping by less than 5 percent, but the median torque loss prediction goes from 40 percent to 55 percent. The torque loss predictions improve slightly from 344 K to 355 K which could be caused by a transition in lubrication regimes.

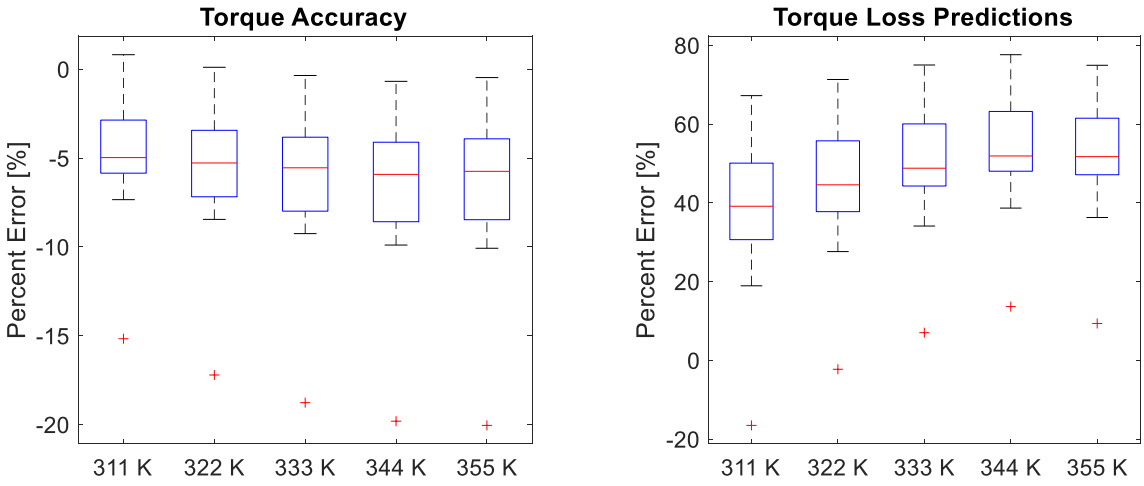

FIGURE 3.20: TORQUE SENSITIVITY TO TEMPERATURE

It was shown that the volumetric efficiency decreases as the temperature increases (less flow rate), but the mechanical efficiency improves (less torque). Therefore, the effect of temperature on the overall efficiency should be minimal if the magnitude of these changes is similar. Figure 3.21 shows the result of this study. As anticipated, the temperature plays an insignificant roll in the total efficiency, particularly below 6 MPa. A feature that is interesting is that at low pressure, the efficiency improves slightly with temperature, but at high pressure, the efficiency gets worse with increasing temperature. This happens because at low pressure the increase in leakage is more than offset by the decrease in torque, but at high pressure the opposite occurs. The leakage starts to dominate, and the efficiency begins to decrease.

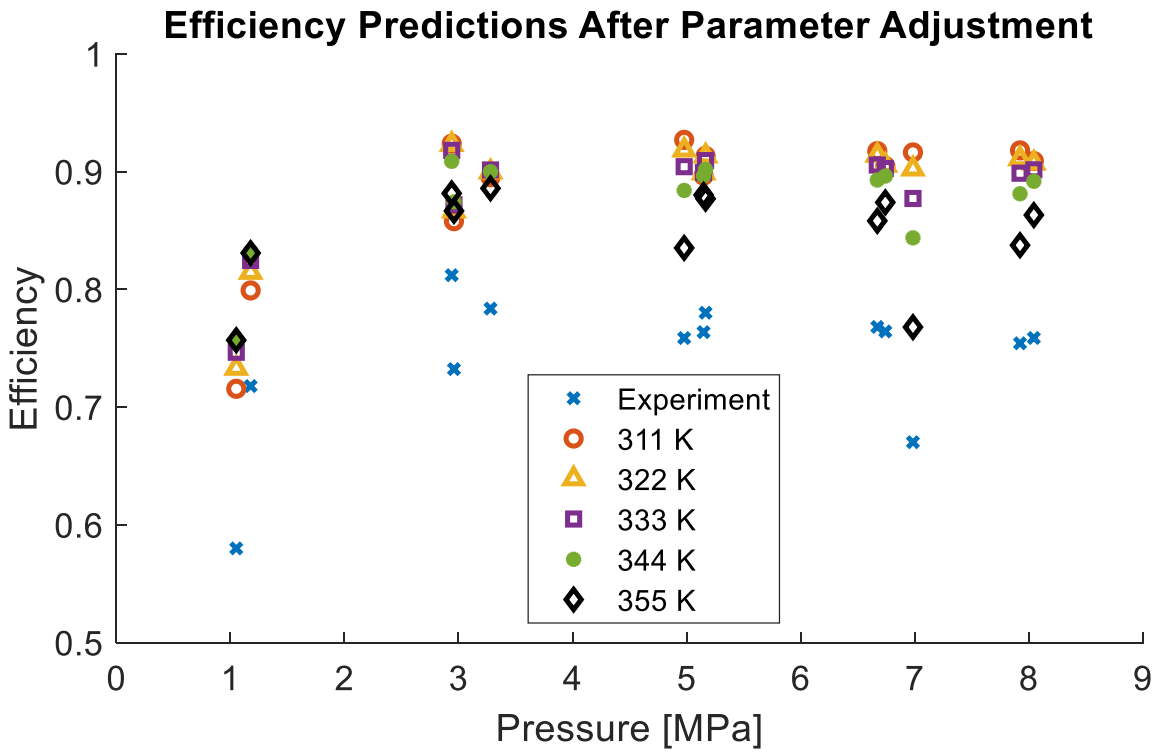

FIGURE 3.21: IMPACT OF TEMPERATURE ON THE OVERALL EFFICIENCY

3.3.4.2 Effect of Clearances on Performance

One other factor that could greatly impact the leakage is the clearances at the interfaces. Small differences in the clearance can result in noticeable differences to the leakage due to the cubic relationship shown in eq (3.19)[6].

$$Q_\vartheta = \frac{h^3}{12\mu r_b \sin\vartheta}\frac{\partial p}{\partial \vartheta} + \frac{U_1 + U_2}{2}h \tag{3.19}$$

This uncertainty can arise in two areas, the initial measurements and the expansion due to high pressure. The clearances were calculated by measuring the ball piston and the cylinder diameters. The ball piston measurements used a micrometer with an accuracy of ±2.54μm, and the cylinders used an air gauge, also with an accuracy of ±2.54μm. Therefore, the diametric clearance could vary by +5.08μm to -5.08μm from the nominal.

The other uncertainty is the expansion at high pressure. The current model uses a thick walled pressure vessel approximation to calculate the expansion of the cylinder, but it doesn't consider any effects on the piston. With the current pressures, the thick walled pressure vessel gives expansion up to a couple microns. It is currently unknown how different this simplified model is from the physical system; however, it is expected that the piston would reduce slightly in radius due to the compression created by the pressure. Therefore, the current model likely is underpredicting the clearance value.

With this in mind, Figure 3.22 and Figure 3.23 shows the flow rate and torque for three different radial clearances: nominal, +1μm, and +2μm. As expected, the flow rate accuracy improves due to the increase in leakage with the losses becoming approximately 25 percent more accurate. Interestingly, the torque is not sensitive to the clearance, which is due to the ball piston dynamics and eccentricity during operation. This phenomenon is explored in more detail during section 4.3.2.2. The important result for this chapter is that the uncertainty in the clearance would increase leakage but have little effect on the torque.

[6] See section 2.2.3.4 for the derivation of this equation.

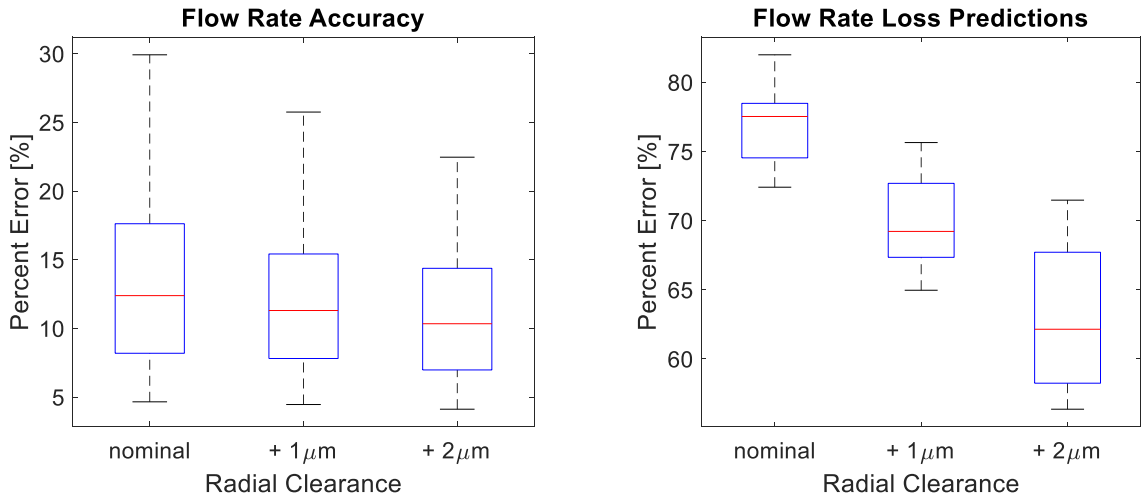

FIGURE 3.22: FLOW RATE SENSITIVITY TO CLEARANCE

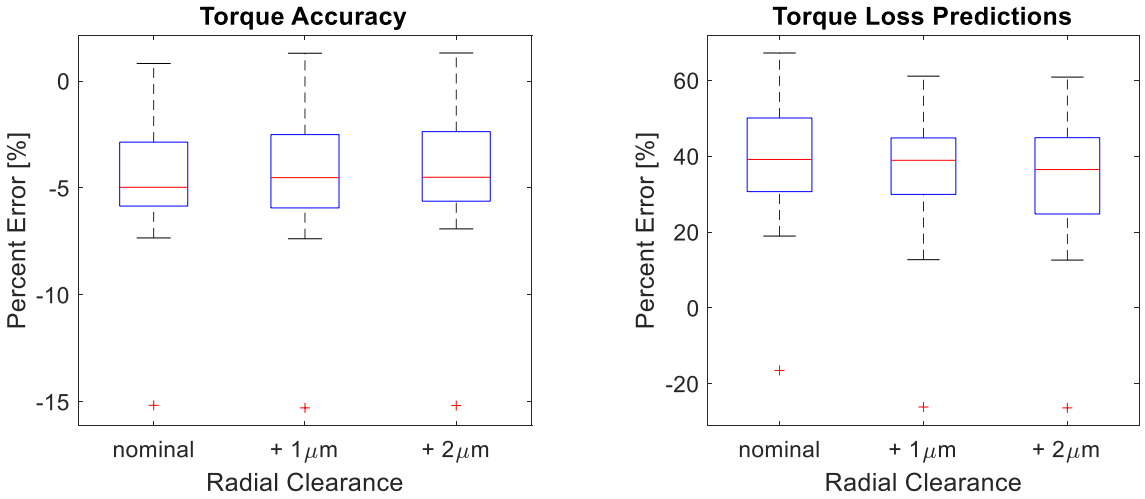

FIGURE 3.23: TORQUE SENSITIVITY TO CLEARANCE

3.3.4.3 Effect of Pressure Dynamics on Volumetric Performance

The previous two sections, 3.3.4.1 and 3.3.4.2, have focused on the sensitivity of the leakage and shear losses at interfaces. The following sections consider the pressure dynamics and how the pump efficiency changes with the dead volume, valve timing, entrained air, and pump eccentricity. These four factors were used in sensitivity studies; the values were varied within a reasonable range to see how the model performance changed. This allows the importance of each parameter to be studied and helps to identify possible root causes for the discrepancy between simulation and experiment.

Boxplots are used to show how the flow predictions change with changing parameters. The boxplots show the accuracy of the predictions when leakage is removed from consideration. This allows the compressibility affects to be isolated based on eq. (3.20).

$$Q^{\%}_{compress} = \frac{Q_i - Q_{leak} - Q_{exp}}{Q_{exp}} \times 100 \tag{3.20}$$

where Q_i is the simulated flow rate from the i^{th} parameter in the sensitivity study. The sensitivity to dead volume, valve timing, and entrained air are presented in Figure 3.24, Figure 3.25, and Figure 3.26 respectfully. Referencing the figures, the dead volume percent is multiplied by the nominal design value and acts as a tolerance for the value. The valve timing parameter was varied by $\pm 5\pi/180$ radians of the value from the technical drawings. Due to the machining of the pintle, it is expected that the largest uncertainty is the valve timing's relationship with bottom and top dead center. Therefore, all timing angles were shifted by the offset.

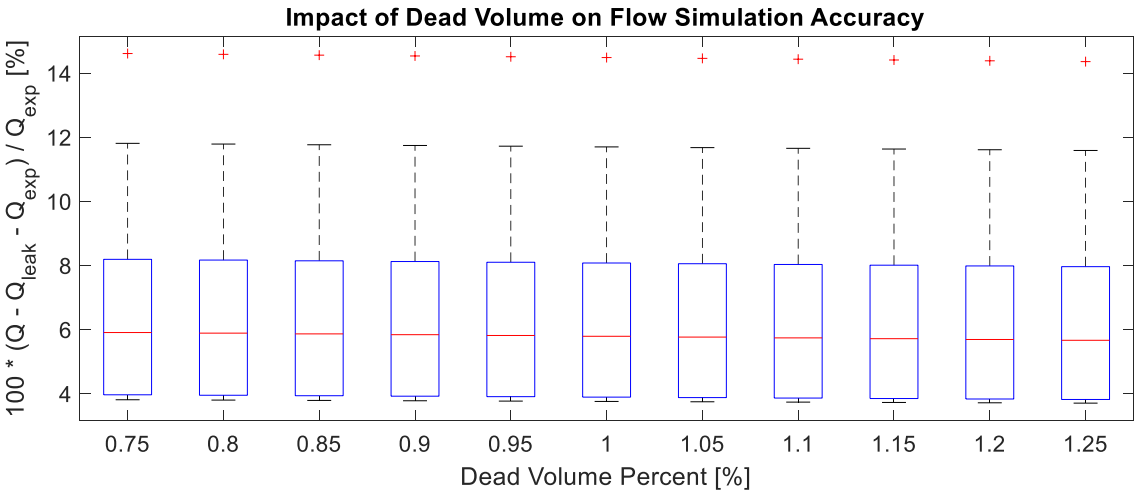

FIGURE 3.24: FLOW RATE SENSITIVITY TO CYLINDER DEAD VOLUME

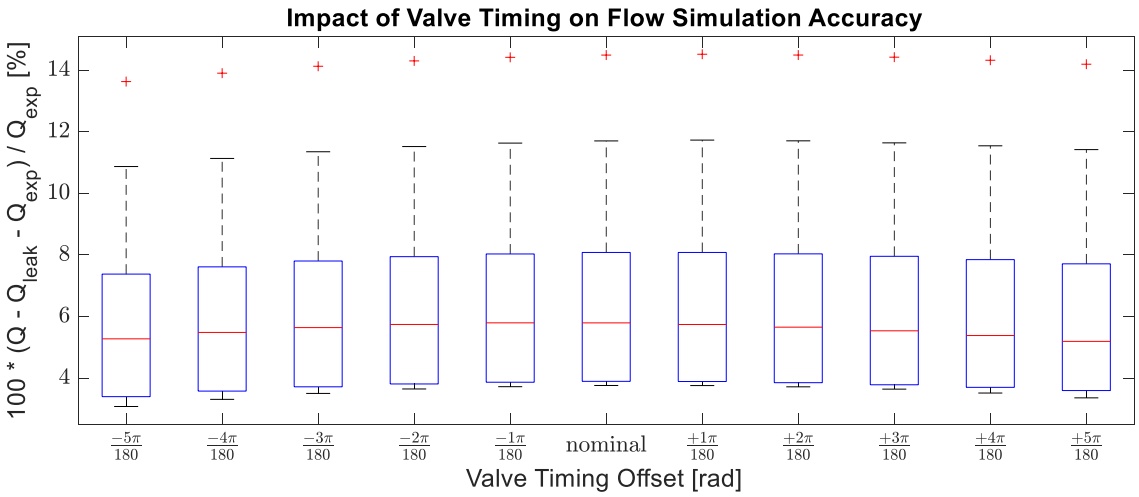

FIGURE 3.25: FLOW RATE SENSITIVITY TO VALVE TIMING

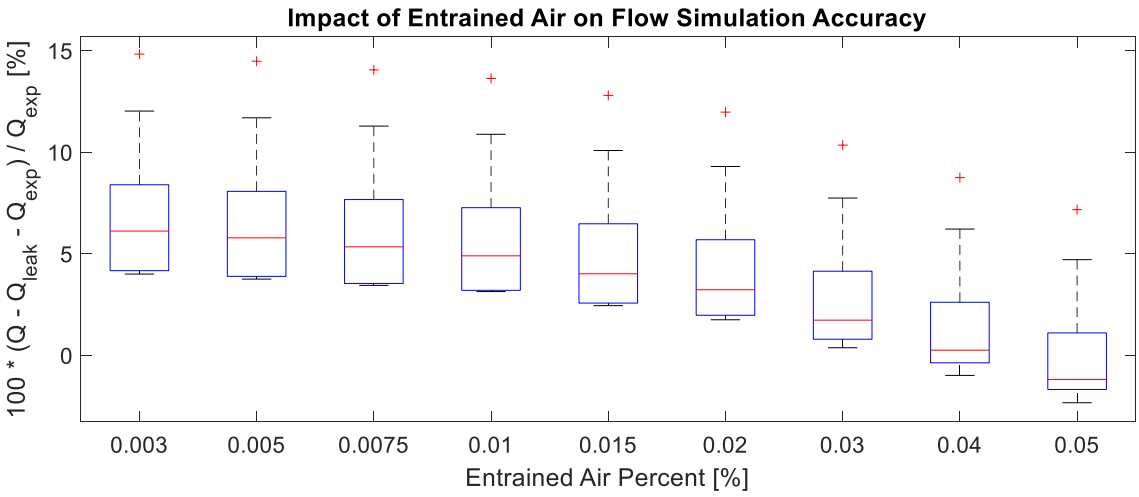

FIGURE 3.26: FLOW RATE SENSITIVITY TO THE PERCENTAGE OF ENTRAINED AIR

From these three figures some trends start to emerge. First the dead volume and valve timing have little effect on the flow rate for the operating conditions that are being analyzed. This implies that the simulation is not sensitivity to these parameters and that these likely are not root causes of the discrepancy between the simulation and experiments. In contrast, the simulation seems sensitive to the entrained air percentage. The simulated flow rate quickly starts to decline near 2 percent entrained air. The original simulation was run with an entrained air of 0.5 percent. These results are from the leakage experiments, *Circuit B* (Figure 3.6), which required fluid to be added back to the reservoir regularly. Adding oil to the reservoir through a filter increases the entrained air within

the system making it plausible that the entrained air was in the 2 to 4 percent range. Based on Figure 3.26, this accounts for a significant portion of the error.

One other variable that was considered in a sensitivity study was the eccentricity of the pump. As shown in Figure 3.27, the flow rate is extremely sensitivity to the eccentricity. This is expected because the flow rate is proportional to the pump displacement which is proportional to the eccentricity. An eccentricity that's 95 percent of the original value used could completely resolve the discrepancies between the simulation and experiment. Note that the eccentricity of the assembled pump could not be accurately measured. Another issue with the eccentricity is that the pump was variable displacement. At high pressures and speeds, the displacement mechanism experienced the greatest deflection and vibration; therefore, it is likely that the eccentricity was different between individual runs. A smaller eccentricity at high pressures would also explain why the flow rate predictions become significantly worse as the pressure increases.

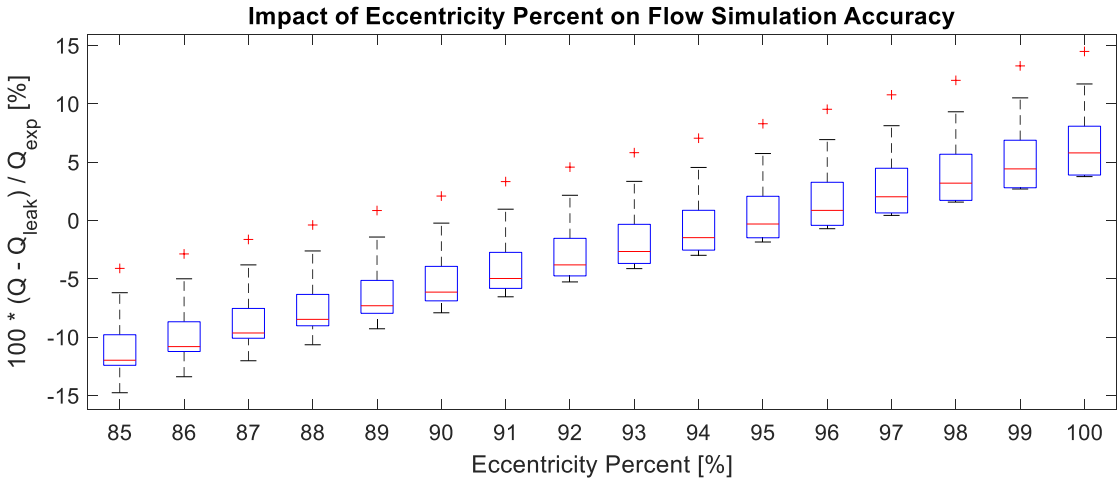

FIGURE 3.27: FLOW RATE SENSITIVITY TO PUMP ECCENTRICITY

3.3.4.4 Effect of Pressure Dynamics on Mechanical Performance

The pressure dynamics sensitivity studies presented for the flow rate also impact the mechanical efficiency. The following analysis only considered the pressure dynamics model because the friction at the interfaces is not affected by the studies presented here. The pressure dynamics model predicts throttling losses within the pump, but these values were converted to a torque using eq. (3.21).

$$\mathrm{T}_{loss} = \frac{1}{\omega_{input} t_{end}} \int_0^{t_{end}} \mathcal{P}_t \, dt \tag{3.21}$$

where $\mathcal{P}_t$ is the total throttling power loss during operation. The boxplots in this section use the metric defined in eq. (3.22) to evaluate the sensitivity to a parameter change. The definition is also shown on the y-axis of each figure.

$$\mathrm{T}_{idl}^{\%} = \frac{\mathrm{T}_{Loss_i}}{\mathrm{T}_{idl}} \times 100 \tag{3.22}$$

where T_{Loss_i} is the torque calculated from eq. (3.21) for the i^{th} parameter in the sensitivity study. This metric was used to normalize the losses. The impact on the torque loss from varying the dead volume, valve timing, and entrained air are given in Figure 3.28, Figure 3.29, and Figure 3.30 respectfully.

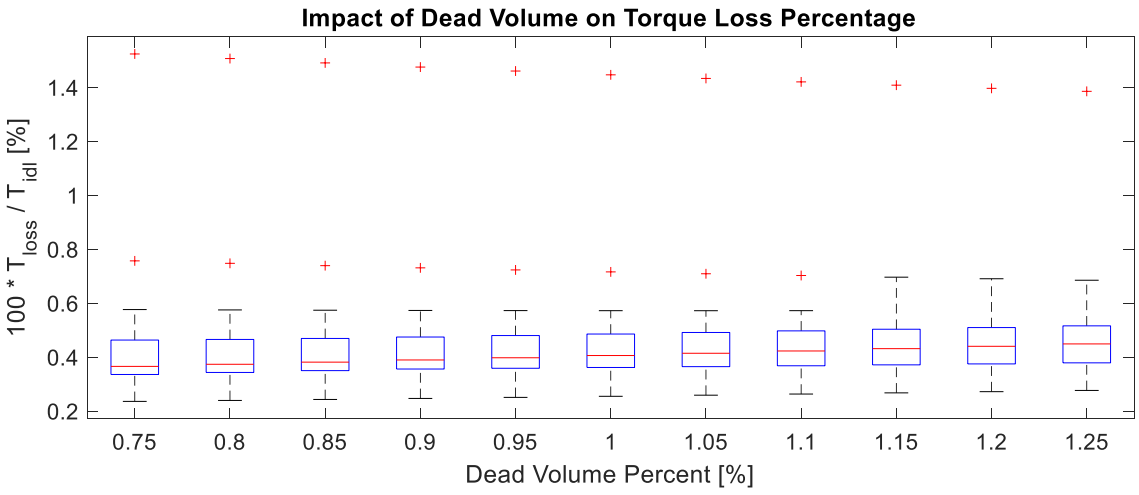

FIGURE 3.28: TORQUE SENSITIVITY TO CYLINDER DEAD VOLUME

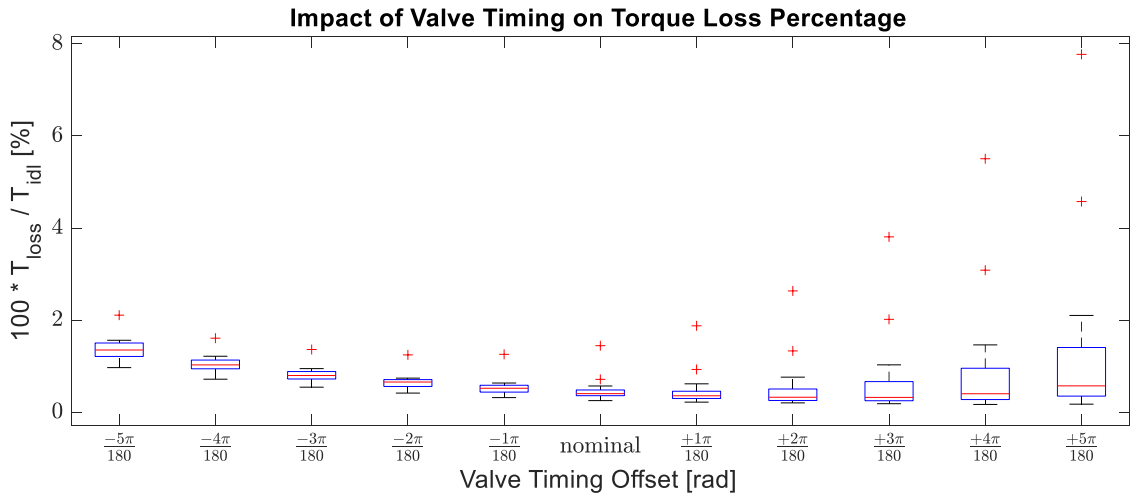

FIGURE 3.29: TORQUE SENSITIVITY TO VALVE TIMING

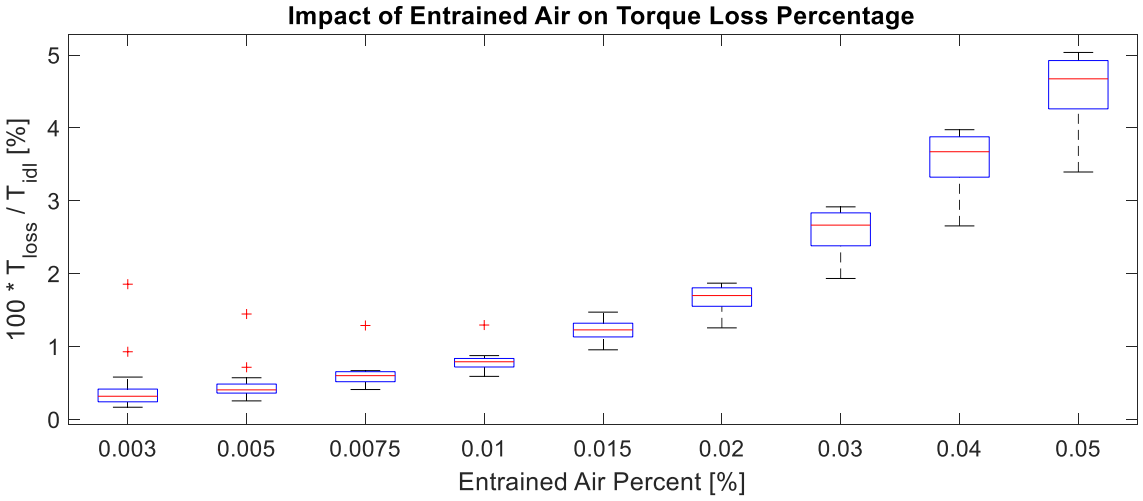

FIGURE 3.30: TORQUE SENSITIVITY TO THE PERCENTAGE OF ENTRAINED AIR

Exactly like the volumetric sensitivity, the dead volume and valve timing have little impact on the amount of torque predicted. The entrained air does impact the torque with it increasing significantly after about 2 percent. This matches the results of the flow rate sensitivity and would result in improvements for the simulation predictions. As stated previously, the original value of 0.5 percent was likely too low because oil was being added back to the reservoir during the leakage experiments, *Circuit B*, increasing the entrained air content.

The last variable that was studied was the eccentricity. The torque is proportional to the displacement, which is proportional to the eccentricity, so reducing the eccentricity will reduce the torque. Figure 3.31 shows this trend. The torque is already underpredicted, so this relationship is

not ideal for matching the simulation to the experimental results. As stated previously, the eccentricity is most likely to fall below 100 percent at high pressure because of the deflection of the mechanism. High pressure is also where the confidence in the empirical relationship for the churning, seal, and bearing breaks down because it could only be measured at atmospheric pressure. The unmodeled ball-cam interface is also likely to increase the torque. For these reasons, it's expected for the simulation torque to be lower than the experimental torque, making it plausible that the eccentricity reduces slightly at higher pressures.

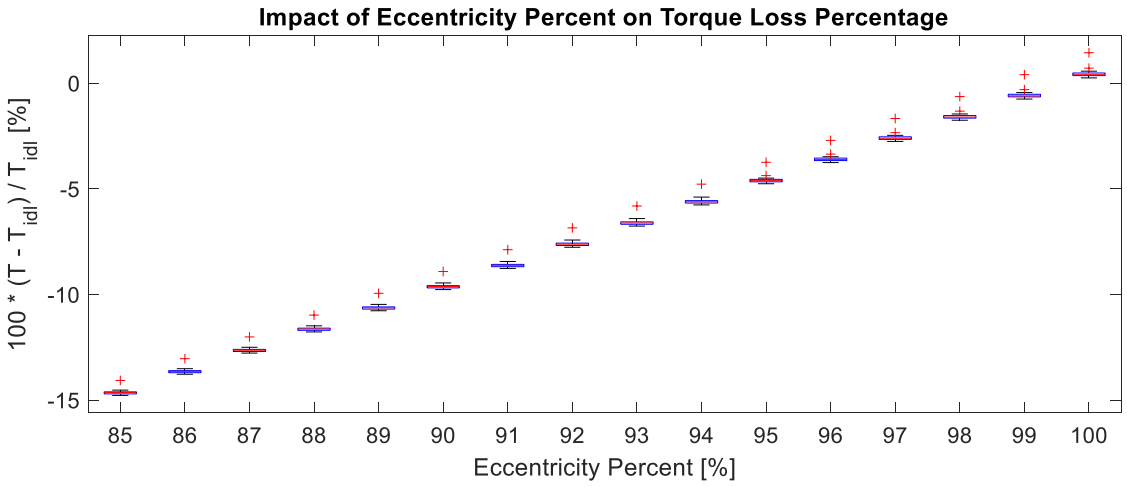

FIGURE 3.31: TORQUE SENSITIVITY TO PUMP ECCENTRICITY

3.3.5 Simulation with Parameter Adjustments

3.3.5.1 Volumetric Efficiency

The knowledge that was gained from the thermal, clearance, and sensitivity analyses was used to rerun the simulation with new input parameters. The baseline and adjusted parameters are showed in Table 3.3. The eccentricity for the adjusted parameters corresponds to a 1 percent drop in eccentricity per 1.38 MPa after 5.52 MPa, with the pressure differential in megapascals. This function attempts to model the increase in deflection of the displacement mechanism as the pressure differential increases.

TABLE 3.3: PARAMETER ADJUSTMENT

Parameter	Baseline Simulation	Adjusted Simulation
Temperature	$\approx 311\ K$ (Experimental Value)	$325\ K$
Clearance	Nominal	Nominal + 2μm (Radial)
Entrained Air	0.5%	3.25%
Eccentricity	Nominal	Nominal × $\min(1, -0.0073\Delta p + 1.04)$

The comparison of the simulation flow rate to the experimental and ideal is shown in Figure 3.32. The results show good trends in the data and the loss prediction has improved from the baseline parameters, but there is still an increasing discrepancy as the pressure increases. The improvement between the original and adjusted parameters is quantified in Figure 3.33. The figure shows that adjusting a couple of parameters was able to significantly change the predictions and improve the loss predictions drastically. This provides insight into the importance of understanding the oil properties, in this case, temperature, clearance, and entrained air percentage.

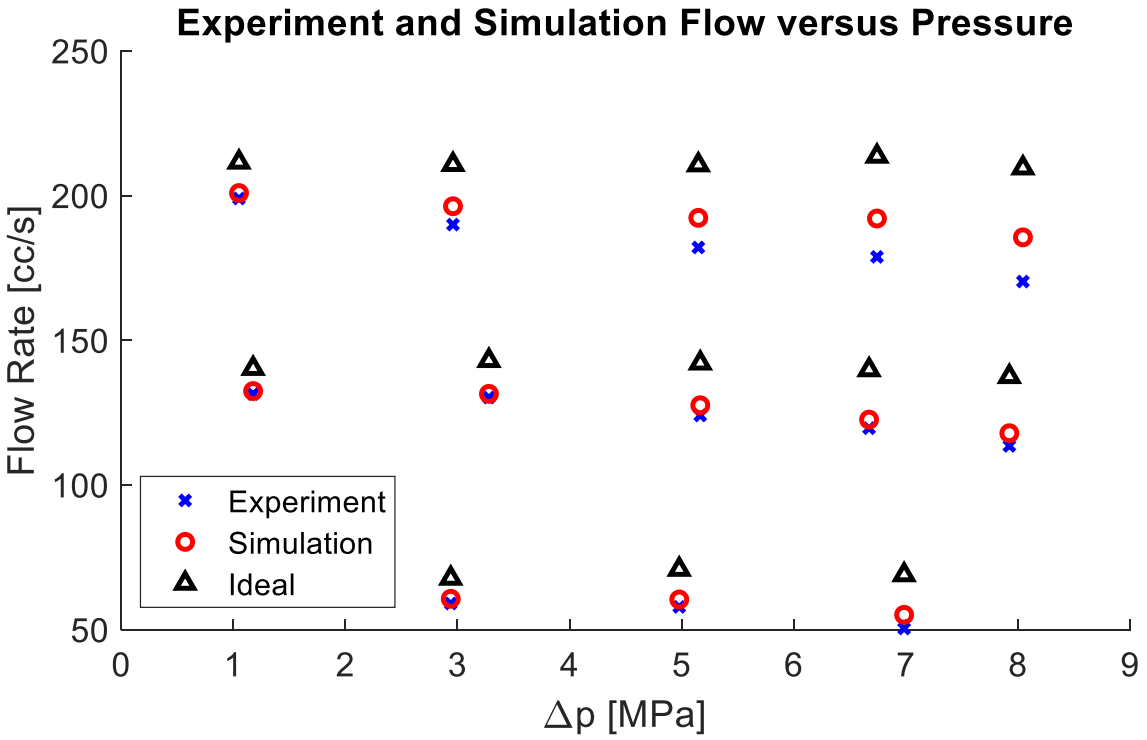

FIGURE 3.32: SIMULATION FLOW RATE PREDICTIONS FOR ADJUSTED PARAMETERS

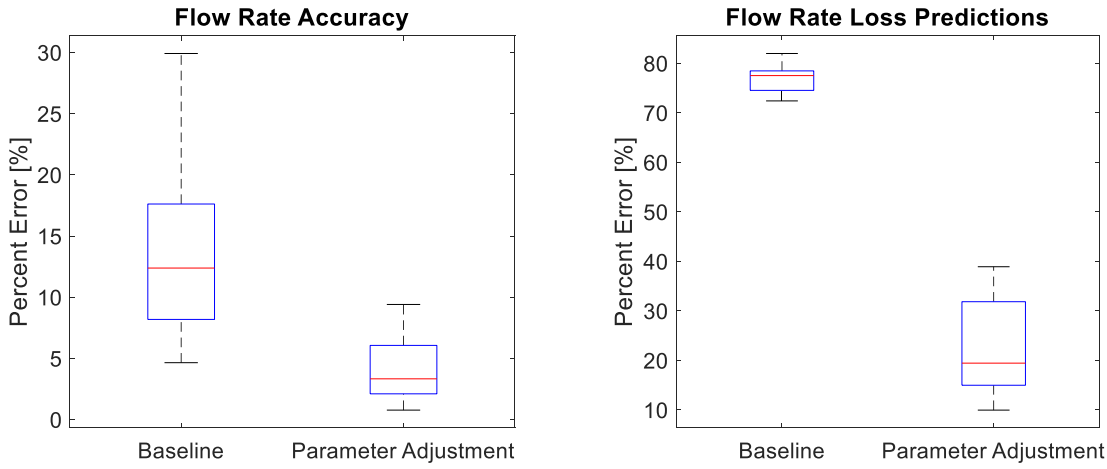

FIGURE 3.33: FLOW RATE ACCURACY AND LOSS COMPARISON BETWEEN SIMULATIONS

Looking at the leakage predictions in Figure 3.34, it is seen that the adjusted parameters improve the accuracy of the leakage. This improvement is due to the increased temperature and increased clearance. It is still underpredicted, but significantly better than the original parameters that were used.

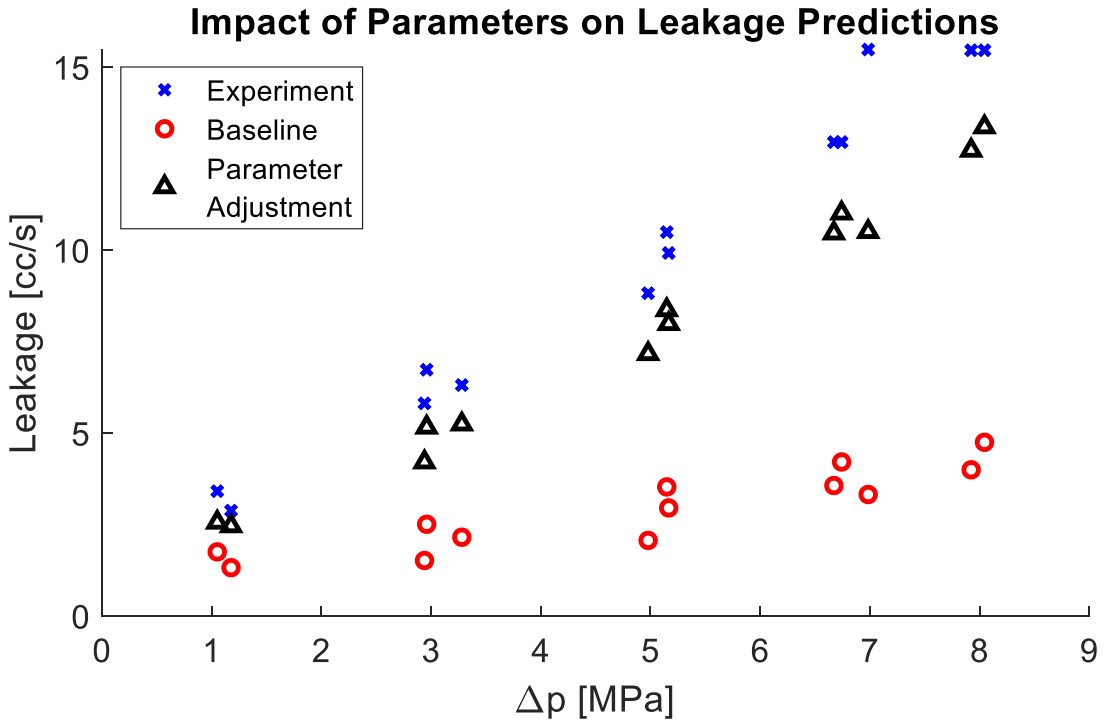

FIGURE 3.34: LEAKAGE PREDICTIONS FOR ADJUSTED PARAMETERS

3.3.5.2 Mechanical Efficiency

The parameters were redefined using the definitions in Table 3.3, and the impact it has on the torque is shown within this section. The higher temperature should decrease the simulated torque, but the increase in the entrained air increases the mechanical losses due to throttling. The simulation predictions are shown in Figure 3.35. The torque values agree with experiment and appear to be an improvement over the initial simulation parameters. Figure 3.36 shows the quantitative comparison between the parameter selections. The accuracy of the predictions improves by a couple percent on average, but the more interesting improvement is the torque loss predictions. The upper bound of the torque loss for the adjusted parameters is very close to the median value from the first set of simulations. However, the maximum pressure and speed simulation (upper right of Figure 3.35) is an outlier in the torque loss predictions. This value is the only one that noticeably overpredicts the losses.

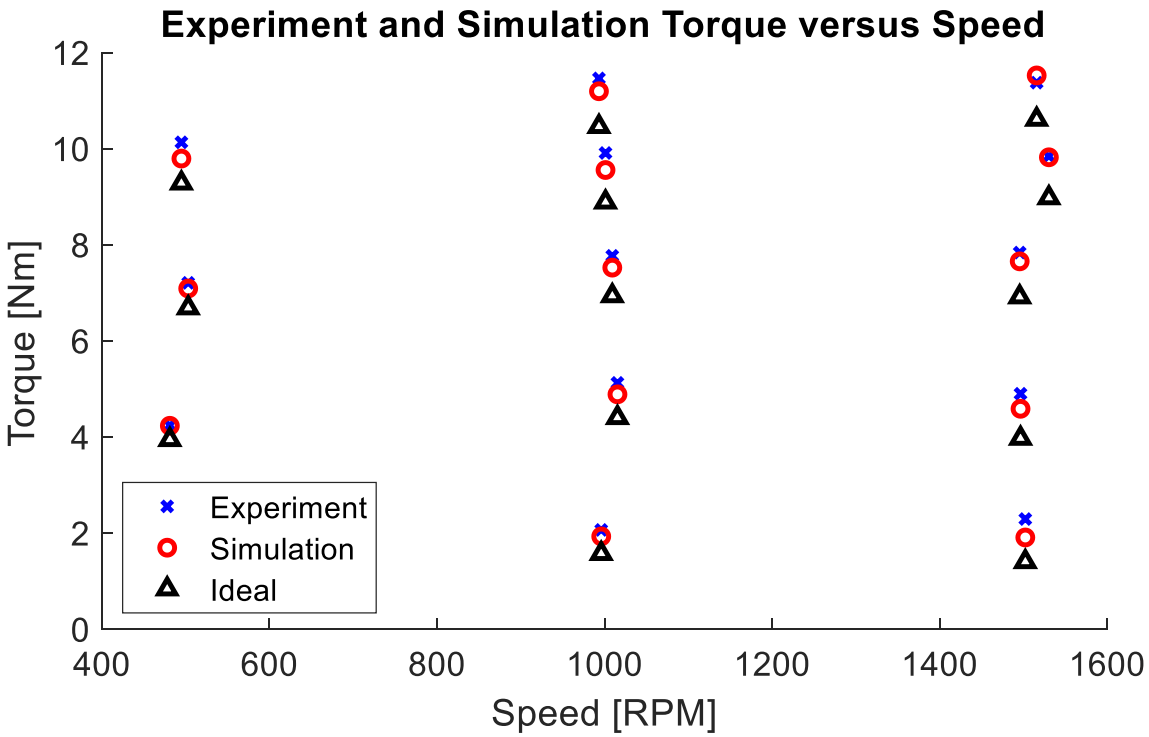

FIGURE 3.35: SIMULATION TORQUE PREDICTIONS FOR ADJUSTED PARAMETERS

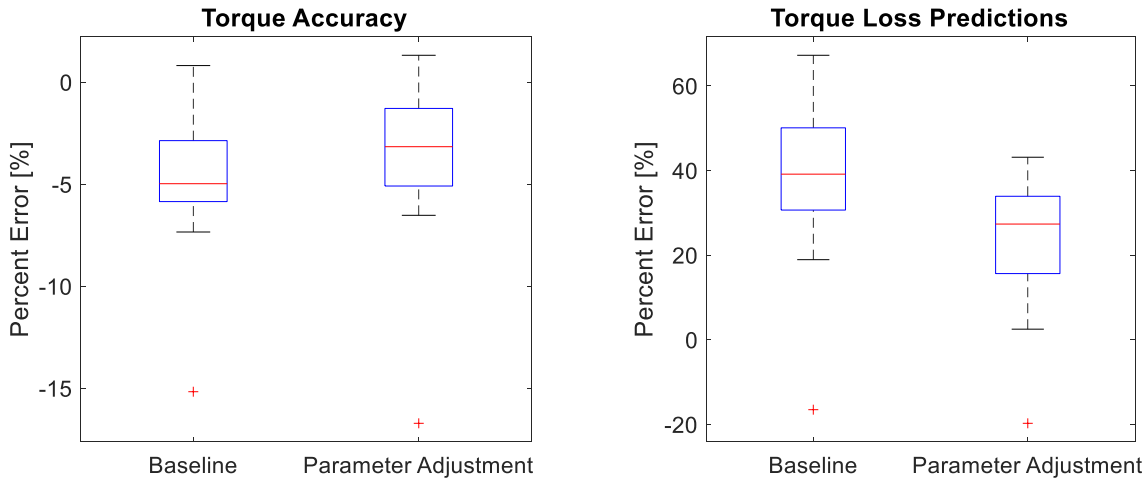

FIGURE 3.36: TORQUE ACCURACY AND LOSS COMPARISON BETWEEN SIMULATIONS

As stated previously, overpredicting the torque is unexpected because there are unmodeled losses within the pump. The empirical losses (churning, bearing, and seal) that had no pressure dependence and the ball-cam interface were not modeled. In particular, the ball-cam interface would provide clarity into the behavior of the ball piston especially regarding if the ball skids on the cam. Other works [29, 30] have shown that [there are complicated dynamics at the ball piston; the friction at the ball-cam interface and ball-cylinder interface trade-off between each other causing the ball to both roll and skid on the cam surface depending on the operating conditions. When the ball skids this increases the mechanical losses and more input torque is required [30].

3.3.5.3 Total Efficiency

The parameter adjustments (Table 3.3) improved the flow rate and torque agreement between simulation and experiment. Figure 3.37 shows that the efficiency predictions also improve as expected. Adjusting the parameter improved the magnitude of the predictions, with most results being off by only 5 to 10 percent (see Figure 3.38). The relationship between neighboring points also improved, with the simulation matching experiments 92 percent of the time (12 out of 13). This is significant improvement and well within the reasonable bounds for the parameters. Based on the results presented in this chapter the model is considered to be validated with reasonable agreement between the experiments and the simulation.

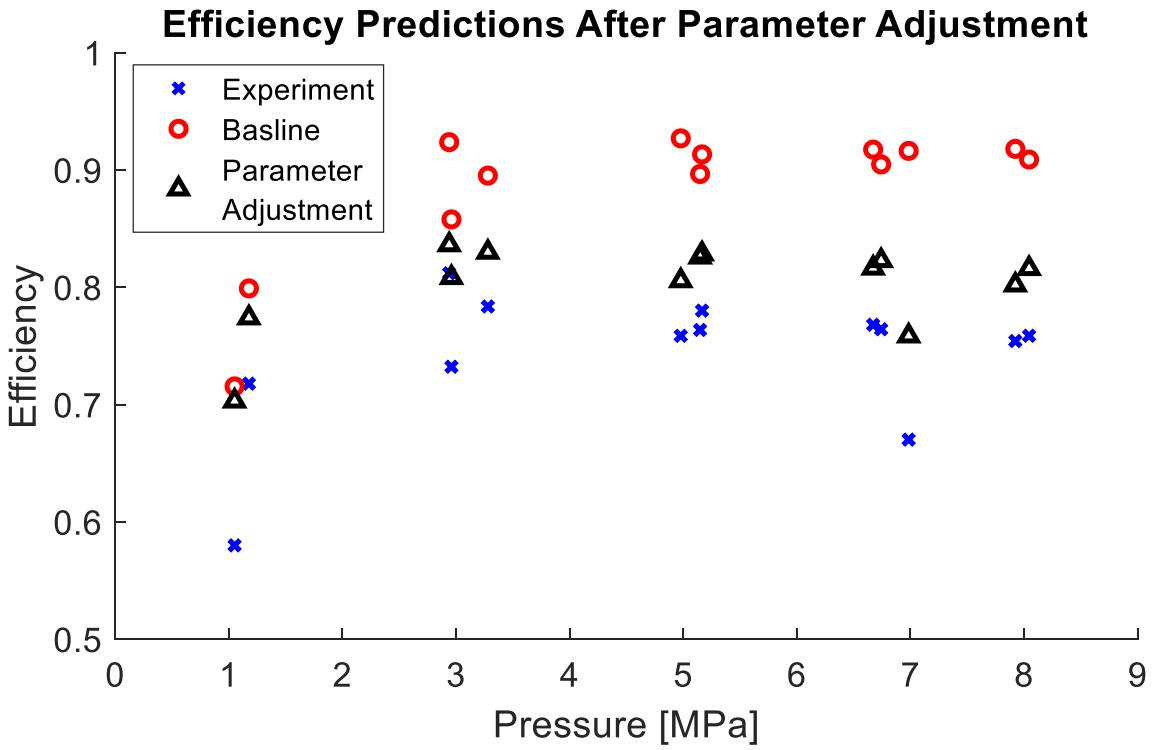

FIGURE 3.37: EFFICIENCY COMPARISON BETWEEN SIMULATIONS

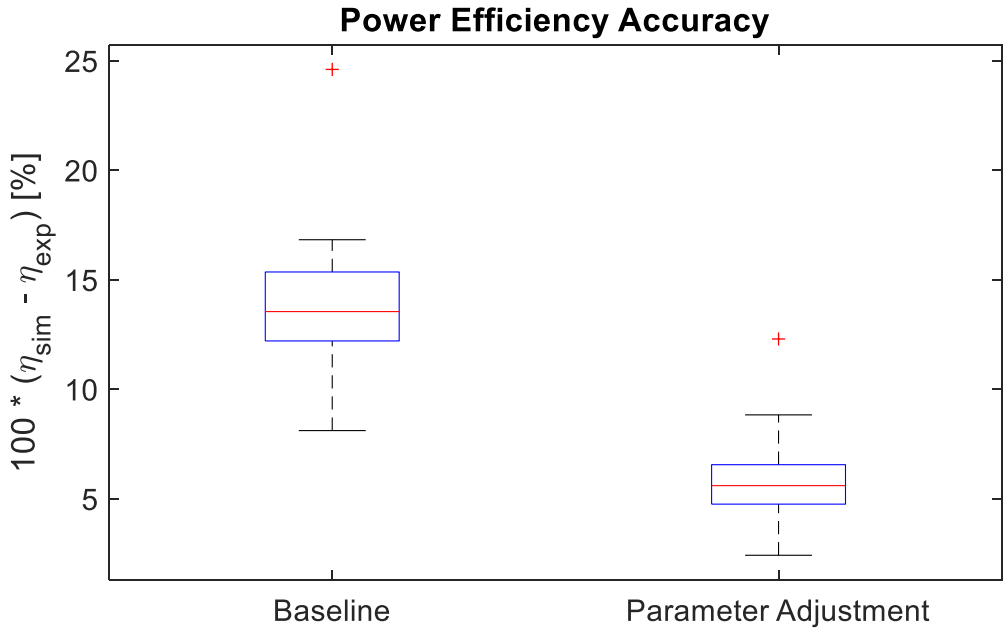

FIGURE 3.38: EFFICIENCY ACCURACY COMPARISON BETWEEN SIMULATIONS

3.4 Conclusion

This chapter showed that the model presented previously can accurately characterize the efficiency of a radial ball piston pump, but that the model is sensitive to several parameters. The initial parameters poorly predicted the volumetric and mechanic efficiency. However, the model performance drastically improved after uncertainties were considered and several realistic parameter adjustments were made. The predictions from the parameter adjusted model matched the trends of the experiment, and the relationship between neighboring points was exceptional, 92 percent. Even the magnitude of the overall efficiency was accurate, with most points off by only 3 to 10 percent.

Several methods were utilized to create this good agreement, such as sensitivity studies, breaking down the losses, and collecting empirical relationships. The sensitivity studies were an iterative process where physical parameters were studied to determine the model's sensitivity to each of them. This process helped to identify which inputs had the biggest impact on the performance of the hydraulic pump. The studies also provide insight about allowable tolerances for different design variables and physical parameters. For example, it was shown that knowing the physical parameters of the oil during operation, temperature and air entrainment, is crucial. However, the valve timing and dead volume could vary within a reasonable range without much performance degradation.

Breaking the losses into mechanical and volumetric components also helped isolate differences between the simulation and experiment. Validating the torque and flow rate predictions not only results in a good model for the efficiency, but it is fundamental to understanding the tradeoffs when designing a hydraulic pump. Separating the losses provides confidence that the model can be leveraged to predict not just the magnitude of losses, but where they occur.

The confidence in the model comes from the fact that it was able to be compared to an off-the-shelf pump. The experimental setups allowed the torque at the shaft to be experimentally determined, the leakage to be directly measured, and the efficiency to be calculated. These setups were shown to be repeatable and reliable across time based on calibrations and multiple experiments over the span of several weeks.

This chapter showed that the model from chapter 2 is valid and can predict pump performance. Now that there is confidence in the model, it can be used to make predictions and generated new radial ball piston designs. The next chapter will show how the model was adopted to drive critical design decisions in a genetic algorithm optimization framework.

4 Design Optimization

4.1 Introduction

The two previous chapters have developed a model of a radial ball piston pump that balances accuracy with computational complexity and demonstrated that the model describes the experimental results of a physical unit. Now, the model can be leveraged to determine the optimal design parameters of the hydraulic unit. This is particularly valuable because the pump design needs to be optimized outside of the operating conditions of conventional pumps driven by an IC engine. Drive cycle information for the HECM was gathered so multiple operating points could be selected to account for the most frequent operating conditions[7]. The multiple operating points are a requirement to create a design that works efficiently at various speeds and in all four quadrants.

The design space for hydraulic pumps is complicated with many interconnected and competing physical phenomena. The parameters that describe the hydraulic unit design are numerous with several clearances, multiple valve timing angles, and various size decisions to be optimized. This creates a solution space that cannot effectively be explored using a gradient descent optimization method due to the multiple local minima. Therefore, a single objective genetic algorithm is used to optimize the design parameters in an efficient manner.

4.1.1 Literature Review

Leveraging the model to design the radial ball piston machine involves adjusting the geometry and determining the impact on the efficiency. There are many variables that are interconnected making it difficult to explore the design space via gradient methods or through designer intuition. Care must be taken to ensure that the geometry is physically realizable before it can be considered as a potential solution.

A genetic algorithm was used because of its robustness against converging on local minima. The algorithm was inspired by evolution and its ability to optimize species for survival. The algorithm generates “chromosomes” which define the characteristics of the radial ball piston design. Each “chromosome” belongs to an “individual”, and each individual is evaluated to determine its “fitness”. After the fitness for each individual is known, the best ones are “bred” to form a new generation of designs. The breeding process involves randomly selecting traits from

[7] HECM drive cycle data courtesy of Jacob Siefert

two chromosomes to generate a new individual. Mutations are also incorporated when breeding to randomly shift the population. Like mutations in biology, some may not be helpful, but others may result in an advantageous change. This equates to the optimization exiting a local minimum. This breeding process continues for multiple generations, gradually improving the overall fitness of the population [53]. The single objective genetic algorithm used for this thesis concludes once a certain number of generations are evaluated or if the fitness plateaus. This genetic algorithm was originally built for Matlab by researchers from the University of Sheffield [54, 55].

The chromosomes define the parameter values, which for a radial ball piston pump includes design decision such as bore-to-stroke ratio, clearances, valve timing, etc. The parameters can be physical dimensions or can encode the information using ratios. It is difficult to set appropriate limits on physical dimensions to guarantee the inclusion of the optimal value. This leads to bounds often being larger than required, hurting the efficiency of the optimization. Ratios are preferred because their bounds often arise naturally from the definition of the ratio. It is easy to include every physically realistic value when using ratios ensuring that the optimal value exists within the limits [56]. Despite the use of ratios, it is possible for dimensions to be selected that create interference between parts leading to an invalid design. Therefore, a constraint function is implemented that checks for interference.

In optimizations, evaluating the performance is done using objective functions. Objective functions take the parameter values as an input and returns the value that is being minimized or maximize. The objective function in this case is the dynamic simulation and energy loss model presented in the previous two chapters. It takes the geometry selected by the optimization and evaluates the pressure dynamics, throttling losses, and interface losses to predict the design performance. For the radial ball piston unit, the objective is to minimize the power loss. The constraint function that checks for valid geometry is enforced by setting the objective function's value to infinity when constraints are violated. Note that the output power is equivalent for each design, which means minimizing power loss also maximizes efficiency. Optimizing the hydraulic architecture within a genetic algorithm framework is a popular technique within the hydraulic academic community [20, 57, 58], but this thesis represents the first optimization study of the radial ball piston architecture.

4.1.2 Overview

The following chapter explains the techniques used to optimize the radial ball piston hydraulic unit. First, the simplified models for the ball-cylinder interface and pintle-rotor interface are

presented. Then the details of the genetic algorithm are explained and the process for determining the physical significance of optimization parameters is shown. Design validity is considered before determining the expected power loss of the machine. Next, a one-dimensional optimization technique for refining the ball-cylinder clearance value is described. The method that was used to determine the operating conditions is shared and lastly, the results of the optimization are presented and analyzed.

4.2 Methods

The radial ball piston model that was described in Chapter 2 and validated in Chapter 3 is faster than numerical FEA solutions but is still too slow to run within a design optimization framework. A genetic algorithm simulates hundreds to thousands of designs to navigate complex design spaces; therefore, each individual design needs to be evaluated quickly (minutes) for the entire optimization to run in a reasonable amount of time (hours). This time constraint forces further model simplifications for optimizations to be realistic.

The ball-cylinder interface is the most computationally intensive piece of the model by a significant margin. This is because of the repeated numerical integrations that are needed to determine the ball eccentricity within each timestep. The amount of time required can be decreased from several hours per simulation to less than a minute if the ball-cylinder interface is ignored. However, ignoring the losses at that interface means there is no penalty for adjusting the design of the ball pistons. To address this, a simplified model of the ball-cylinder interface is developed to capture the trends of the original model in a time efficient manner.

Similarly, the pintle-rotor interface also becomes a bottleneck to the computation speed after the ball-cylinder interface is simplified. Simplifying the fluid mechanics at this interface by ignoring the dynamics and assuming concentricity between the pintle and the rotor greatly reduces the computational speed required. Fortunately, the HECM design utilizes a bearing between the pintle and rotor which keeps the two elements concentric; justifying the simplification of removing the dynamics. Therefore, a simplified pintle-rotor model is also presented.

4.2.1 Simplified Ball-Cylinder Interface

The simplified ball-cylinder interface makes two additional assumptions compared with the model presented earlier: the ball piston stays centered, and fluid temperature is constant. These two assumptions simplify the computations immensely because centering the ball piston removes the need to calculate the pressure distribution and net force acting on the ball piston. The

elastohydrodynamic lubrication approximations can also be removed, and the full heat transfer model is removed due to the isothermal assumption. The simplified ball-cylinder interface model as used in the optimization is now presented.

4.2.1.1 Cylinder Expansion

To calculate the losses at the ball-cylinder interface, the clearance between the ball piston and the cylinder wall is fundamental to understanding the behavior. The initial clearance can be measured, but the pressure during operation will elastically deform the cylinder. Therefore, a rough model of the cylinder expansion was created to approximate the change in clearance between the two surfaces. The geometry is shown in Figure 4.1.

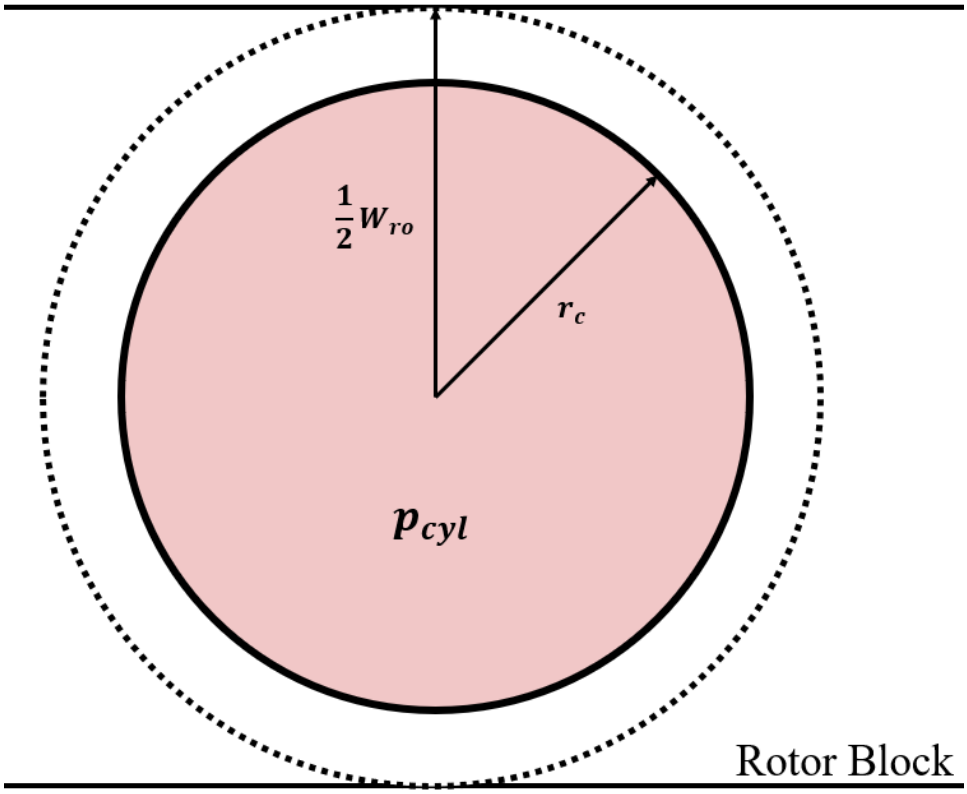

FIGURE 4.1: BALL-CYLINDER PRESSURE VESSEL GEOMETRY

The expansion was modeled using a thick walled pressure vessel assumption with only internal pressure. Note that this change in radius and the clearance will be a function of time because the cylinder pressure changes throughout operation.

$$\Delta r_c = \frac{p_{cyl} r_c}{E}\left(\nu + \frac{\left(\frac{1}{2}W_{ro}\right)^2 + r_c^2}{\left(\frac{1}{2}W_{ro}\right)^2 - r_c^2} \right) \tag{4.1}$$

where E is the elastic modulus, and ν is Poisson's ratio. The radial clearance between the parts is given in eq. (2.91).

$$h_o = r_c + \Delta r_c - r_b \tag{4.2}$$

The change in radius calculated by eq. (2.90) overpredicts the expansion because $\frac{1}{2}W_{ro}$ is the thinnest value of the wall. However, this provides a conservative estimate for the power loss since the leakage is more sensitive to the clearance than the shear rate. The radial expansion is typically about a micron with the specific value depending on the operating condition.

4.2.1.2 Ball-Cylinder Interface Fluid Mechanics

The leakage and shear between the ball pistons and cylinders is a primary source of energy loss in radial ball piston pumps. Figure 4.2 and Figure 4.3 show this geometry. The clearance is greatly exaggerated in the figures with the actual difference between r_b and r_c being in the micron range. Jamzedeh showed that for this geometry the distance between the ball piston and the cylinder at any location can be found with eq. (4.3) [10].

$$h = h_o + r_b - r_b \sin\vartheta - e_b \cos\varphi \tag{4.3}$$

where

$$h_o = r_c - r_b \tag{4.4}$$

Assuming the ball stays centered.

$$e_b = 0 \tag{4.5}$$

$$h = h_o + r_b - r_b \sin\vartheta \tag{4.6}$$

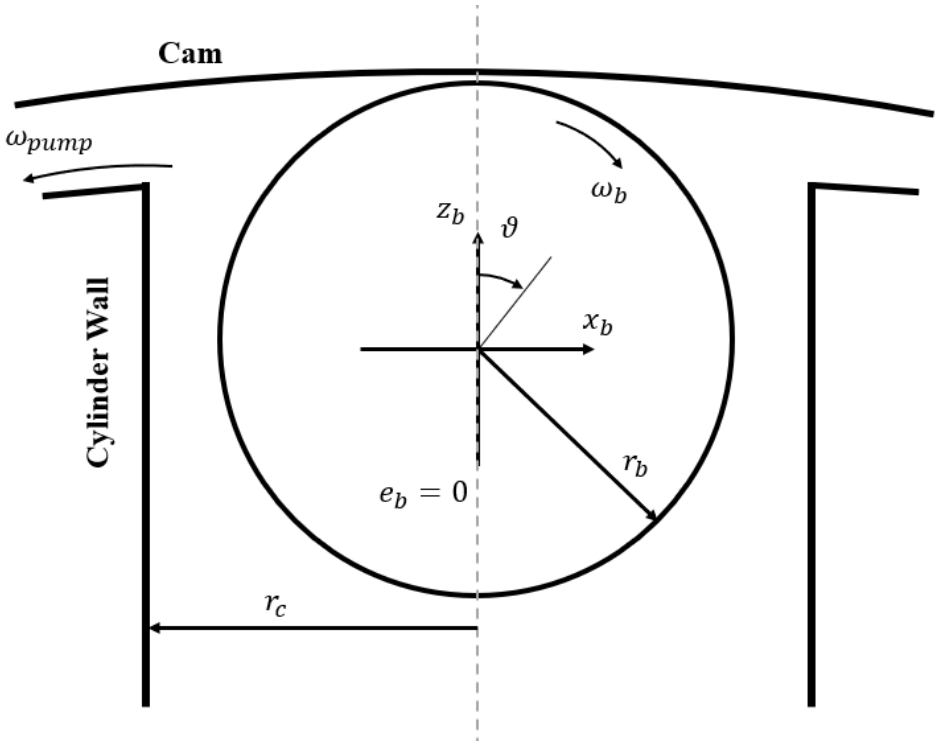

FIGURE 4.2: BALL-CYLINDER X-Z CROSS SECTION

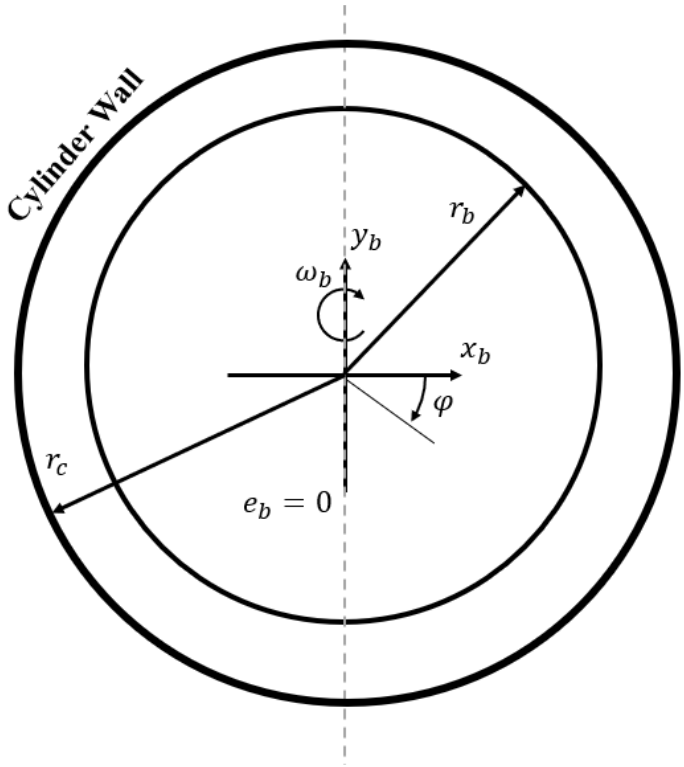

FIGURE 4.3: BALL-CYLINDER X-Y CROSS SECTION

The extremely thin gap between the ball and cylinder means that lubrication theory is needed to describe the fluid mechanics in the gap, therefore Reynold's equation is used. The full Reynold's equation can be written using the coordinates defined in Figure 4.2 and Figure 4.3.

$$\frac{\partial}{\partial z_b}\left(-\frac{h^3}{12\mu}\frac{\partial p}{\partial z_b}+(U_1+U_2)\frac{h}{2}\right)+\frac{\partial}{\partial y_b}\left(-\frac{h^3}{12\mu}\frac{\partial p}{\partial y_b}+(V_1+V_2)\frac{h}{2}\right)+\frac{dh}{dt}=0 \quad (4.7)$$

Assuming the ball stays centered and assuming the cylinder expansion results in negligible changes in gap height with time further simplifies the fluid mechanics.

$$\frac{dh}{dt}\approx 0 \quad (4.8)$$

Using the geometry defined in Figure 4.2 and applying eq. (4.7) to the thin gap (where $z_b \approx 0$), then there is no significant velocity or pressure differential in the y_b direction. Applying this assumption with eq. (4.8) simplifies the Reynold's equation.

$$\frac{\partial}{\partial z_b}\left(-\frac{h^3}{12\mu}\frac{\partial p}{\partial z_b}+(U_1+U_2)\frac{h}{2}\right)=0 \quad (4.9)$$

Converting from Cartesian to spherical coordinates can be done using eq. (4.10) - (4.12).

$$x_b = r_b \sin\vartheta \cos\varphi \quad (4.10)$$

$$y_b = r_b \sin\vartheta \sin\varphi \quad (4.11)$$

$$z_b = r_b \cos\vartheta \quad (4.12)$$

Writing Reynold's equation with spherical coordinates.

$$\frac{-1}{r_b \sin\vartheta}\frac{\partial}{\partial\vartheta}\left(-\frac{h^3}{12\mu}\frac{-1}{r_b \sin\vartheta}\frac{\partial p}{\partial\vartheta}+(U_1+U_2)\frac{h}{2}\right)=0 \quad (4.13)$$

where ϑ is the polar angle and φ is the azimuthal angle. Using spherical coordinates, the tangential velocity at each point on the ball surface can be determined.

$$U_b = r_b\omega_b\sqrt{\cos^2\vartheta+\sin^2\vartheta\cos^2\varphi}+e_{pump}\omega_{pump}\sin\theta_{cyl} \quad (4.14)$$

Equation (4.14) is simplified because only the thin gap region is considered.

$$U_b = r_b\omega_b \cos\varphi + e_{pump}\omega_{pump} \sin\theta_{cyl} \qquad (\vartheta \approx \pi/2) \tag{4.15}$$

Rearranging the equations and integrating by ϑ.

$$\frac{h^3}{12\mu r_b \sin\vartheta}\frac{\partial p}{\partial \vartheta} + U_b\frac{h}{2} = C_o \tag{4.16}$$

Letting $C_1 = 12r_bC_o$.

$$\frac{\partial p}{\partial \vartheta} = C_1\frac{\mu \sin\vartheta}{h^3} - 6r_bU_b\frac{\mu \sin\vartheta}{h^2} \tag{4.17}$$

To determine the change in pressure at each point around the ball, two boundary conditions are needed so that eq. (4.17) can be integrated:

$$\vartheta = 0 \quad \rightarrow \quad p = p_{case}$$
$$\vartheta = \pi \quad \rightarrow \quad p = p_{cyl}$$

μ and h both are functions of ϑ so integrating the equation is done numerically.

$$\int_{p_{case}}^{p_{cyl}} dp = C_1\int_0^{\pi}\frac{\mu \sin\vartheta}{h^3}d\vartheta - 6r_bU_b\int_0^{\pi}\frac{\mu \sin\vartheta}{h^2}d\vartheta \tag{4.18}$$

The definite integrals are computed using eq. (4.19) - (4.22), which then are used to form an expression for the constant C_1.

$$\Delta p = p_{cyl} - p_{case} \tag{4.19}$$

$$S_2 = \int_0^{\pi}\frac{\mu \sin\vartheta}{h^2}d\vartheta \tag{4.20}$$

$$S_3 = \int_0^{\pi}\frac{\mu \sin\vartheta}{h^3}d\vartheta \tag{4.21}$$

$$C_1 = (\Delta p + 6r_bU_bS_2)\frac{1}{S_3} \tag{4.22}$$

Substituting these equations into eq. (4.17) gives an expression for the change in pressure.

$$\frac{\partial p}{\partial \vartheta} = \frac{\Delta p \mu \sin \vartheta}{S_3 h^3} + 6 r_b U_b \frac{\mu \sin \vartheta}{h^3} \left(\frac{S_2}{S_3} - h \right) \tag{4.23}$$

Once the change in pressure distribution is known, the leakage and shear that occur at the ball piston can be determined. It is assumed that in the gap, there is not significant leakage circumferentially around the ball so only the zenith direction is considered. The general equation for the leakage in the ϑ direction is given in eq. (4.24).

$$Q_\vartheta = \frac{h^3}{12 \mu r_b \sin \vartheta} \frac{\partial p}{\partial \vartheta} + \frac{U_1 + U_2}{2} h \tag{4.24}$$

Substituting the expression found for $\partial p / \partial \vartheta$.

$$Q_\vartheta = \frac{\Delta p}{12 r_b S_3} + \frac{U_b}{2} \frac{S_2}{S_3} \tag{4.25}$$

The same process can be done for the shear distribution on the ball where eq. (4.26) is the general form.

$$\tau_{ball} = -\frac{h}{2 r_b \sin \vartheta} \frac{\partial p}{\partial \vartheta} + \mu \frac{U_1 - U_2}{h} \tag{4.26}$$

Again, substituting the expression found for $\partial p / \partial \vartheta$.

$$\tau_{ball} = -\frac{\mu}{h^2} \left[\frac{\Delta p}{2 r_b S_3} + 4 U_b \left(\frac{3 S_2}{4 S_3} - h \right) \right] \tag{4.27}$$

The shear on the ball will create a resistive torque acting on the ball piston that must be overcome to keep the ball from skidding.

$$\mathrm{T}_{ball} = \int_0^{2\pi} \int_{\vartheta_1}^{\vartheta_2} \tau_{ball}(\vartheta, \varphi) \cdot r_b^3 \sin \vartheta \sqrt{\cos^2 \vartheta + \sin^2 \vartheta \cos^2 \varphi} \cdot sign(\cos \varphi) d\vartheta d\varphi \tag{4.28}$$

The $sign(\cos \varphi)$ term is necessary to determine the direction of the torque. A positive T_{ball} implies that it is assisting the ball in rotating. The square root term gives the correct distance from the axis of rotation to the point on the ball surface.

An important note is that the fluid mechanics derivation applies to a given azimuthal angle, φ, and that to determine the pressure, shear, and leakage distributions around the ball, each azimuthal angle must be analyzed.

4.2.2 Simplified Pintle-Rotor Interface

The pintle-rotor interface was simplified to improve the computational efficiency and to more accurately represent the physical design. The original model presented in section 2.2.2 was developed to represent the Eaton radial ball piston pump, which used the pintle as a journal bearing to support the rotor block. The HECM requires near zero speed operation making a journal bearing infeasible for load support; therefore, the HECM uses ball bearings to support the pintle-rotor interface. The bearings maintain concentricity between the pintle and the rotor block, allowing the journal bearing dynamics and kinematics to be ignored. The heat transfer at the interface is also assumed to be negligible during the optimization, further improving the computation speed and simplifying the fluid mechanics.

The loss calculations at the interface are simplified by assuming the ports are rectangular in geometry. To create a conservative model for the losses, the cylinder valve openings are ignored when determining the area where shearing occurs. Figure 4.4 shows the pintle-rotor geometry where the circumferential clearance is unwrapped, as used to perform the simplified torque calculations. The torque can be found by assuming the Couette component of the flow dominates the shear.

$$\mathrm{T}_{\tau} = \mu \frac{R_p \omega_{pump}}{H_p} \cdot \left[2\pi R_p w_{ri} - H_{port} R_p (\theta_{A_c} - \theta_{A_o} + \theta_{B_c} - \theta_{B_o})\right] \cdot R_p \qquad (4.29)$$

where H_p is the clearance between the pintle and the rotor, μ is the viscosity, and the rest of the variables are given in Figure 4.4.

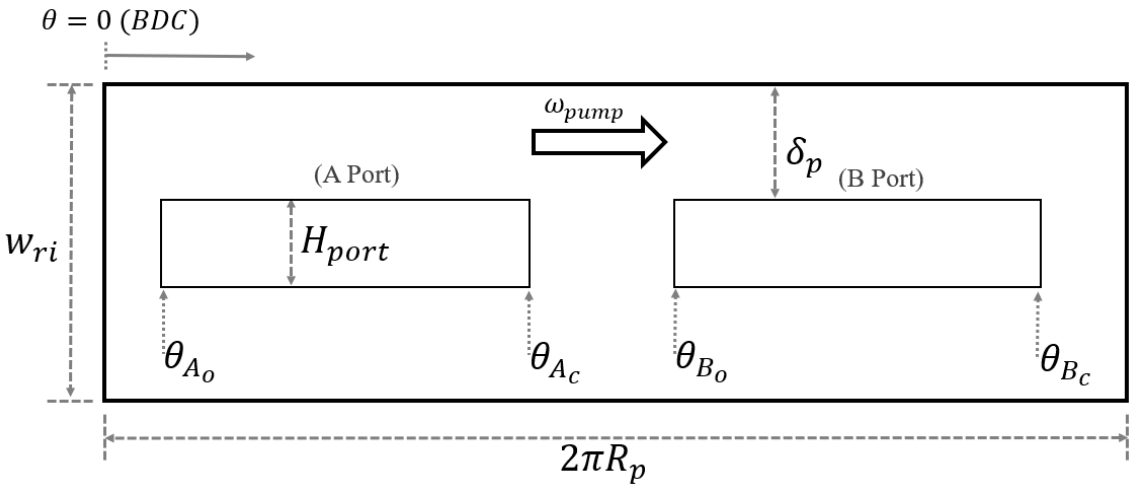

FIGURE 4.4: SIMPLIFIED PINTLE-ROTOR INTERFACE GEOMETRY

The geometry of Figure 4.5 was used to calculate a conservative estimate of the leakage while still maintaining computational speed. Instead of assuming a linear pressure profile between the ports, the port pressures are extended into the transition region. This is a reasonable assumption because the transition region usually contains a cylinder valve whose pressure is approximately one of the port pressures. Note from the figure that the midpoint between the ports can wrap around the pintle depending on the specific geometry. Equation (4.30) determines the leakage to the case. It assumes the Poiseuille component of the flow profile dominates.

$$Q_{Case} = \frac{(p_A - p_{case})H_p^3}{6\mu\delta_p} \cdot R_p \left(\frac{\theta_{A_c} + \theta_{B_o}}{2} - \frac{\theta_{A_o} + \theta_{B_c} - 2\pi}{2} \right) + \frac{(p_B - p_{case})H_p^3}{6\mu\delta_p} \cdot R_p \left(\frac{\theta_{B_c} + \theta_{A_o} + 2\pi}{2} - \frac{\theta_{B_o} + \theta_{A_c}}{2} \right) \tag{4.30}$$

The leakage power loss from the ports to case can be found using eq. (4.31).

$$\mathcal{P}_{Q_{pintle}} = \frac{(p_A - p_{case})^2 H_p^3}{6\mu\delta_p} \cdot R_p \left(\frac{\theta_{A_c} + \theta_{B_o}}{2} - \frac{\theta_{A_o} + \theta_{B_c} - 2\pi}{2} \right) + \frac{(p_B - p_{case})^2 H_p^3}{6\mu\delta_p} \cdot R_p \left(\frac{\theta_{B_c} + \theta_{A_o} + 2\pi}{2} - \frac{\theta_{B_o} + \theta_{A_c}}{2} \right) \tag{4.31}$$

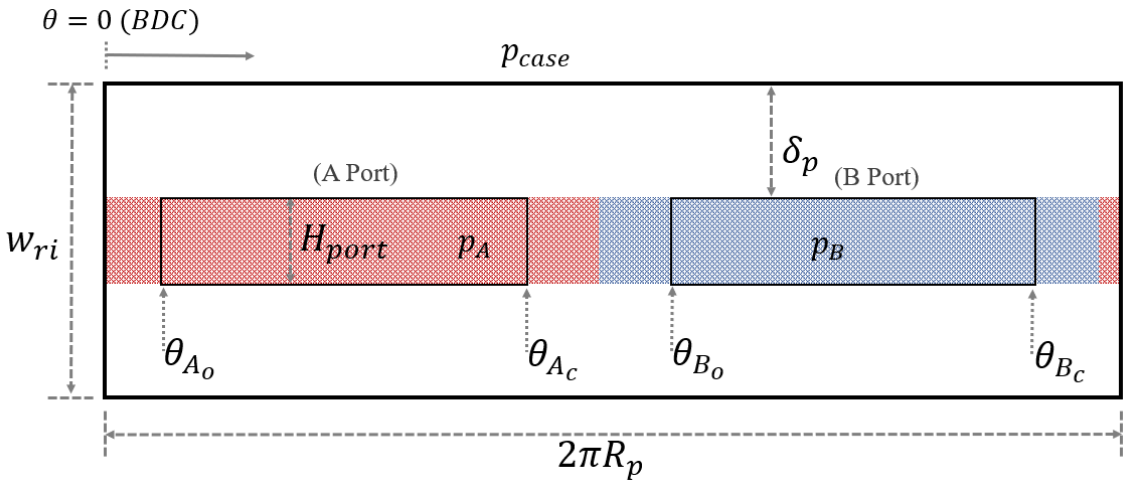

FIGURE 4.5: SIMPLIFIED PINTLE-ROTOR INTERFACE PRESSURE DISTRIBUTION

4.2.3 Optimization Strategy

After the simplification to the ball-cylinder interface, the model can evaluate a design in less than a minute, which makes optimizations possible. This allows various operating points to be evaluated to create a hydraulic unit that functions well as both a pump and a motor. The optimization is broken up into two steps. The first determines the optimal size and proportions of the pump using the simplified model. The second step refines the ball-cylinder clearance using the more accurate dynamic model.

4.2.3.1 Size Optimization Parameters

The genetic algorithm was used to determine the primary geometric features of the radial ball piston machine. When selecting variables, it is useful to use ratios where possible because that creates natural bounds on the parameters. The variables that were used for the optimization are given in Table 4.1 and further defined in the paragraphs below. These variables define the geometry of the pump and directly influence the performance of the hydraulic unit. Below are rules for variable names:

1. All genetic algorithm parameters are denoted with a superscript apostrophe, " $'$ ".
2. $\mathcal{R}$ is reserved for ratios.
3. Variables other than $\mathcal{R}$ correspond to physical values.
4. Subscript b is a variable related to the ball piston.
5. Subscript p is a variable related to the pintle.

TABLE 4.1: OPTIMIZATION PARAMETERS

Parameter	Description
n_b'	Number of ball pistons
$\mathcal{R}_{d/s}'$	Bore to stroke ratio
h_{b_o}'	Ball-cylinder clearance (in microns)
$\phi_{pump_{max}}'$	Maximum pressure angle during rotation (in radians)
$\mathcal{R}_{R_p}'$	Ratio for pintle radius
H_{p_o}'	Pintle-rotor clearance (in microns)
δ_p'	Leakage distance from the ports to the case (in microns)
$\mathcal{R}_{r_v}'$	Ratio for cylinder valve opening radius
$\mathcal{R}_{H_v}'$	Ratio for cylinder valve height
v_{bdc}'	Primary bottom dead center (BDC) valve timing angle (in radians)
s_{bdc}'	Secondary bottom dead center (BDC) valve timing angle (in radians)
v_{tdc}'	Primary top dead center (TDC) valve timing angle (in radians)
s_{tdc}'	Secondary top dead center (TDC) valve timing angle (in radians)

The first step to determining the geometry of the pump is knowing the maximum speed, ω_{max}, and flow rate, Q_{max}, that the unit will support. This allows the displacement of the machine to be determined.

$$D = \frac{2\pi Q_{max}}{\eta_v \omega_{max}} \tag{4.32}$$

where η_v is an assumed volumetric efficiency. The displacement of the unit is determined by several geometric features.

$$D = 2n_b \pi r_b^2 e_{pump} \tag{4.33}$$

where n_b is the number of pistons, r_b is the radius of the ball piston, and e_{pump} is the eccentricity of the pump. Notice that $2e_{pump}$ is the stroke of the ball piston during a revolution. The parameter n_b' sets the number of pistons and for most optimizations is a constant of 5, 7, or 9 pistons.

$$n_b = n_b' \tag{4.34}$$

The bore to stroke ratio is an optimization parameter and is given below.

$$\mathcal{R}'_{d/s} = \frac{2r_b}{2e_{pump}} = \frac{r_b}{e_{pump}} \tag{4.35}$$

Therefore, after the bore to stroke ratio is defined, the pump eccentricity and the ball radius can be found according to eq. (4.36) and (4.37).

$$e_{pump} = \left(\frac{D}{2\pi n_b \mathcal{R}_{d/s}{}^2}\right)^{1/3} \tag{4.36}$$

$$r_b = \mathcal{R}_{d/s} e_{pump} \tag{4.37}$$

The ball cylinder clearance optimization parameter value is in microns. Equation (4.38) and eq. (4.39) are used to set the physical clearance and the cylinder radius respectfully.

$$h_{b_o} = h'_{b_o} \cdot 10^{-6} \tag{4.38}$$

$$r_c = r_b + h_{b_o} \tag{4.39}$$

The pressure angle, ϕ_{pump}, can be determined geometrically from Figure 4.6 using the law of sines.

$$\sin(\phi_{pump}) = \frac{e_{pump}}{R_o}\sin(\theta) \tag{4.40}$$

where $R_o = R_{cam} - r_b$. The maximum pressure angle occurs when $\sin(\theta)$ is one and after the optimization selects $\phi_{pump_{max}}$ the cam radius is calculated.

$$R_{cam} = \frac{e_{pump}}{\sin\left(\phi_{pump_{max}}\right)} + r_b \tag{4.41}$$

In Figure 4.6, O_R is the center of the rotor block, O_C is the center of the cam, O_b is the center of the ball, and R_b is the distance from O_R to O_b. The radial position is found using the law of cosines, eq. (2.74).

$$R_o^2 = R_b^2 + e_{pump}^2 - 2R_b e_{pump}\cos\theta$$

$$0 = R_b^2 - R_b\left(2e_{pump}\cos\theta\right) + \left(e_{pump}^2 - R_o^2\right)$$

$$R_b = \frac{1}{2}\left(2e_{pump}\cos\theta \pm \sqrt{4e_{pump}^2\cos^2\theta - 4\left(e_{pump}^2 - R_o^2\right)}\right)$$

$$R_b = e_{pump}\cos\theta + \sqrt{R_o^2 + e_{pump}^2(\cos^2\theta - 1)} \tag{4.42}$$

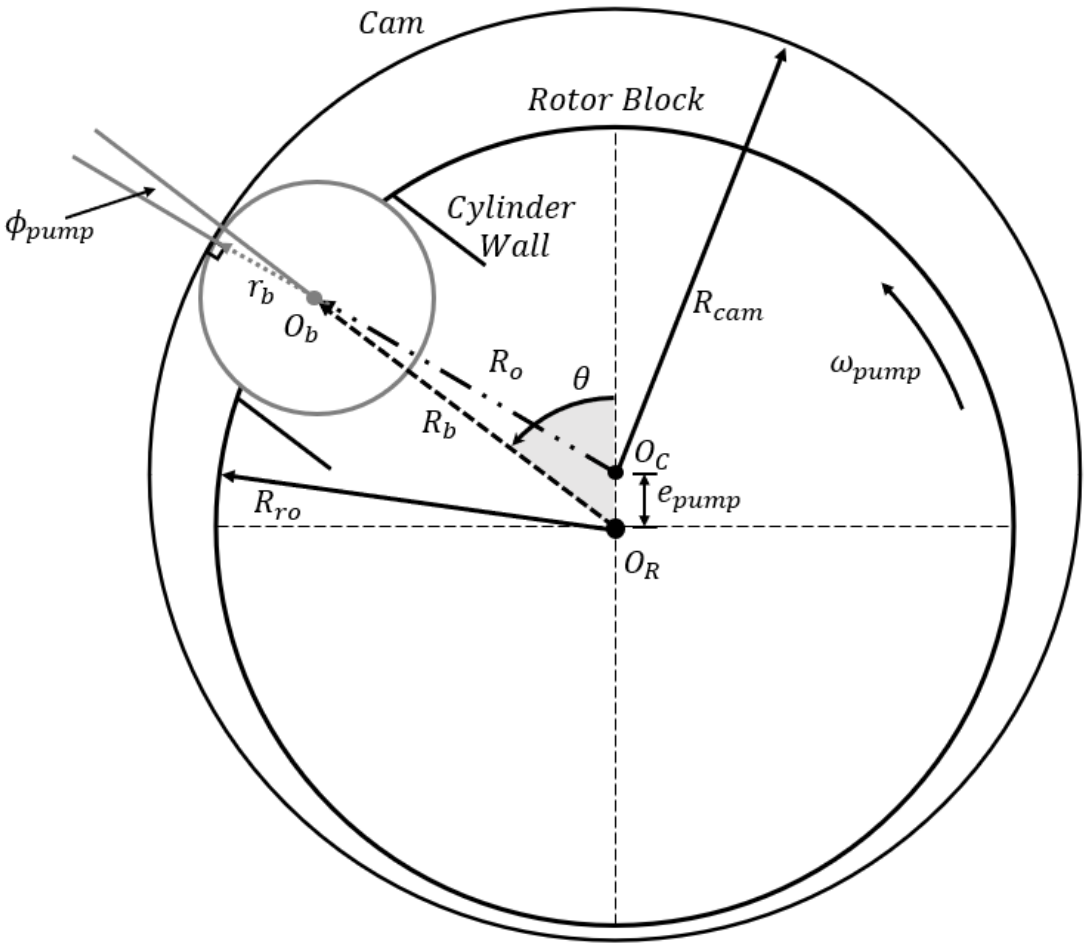

FIGURE 4.6: PRESSURE ANGLE AND DISTANCE TO THE CENTER OF THE BALL

Solving eq. (2.74) for the maximum and minimum values of R_b gives the value for the ball piston position at bottom dead center (BDC) and top dead center (TDC). These values occur at $\theta = 0$ and $\theta = \pi$ respectfully.

$$R_b = R_o + e_{pump} \qquad (\theta = 0) \tag{4.43}$$

$$R_b = R_o - e_{pump} \qquad (\theta = \pi) \tag{4.44}$$

The outside radius of the rotor block, R_{ro}, needs to be selected so that there is not a conflict with the rest of the geometry. Clearance is designed between the cam ring and the rotor block to ensure the two parts do not collide or wear on each other. The clearance, denoted as H_{ro}, is calculated using eq. (4.45). Selecting $\mathcal{R}'_{d/s} > 2.22$ ensures the clearance will be positive[8].

$$H_{ro} = 0.9r_b - 2e_{pump} = \left(0.9\mathcal{R}_{d/s} - 2\right)e_{pump} \tag{4.45}$$

Based on the geometry in Figure 4.7, once the clearance is known, the outside radius of the rotor block can be found using eq. (4.46).

$$R_{ro} = R_{cam} - e_{pump} - H_{ro} \tag{4.46}$$

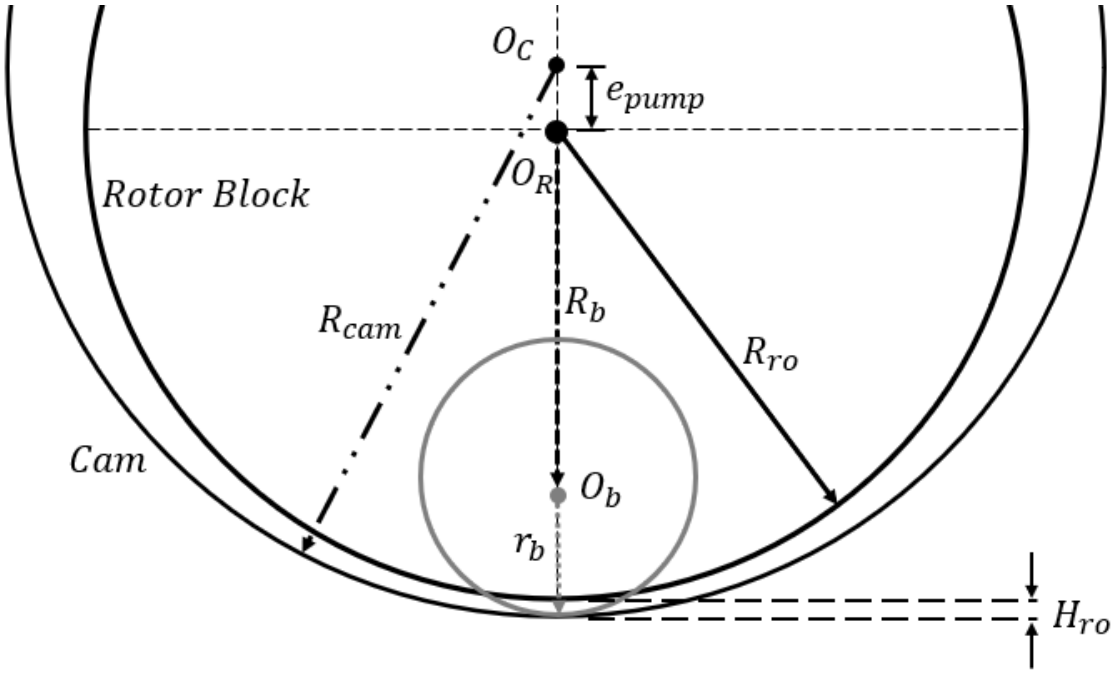

FIGURE 4.7: ROTOR BLOCK AND CAM CLEARANCE AT TOP DEAD CENTER

The fifth optimization parameter, $\mathcal{R}'_{R_p}$ sets the radius of the pintle.

$$R_p = \mathcal{R}'_{R_p} \cdot R_{ro} \tag{4.47}$$

[8] $0.9\mathcal{R}'_{d/s} - 2 > 0 \quad \Rightarrow \quad \mathcal{R}'_{d/s} > 2/0.9 \quad \Rightarrow \quad \mathcal{R}'_{d/s} > 2.22$

The pintle-rotor clearance, H_{p_o}, and pintle leakage length, δ_p, determine the tradeoff between leakage and shear losses at the interface. These two values are found using eq. (4.48) and (4.49).

$$H_{p_o} = H'_{p_o} \cdot 10^{-6} \tag{4.48}$$

$$\delta_p = \delta'_p \cdot 10^{-6} \tag{4.49}$$

The clearance value then defines the inside radius of the rotor block.

$$R_{ri} = R_p + H'_{p_o} \tag{4.50}$$

The optimization parameter $\mathcal{R}'_{r_v}$ sets the valve radius according.

$$r_v = \mathcal{R}'_{r_v} \cdot r_c \tag{4.51}$$

The seat angle, Ψ_s, is a constant determined by the machining bit used to make the ball cylinder. A bit with a tip angle, Ψ_{bit}, determines the seat angle using the geometry in Figure 4.8 and eq. (4.52).

$$\Psi_s = 180° - \frac{1}{2}(180° - \Psi_{bit}) - 90° = \frac{1}{2}\Psi_{bit} \tag{4.52}$$

The height of the seat is also known after Ψ_s is found.

$$H_s = \frac{r_c - r_v}{\tan(\Psi_s)} \tag{4.53}$$

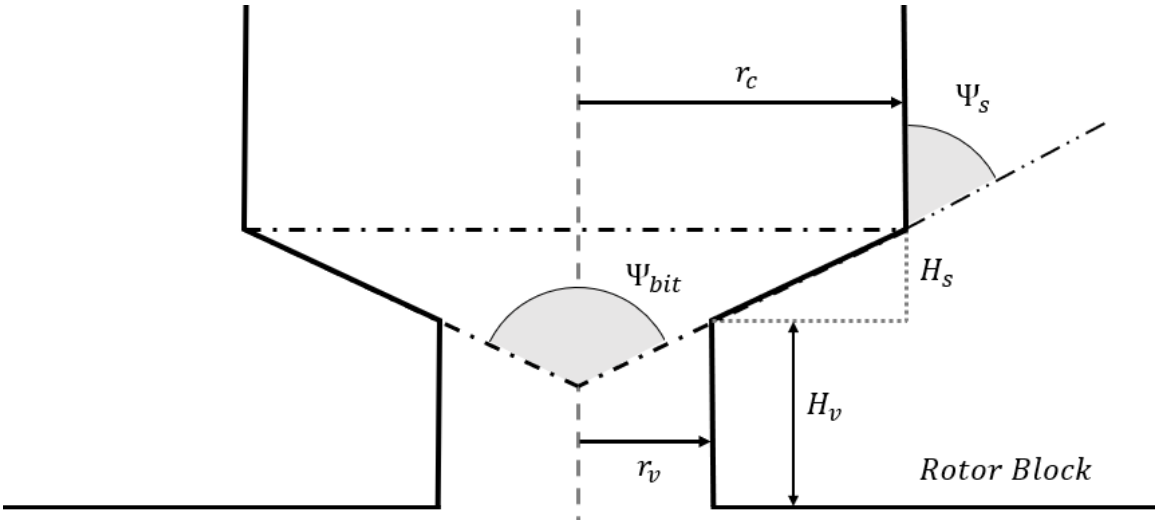

FIGURE 4.8: SEAT ANGLE GEOMETRY

The geometry of the dead volume occurs at TDC as shown in Figure 4.9. The figure simplifies the geometry by ignoring the curvature of the rotor block and cam; however, the cylinder bores are machined perpendicular to the outer rotor block surface making the dead volume unaffected by the curvature. The figure relates several different variables: cam radius, R_{cam}, rotor block outer radius, R_{ro}, rotor block inner radius, R_{ri}, ball piston center, R_b, ball piston radius, r_b, valve radius, r_v, cylinder radius, r_c, rotor block clearance, H_{ro}, seat angle, Ψ_s, seat height, H_s, and valve opening height, H_v. The value for the valve height is found with eq. (4.54), but it does not ensure a geometry without interference.

$$H_v = \mathcal{R}'_{H_v} \cdot (R_{ro} - R_{ri} - r_b - H_s) \tag{4.54}$$

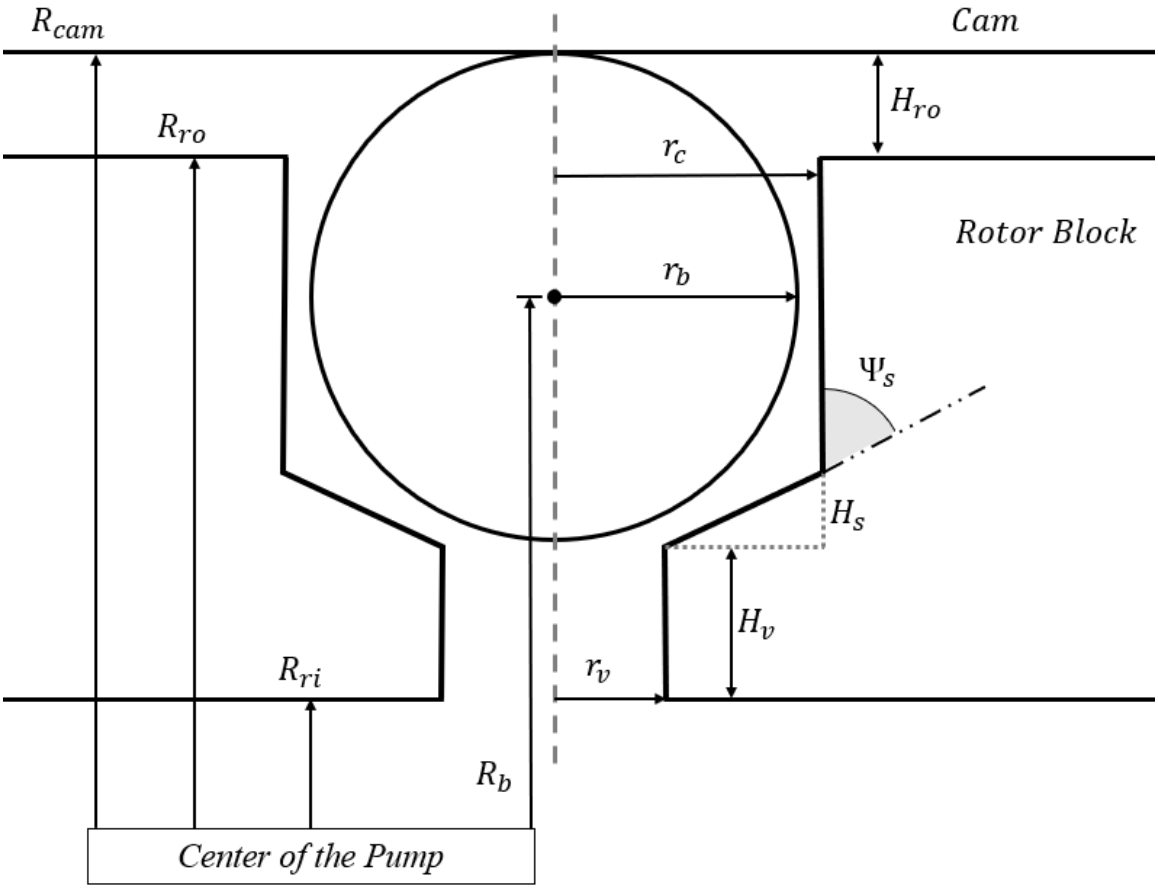

FIGURE 4.9: DEAD VOLUME GEOMETRY

The dead volume is found by calculating the volume of different regions using eq. (4.55) to eq. (4.58). The regions are shown in Figure 4.10 for clarity.

$$V_1 = \pi r_v^2 (R_b - R_{ri}) \tag{4.55}$$

$$V_2 = \pi (r_c^2 - r_v^2)(R_b - R_{ri} - H_v - H_s) \tag{4.56}$$

The third volume can be found using the equation for the volume of a conical frustum and then subtracting the inner cylinder volume.

$$V_3 = \frac{\pi H_s}{3}(r_c^2 + r_c r_v + r_v^2) - \pi r_v^2 H_s \tag{4.57}$$

$$V_3 = \frac{\pi H_s}{3}(r_c^2 + r_c r_v - 2r_v^2) \tag{4.58}$$

The dead volume can be found by summing these three volumes together and removing the space that the ball occupies. The remaining volume is the dead volume, V_D, assuming R_b is at BDC.

$$V_D = V_1 + V_2 + V_3 - \frac{2}{3}\pi r_b^3 \tag{4.59}$$

$$\begin{aligned} V_D = {} & \pi r_v^2 (R_b - R_{ri}) + \pi (r_c^2 - r_v^2)(R_b - R_{ri} - H_v - H_s) \\ & + \frac{\pi H_s}{3}(r_c^2 + r_c r_v - 2r_v^2) - \frac{2}{3}\pi r_b^3 \end{aligned} \tag{4.60}$$

where R_b is at TDC.

$$R_b = R_{cam} - e_{pump} - r_b \qquad (\theta = \pi) \tag{4.61}$$

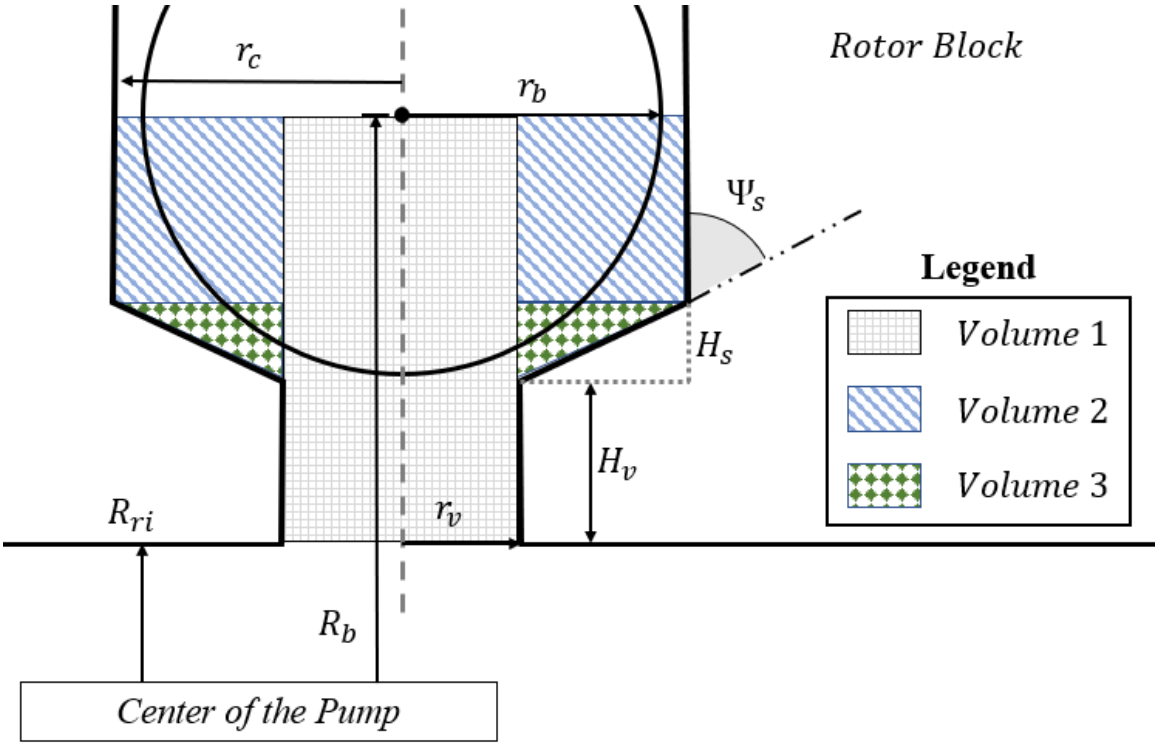

FIGURE 4.10: DEAD VOLUME REGIONS

The final four optimization parameters from Table 4.1 (v'_{bdc}, s'_{bdc}, v'_{tdc}, and s'_{tdc}) determine the valve timing of the hydraulic unit. These variables were selected because their definition is directly applicable to the manufacturing process that is used to machine the pintle ports. However, the model requires the timing angles for opening and closing the ports from BDC: θ_{A_o}, θ_{A_c}, θ_{B_o}, and θ_{B_c}. Therefore, the optimization parameters need to be converted to the model's timing angles. The geometric relationships between the parameters are shown in Figure 4.11.

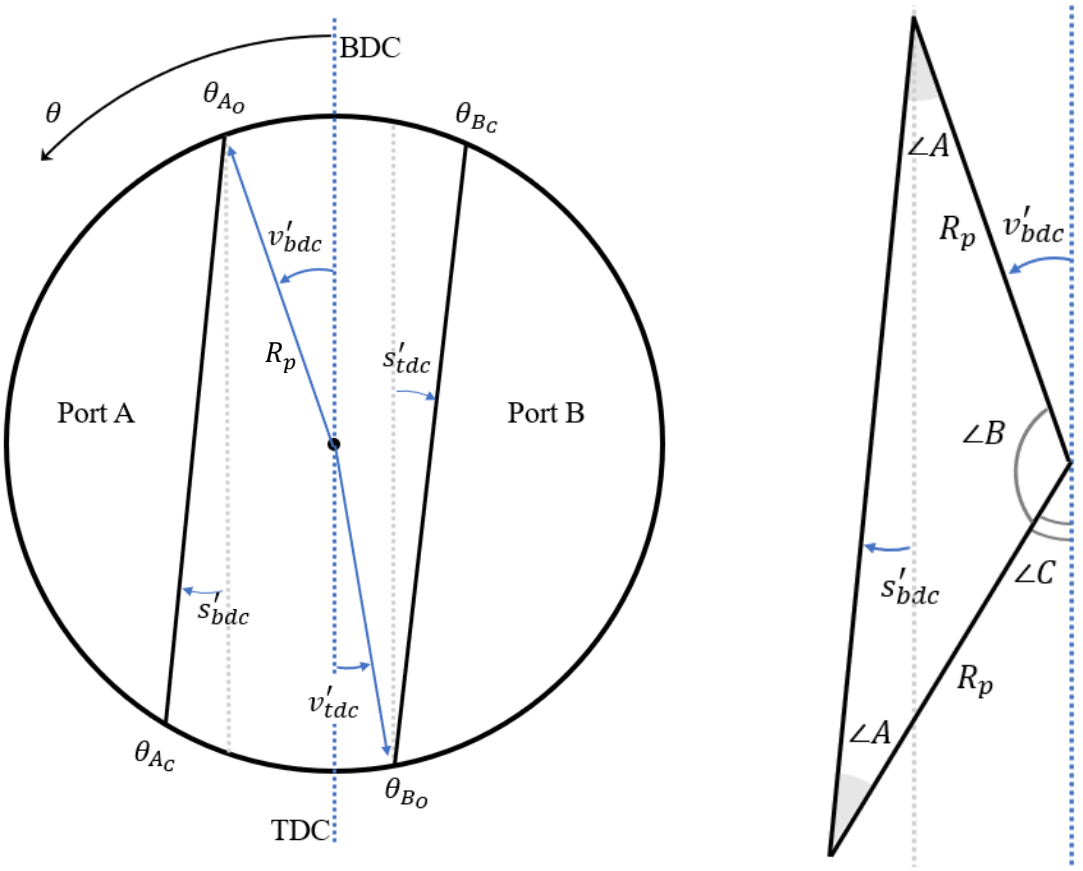

FIGURE 4.11: RELATIONSHIP BETWEEN OPTIMIZATION PARAMETERS AND VALVE TIMING ANGLES

From Figure 4.11 the geometric relationships for the valve timing angles are determined.

$$\theta_{A_o} = v'_{bdc} \tag{4.62}$$

Using the fact that an isosceles triangle is formed.

$$\angle A = v'_{bdc} + s'_{bdc}$$

$$\angle B = 180° - 2\angle A = 180° - 2v'_{bdc} - 2s'_{bdc}$$

$$\theta_{A_c} = v'_{bdc} + \angle B = 180° - v'_{bdc} - 2s'_{bdc} \tag{4.63}$$

Similar logic is used to determine the timing angles for Port B from BDC.

$$\theta_{B_o} = 180° + v'_{tdc} \tag{4.64}$$

$$\theta_{B_c} = 360° - v'_{tdc} - 2s'_{tdc} \tag{4.65}$$

4.2.3.2 Size Optimization Constraints

The use of ratios for the optimization parameters helps to create a valid geometry. However, there are still parameter combinations that can lead to invalid results or other edge cases that should be avoided. Therefore, constraints were added to the optimization to check the validity of the geometry before evaluating the performance of the design.

The first check is that the rotor block clearance (see Figure 4.7) is not too small. This check is because the churning losses are not included in evaluating the performance of the pump. These losses increase in magnitude as the clearance decreases. Therefore, a minimum clearance of $300\mu m$ was set for the rotor block clearance, H_{ro}.

The next constraint is that the ball cannot exceed the lip of the cylinder. This could occur at bottom dead center (BDC) and therefore inequality (4.66) must be valid.

$$R_{cam} + e_{pump} - r_b < R_{ro} \tag{4.66}$$

At top dead center (TDC), it is necessary to check that the ball does not interfere with the pintle as illustrated in Figure 4.12. Equation (4.67) must hold to ensure no interference between the parts.

$$R_{cam} - e_{pump} - 2r_b > R_{ri} \tag{4.67}$$

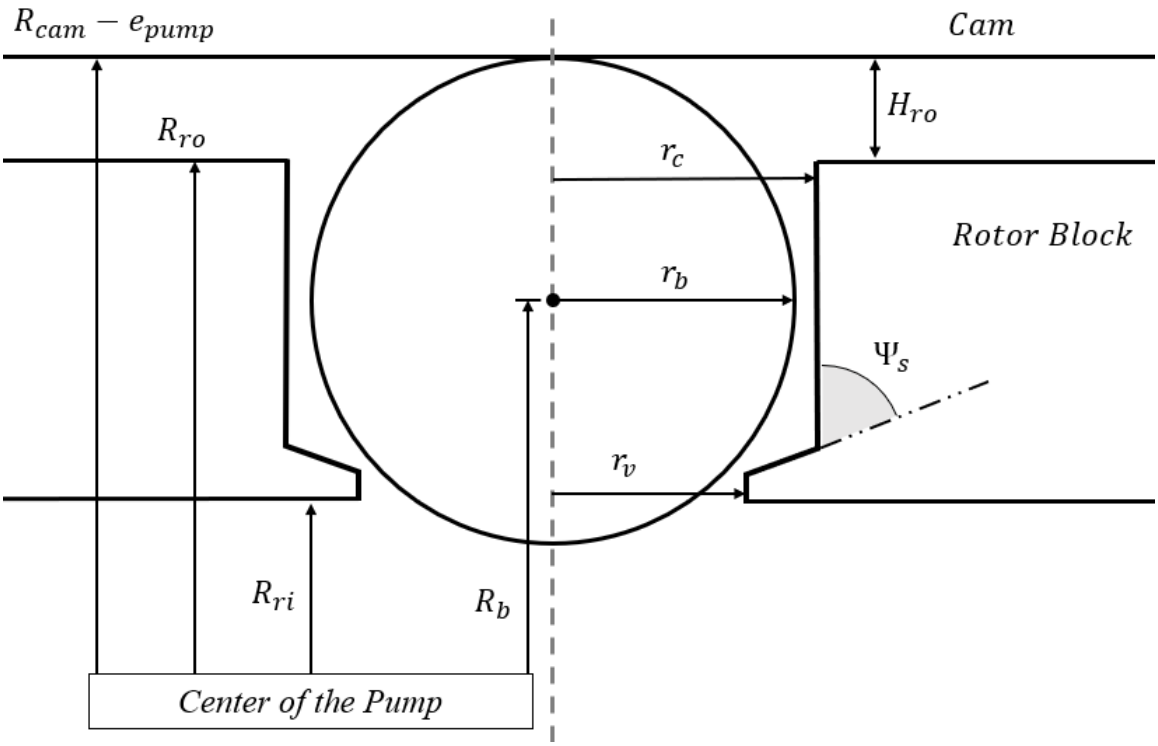

FIGURE 4.12: BALL PISTON AND PINTLE INTERFERENCE AT TOP DEAD CENTER

At TDC the ball could hit the seat at the bottom of the cylinder as shown in Figure 4.13. The general formula for the distance between a point and a line is given in eq. (4.68).

$$d = \frac{|ar_o + bz_o + c|}{\sqrt{a^2 + b^2}} \tag{4.68}$$

where the equation for the line is written as $ar + bz + c = 0$ and (r_o, z_o) is the point of interest. In this case, the equation for the line is given in eq. (4.69) and the point of interest is the center of the circle, $(0, O_b')$.

$$f_s: \quad z = \frac{H_s}{r_c - r_v}(r - r_v)$$

$$f_s: \quad 0 = \frac{H_s}{r_c - r_v} \cdot r - z - \frac{H_s r_v}{r_c - r_v} \tag{4.69}$$

Therefore, combining eq. (4.68) and (4.69) to calculate the distance at TDC.

$$d = \frac{\left|-O_b' - \frac{H_s r_v}{r_c - r_v}\right|}{\sqrt{\left(\frac{H_s}{r_c - r_v}\right)^2 + 1^2}} \tag{4.70}$$

Checking the constraint, eq. (4.71) needs to be satisfied.

$$d - r_b > 0 \tag{4.71}$$

where at TDC, O_b' is measured as the distance above the bottom of the seat.

$$O_b' = R_b - R_{ri} - H_v$$

$$O_b' = R_{cam} - e_{pump} - r_b - R_{ri} - H_v \tag{4.72}$$

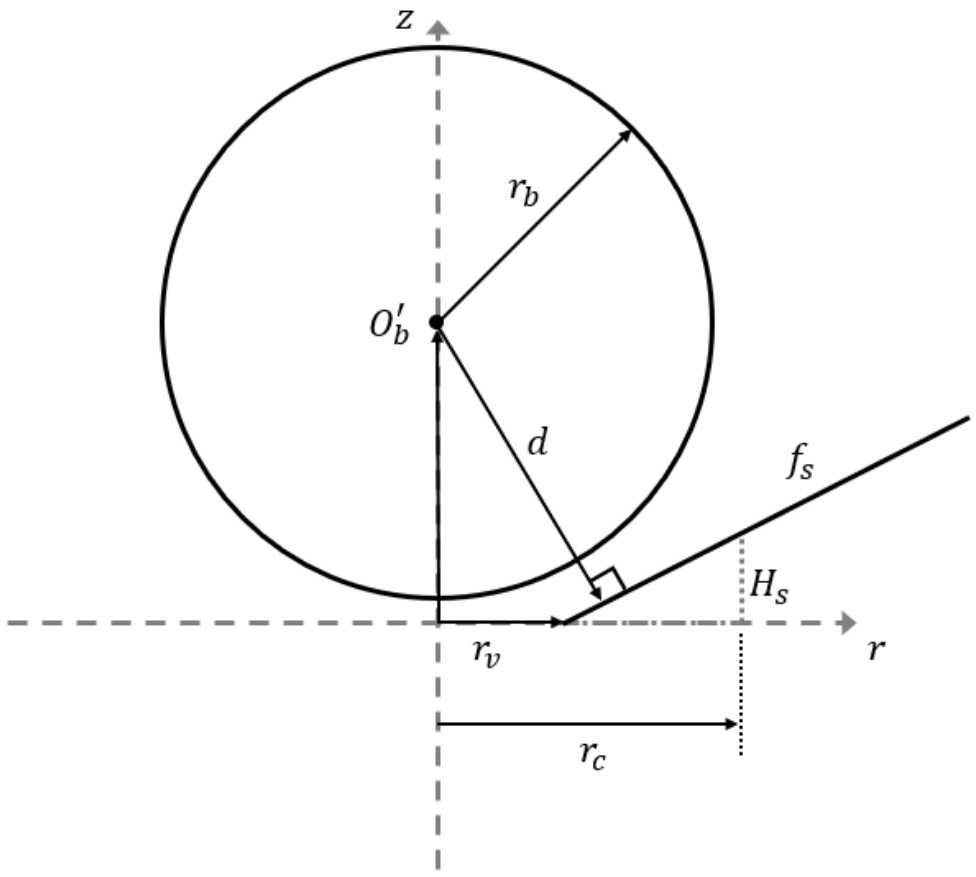

FIGURE 4.13: DISTANCE BETWEEN BALL CENTER AND SEAT AT TOP DEAD CENTER

The last constraints that need to be considered ensure the cylinders fit within the cylinder block. The geometry is shown in Figure 4.14 and the angular span for the valves and the seat can be calculated using eq. (4.73) to eq. (4.76).

$$\psi_v = \sin^{-1}\left(\frac{r_v}{R_{ri}}\right) \tag{4.73}$$

To ensure there is not interference between neighboring cylinders the following inequality needs to hold.

$$2\psi_v n_b < \zeta_v 2\pi \tag{4.74}$$

where ζ_v is the percentage of the inside rotor surface that can have a valve opening. Similar equations can be found to make sure the seat regions of the cylinders do not overlap with each other.

$$\psi_s = \tan^{-1}\left(\frac{r_c}{R_{ri}\cos(\psi_v) + H_v + H_s}\right) \tag{4.75}$$

To avoid interference.

$$2\psi_s n_b < \zeta_s 2\pi \tag{4.76}$$

where ζ_s is the percentage of the rotor block that will not have material through the cross section.

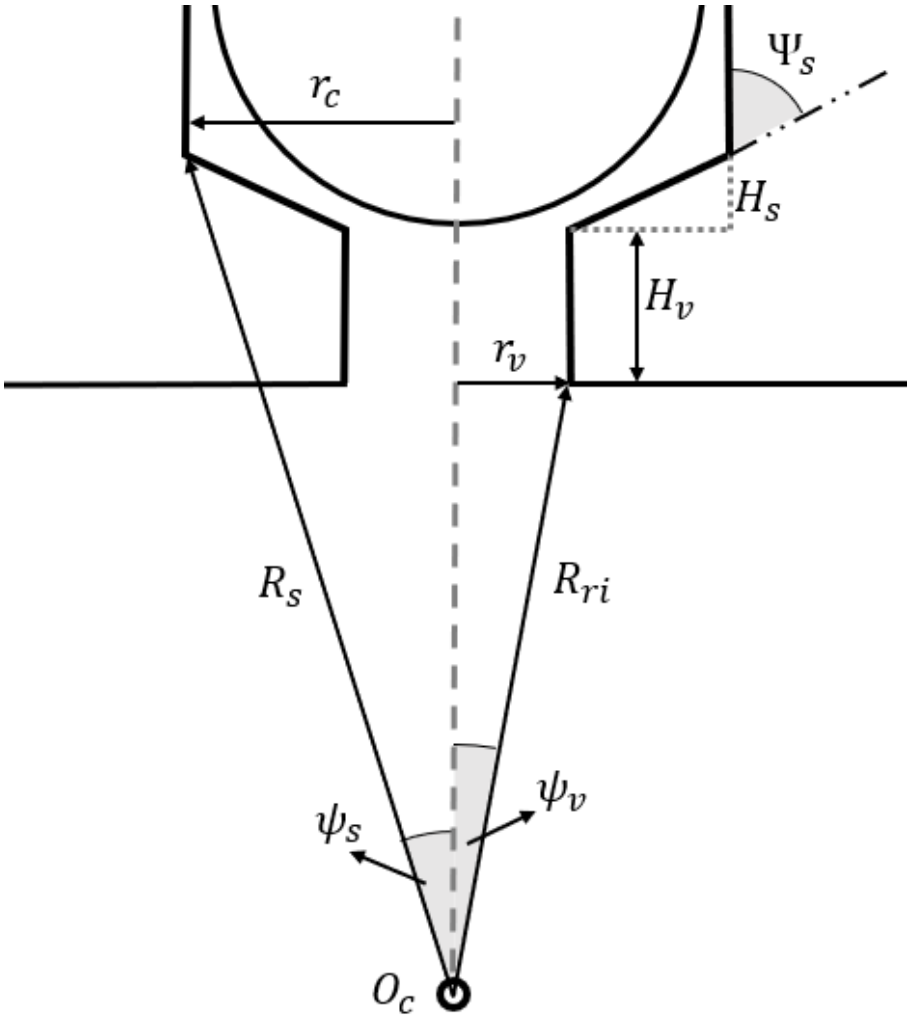

FIGURE 4.14: ANGULAR SPACING CONSTRAINTS

4.2.3.3 Ball-Cylinder Clearance Optimization

The genetic algorithm described in the previous sections optimizes the pintle-rotor interface and the valve timing; it determines the size of the pump, pistons, valve opening, and ensures a valid design. An important assumption needed to make the computation time of the model feasible for an optimization is that the ball piston remains centered in the cylinder, as described in Section 4.2.1, which results in a non-optimal ball-cylinder clearance. Therefore, the clearance needs to be reevaluated using the complete ball-cylinder model that includes the fluid mechanics, heat transfer, dynamics, and kinematics. This is the model described in section 2.2.3. Due to the significant computation time of the dynamic model, a grid search method is used to determine a desirable ball-cylinder clearance. This also avoids the problem of convergence on local minima, as can occur for a gradient optimization method.

4.2.4 Operating Conditions

The operating conditions to evaluate the hydraulic unit in the optimization were selected using drive cycle data for the HECM unit. The data is based on the bucket actuator of a 22 tonne excavator. Three different drive cycles were analyzed to capture the full operating range of the HECM. Work by Siefert identified a maximum flow rate of 185 Lpm and a maximum pressure differential of 7 MPa, which is a corner power just over 20kW. Figure 4.15 is a contour plot of the total energy associated with an HECM operating point. The data within the contour plot was found using eq. (4.77).

$$E_{OP} = P_{OP} \times f_{OP} \tag{4.77}$$

where E_{OP} is the energy of the operating point, P_{OP} is the power of the operating point, and f_{OP} is the frequency the operating point occurs within the drive cycle. The red circles show the four operating points that were selected for the optimization.

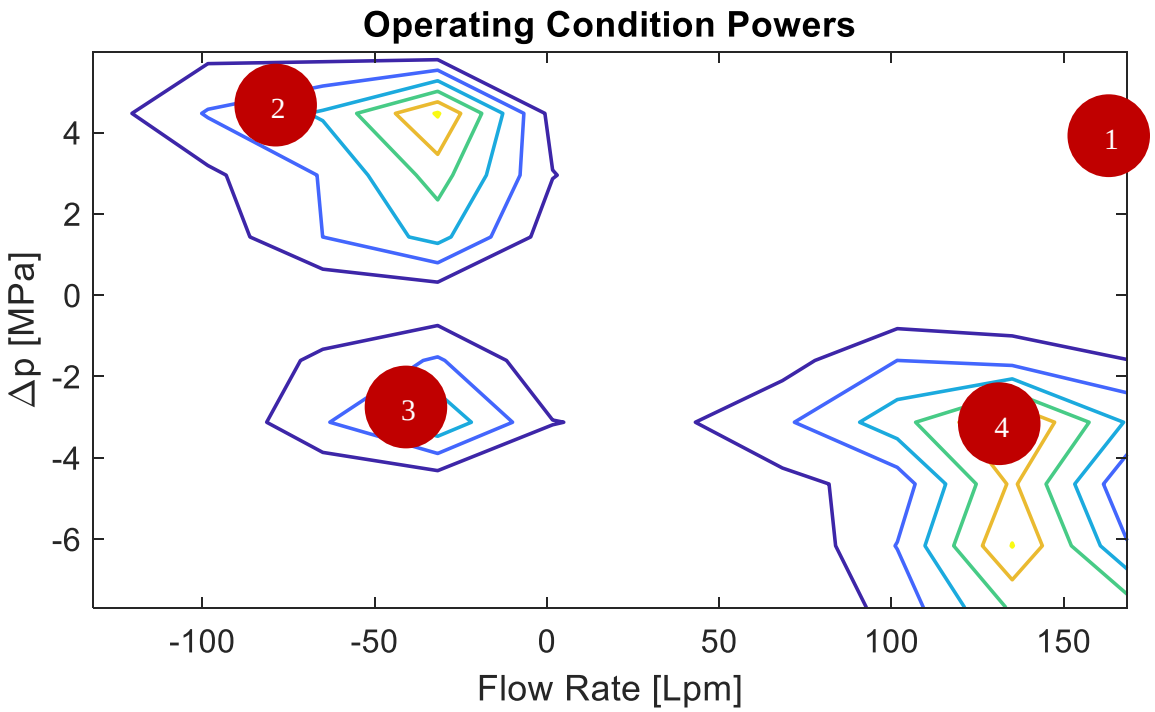

FIGURE 4.15: ENERGY OF OPERATING POINTS

Four operating conditions were selected using this information. However, for computational speed, only two torque values are represented within those four points. Therefore, the pressure differentials had to be selected with care to ensure the operating conditions only had two electric

machine torques. This is done because the electric machine model created by Nishanth simulates the torque using time consuming FEA calculations [8]. The relationship between torque and pressure can be determined for both pumping and motoring operating conditions, eq. (4.78) and eq. (4.79) respectfully.

$$\mathrm{T}_P = \frac{D\Delta p_P}{2\pi\eta_m} \qquad (pumping) \tag{4.78}$$

$$T_M = \frac{D\Delta p_M \eta_m}{2\pi} \qquad (motoring) \tag{4.79}$$

where T is the torque, Δp is the pressure differential, D is the displacement, η_m is the mechanical efficiency, and the subscripts P and M corresponds to pumping and motoring respectively. Equation (4.80) sets the two torques equal and solves for the relationship between pressures.

$$\Delta p_P = \eta_m^2 \Delta p_M \tag{4.80}$$

The operating points presented in Figure 4.15 are laid out in detail in Table 4.2 and the equivalent electric operating conditions are in Table 4.3, for completing the table, an assumption is made of $\eta_m = 0.9$. The hydraulic operating conditions are constant for each design, but the electric machine conditions will change based on the maximum speed that is being studied.

TABLE 4.2: HYDRAULIC OPERATING CONDITIONS

	Weight	$\boldsymbol{\Delta p}$	$\boldsymbol{Q}$
1	50%	$\Delta p_1 = \eta_H^2 \Delta p_2 = 4.05\ MPa$	$Q_{max} = 185\ Lpm$
2	25%	$\Delta p_2 = 5.00 MPa$	$-0.45 Q_{max} = -83.25\ Lpm$
3	15%	$\Delta p_3 = \eta_H^2 \Delta p_4 = -2.43 MPa$	$-0.2 Q_{max} = -37\ Lpm$
4	10%	$\Delta p_4 = -3.00\ MPa$	$0.75 Q_{max} = 138.75\ Lpm$

TABLE 4.3: ELECTRIC OPERATING CONDITIONS

	Weight	**T**	$\boldsymbol{\omega}$
1	50%	$T_1 = \frac{Q_{max}\Delta p_1}{\eta_H \omega_{max}}$	ω_{max}
2	25%	$T_2 = \frac{\eta_H Q_{max}\Delta p_2}{\omega_{max}}$	$-0.45\omega_{max}$
3	15%	$T_3 = \frac{Q_{max}\Delta p_3}{\eta_H \omega_{max}}$	$-0.2\omega_{max}$
4	10%	$T_4 = \frac{\eta_H Q_{max}\Delta p_4}{\omega_{max}}$	$0.75\omega_{max}$

The values within the weight column were selected to ensure that the design would work in all four quadrants. Despite this condition not appearing in Figure 4.15, extra emphasis was placed on running at high speeds because this is the operating condition that is unique to the research project. Also, adding emphasis to the high speed condition should ensure that the ball piston in the final solution does not seize within the cylinder.

4.2.5 Full Optimization Definition

The goal of the optimization is to minimize power loss subject to the parameter bounds. A full optimization definition is given to summarize the information presented throughout the method section.

$$\begin{aligned} &\min \boldsymbol{w}^{\mathrm{T}}\boldsymbol{v} \\ &s.t.\ \boldsymbol{c_{LB}} \leq \boldsymbol{x} \leq \boldsymbol{c_{UB}} \end{aligned} \tag{4.81}$$

where $\boldsymbol{w}$ is a vector of the weights for each operating condition.

$$\boldsymbol{w} = [0.5, 0.25, 0.15, 0.1] \tag{4.82}$$

$\boldsymbol{v}$ is a vector of the power loss for each operating condition and is a function of the optimization parameters, $\boldsymbol{x}$.

$$\boldsymbol{v}(\boldsymbol{x}) = \left[\mathcal{P}_{loss_1}, \mathcal{P}_{loss_2}, \mathcal{P}_{loss_3}, \mathcal{P}_{loss_4}\right] \tag{4.83}$$

The power loss is calculated from eq. (4.84) using the simplified model and the appropriate operating condition from Table 4.2.

$$\mathcal{P}_{loss} = \frac{n_b}{t_{end}} \int_0^{t_{end}} \Big\{ \mathrm{T}_{ball}\omega_{ball} + Q_{ball}\big(p_{cyl} - p_{case}\big) + \frac{1}{n_b}\mathrm{T}_{pintle}\omega_{pump} + \frac{1}{n_b} Q_{pintle}\big(p_{pintle} - p_{case}\big) + \big|Q_A\big(p_A - p_{cyl}\big)\big| + \big|Q_B\big(p_B - p_{cyl}\big)\big| \Big\} dt + \Pi \tag{4.84}$$

where Π is a piece-wise penalty function given by eq. (4.85).

$$\Pi = \begin{cases} 0, & valid\ geometry \\ \infty, & invalid\ geometry \end{cases} \tag{4.85}$$

Section 4.2.3.2 is used to determine the geometry's validity. The variables $\boldsymbol{x}$, $\boldsymbol{c_{LB}}$, and $\boldsymbol{c_{UB}}$ are the optimization parameters, lower bounds, and upper bounds respectively. Their values are given in Table 4.4. This example is a 7 piston design but can be adjusted to a different number of pistons.

TABLE 4.4: OPTIMIZATION PARAMETER CONSTRAINTS

x	Units	Description	c_{LB}	c_{UB}
n_b'	unitless	Number of ball pistons	7	7
$\mathcal{R}_{d/s}'$	unitless	Bore to stroke ratio	2.25	5
h_{b_o}'	microns	Ball-cylinder clearance	5	40
$\phi_{pump_{max}}'$	radians	Maximum pressure angle during rotation	$\frac{3\pi}{180}$	$\frac{10\pi}{180}$
$\mathcal{R}_{R_p}'$	unitless	Ratio for pintle radius	0.25	0.75
H_{p_o}'	microns	Pintle-rotor clearance	5	40
δ_p'	microns	Leakage distance from the ports to the case	200	3000
$\mathcal{R}_{r_v}'$	unitless	Ratio for cylinder valve opening radius	0	1
$\mathcal{R}_{H_v}'$	unitless	Ratio for cylinder valve height	0	1
v_{bdc}'	radians	Primary bottom dead center valve timing angle	$\frac{10\pi}{180}$	$\frac{30\pi}{180}$
s_{bdc}'	radians	Secondary bottom dead center valve timing angle	$-\frac{5\pi}{180}$	$\frac{5\pi}{180}$
v_{tdc}'	radians	Primary top dead center valve timing angle	$\frac{10\pi}{180}$	$\frac{30\pi}{180}$
s_{tdc}'	radians	Secondary top dead center valve timing angle	$-\frac{5\pi}{180}$	$\frac{5\pi}{180}$

4.3 Results and Discussion

The optimization results are presented in two sections, a parameter analysis and a design analysis. The first part looks at the optimal parameter results for the 5 piston, 7 piston, and 9 piston optimizations. Trends are discussed between these optimizations, and how the parameters evolve between generations is analyzed. Then, the preferred design is presented, and a detailed look at the valve timing and ball-cylinder interface is shared.

4.3.1 Genetic Algorithm Parameter Analysis

The genetic algorithm optimization was run with 300 individuals per generations for 100 generations for three separate numbers of pistons: 5,7, and 9. The optimizations were done four separate times for each of the pistons resulting in 12 total optimization runs. Each run took between 10 and 11 hours on the Minnesota supercomputer. Multiple runs were used to improve confidence

that the solution had converged on the global optimal. Another feature that was included in the optimization was that the initial population had to have at least 50 valid designs before continuing to the next generation. This improved the variety within the initial population, again improving confidence in the optimality of the final design. The optimal parameters found for the 5 piston, 7 piston, and 9 piston hydraulic units are given in Table 4.5. The optimization results shown use the simplified ball-cylinder model presented in Section 4.2.1, therefore, the ball-cylinder clearance and total power loss do not consider the ball piston's eccentricity.

TABLE 4.5: GENETIC ALGORITHM OPTIMAL PARAMETERS

Parameter	**5 Piston**	**7 Piston**	**9 Piston**
n_b' [unitless]	5	7	9
$\mathcal{R}_{d/s}'$ [unitless]	2.54	2.49	2.44
h_{b_o}' [microns]	39.99	40.00	39.99
$\phi_{pump_{max}}'$ [radians]	$5.70\pi/180$	$4.99\pi/180$	$4.41\pi/180$
$\mathcal{R}_{R_p}'$ [unitless]	0.45	0.48	0.48
H_{p_o}' [microns]	21.25	20.51	26.04
δ_p' [microns]	869.94	807.05	1155.10
$\mathcal{R}_{r_v}'$ [unitless]	0.79	0.73	0.68
$\mathcal{R}_{H_v}'$ [unitless]	0.17	0.39	0.52
v_{bdc}' [radians]	$23.23\pi/180$	$18.54\pi/180$	$14.42\pi/180$
s_{bdc}' [radians]	$-0.02\pi/180$	$-0.65\pi/180$	$0.12\pi/180$
v_{tdc}' [radians]	$21.85\pi/180$	$18.30\pi/180$	$14.28\pi/180$
s_{tdc}' [radians]	$0.34\pi/180$	$-0.44\pi/180$	$0.11\pi/180$
Valve Timing Losses [Watts]	500.35	381.07	386.86
Ball-Cylinder Losses [Watts]	1177.59	1528.73	1973.17
Pintle-Rotor Losses [Watts]	313.18	327.37	351.04
Total Power Loss [Watts]	1991.12	2237.17	2711.07

The most important trend found in Table 4.5 is that the power loss decreases with a decreasing number of pistons. This is expected because the ball-cylinder interface accounts for the largest portion of the losses as seen in Table 4.5. Therefore, for a given displacement, decreasing the number of pistons typically decreases the losses. Another physical way to rationalize this reduction in losses is to consider that fewer pistons requires larger pistons to achieve the same flow rate. Increasing the radius of ball piston increases their cross-sectional area when compared to their circumference. This ratio of area to perimeter is important because power output scales with the cross-sectional area and losses scale with the circumference. Thus, increasing the ratio increases the power output per loss. Also, from Table 4.5, the pintle-rotor losses increase with the number of pistons. This happens because the pintle radius increases to fit the valve openings, which also increases torque and leakage losses.

The next obvious result is that the ball-cylinder clearance for all three designs converges to 40 microns of radial clearance. This is the upper bound placed on the parameter. The upper bound was not increased because the simplified model was used at this stage, and it was known from preliminary studies with the complete model that the ball-cylinder interface would be a major contributor to losses within the pump. Therefore, the upper bound was selected so that the interface contributed about 60 to 70 percent of the losses at maximum speed even in the simplified case. Having a similar magnitude of losses at the interface forces the optimization to size the unit correctly even when using the simplified model. This allows the ball-cylinder clearance to be optimized after the genetic algorithm has finished without losing confidence in the near-optimality of the design parameters.

A few other trends are that the bore to stroke ratio and maximum pressure angle decrease as the number of pistons increases. The ball piston diameter decreases with decreasing bore to stroke ratio, making it easier to package the larger number of pistons. Decreasing the maximum pressure angle increases the radius of the cam and overall size of the hydraulic unit, eq. (4.86). The increased radial size is another compensation to fit the extra pistons.

$$R_{cam} = \frac{e_{pump}}{\sin\left(\phi_{pump_{max}}\right)} + r_b \tag{4.86}$$

The height of the valve opening, $\mathcal{R}'_{H_v}$, which determines the distance between the piston seat and the pintle, is another variable that changes to account for the increase in number of pistons. As the number of pistons grows, it becomes more difficult to fit features near the inside radius of the rotor block and the valve height ratio increases to account for this.

These trends in optimization results show that with fewer ball pistons the radial size and power loss of the hydraulic unit decreases. The primary advantage of hydraulic units with more pistons is the reduction of flow ripple, but this was not an objective in this optimization. Therefore, the rest of the chapter focuses on the optimal 5 piston design because reducing power loss is the primary goal of the HECM hydraulic unit.

4.3.1.1 Parameter Evolution

The parameter evolution of the optimal 5 piston design (referred to as optimal design from this point forward) can provide insights into how the genetic algorithm works and how the design was selected. Figure 4.16, Figure 4.17, and Figure 4.18 show the evolution of individual parameters versus total power loss across generations 1, 10, 30, 65, and 100. The figures limit the x-axis (power loss) from the minimum power loss to three times the minimum power loss. This is done so differences near the minimum power loss are clearly visible. Also, the black horizontal lines on each figure are the bounds for each parameter. The ball-cylinder clearance is the only value that appears constrained by the choice of limits, which was done intentionally as mentioned previously.

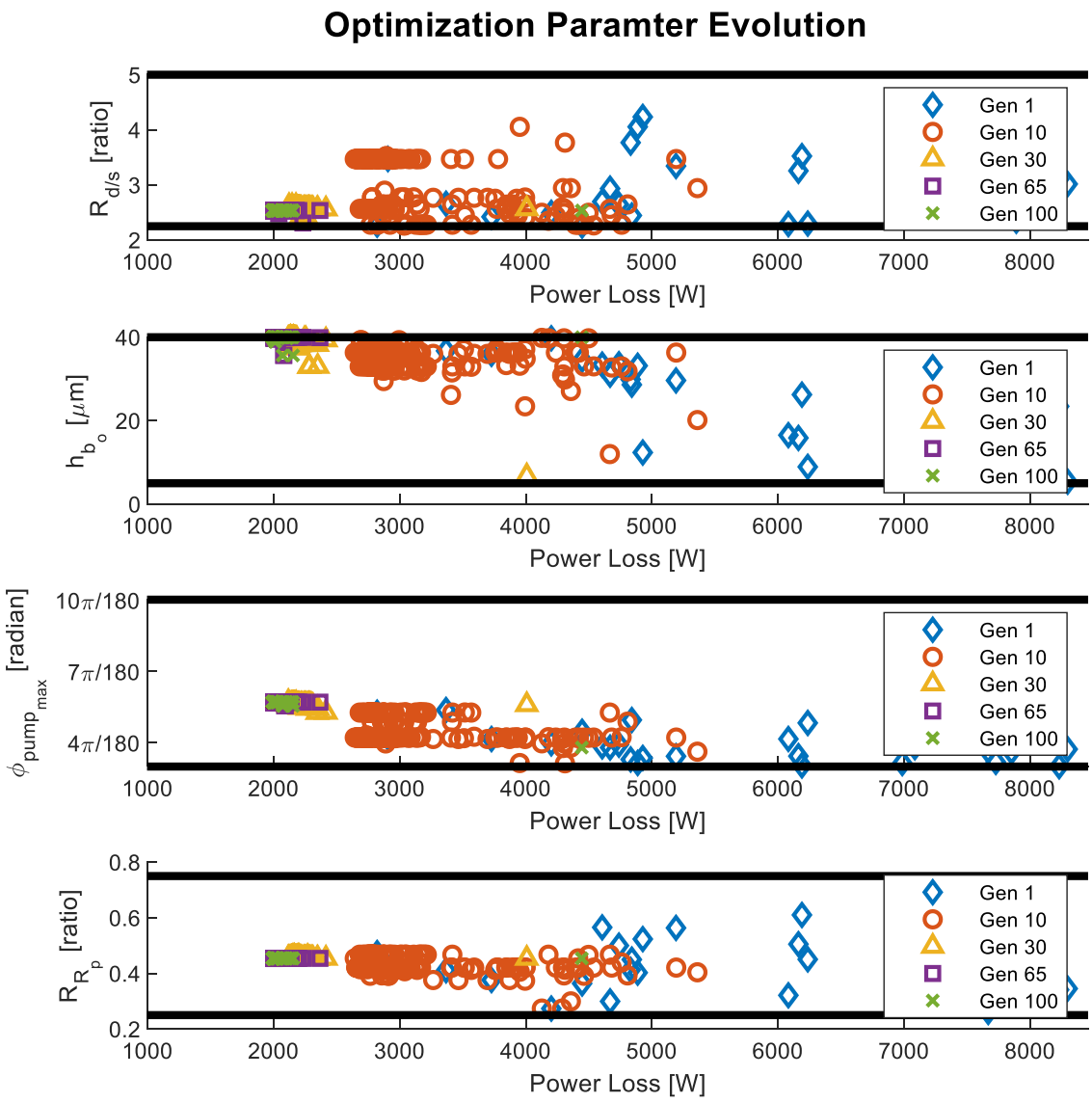

FIGURE 4.16: GENERATIONAL EVOLUTION FOR OPTIMAL DESIGN PARAMETERS (1)

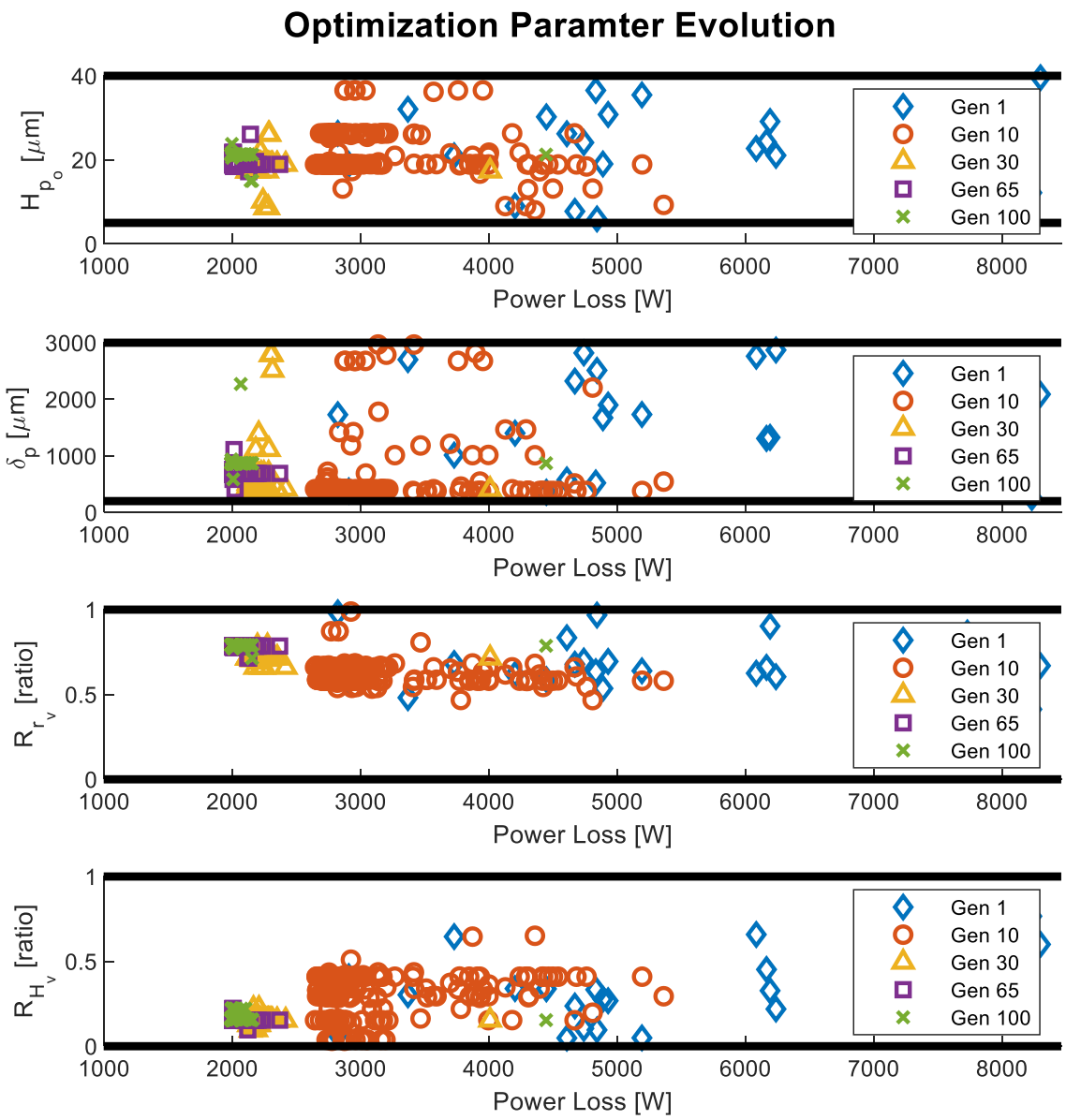

FIGURE 4.17: GENERATIONAL EVOLUTION FOR OPTIMAL DESIGN PARAMETERS (2)

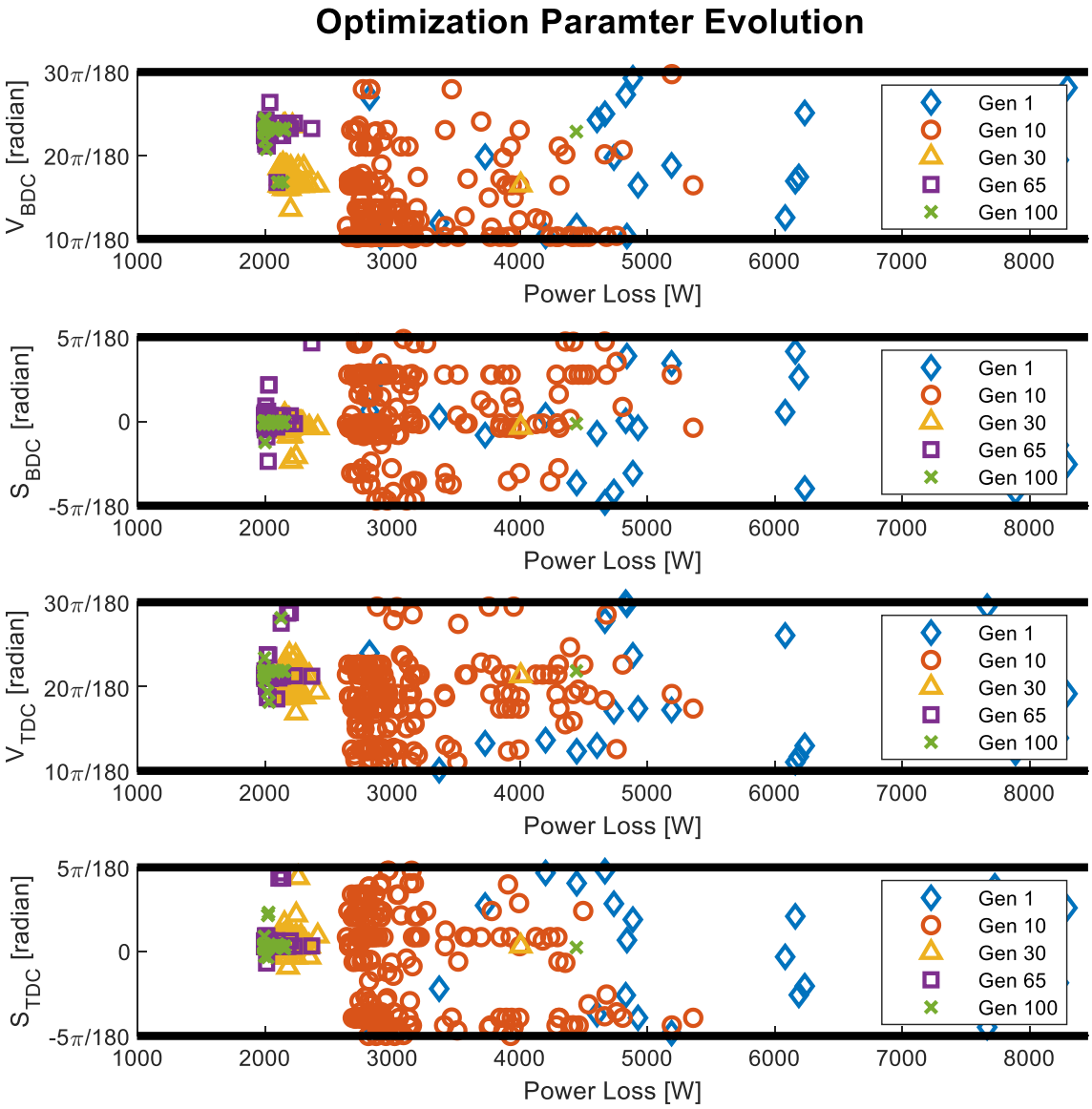

FIGURE 4.18: GENERATIONAL EVOLUTION FOR OPTIMAL DESIGN PARAMETERS (3)

Analyzing the figures provides a few key insights into the optimization and the parameters themselves. First, consider variables like maximum pressure angle, $\phi'_{pump_{max}}$, and valve radius, $\mathcal{R}'_{r_v}$, where very clear limits form. For example, $\phi'_{pump_{max}}$ never exceeds roughly $6\pi/180$ even within the first generation. This implies that any design outside of this range either was invalid, or the losses increased sharply as the parameter neared the limit. It is expected that $\phi'_{pump_{max}}$ has strict limits because generating valid design outside of this region is extremely difficult. In contrast,

the lower limit for the valve radius, $\mathcal{R}'_{r_v}$ is because throttling losses increase rapidly as the valve size decreases, pushing small values of the valve radius outside of the x-axis (power loss) limits.

Another feature is the relationship between different parameters. Good examples of this are: the bore-to-stroke ratio and maximum pressure angle, $\mathcal{R}'_{d/s}$ and $\phi'_{pump_{max}}$, pintle clearance and pintle leakage length, H_{p_o} and δ_p, and the valve timings. In the early generations, such as generation 10, high density horizontal lines form in the figures indicating a preferred parameter value. These dense lines of individual designs form for both coupled parameters because the parameter combination is a low power loss state. As the generations continue to increase, the optimization selects one of these parameter combinations as a preferred optimal solution eventually forcing all the individual designs to one parameter value by the final generation.

The final insight gained from the parameter evolution figures is the rate of convergence for different parameters. Several of the parameters appear converged by the 30th generation while others are not converged by generation 65 or even 100. The parameters that appear nearly converged by generation 30 are: $\mathcal{R}'_{d/s}$, $\phi'_{pump_{max}}$, h'_{p_o}, $\mathcal{R}'_{R_p}$, $\mathcal{R}'_{r_v}$, and $\mathcal{R}'_{H_v}$. The values that do not seem converge even by generation 100 are the valve timing parameters, v'_{BDC}, s'_{BDC}, v'_{TDC}, and s'_{TDC}. The pintle clearance and length appear to converge sometime between generation 30 and 65.

There are several reasons why some parameters converge faster than others. If the power loss is extremely sensitive to a parameter, then it is easy for the optimization to converge to an optimal value. In the case of the ball-cylinder clearance, the optimal was also at a boundary simplifying the convergence process. In contrast, the valve timing may have several good designs but no clear optimal. The optimization is left with solutions that do not dominate each other and reducing the power loss becomes a slow process of many small advances.

Another reason for the differing convergence rates is the use of ratios. Every ratio converged before the 30th generation. Ratios allow two geometric values to be coupled and reduced to a single parameter. Also, the power loss is typically strongly related to the ratio instead of the individual values, the bore-to-stroke ratio is a good example of this. The convergence rate for the pintle clearance and length likely would have been faster if one of the values become a ratio instead of two decoupled geometric parameters.

4.3.2 Detailed Analysis of the Selected Optimal Design

This section analyzes the optimized 5 piston design in two parts. First, the dimensions for the hydraulic unit and the valve timing angles are presented. The impact of the valve timing on the

pressure dynamics and the throttling losses is shown for each operating condition. Next, the ball-cylinder clearance optimization is presented. The kinematics and heat transfer at the interface are presented, and the shear and leakage trends are examined.

4.3.2.1 Optimized Valve Timing

The optimal five-piston solution is presented in Figure 4.19, which shows all dimensions to scale except for the ball-cylinder and pintle-rotor clearances. The constraints within the optimization ensured a valid and well packaged design, with the outside diameter of the 20kW machine being approximately 100 millimeters. Even though the optimization did not consider minimizing size as an objective, the packaging still became as small as possible given the constraints. This makes sense because the objective was to minimize losses and reducing the radial size reduces the torque loss. Another takeaway from the design is that the valve timing is nearly symmetric.

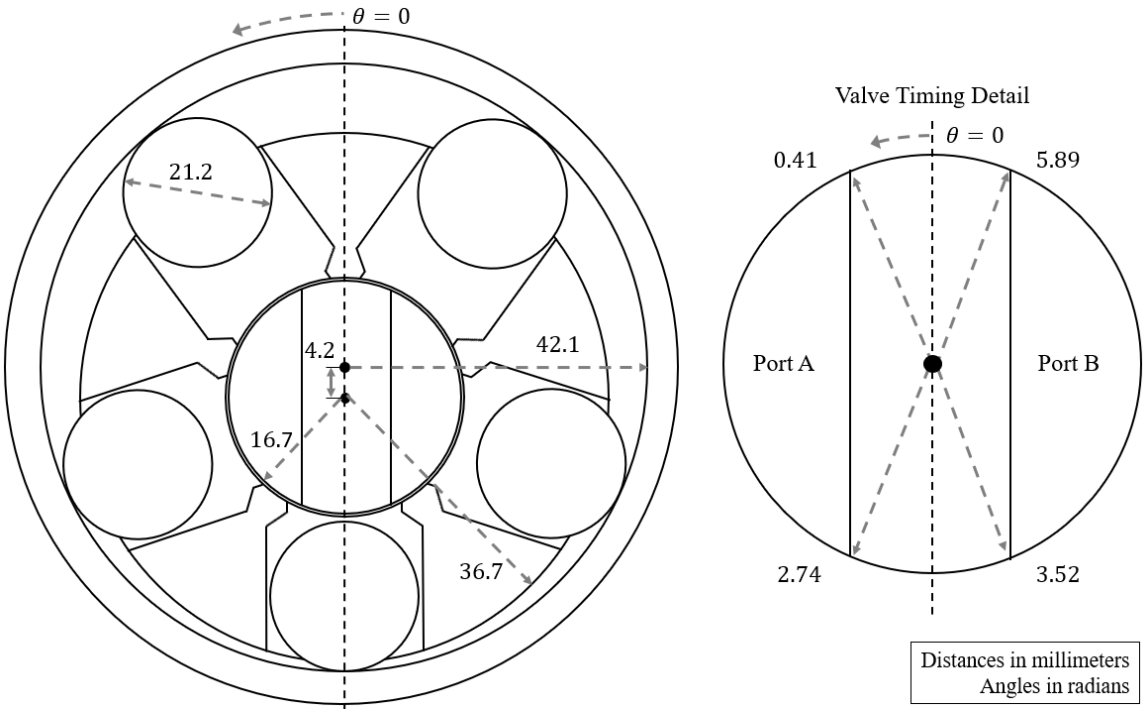

FIGURE 4.19: OPTIMAL DESIGN DIMENSIONS AND VALVE TIMING

It is understood that the optimal valve timing of a pump or motor varies for different operating conditions [59]. Four operating conditions, one in each operating quadrant, were used in the optimization to help balance the different tradeoffs and create a valve timing that worked well

everywhere. The area profile for the valve timing when rotating in the counterclockwise (positive) direction is shown in Figure 4.20. Notice at bottom dead center (BDC) and top dead center (TDC) there is a short period where the cylinder is connected to port A and port B, this is known as cross porting[9]. The area profile opens gradually, but the maximum area is relatively large compared to the peak flow rate into and out of the cylinder. At maximum operation speed, there is only 90 kPa[10] of pressure drop.

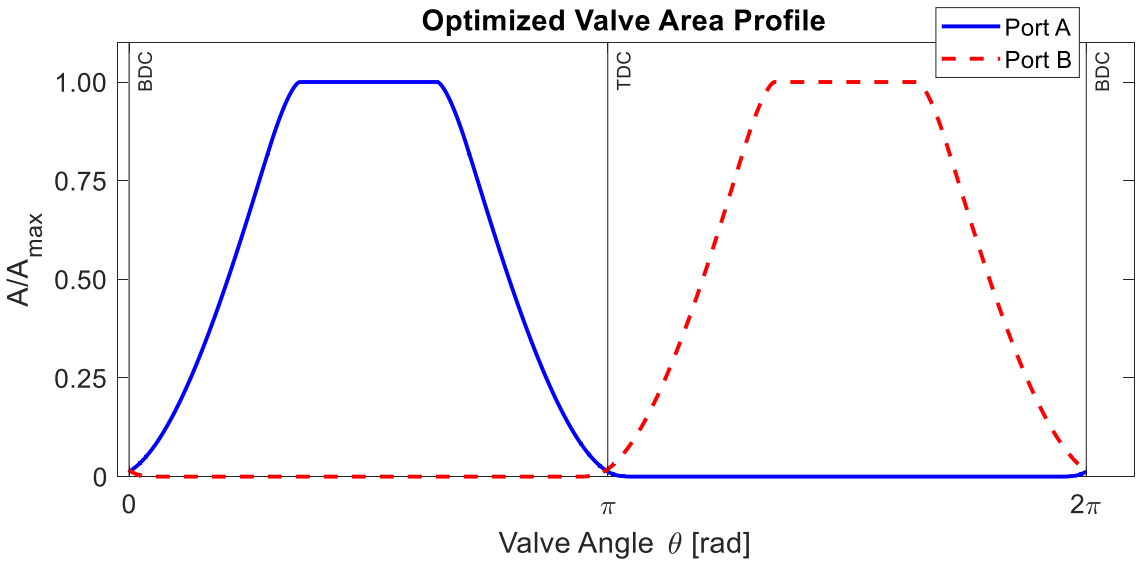

FIGURE 4.20: VALVE TIMING AREA PROFILE

The valve timing directly impacts the pressure dynamics, which are shown in Figure 4.21, for each of the operating conditions. There are two pressure traces shown in the figure. The cylinder pressure is the pressure at the bottom of the ball piston, and the transition pressure is the pressure at the inside radius of the rotor block. The transition pressure is the value used when calculating the flow transitioning between the ports and the cylinder. There is a pressure gradient created by the rotating cylinder block that increases with radius that needs to be considered when calculating flow rates into and out of the cylinders. The small radial size limits the centripetal effects, thus the

[9] Cross porting is considered a bad design practice in typical hydraulic units because high pressure fluid can easily flow to the low pressure side resulting in a power loss. However, as operating speed increases, the power lost due to cross porting becomes less significant.

[10] 90 kPa $= \Delta p = \rho/2 \cdot \left(\pi r_b^2 e_{pump} \omega_{pump} / C_d A_{max}\right)^2$

deviation between the two traces is clear only in quadrants 1 and 4 where the rotation speed is higher. Each plot starts at bottom dead center, which means the first half of the simulation is when the unit is discharging fluid from the cylinder. When pumping, quadrants 1 and 3, the discharged fluid pressure is approximately equal to the high pressure port and when motoring, quadrants 2 and 4, the discharged fluid is equal to the low pressure port.

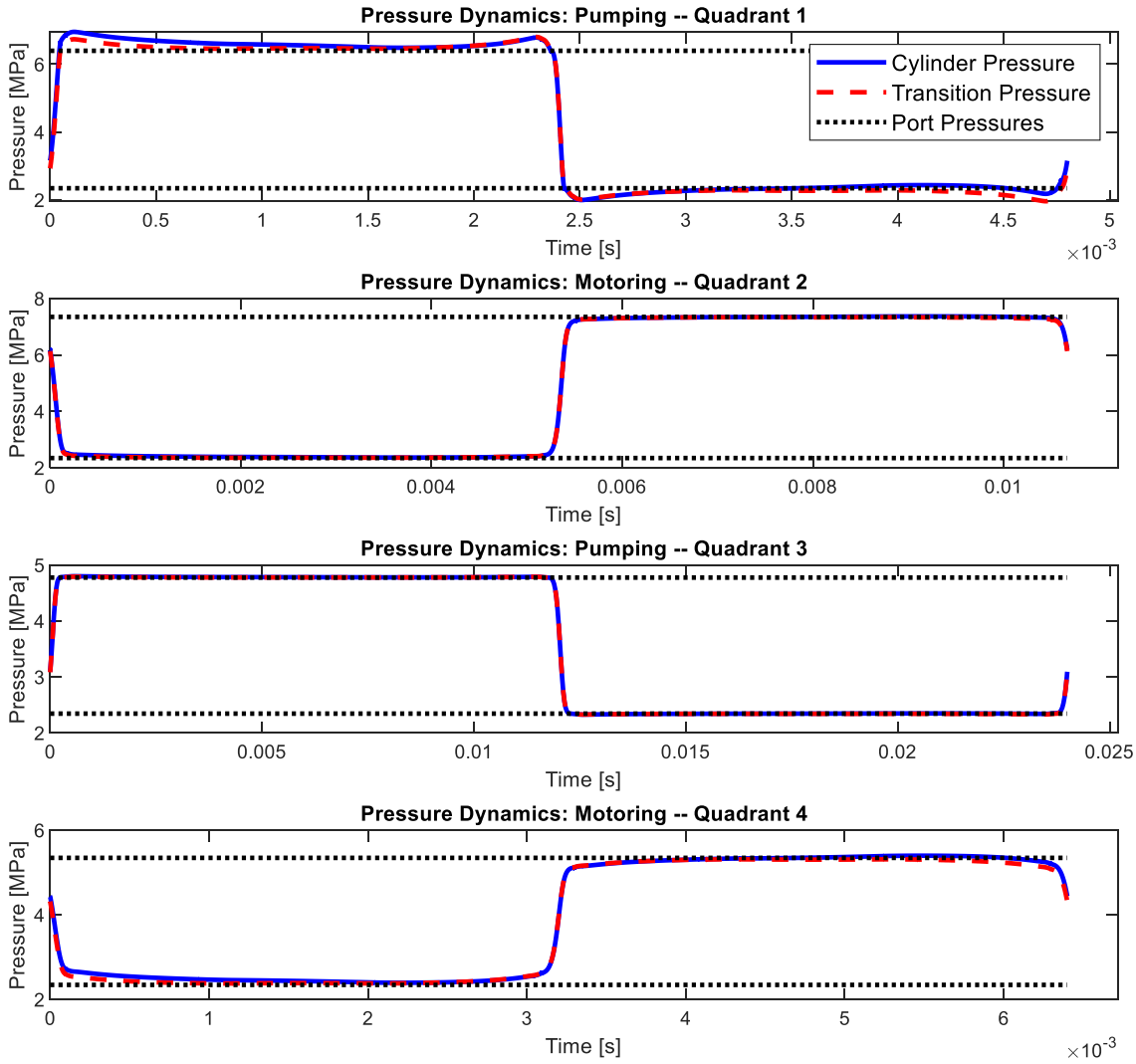

FIGURE 4.21: OPTIMAL DESIGN PRESSURE DYNAMICS

Overall, the pressure dynamics in Figure 4.21 look well behaved with minimal pressure spikes. However, to determine the quality of the valve timing, the throttling losses need to be considered. The throttling losses for both the A and B port are presented for the four operating conditions in Figure 4.22. For each operating condition, there is a spike in losses at bottom dead center (start and

end of cycle) and top dead center (middle of cycle) because the valve is transitioning between the ports and there is cross porting in this valve timing design. The next feature to notice in Figure 4.22 is the relatively constant magnitude of throttling loss during much of the cycle for operating conditions 1 and 4. These are the two highest speed operating conditions and require the greatest flow rate across the valve. This increased flow rate creates a greater pressure drop and an overall less efficient valve timing. Increasing the valve size would reduce the resistance and improve the throttling losses but doing so requires the unit to grow radially. Therefore, the optimization has struck a balance between the valve size and the overall size of the unit.

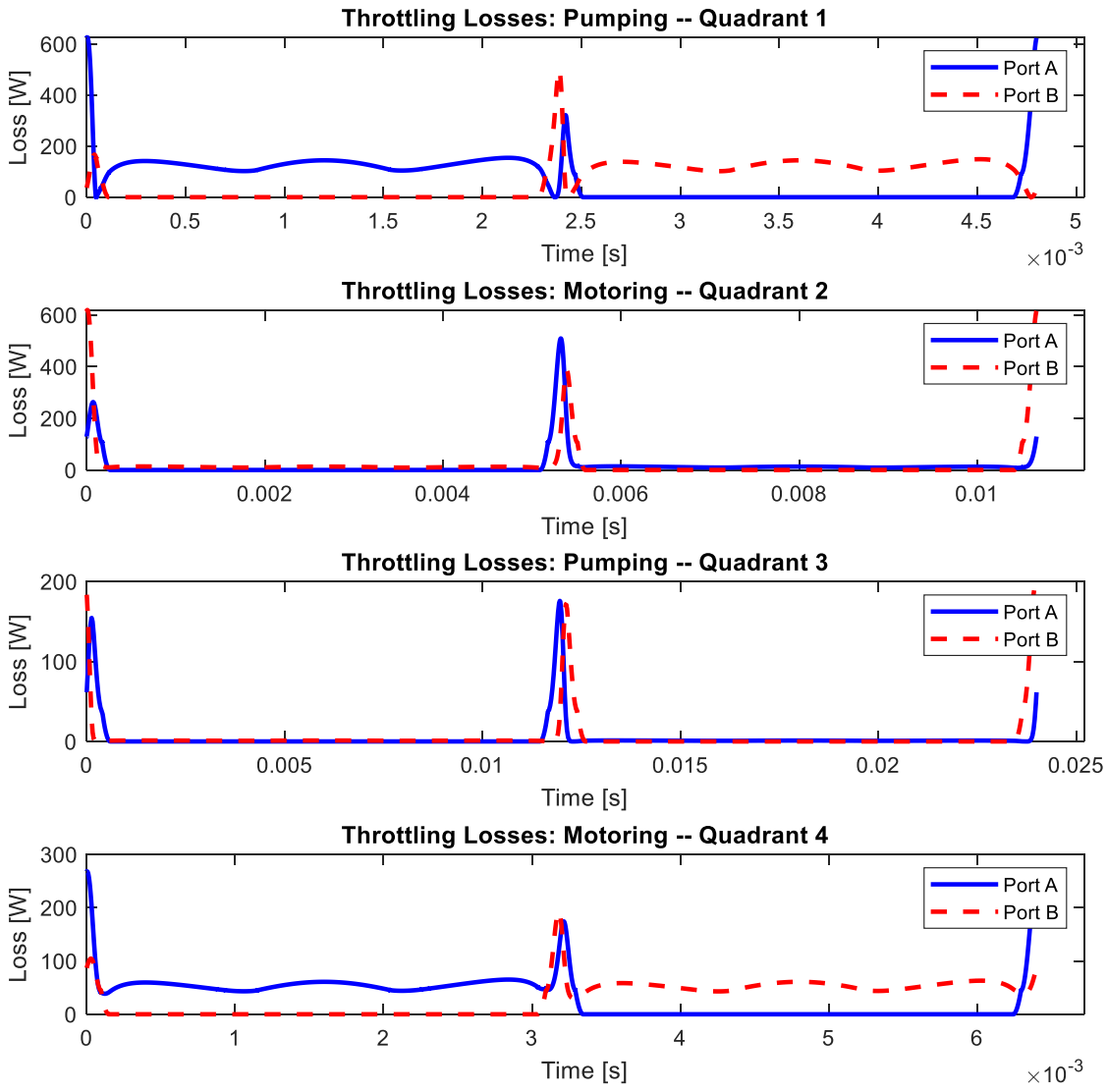

FIGURE 4.22: OPTIMAL DESIGN THROTTLING LOSSES

4.3.2.2 Optimized Ball-Cylinder Interface

The optimization results presented thus far have considered the simplified ball cylinder model, but to be accurate, the more complicated dynamic model needs to be run. Figure 4.23 shows the normalized eccentricity of the ball piston for each operating condition for two different radial clearances, 20 and 100 microns. Note that values of 1 and -1 correspond to the ball piston moving next to the cylinder wall in the positive and negative directions respectively. The ball piston can move freely within the cylinder and this is true for each operating condition. The lag in response of the 100 micron ball position is because it has a greater distance to travel to reach the wall.

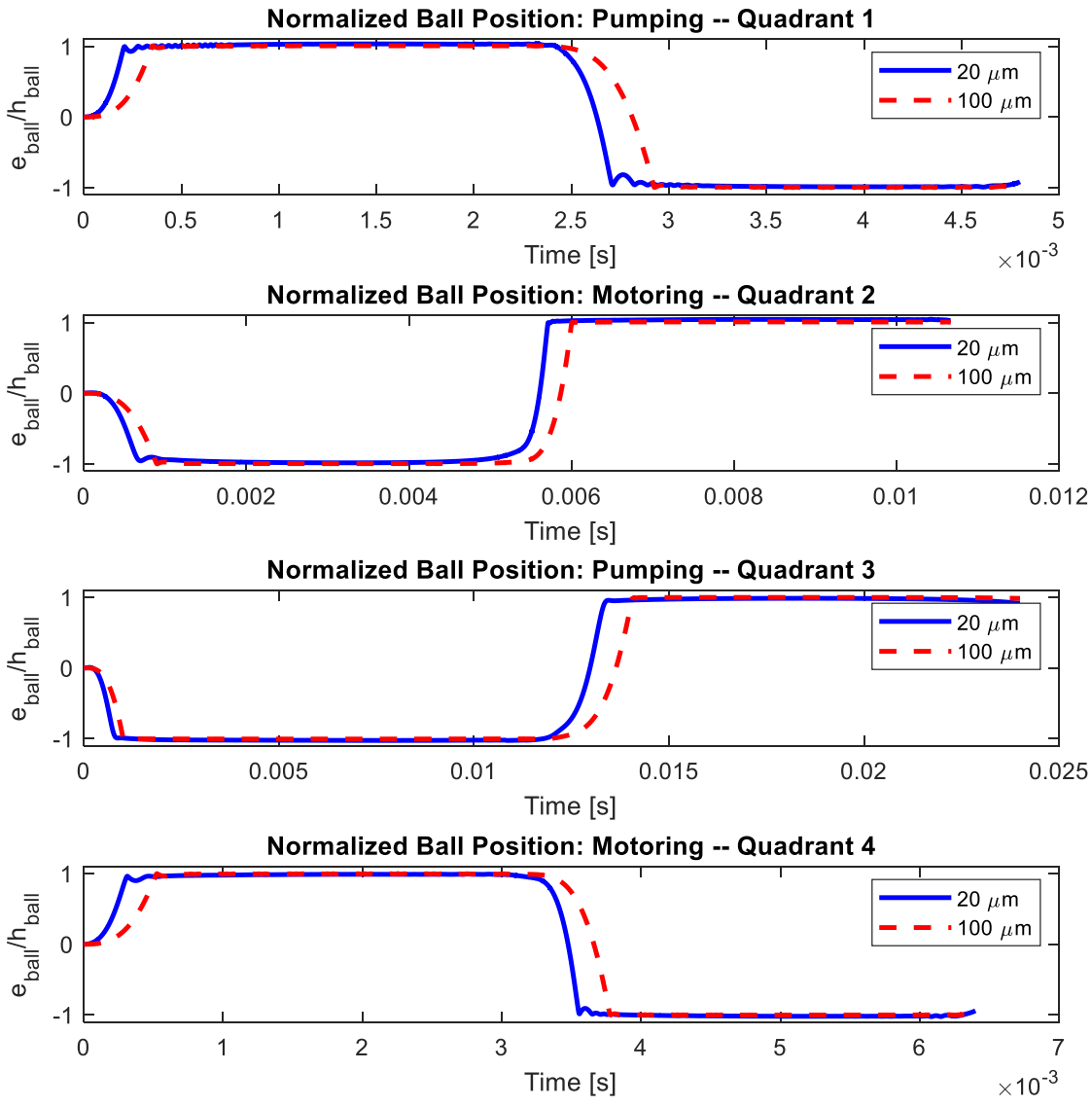

FIGURE 4.23: NORMALIZED BALL ECCENTRICITY DURING OPERATION

Even with the normalized ball positions being nearly identical, the amount of radial clearance should make a difference for the thermal conditions at the ball. For example, it is true that the 20 micron radial clearance will have about 40 microns clearance on the side away from the wall and the 100 micron radial clearance will have about 200 microns of clearance. This creates a large difference in fluid volume that should cause temperature differences around the ball. The region around the ball piston is broken into eight control volumes as shown in Figure 4.24. Note that the figure exaggerates the clearance between the cylinder wall and the ball piston. A positive ball eccentricity reduces the size of control volumes 1 and 8, while a negative eccentricity reduces control volumes 4 and 5. Due to the geometric symmetry, control volumes 1 and 8 have similar temperatures and the same is true for control volumes 2 and 7, 3 and 6, and 4 and 5.

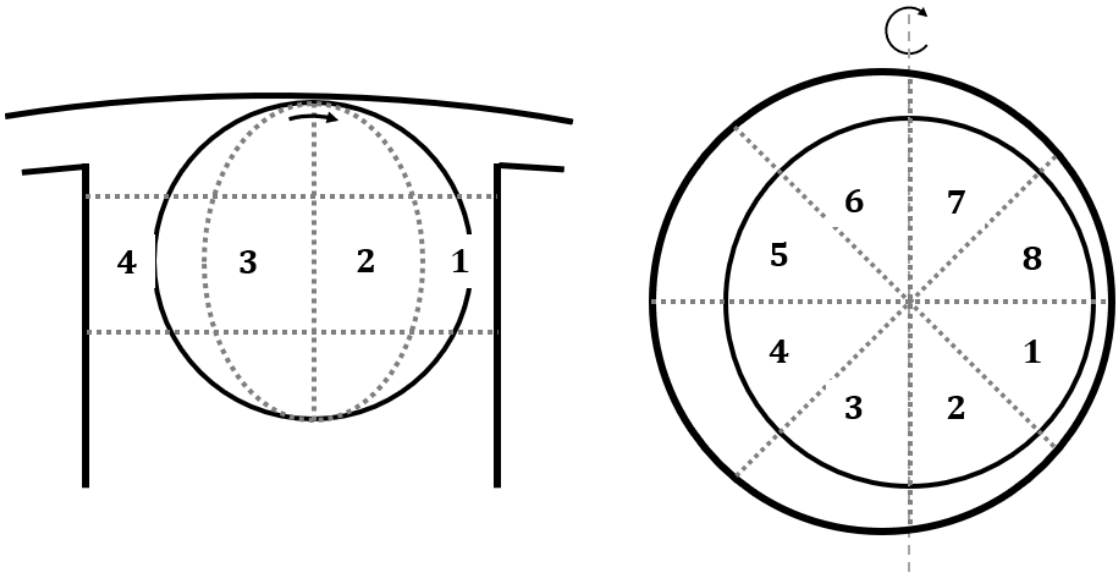

FIGURE 4.24: HEAT TRANSFER CONTROL VOLUMES AT BALL-CYLINDER INTERFACE

The temperature in each of these regions is calculated using the heat transfer model presented in section 2.2.3.5. It is known from Figure 4.23 that during HECM operation, the ball piston moves between positive and negative eccentricity, which means control volumes will shrink and grow based on the ball position. The shearing adds heat to the oil increasing the temperature while leakage carries energy out of the control volume in the mass. Figure 4.25 shows the dynamic temperature within control volumes 1 and 4 for each operating condition and two radial clearances, 20 and 100 microns. These control volumes were selected because their temperatures vary the most

and impact the fluid viscosity at the points of minimal clearance. As expected, the temperature increases when the eccentricity of the ball piston reduces the fluid mass in the control volume. For each operating condition, the temperature for the 100 micron radial clearance lags the 20 micron one and never reaches the same peak values. This is caused by the larger thermal mass and because the ball reaches the wall sooner in the 20 micron design. Figure 4.25 shows that smaller radial clearances tend to have higher fluid temperatures.

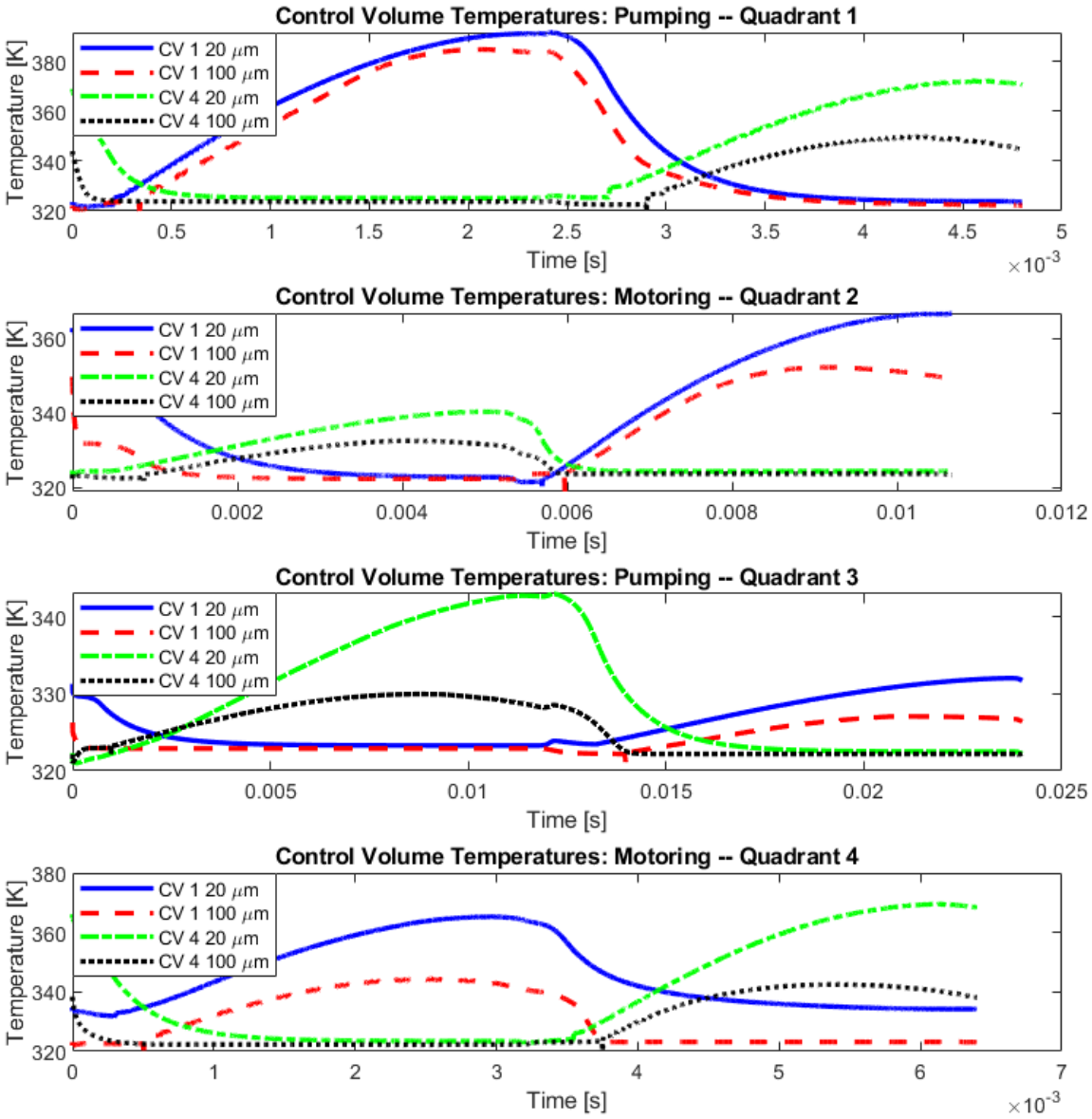

FIGURE 4.25: CONTROL VOLUME TEMPERATURE AROUND BALL PISTON

Now that the kinematics and thermal conditions of the ball piston are known, the shearing and leakage losses can be examined in detail. A grid search of radial clearances from 10 microns to 100 microns was performed to analyze these trends. Figure 4.26 highlights the shearing losses and the complexity of the ball-cylinder interface due to the slightly different trends appearing for each of the different operating conditions. The quadrant 1 operating condition has the highest torque loss, which is expected since the operating speed is the highest. The loss increases with clearance which is contrary to the general expectation. In quadrant 2 the losses also increase with clearance. Quadrant 3 has the slowest operating speed and therefore the least torque losses, but the torque loss does appear to reach a minimum around 70 microns. Quadrant 4 is the only operating condition where the torque loss clearly decreases with increasing clearance. This results in the losses for quadrants 2 and 4 at 100 microns being approximately equal despite quadrant 4's operating speed being over 65 percent faster. The relatively constant torque with increasing clearance is a result of the ball nearing the wall and the fluid mechanics entering the elastohydrodynamic lubrication (EHL) regime, which is characterized by localized pressure spikes which create localized deformations and viscosity increases. The combination of the ball moving close to the walls, the ball rotation creating high relative velocity, and the increased fluid viscosity of the EHL regime all tend to increase the shearing losses and cannot be avoided by increasing the clearance.

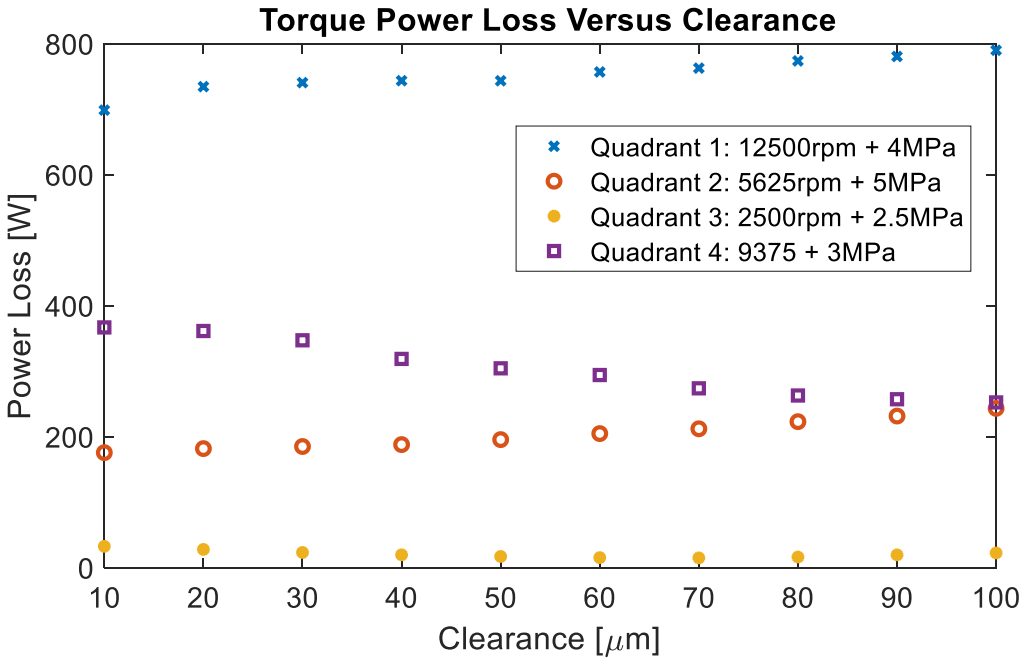

FIGURE 4.26: BALL-CYLINDER CLEARANCE AND TORQUE POWER LOSS

Figure 4.27 shows the torque acting on the ball piston throughout the cycle. The plots show dynamics that arise after the ball piston reaches the cylinder wall. This behavior has physical origins created by the ball rebounding off the cylinder wall with minimal damping due to the low fluid viscosity. The plots also demonstrate the complicated nature of the ball-cylinder interface. The operating condition impacts the trace and magnitude for the torque. The clearance also impacts the torque, but because of the interconnected nature of the fluid mechanics, kinematics, and heat transfer a relatively consistent magnitude of torque is maintained as clearance changes.

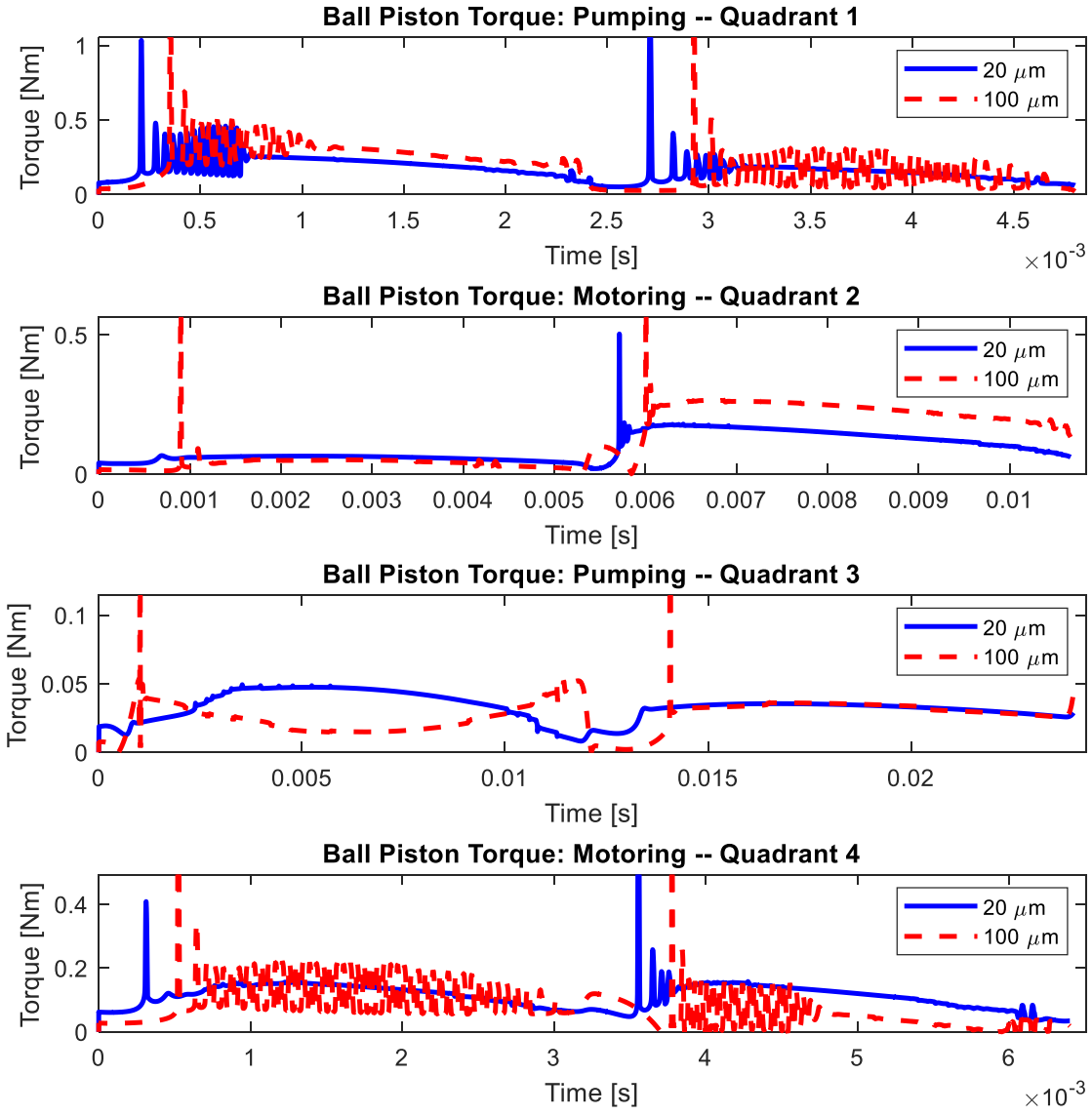

FIGURE 4.27: BALL PISTON TORQUE DURING OPERATION

The second component of the losses at the ball-cylinder interface is the leakage. Figure 4.28 shows how the leakage power loss changes for each operating condition with increasing clearance. As expected, increasing the clearance rapidly increases the leakage power loss at the interface. An increase in operating pressure also increases the losses.

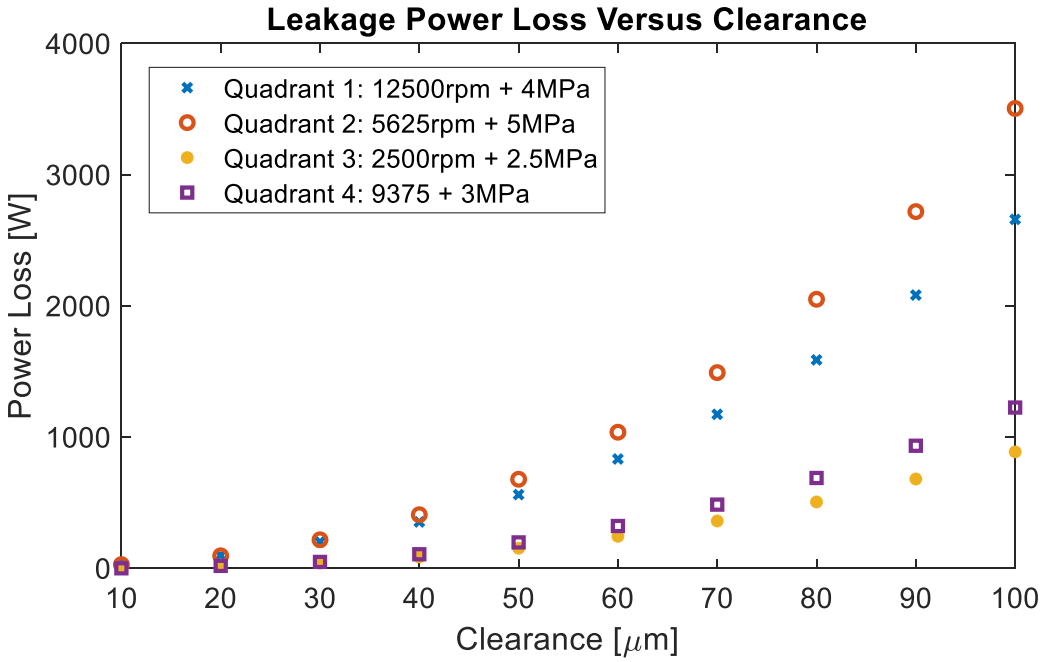

FIGURE 4.28: BALL-CYLINDER CLEARANCE AND LEAKAGE POWER LOSS

The leakage trends are much easier to characterize then the torque ones, but the kinematics do create important behavior that should be analyzed in more detail. The interesting results are the differences between pumping and motoring. To study this the same operating speed and pressure differential were simulated for a pumping and motoring case. These results are presented in Figure 4.29. The figure shows the leakage from the cylinder to case, the pressure in the cylinder, and the power loss at each instant from this leakage. The leakage for the pump operating condition varies greatly even becoming negative during the suction portion of the stroke. A negative leakage is when the net flow is from the case to the cylinder. For motoring the leakage is more consistent, but it does decrease during the latter half of the simulation. This is counterintuitive because the cylinder pressure increases during this portion of the stroke and an increase in pressure should drive more flow to the case. The last figure shows the power loss, and for these operating conditions, the overall energy loss is greater when pumping compared to the motoring.

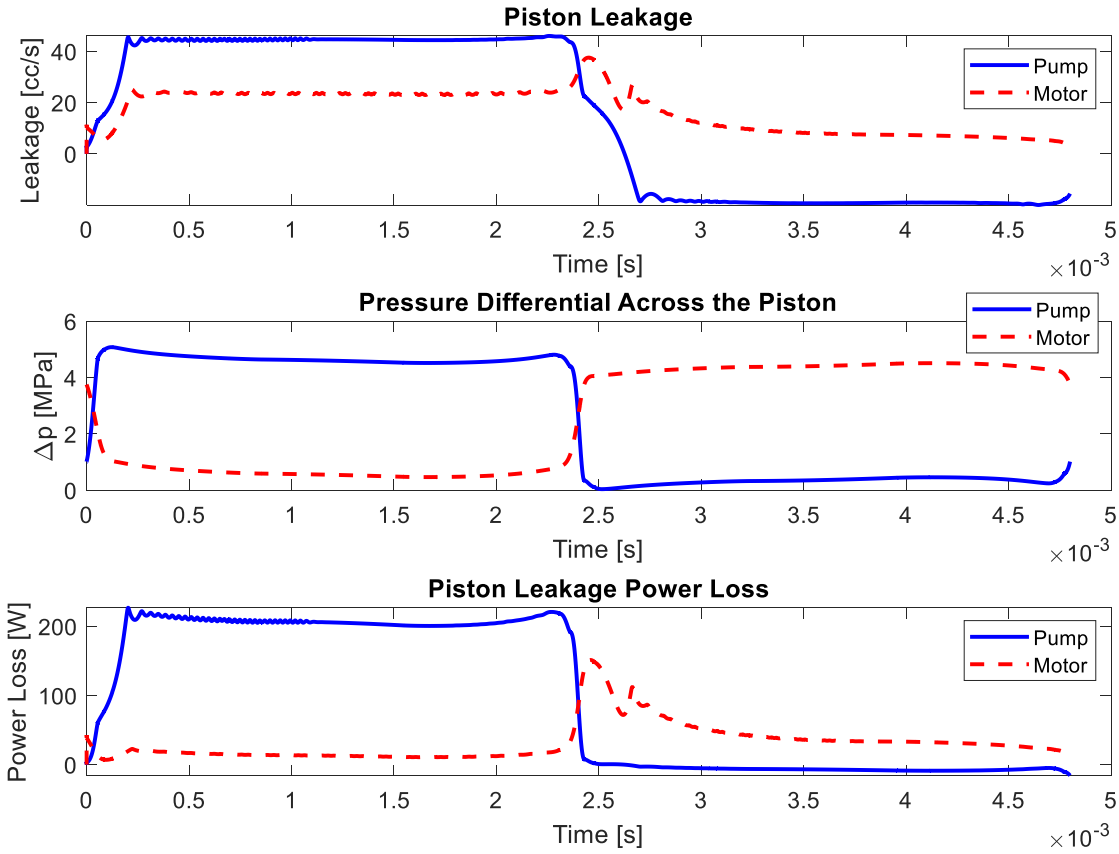

FIGURE 4.29: PUMPING AND MOTORING LEAKAGE COMPARISON

The leakage at the ball cylinder interface is caused by two physical phenomena. The first is the pressure driven flow, which is the primary driver of leakage in most hydraulic pumps and motors. The second is the Couette driven flow created by the ball piston rotation. In a cylindrical piston pump, especially at low speed, the pressure driven flow greatly exceeds the velocity driven flow. The ball piston rotation and high speeds of the HECM make both flow profiles significant contributors to the leakage.

The fundamental difference between the pumping and motoring operating conditions is the ball eccentricity when the cylinder pressure is high and the impact that has on the flow profiles. The physical situation is shown in Figure 4.30. When pumping, the ball eccentricity at high pressure is such that the clearance is greatest when the pressure driven flow and velocity driven flow act in the same direction. This drastically increases the leakage going to the case because the clearance is roughly twice the size of the nominal radial clearance. In contrast, the ball eccentricity during motoring forces the pressure driven flow and velocity driven flow to act in opposite directions when the pressure is highest. During the second half of the pumping cycle the leakage becomes negative

because the ball moves to a position where the pressure driven flow and velocity driven flow are in opposite directions, but the low pressure results in the velocity profile creating net flow into the cylinder.

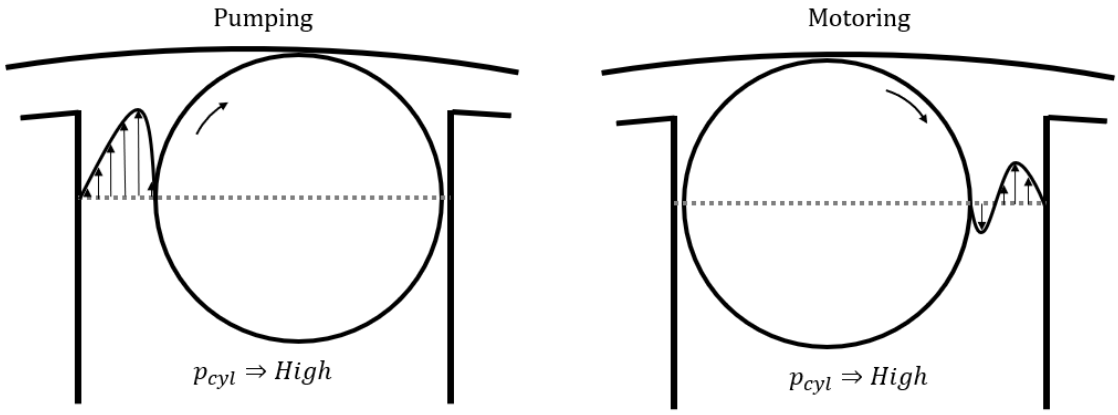

FIGURE 4.30: FLOW PROFILES DURING PUMPING AND MOTORING OPERATION

Figure 4.31 shows the total losses for each operating condition as the clearance is increased by combining the shearing and leakage power losses from Figure 4.26 and Figure 4.28 respectfully. The strictly increasing behavior shown in Figure 4.31 is not typical of hydraulic clearance optimizations. The losses increase as the clearance grows because the leakage increases while the shearing stays relatively constant; therefore, a small radial clearance is optimal. However, it is known that at a small enough clearance, the model assumptions break down and the torque will increase to the point where the ball piston seizes within the cylinder. When the ball stops spinning, excessive wear occurs, and the life of the unit is reduced. The simulation at a radial clearance of 10 microns found that the temperature became exceedingly high, which reduces the viscosity. The low viscosity reduces the load carrying capability of the fluid and shrinks the minimum distance between the ball and the cylinder wall. This is when an elastohydrodynamic lubrication regime will start to transition to a mixed regime and metal to metal contact can occur. There is also limited reduction in power loss as the clearance becomes smaller. For these reasons, 20 microns was selected as the lower bound for the radial clearance.

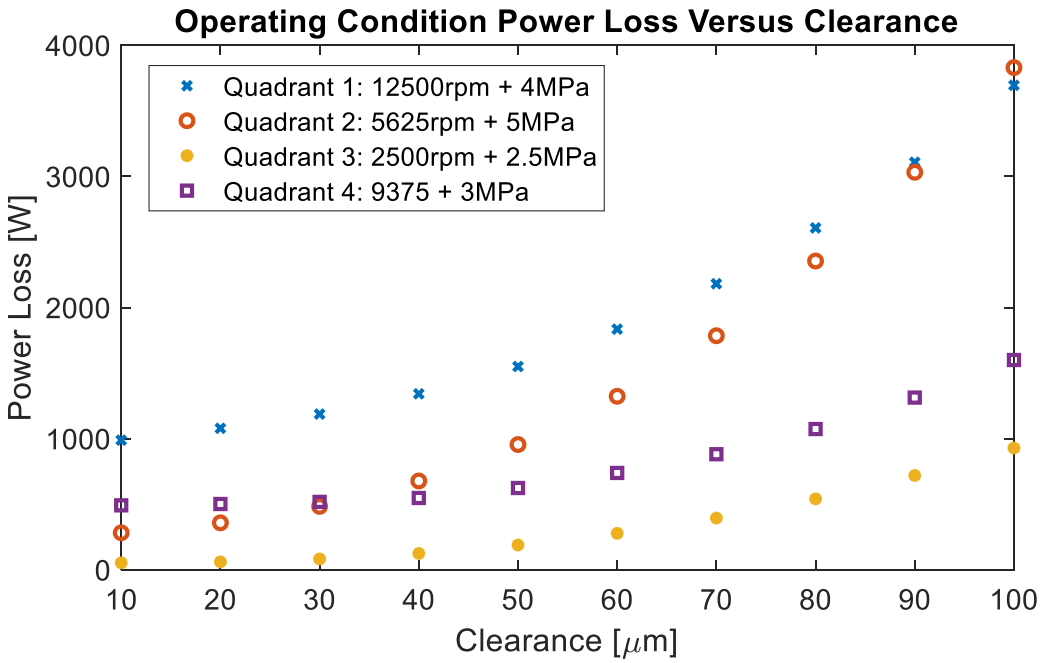

FIGURE 4.31: RADIAL CLEARANCE GRID SEARCH

The analysis of the ball-cylinder interface provides insight into what clearance should be selected. Selecting a smaller clearance reduces the power loss for each operating condition, but it is known that the model becomes invalid at extremely small clearances. The smallest trusted radial clearance is 20 microns, so it is selected as the optimal value. This choice finalizes the optimal design allowing the overall performance to be calculated. Table 4.6 shows the efficiency and power loss for each of the operating conditions that were tested. Quadrants 1 and 4 had the fastest operating speeds at 12500rpm and 9375rpm respectively. Also, quadrant 1 has the second worst efficiency, despite its power loss accounting for 50 percent of the optimization weighting.

TABLE 4.6: OPTIMIAL DESIGN PERFORMANCE

	Quadrant 1	**Quadrant 2**	**Quadrant 3**	**Quadrant 4**
Efficiency [%]	83.14	88.99	88.14	82.87
Power Loss [W]	5397	1794	305	2511

The losses can be broken down into components to determine how each loss mechanism contributes to the overall total. Figure 4.32 does this graphically for each of the four operating conditions. The torque acting on the ball piston is the largest loss contributor for each of the operating conditions, even quadrant 3 where the speed was 2500rpm. Combining the ball piston

leakage and torque, this interface accounts for about 75 percent of all the losses for each operating condition. Unfortunately, there is no way to reduce these losses by changing the clearance since the torque power loss does not reduce with increasing clearance and the leakage power loss only increases.

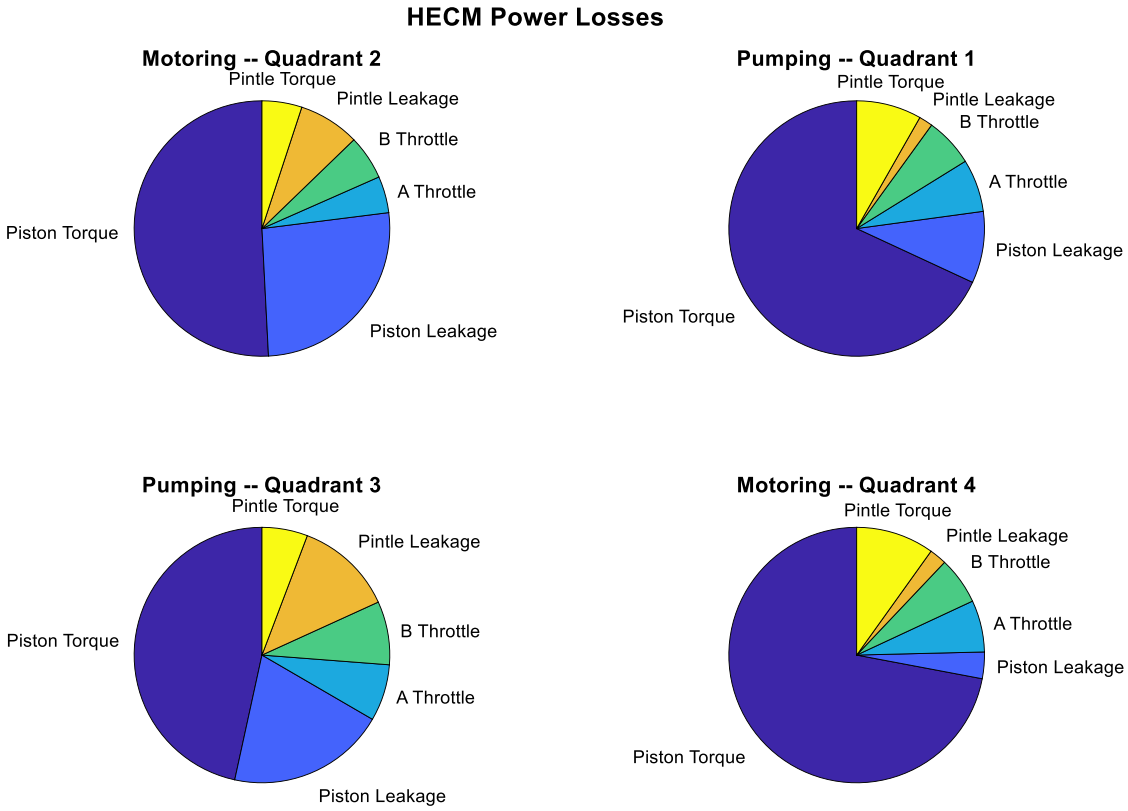

FIGURE 4.32: LOSS BREAKDOWN

The pintle-rotor interface and throttling losses evenly make up the last 20 to 35 percent of the losses. The throttling losses for ports A and B are similar which, as mentioned previously, is a consequence of the symmetric valve timing. Whether the torque or leakage power losses at the pintle-rotor interface is greater depends on the specific operating condition. Under high-speed operation, quadrants 1 and 4, the torque dominates over the leakage, while the reverse is true under low speed, quadrant 3.

4.4 Conclusion

This chapter explained how the model developed in Chapter 2, which was validated in Chapter 3, was used to formulate an optimization framework for the radial ball piston unit. The final design packaged a 20kW hydraulic machine within a 100mm outer diameter and determined critical dimensions such as piston size, clearances, and valve timing. The predicted performance was also impressive with efficiency between 80 and 90 percent across four quadrants of operation.

The optimization required searching a complex multi-variable design space that contained several local minima. This meant a typical gradient method would be ineffective, so a genetic algorithm was used to handle the unknowns of the design space. The cylinder spacing, ball piston stroke, and overall size of the unit were optimized and checked within the framework to ensure a valid design. The operating conditions were selected by considering drive cycle data for an HECM and a set that spanned the full range of operating points was found. This selection was successful at creating a design that worked well at all operating points as demonstrated by the consistent efficiency across four quadrants.

For the genetic algorithm to be successful, hundreds of individuals needed to be analyzed over several generations. Due to the number of simulations required to generate a quality design, the model was simplified to increase the computation speed. The ball-cylinder interface was simplified by ignoring the kinematics and assuming the ball stayed in the cylinder center. This simplification keeps losses in the correct order of magnitude but does not preserve the expected relationship between clearance and losses. Therefore, after the size of the pump was determine, a grid search of the clearance was performed with the validated ball-cylinder interface model. The pintle-rotor interface was also simplified to improve the computation speed.

This chapter is the culmination of all the previously presented work. The development of a mathematical model allowed for a radial ball piston unit to be quickly and accurately analyzed using analytical and numerical techniques. This model was experimentally validated against an existing radial ball piston pump providing confidence that it could predict the behavior of different designs. This model was then implemented into an optimization framework to allow for hydraulic pump and motor design outside of the typical operating conditions. This demonstrated that radial ball piston units can be used for high speed applications across pumping and motoring operations while maintaining acceptable efficiency.

5 Conclusion

5.1 Review

This thesis developed a radial ball piston pump model that was both computationally fast and accurate by utilizing analytical, numerical, and empirical techniques. Confidence in the model was established by experimentally validating the model using an off-the-shelf radial ball piston pump. Finally, the model was implemented within an optimization framework to develop a design that worked at high speeds and across four quadrants.

Chapter 1 looked at electric and hydraulic integration research and the growing interest it is receiving due to the emphasis placed on improving efficiency and reducing emissions. Multiple attempts have been made within industry and academia to completely integrate electric motors and hydraulic pumps with limited commercial success. Two takeaways from the previous efforts are that a preferred hydraulic pump architecture has not been identified and the system speed has not been pushed. Increasing the speed allows the electric machine to be more efficient and improves the overall power density. The chapter briefly summarizes electrohydraulic actuators (EHAs), which are the current state-of-the-art for high-speed hydraulic pumps. For this thesis, a radial ball piston unit was selected to be studied, and the chapter reviews the research surrounding this architecture. The radial ball piston architecture is not new but is somewhat uncommon in commercial hydraulics. It was considered a promising candidate for integration because it addressed many of the current limitations seen in EHAs when increasing rotation speed. This thesis represents, to the best of the author's knowledge, the first detailed analysis and optimization of a radial ball piston unit for high-speed operation.

Chapter 2 presented the mathematical model that was developed to simulate a radial ball piston pump. The model used analytical approaches when appropriate to improve the computation speed and numerical ones for more complicated phenomena. The combination of methods led to a model that was relatively fast computationally, but also detailed enough to describe a wide range of operating conditions. The developed model consisted of three main components, the first was the cylinder pressure dynamics. This section of the model utilized the valve area profile to describe the power output and losses incurred by filling and discharging the piston cylinder. The second component of the model calculated the losses at the ball-cylinder interface during operation. This was the most complicated section requiring the dynamics, kinematics, heat transfer, and fluid mechanics of multiple lubrication regimes to be analyzed. The final section considered the losses at the pintle-rotor interface using a quasi-static assumption for the kinematics, heat transfer, and

fluid mechanics. These were then summed to determine the overall power loss and efficiency of the radial ball piston unit.

Chapter 3 described the experimental system to test the Eaton radial ball piston pump and the experimental results that were collected to validate the previously presented model. Multiple experimental setups were used, and multiple operating conditions were tested to determine the accuracy of the developed model. Sensitivity studies were also done to determine which design variables influenced the losses most. The results showed that after refining the parameters, the model could predict the overall pump performance, including the volumetric and mechanical subcomponents of the losses. This provided confidence that the model was accurate and capable of driving design decisions.

Chapter 4 leveraged the validated model to create a design optimization framework. This process required careful consideration of the design parameters to be optimized, the geometric constraints that needed to be checked, and the operating conditions to be analyzed. Model simplifications were used to improve the computation efficiency of the pump analysis. These simplifications allowed a genetic algorithm to quickly identify valid geometries and push the design to a near optimal value. Then, a grid search was used with the fully developed model from Chapter 2 to generate the final design. The optimization used operating points in four quadrants, which created a final design with efficiency between 80 and 90 percent in all four quadrants and across a wide pressure and speed range.

5.2 Conclusions

The goal of this thesis was to study the feasibility of integrating a radial ball piston pump with a high-speed electric motor as a component within the Hybrid Hydraulic-Electric Architecture (HHEA) [2]. This objective was accomplished by developing a radial ball piston pump model, validating the model experimentally, and utilizing the model within a design optimization. The following statements can be made as a conclusion of this work:

- There is little research on radial ball piston pumps, with the majority of the work produced in the last 10 – 15 years. None of the work thus far has involved optimization of ball piston pumps; instead, the work has focused on the tribology of the interfaces and analyzing specific losses.
- Few researchers have focused on integrating electric motors and hydraulic pumps. Several interesting questions remain to be answered, such as: what hydraulic pump architecture

should be used, what maximum speeds can be achieved, and what cooling performance is feasible with the hydraulic oil.

- The HHEA architecture offers several benefits for high-speed electric motor and hydraulic pump design. The pressure rail system results in smaller pressure differentials, limiting the torque the electric machine needs to produce, and it boosts the inlet pressure of the hydraulic pump, preventing cavitation at higher operating speeds.
- The centripetal force in a high-speed radial piston pump creates a nontrivial pressure distribution within the pumping chamber that needs to be considered when analyzing the pressure dynamics. A 220 kPa change in pressure was observed within the cylinder at an operating speed of 12,500 rpm for the optimal radial ball piston design. However, this pressure differential would be higher if not for the radial compactness of the design.
- Models of the thin fluid film gaps are critical for understanding the losses within the hydraulic pump. The ball-cylinder interface is particularly important and accounts for a significant portion of the losses within the pump, because of this, designs with fewer pistons tend to be more efficient.
- The temperature within the thin film regions can vary greatly (10-30 K) from the bulk fluid temperature due to localized heating due to fluid shearing. This temperature variance effects the load carrying capacity of the fluid, which can change the lubrication regime at the interface. Knowing the lubrication regime and temperature in the thin film is necessary to determine the leakage and shearing at these surfaces.
- The forces on the ball piston move it to an eccentric position in the cylinder with the position stabilizing once the ball is next to the cylinder wall. Reaching this equilibrium often involves the fluid mechanics transitioning from the hydrodynamic to elastohydrodynamic lubrication regime. The transition depends strongly on the operating conditions; increasing pressure, increasing oil temperature, or decreasing rotation speed all increase the likelihood of elastohydrodynamic effects occurring. This transition significantly increases the shearing losses at the interface, and because the ball always moves close to the cylinder wall, increasing the clearance has little to no effect on the shearing losses. Finally, the rotation of the ball piston creates high relative velocity between the ball and the cylinder further increasing the shearing losses.
- As expected, adjusting the ball-cylinder clearance increases the leakage at the interface. Interestingly, there is less leakage power loss at the interface when motoring versus pumping because of the eccentric ball position and its interaction with the pressure driven

and velocity driven flow profiles. This phenomenon could be exploited to optimize the volumetric efficiency of a radial ball piston motor.

- If ball bearings are not used to support the rotor, then the pintle-rotor interface needs to assume journal bearing behavior to accurately account for the losses. When accounting for rotor eccentricity, the gap height is largest near the high pressure port resulting in a significant leakage increase compared with a concentric pintle-rotor interface.
- After parameter adjustment, the radial ball piston model predicts the performance of an off-the-shelf pump with acceptable accuracy (3 – 10 percent).
- The pump design is sensitive to the ball-cylinder clearance and the pump eccentricity, making them critical dimensions when attempting to optimize a design. The fluid temperature and entrained air percentage are critical testing conditions that impact pump performance as well.
- Optimization of the radial ball piston architecture demonstrated that 80 – 90 percent efficiency was possible across four quadrants of operation and at speeds up to 12,500 rpm. The power density of the optimized unit was also impressive with a 20 kW machine fitting within a 100mm outside diameter. However, the maximum efficiency of the architecture is limited by the ball-cylinder interface and the inability to decrease the shearing losses at high speeds.
- The radial ball piston architecture is a promising candidate for integration with high-speed electric motors, but it is not ideal for the proposed HHEA [2]. The ball-cylinder interface is particularly problematic when attempting to design for efficient operation at both high and low speeds. The ball-cylinder clearance must be large, so the ball does not seize and stop rolling at high speeds, but this results in excessive leakage when operating at low speeds. Therefore, it is expected that a radial cylindrical piston pump will perform well within the HHEA because it retains the benefits of a radial topology, while allowing greater design freedom when optimizing the piston-cylinder interface for high and low operating speeds. Future work by other researchers on the project are investigating this pump architecture.

5.3 Future Work

The recommended next steps are completing the detailed design and building a prototype of the optimized solution. The dimensions and oil properties need to be closely measured to ensure an accurate comparison. Also, the work in this thesis represents the hydraulic component of the

integrated hydraulic-electric machine. Parallel work at the University of Wisconsin – Madison has optimized a preferred electric machine. Current research, which extends this thesis, incorporates the thermal and mechanical interactions of the electrical motor and the hydraulic pump. Developing a robust test setup that can decouple the electric and hydraulic interactions within the prototype would allow for validation of the hydraulic model presented here, the electric model developed by UW-Madison, and the combined model that is being developed.

The validation of the hydraulic, electric, and integrated models creates an opportunity to extend this work and electrify other hydraulic fields. Utilizing this hydraulic model, other operating conditions can be analyzed, and this work can be extended to an increasing number of applications. The operating conditions presented here are for a 22 ton excavator with 5 pressure rails, but other mobile hydraulic applications could benefit from the electrification presented here. However, it is important to consider the pressure requirements for different applications because the radial ball piston pump does not perform well at high pressure differentials due to leakage. Outside of mobile hydraulics, aerospace applications value compactness and robustness over efficiency, making the radial ball piston architecture a perfect fit. Also, switching to a radial ball piston pump eliminates several of the challenges associated with increasing the speed. Future work to determine the maximum operating speed of the radial ball piston architecture would be valuable for aerospace and other applications that require extreme power density.

Despite the robustness and care taken in developing the ball-cylinder model, the assumption that the ball piston always rotates on the cam ring is a limiting one. The ball-cam ring interface has been modeled previously [30] and involves point contact elastohydrodynamic lubrication. This work also showed that the ball can skid on the cam under certain operating conditions. Before pushing the model developed here to optimize higher speed applications, a model of the ball-cam ring interface would need to be developed to accurately determine the conditions when the ball is skidding versus rolling on the cam surface.

Other assumptions can be relaxed in future versions of the model. The ball-cylinder interface uses a thin gap approximation allowing for one-dimensional fluid flow. This is a good assumption when the ball position is relatively stable, but when the ball moves rapidly towards the cylinder wall, the normal squeeze component of the fluid flow is not expected to be one dimensional. Similarly, the heat transfer model assumed that the heat is absorbed by the oil with no convection to other control volumes or to the surrounding metal surfaces. Relaxing this assumption dissipates energy between neighboring regions and reduces the overall energy contained within the oil. Finally, if the final design does not use a ball bearing to maintain concentricity between the pintle

and rotor, then the quasi-static assumption for this interface should be relaxed or testing to identify when it is no longer valid.

These possible improvements do not detract from the work presented here, in fact, many of the model assumptions that could be relaxed were made purposefully to improve the overall computation speed. The model development in Chapter 2 extends the work done previously by Jamzedeh and provides an example of how to effectively trade-off between model speed and accuracy. The integration of this model within the genetic algorithm framework of Chapter 4 is particularly valuable for radial ball piston design, where the current work focuses on analysis of existing designs instead of the optimization of new ones. Such a framework opens the possibility for the radial ball piston architecture to expand to a more prominent role, especially in mobile and high-speed hydraulic applications.

Bibliography

[1] Climate Transparency, “Brown to Green: The G20 transition towards a net-zero emissions economy,” *Clim. Transpar.*, vol. 53, no. 9, pp. 1689–1699, 2019, [Online]. Available: http://www.climate-transparency.org/g20-climate-performance/g20report2019.

[2] P. Y. Li, J. Siefert, and D. Bigelow, “A Hybrid Hydraulic-Electric Architecture (HHEA) for High Power Off-Road Mobile Machines,” in *ASME/BATH 2019 Symposium on Fluid Power and Motion Control*, Oct. 2019, doi: 10.1115/FPMC2019-1628.

[3] H. Vukovic, M., Leifield, R., and Murrenhoff, “STEAM - a hydraulic hybrid architecture for excavators,” 2006.

[4] J. Siefert and P. Y. Li, “Optimal Control and Energy-Saving Analysis of Common Pressure Rail Architectures: HHEA and STEAM.” Sep. 09, 2020, doi: 10.1115/FPMC2020-2799.

[5] G. R. Bohach, Nishanth, E. Severson, and J. D. Van de Ven, “Modeling and Optimization Study of a Tightly Integrated Rotary Electric Motor-Hydraulic Pump,” in *ASME/BATH 2019 Symposium on Fluid Power and Motion Control*, Oct. 2019, pp. 1–10, doi: 10.1115/FPMC2019-1626.

[6] A. F. Bohnhoff, “Radial Ball Piston Pump,” 3056357, 1962.

[7] F. N. U. Nishanth, G. Bohach, J. Van De Ven, and E. L. Severson, “Design of a Highly Integrated Electric-Hydraulic Machine for Electrifying Off-Highway Vehicles,” *2019 IEEE Energy Convers. Congr. Expo. ECCE 2019*, pp. 3983–3990, 2019, doi: 10.1109/ECCE.2019.8912685.

[8] F. Nishanth, G. Bohach, M. M. Nahin, J. Van de Ven, and E. L. Severson, “Design of an Axial Flux Machine With an Integrated Hydraulic Pump for Off-Highway Vehicle Electrification,” in *2020 IEEE Energy Conversion Congress and Exposition (ECCE)*, 2020, pp. 1772–1779, doi: 10.1109/ECCE44975.2020.9235731.

[9] Eaton, “Light Duty Hydrostatic Data Sheet,” 2016.

[10] F. Jamzadeh, “Study of Losses in a Ball Piston Pump,” University of Wisconsin - Madison, 1983.

[11] KersTech, “TwinTorq Electric Hydraulic Motor,” 2017. http://kerstech.com/twintorq/.

[12] M. M. E. Lester, “TwinTorq Electric-Hydraulic Motor,” Beaverton, Oregon.

[13] KersTech, “TwinTorq Technology,” 2017. http://kerstech.com/tt-technology/.

[14] “Motor / pump hybrid system EPAI for high and medium-pressure applications.”

[15] P. Gamez-Montero *et al.*, “GeroMAG: In-House Prototype of an Innovative Sealed, Compact and Non-Shaft-Driven Gerotor Pump with Magnetically-Driving Outer Rotor,” *Energies*, vol. 10, no. 4, p. 435, Mar. 2017, doi: 10.3390/en10040435.

[16] W. Fiebig, D. Ignacy, C. Marek, and K. Hubert, “A vane pump integrated with an electric motor,” in *The 9th International Fluid Power Conference. Aachen, Germany*, 2014, no. March 24-26.

[17] E. Leati, F. Poltschak, R. Scheidl, “An electromagneticallly actuated high frequency oscillation pump,” *Mechatronics*, 2017.

[18] F. Nishanth, A. Khamitov, and E. L. Severson, “Comparison of Linear and Rotary Electric Machine Topologies for a Hybrid Hydraulic Electric Architecture of Off-Highway Vehicles,” in *2020 IEEE Transportation Electrification Conference & Expo (ITEC)*, 2020, pp. 1063–1068, doi: 10.1109/ITEC48692.2020.9161495.

[19] P. H. Hogan, “A Linear Electromagnetic Piston Pump,” University of Minnesota - Twin Cities, 2017.

[20] P. H. Hogan and J. D. Van de Ven, “Dynamic modeling of a linear electromagnetic piston pump,” *ASME/BATH 2017 Symp. Fluid Power Motion Control. FPMC 2017*, pp. 1–10, 2017, doi: 10.1115/FPMC2017-4324.

[21] A. Khamitov, J. Swanson, J. V. de Ven, and E. L. Severson, “Modeling and Design of a Linear Electric-Hydraulic Conversion Machine for Electrification of Off-Highway Vehicles,” in *2019 IEEE Energy Conversion Congress and Exposition (ECCE)*, 2019, pp. 6126–6133, doi: 10.1109/ECCE.2019.8913134.

[22] B.-D. You, D. Huang, and Z.-R. Ke, “Contact stress analysis of ball piston pump,” *Nanchang Daxue Xuebao-Gongke Ban(Journal Nanchang Univ. Technol. Ed.*, vol. 33, no. 4, pp. 378–382, 2011.

[23] F. U. B. Y. O. U. Bu-dong and K. E. Z. Z. Rui-hua, “Kinematical Equations of High Flow Sea (Fresh) Water Ball Piston Pump [J],” *Hydraul. Pneum. Seals*, vol. 4, 2009.

[24] F. U. B. Y. O. U. Bu-dong and K. E. Z. Z. Rui-hua, “Kinetic Analysis of Sea (Fresh) Water Ball Piston Pump [J],” *Fluid Power Transm. Control*, vol. 6, 2009.

[25] Z. R. Ke, X. Zhang, and B. B. Fu, “Study on Friction Pairs in Low Pressure Ball Piston Pump With Water Lubricants,” *Fluid Power Transm. Control*, vol. 5, pp. 8–11, 2009.

[26] J. B. Hu, X. J. Zhang, and S. H. Yuan, “Theoretical Study on Leakage of Ball Piston Pump’s Ball Piston Pair,” *Mach. Tool Hydraul*, vol. 8, pp. 100–102, 2005.

[27] Y. S. Z. X. H. Jibin, “Influence of Varying Oil Viscosity on Leakage of Ball Piston Pump’s

Ball Piston Pair [J]," *Trans. Chinese Soc. Agric. Mach.*, vol. 4, 2007.

[28] Y.-Z. Hu and D. Zhu, "A Full Numerical Solution to the Mixed Lubrication in Point Contacts ," *J. Tribol.*, vol. 122, no. 1, pp. 1–9, Jun. 1999, doi: 10.1115/1.555322.

[29] H. Zhao, C. Wei, C. Jing, and S. Lin, "Lubrication characteristics of ball–cylinder pair in eccentric ball piston pumps," *Proc. Inst. Mech. Eng. Part J J. Eng. Tribol.*, vol. 230, no. 6, pp. 680–689, Oct. 2015, doi: 10.1177/1350650115610356.

[30] L. Xu, C. Wei, C. Jing, and J. Liu, "A Study on Force and Lubrication Characteristics of Ball Piston in Eccentric Ball Piston Pump," *J. Tribol.*, vol. 139, no. 4, Mar. 2017, doi: 10.1115/1.4034955.

[31] J. Zhou, C. Jing, and J. Liu, "On the steady posture of conical spindle distribution used in ball piston pump," *Proc. Inst. Mech. Eng. Part J J. Eng. Tribol.*, vol. 234, no. 4, pp. 490–499, Dec. 2019, doi: 10.1177/1350650119893900.

[32] Q. Chao, J. Zhang, B. Xu, H. Huang, and M. Pan, "A Review of High-Speed Electro-Hydrostatic Actuator Pumps in Aerospace Applications: Challenges and Solutions," *J. Mech. Des. Trans. ASME*, vol. 141, no. 5, May 2019, doi: 10.1115/1.4041582.

[33] P. Hannifin, "Compact Electro-Hydraulic Actuator (EHA)," 2020. https://ph.parker.com/us/17560/en/compact-electro-hydraulic-actuator.

[34] G. E. Totten, Y. H. Sun, R. J. Bishop Jr, and X. Lin, "Hydraulic system cavitation: a review," *SAE Trans.*, pp. 368–380, 1998.

[35] R. J. Bishop and G. E. Totten, "Effect of pump inlet conditions on hydraulic pump cavitation: A review," in *Hydraulic Failure Analysis: Fluids, Components, and System Effects*, ASTM International, 2001.

[36] G. E. Totten and R. J. Bishop, "The hydraulic pump inlet condition: impact on hydraulic pump cavitation potential," SAE Technical Paper, 1999.

[37] N. D. Manring, V. S. Mehta, B. E. Nelson, K. J. Graf, and J. L. Kuehn, "Scaling the speed limitations for axial-piston swash-plate type hydrostatic machines," *J. Dyn. Syst. Meas. Control*, vol. 136, no. 3, 2014.

[38] R. M. Harris, K. A. Edge, and D. G. Tilley, "The suction dynamics of positive displacement axial piston pumps," 1994.

[39] M. Kunkis and J. Weber, "Experimental and numerical assessment of an axial piston pump's speed limit," in *BATH/ASME 2016 Symposium on Fluid Power and Motion Control*, 2016.

[40] J. Darling and K. A. Edge, "A Theoretical Model of Axial Piston Pump Flow Ripple," in *Proceedings of 1st Bath International Fluid Power Workshop*, 1988.

[41] J. M. Bergada, S. Kumar, D. L. Davies, and J. Watton, “A complete analysis of axial piston pump leakage and output flow ripples,” *Appl. Math. Model.*, vol. 36, no. 4, pp. 1731–1751, 2012.

[42] B. Xu, M. Hu, and J. Zhang, “Impact of typical steady-state conditions and transient conditions on flow ripple and its test accuracy for axial piston pump,” *Chinese J. Mech. Eng.*, vol. 28, no. 5, pp. 1012–1022, 2015.

[43] J.-K. Kim, H.-E. Kim, J.-Y. Jung, S.-H. Oh, and S.-H. Jung, “Relation between pressure variations and noise in axial type oil piston pumps,” *KSME Int. J.*, vol. 18, no. 6, pp. 1019–1025, 2004.

[44] J. Darling, “Piston-cylinder dynamics in oil hydraulic axial piston pumps.” University of Bath, 1985.

[45] N. D. Manring, “The discharge flow ripple of an axial-piston swash-plate type hydrostatic pump,” *J. Dyn. Sys., Meas., Control*, vol. 122, no. 2, pp. 263–268, 2000.

[46] M. E. Pettersson, K. G. Weddfelt, and J.-O. S. Palmberg, “Methods of reducing flow ripple from fluid power piston pumps–a theoretical approach,” *SAE Trans.*, pp. 158–167, 1991.

[47] B. J. Hamrock, *Fundamentals of Fluid Film Lubrication*. NASA Reference, 1991.

[48] M. Pelosi and M. Ivantysynova, “Heat transfer and thermal elastic deformation analysis on the Piston/Cylinder interface of axial piston machines - Not Done,” *J. Tribol.*, vol. 134, no. 4, pp. 1–15, 2012, doi: 10.1115/1.4006980.

[49] S. Widnall and J. Peraire, “Other Coordinate Systems,” 2008. [Online]. Available: https://ocw.mit.edu/courses/aeronautics-and-astronautics/16-07-dynamics-fall-2009/lecture-notes/MIT16_07F09_Lec05.pdf.

[50] D. Dowson, *History of tribology*. Addison-Wesley Longman Limited, 1978.

[51] X. Tian and F. E. Kennedy Jr., “Maximum and Average Flash Temperatures in Sliding Contacts,” *J. Tribol.*, vol. 116, no. 1, pp. 167–174, Jan. 1994, doi: 10.1115/1.2927035.

[52] J. Bos and H. Moes, “Frictional Heating of Tribological Contacts,” *J. Tribol.*, vol. 117, no. 1, pp. 171–177, Jan. 1995, doi: 10.1115/1.2830596.

[53] W. Banzhaf, P. Nordin, R. E. Keller, and F. D. Francone, *Genetic programming*. Springer, 1998.

[54] A. J. Chipperfield, P. J. Fleming, H. Pohlheim, and C. M. Fonseca, “A genetic algorithm toolbox for MATLAB,” in *Proc. International Conference on Systems Engineering, Coventry, UK*, 1994, vol. 6, no. 8.

[55] A. J. Chipperfield and P. J. Fleming, “The MATLAB genetic algorithm toolbox,” 1995.

[56] T. Sullivan, “Multi-domain Multi-objective Optimization of Mechanisms: A General Method with Two Case Studies,” University of Minnesota - Twin Cities, 2013.

[57] S. Wilhelm and J. D. Van de Ven, “Design of a variable displacement triplex pump,” *Int. Fluid Power Expo. Vegas, NV*, 2014.

[58] A. Robison and A. Vacca, “Multi-objective optimization of circular-toothed gerotors for kinematics and wear by genetic algorithm,” *Mech. Mach. Theory*, vol. 128, pp. 150–168, 2018.

[59] G. C. Boyce-Erickson, T. R. Chase, and J. D. Van de Ven, “Valve Timing and Area Profile Selection for Hydraulic Pumps and Motors.” Sep. 09, 2020, doi: 10.1115/FPMC2020-2779.

Appendices

Appendix A: Architecture Selection

The decision to study the radial ball piston pump for the Hybrid Hydraulic-Electric Architecture (HHEA) was a non-trivial one that required careful consideration of different hydraulic pump/motor architectures and their tradeoffs. This appendix walks through the design criteria and tradeoff analysis that was performed to determine that a radial ball piston pump should be studied. The hydraulic architectures that were considered are: external gear, internal gear, gerotor, vane, axial piston, and radial piston. The design criteria are given in Table A.1.

TABLE A.1: DESIGN CRITERIA

Criteria	Description
Low pump displacement scalability	As the pump displacement gets smaller, how does the pump perform
High pump displacement scalability	As the pump displacement (size) gets bigger, how does the pump perform
Maximum speed capability	Does the pump have the potential to run at high speeds
Displacement density	How much fluid is displaced for a given packaging mass (mass can't become too large for most mobile applications)
Cost	Dollar amount
Volumetric eff @ high pressure	How volumetrically efficient is the system at high pressure
Mechanical eff @ low speed	How mechanically efficient the system is at low speed
Mechanical eff @ high speed	How mechanically efficient the system is at high speed
Ease of integration	How easy can the pump become electrically integrated
Ease of valves	How easy can the pump have active valves
Stick-Slip @ low speed	How noticeable is the stick-slip behavior of the pump at very low speeds
Wear and reliability	How much wear occurs within the pump
Noise	How loud is the pump/motor

The evaluation was performed by assigning each design a score for each criterium. Also, each criterium was assigned a weight based on its importance for the application. Finally, the score for each criterium is multiplied by its weight, and those values are summed to determine the overall performance value. The overall performance matrix and final scores are shown in Table A.2.

TABLE A.2: HYDRAULIC ARCHITECTURE EVALUATION MATRIX

Criteria	Weight (0 - 10)	External Gear	Internal Gear	Gerotor	Vane	Axial Piston	Radial Piston
Low pump displacement scalability	8	8	7	9	6	8	5
High pump displacement scalability	3	6	7	3	9	7	10
Maximum speed capability	8	7	7	7	8	2	6
Displacement density	6	7	6	8	9	6	5
Cost	4	8	6	10	6	5	4
Volumetric eff @ high pressure	8	6	7	3	6	9	10
Mechanical eff @ low speed	8	7	8	7	3	5	9
Mechanical eff @ high speed	8	7	8	7	8	8	9
Ease of integration	10	2	5	7	7	7	7
Total Score		392	427	431	423	403	458

As can be seen from Table A.2, the ordering of the preferred architectures are as follows:

1. Radial Piston
2. Gerotor
3. Internal Gear
4. Vane
5. Axial Piston
6. External Gear

The primary detriment for the external gear was the difficulty of tightly integrated the electrical motor to the unit. A shaft would likely have been required between the electric machine and the gear pump defeating the primary goal of a tight integration.

The axial piston unit was not ideally suited for this research because of the side loads arising from the centripetal force under high speed operation. This issue requires significant engineering to overcome especially as the pump displacement increases. Also, the axial piston is popular as a variable displacement unit, but that is not desirable for this application.

The hydraulic architectures described after this point were all considered reasonable options and could possibly be preferred for a different high speed application. The vane pump had the potential to package well within a radial flux electric machine, had good pressure capability, and a smooth flow rate. It also could be balanced to reduce the dynamic forces acting on it, but that would decrease the maximum operating speed. The key concern was the pump performance at low speed, when stick-slip behavior is likely, and the components tend to wear, reducing overall life.

The next reasonable solution was an internal gear pump. It could package well with a radial flux electric motor, has good displacement density, and has shown the ability to reach high speeds and reasonable pressures. Internal gear pumps are currently being made that can reach 10,500 rpm and 28 MPa. Unfortunately, the efficiency of this architecture is limited as there is a large sliding surface area. This large area creates a tradeoff between shearing and leakage losses that is difficult to optimize for efficient performance, especially across the wide set of operating speeds seen in the HHEA.

The gerotor is similar to the internal gear but offers better displacement density, packaging, and cost. However, the efficiency is even more limited than the internal gear. The first concern is that as the pump displacement increases, filling the ports becomes increasingly difficult at high speeds. Another deterrent is poor volumetric efficiency at high pressures as there is limited sealing surface. Fortunately, the pressure rail spacing reduces the pressure differential at the pump and that limits the expected amount of leakage.

The radial piston design was selected as the best option for the HHEA application. It packages well, can reach high pressures, has good mechanical efficiency, and can reach high speeds. If the design is inside impinged, then the centripetal forces help with filling the cylinders at high speeds. A ball piston was preferred over a cylindrical piston because it simplifies the design, reduces the cost, and improves the compactness of the unit. Also, the ball piston can take advantage of the reduced pressure differentials created by the pressure rail system of the HHEA. Lastly, the ball pistons can roll on the cam allowing good tribological performance at both high and low speeds. This limits concerns regarding excessive wear.

Appendix B: Valve Timing – Area Intersections

The area profile can be calculated using analytical integrals that describe the intersection of the valve's circular cross section with the ports of the pintle. As the valve moves along the pintle from bottom dead center, it intersects with three distinct geometric features of the ports: the opening ramp, the main port, and the closing ramp. Figure B.1 shows the geometry.

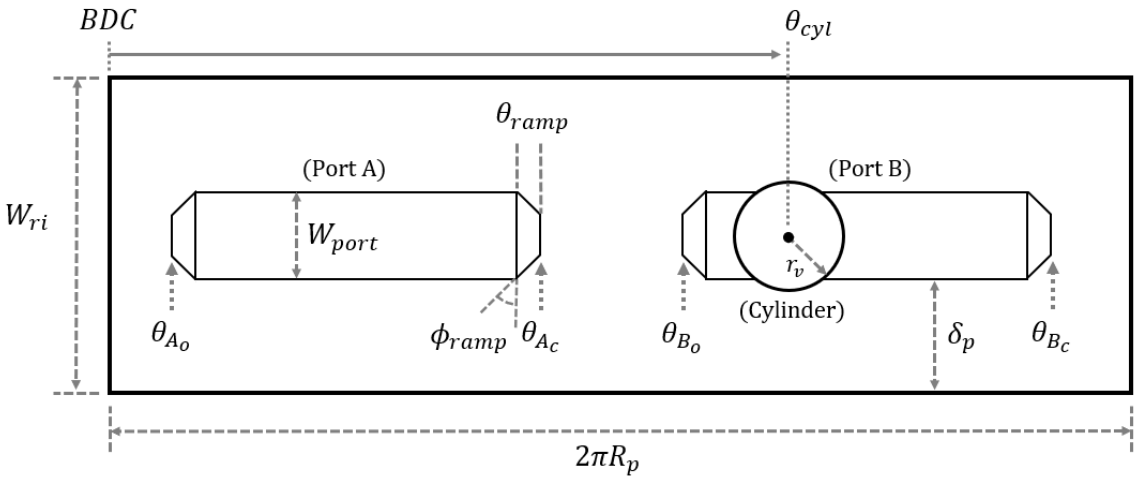

FIGURE B.1: UNWRAPPED PINTLE GEOMETRY AND VALVE TIMING

The opening ramp is the first piece the valve cylinder intersects, and its geometry is shown in Figure B.2. When calculating the intersection, the geometry always defines the cylinder center as the origin, and the port ramp bound, x_L and x_R, are shifted to this reference frame. To convert between the cartesian coordinates in Figure B.2 and angular positions of the pintle, the definition for arc length is used, eq. (B.1).

$$x = R_p(\theta - \theta_{cyl}) \tag{B.1}$$

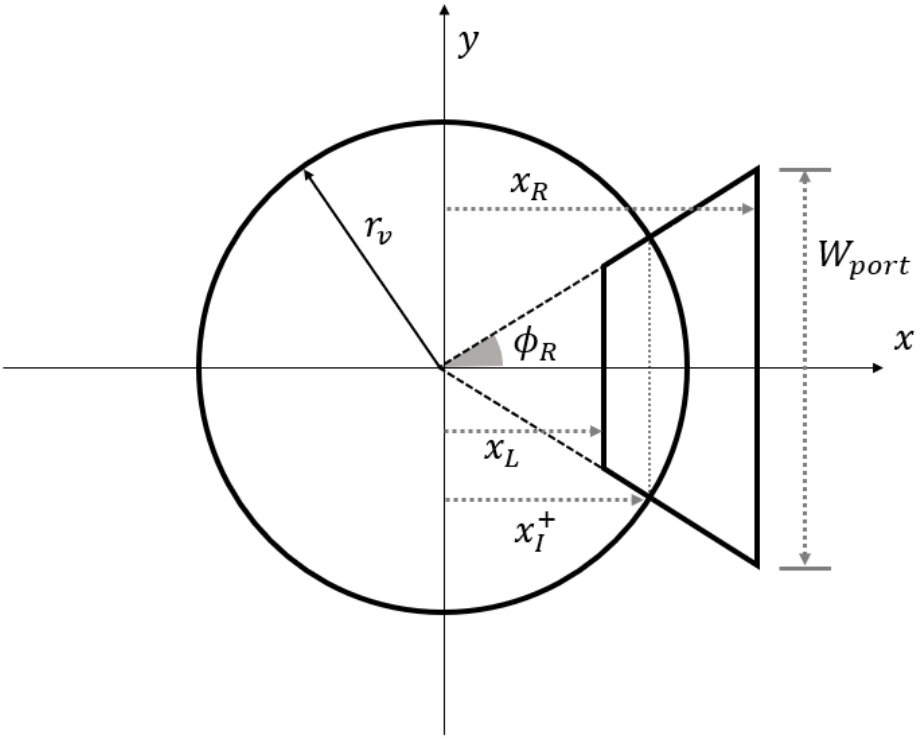

FIGURE B.2: VALVE CYLINDER INTERSECTING OPENING RAMP AREA

Utilizing this local reference frame, the circle and the port ramp equations are given in (B.2) and (B.3), respectively.

$$y_{circle} = \sqrt{r_v^2 - x^2} \tag{B.2}$$

$$y_{ramp} = (x - x_{int}) \tan \phi_R \tag{B.3}$$

where x_{int} is the x-intercept of the function.

$$x_{int} = x_R - x_{base} \tag{B.4}$$

where x_{base} is the total length of the port ramp triangle.

$$x_{base} = \frac{1}{2} \frac{W_{port}}{\tan \phi_R} \tag{B.5}$$

Setting eq. (B.2) and (B.3) equal to each other allows the x-value for the intersection of the port ramp and the valve to be calculated, eq. (B.6).

$$\sqrt{r_v^2 - x^2} = (x - x_{int}) \tan \phi_R$$

$$0 = (1 + \tan^2 \phi_R)x^2 + (-2x_{int} \tan^2 \phi_R)x + \left(x_{int}^2 \tan^2 \phi_R - r_v^2\right)$$

$$x_I^+, x_I^- = \frac{2x_{int} \tan^2 \phi_R \pm \sqrt{4x_{int}^2 \tan^4 \phi_R - 4(1 + \tan^2 \phi_R)\left(x_{int}^2 \tan^2 \phi_R - r_v^2\right)}}{2(1 + \tan^2 \phi_R)} \tag{B.6}$$

This information allows a piece-wise definition for the area profile, eq. (B.7), to be established. Each bound of the piece-wise function corresponds to a case from Figure B.3.

$$A(x) = \begin{cases} 0 & \text{Case A: } r_v < x_L \\ \displaystyle\int_{x_L}^{r_v} \sqrt{r_v^2 - x^2}\, dx & \text{Case B: } x_I^+ < x_L < r_v \\ \displaystyle\int_{x_L}^{x_I^+} (x - x_{int}) \tan \phi_R\, dx + \int_{x_I^+}^{r_v} \sqrt{r_v^2 - x^2}\, dx & \text{Case C: } x_I^- < x_L < x_I^+ < r_v \\ \displaystyle\int_{x_L}^{x_I^+} (x - x_{int}) \tan \phi_R\, dx + \int_{x_I^+}^{x_R} \sqrt{r_v^2 - x^2}\, dx & \text{Case D: } x_I^- < x_L < x_I^+ < x_R \\ \displaystyle\int_{x_L}^{x_R} (x - x_{int}) \tan \phi_R\, dx & \text{Case E: } x_I^- < x_L < x_R < x_I^+ \\ \displaystyle\int_{x_L}^{x_I^-} \sqrt{r_v^2 - x^2}\, dx + \int_{x_I^-}^{x_R} (x - x_{int}) \tan \phi_R\, dx & \text{Case F: } -r_v < x_L < x_I^- < x_R \\ \displaystyle\int_{-r_v}^{x_I^-} \sqrt{r_v^2 - x^2}\, dx + \int_{x_I^-}^{x_R} (x - x_{int}) \tan \phi_R\, dx & \text{Case G: } -r_v < x_I^- < x_R \\ \displaystyle\int_{-r_v}^{x_R} \sqrt{r_v^2 - x^2}\, dx & \text{Case H: } -r_v < x_R < x_I^- \\ 0 & \text{Case I: } x_R < -r_v \end{cases} \tag{B.7}$$

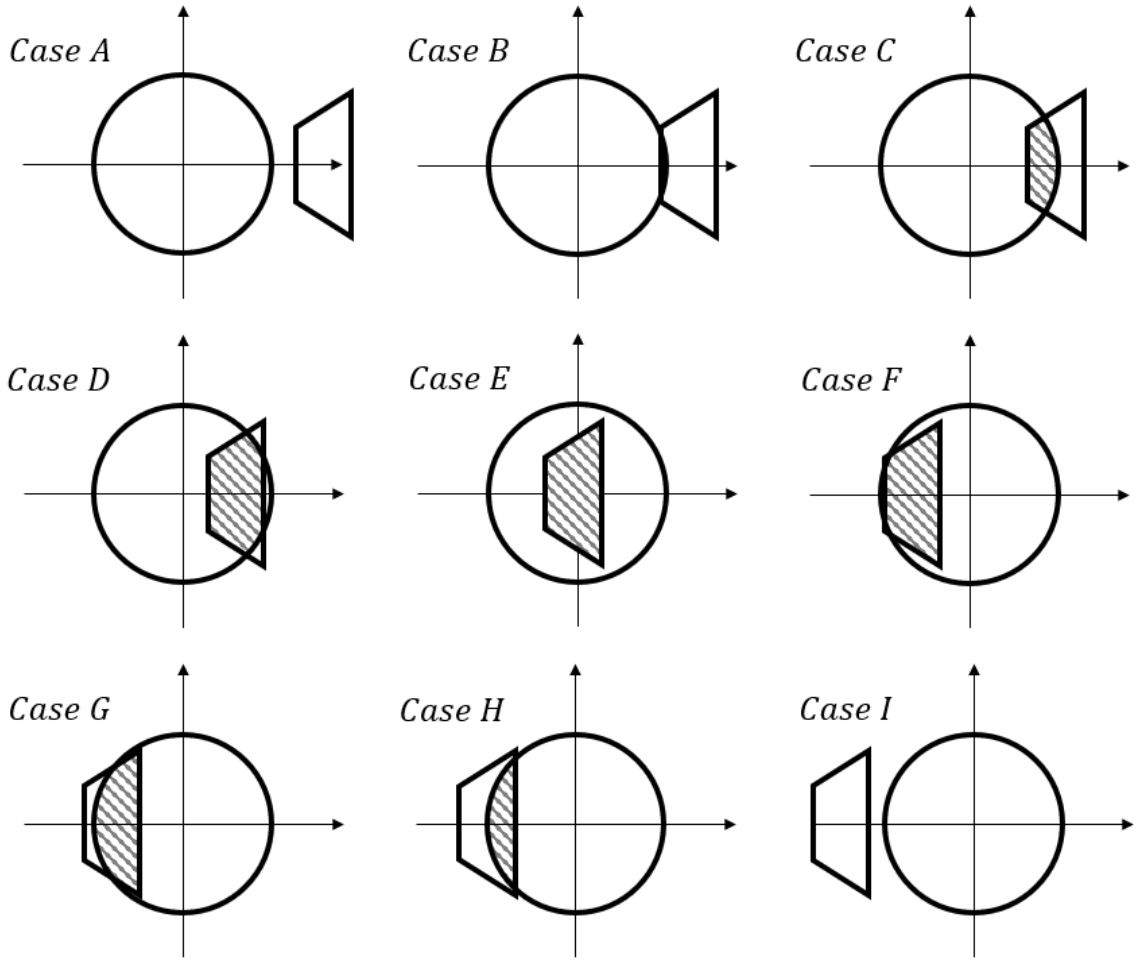

FIGURE B.3: VALVE CYLINDER AND OPENING RAMP INTERSECTION CASES

The integrals for the area under a circle and area under a line are solved for generic bounds in eq. (B.8) and (B.9), respectively.

$$\int_a^b \sqrt{r_v^2 - x^2}\, dx = \frac{1}{2}\left(r_v^2 \sin^{-1}\left(\frac{b}{r_v}\right) + x\sqrt{r_v^2 - b^2} - r_v^2 \sin^{-1}\left(\frac{a}{r_v}\right) + x\sqrt{r_v^2 - a^2}\right) \quad \text{(B.8)}$$

$$\int_a^b (x - x_{int}) \tan\phi_R\, dx = \tan\phi_R \left[\frac{b^2}{2} - x_{int} \cdot b - \frac{a^2}{2} + x_{int} \cdot a\right] \quad \text{(B.9)}$$

The next geometric feature that the valve intersects is the main port. The geometry is shown in Figure B.4 with the valve again shifted to the origin of the local reference frame and x_L and x_R defining the left and right position of the port ramp.

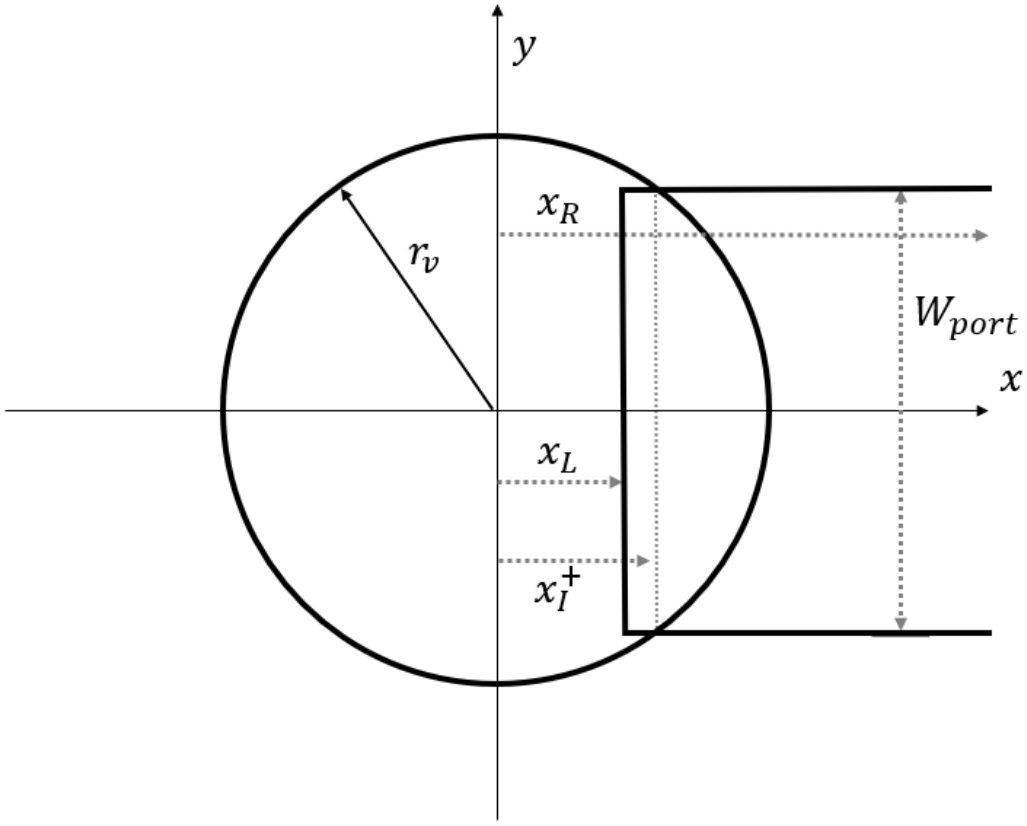

FIGURE B.4: VALVE CYLINDER INTERSECTING MAIN PORT

Utilizing this local reference frame, the circle and the main port equations are given in (B.10) and (B.11), respectively.

$$y_{circle} = \sqrt{r_v^2 - x^2} \tag{B.10}$$

$$y_{port} = \frac{1}{2} W_{port} \tag{B.11}$$

Setting eq. (B.10) and (B.11) equal to each other allows the x-value for the intersection of the port ramp and the valve to be calculated, eq. (B.12).

$$\sqrt{r_v^2 - x^2} = \frac{1}{2} W_{port}$$

$$x_I^+, x_I^- = \pm\sqrt{r_v^2 - \frac{W_{port}^2}{4}} \tag{B.12}$$

This information allows a piece-wise definition for the area profile, eq. (B.13), to be established. Each bound of the piece-wise function corresponds to a case from Figure B.5.

$$A(x) = \begin{cases} 0 & \text{Case A: } r_v < x_L \\ \displaystyle\int_{x_L}^{r_v} \sqrt{r_v^2 - x^2}\, dx & \text{Case B: } x_I^+ < x_L < r_v \\ \displaystyle\int_{x_L}^{x_I^+} \frac{1}{2} W_{port}\, dx + \int_{x_I^+}^{r_v} \sqrt{r_v^2 - x^2}\, dx & \text{Case C: } x_I^- < x_L < x_I^+ < r_v \\ \displaystyle\int_{x_L}^{x_I^-} \sqrt{r_v^2 - x^2}\, dx + \int_{x_I^-}^{x_I^+} \frac{1}{2} W_{port}\, dx + \int_{x_I^+}^{r_v} \sqrt{r_v^2 - x^2}\, dx & \text{Case D: } -r_v < x_L < x_I^- < x_I^+ < r_v < x_R \\ \displaystyle\int_{-r_v}^{x_I^-} \sqrt{r_v^2 - x^2}\, dx + \int_{x_I^-}^{x_I^+} \frac{1}{2} W_{port}\, dx + \int_{x_I^+}^{r_v} \sqrt{r_v^2 - x^2}\, dx & \text{Case E: } x_L < -r_v < x_I^- < x_I^+ < r_v < x_R \\ \displaystyle\int_{-r_v}^{x_I^-} \sqrt{r_v^2 - x^2}\, dx + \int_{x_I^-}^{x_I^+} \frac{1}{2} W_{port}\, dx + \int_{x_I^+}^{x_R} \sqrt{r_v^2 - x^2}\, dx & \text{Case F: } x_L < -r_v < x_I^- < x_I^+ < x_R < r_v \\ \displaystyle\int_{-r_v}^{x_I^-} \sqrt{r_v^2 - x^2}\, dx + \int_{x_I^-}^{x_R} \frac{1}{2} W_{port}\, dx & \text{Case G: } -r_v < x_I^- < x_R \\ \displaystyle\int_{-r_v}^{x_R} \sqrt{r_v^2 - x^2}\, dx & \text{Case H: } -r_v < x_R < x_I^- \\ 0 & \text{Case I: } x_R < -r_v \end{cases} \tag{B.13}$$

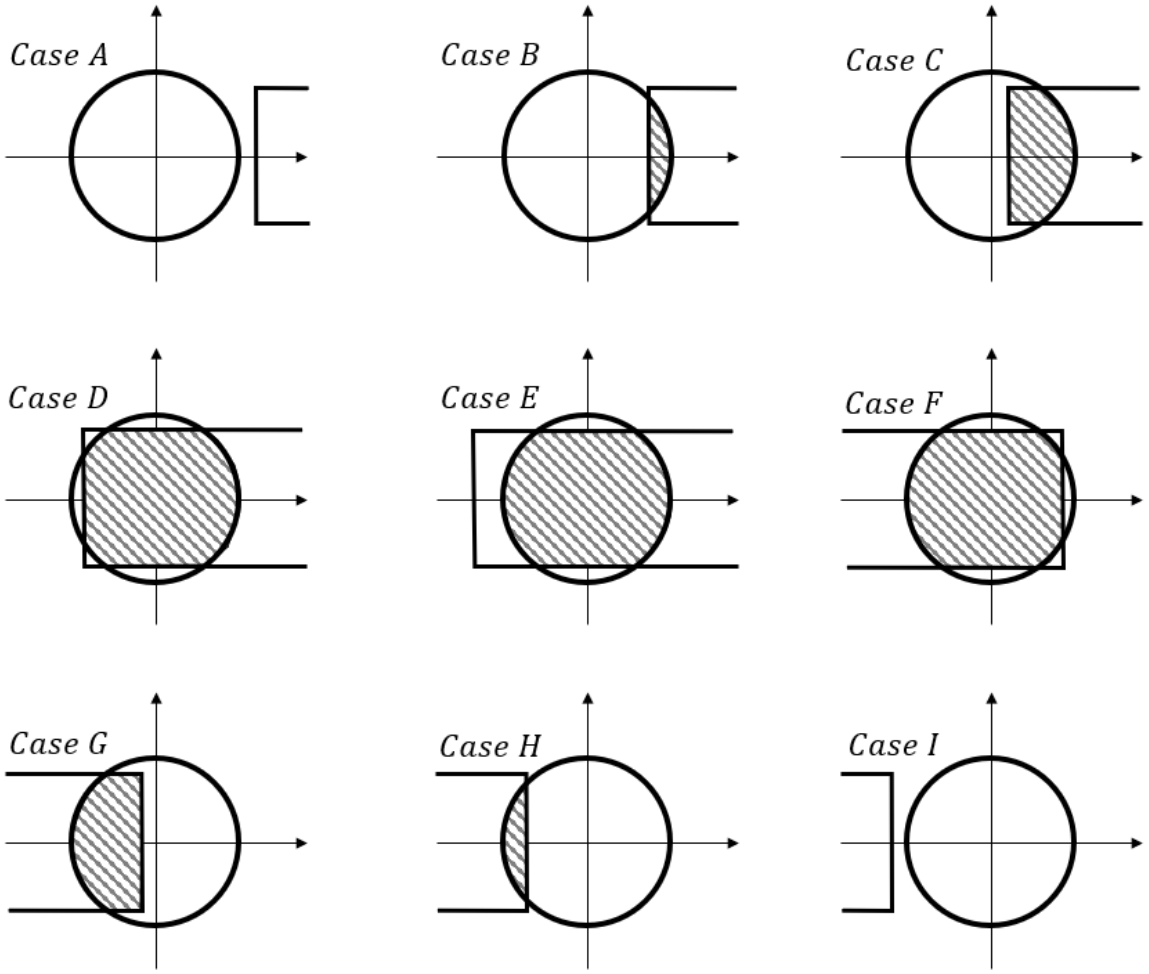

FIGURE B.5: VALVE CYLINDER AND MAIN PORT INTERSECTION CASES

The integral for the area under a circle is given in eq. (B.8) and for under the main port, eq. (B.14) is used.

$$\int_a^b \frac{1}{2} W_{port}\, dx = \frac{1}{2} W_{port}(b-a) \tag{B.14}$$

The last geometric feature that the valve intersects with is the closing ramp. Repeating the procedure, the geometry is shown in Figure B.6 with the valve again shifted to the origin of the local reference frame and x_L and x_R defining the left and right position of the port ramp.

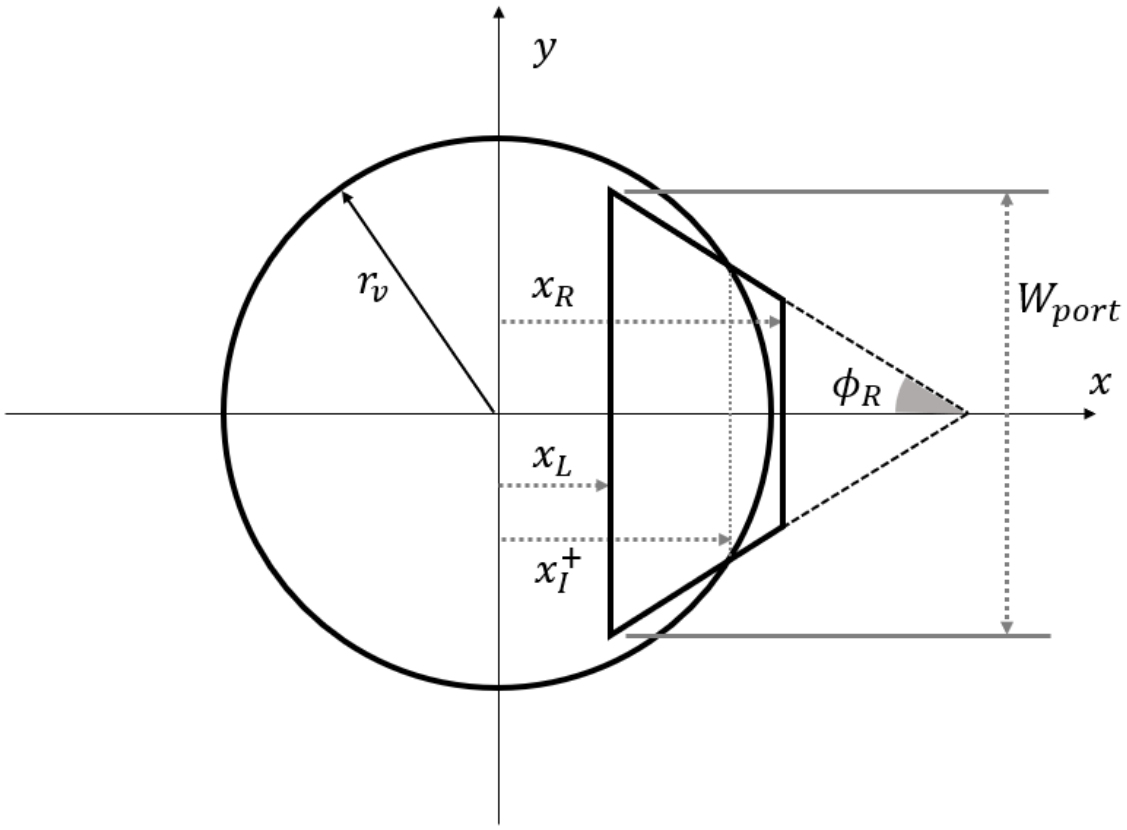

FIGURE B.6: VALVE CYLINDER INTERSECTING CLOSING RAMP

Utilizing this local reference frame, the circle and the main port equations are given in (B.15) and (B.16), respectively.

$$y_{circle} = \sqrt{r_v^2 - x^2} \tag{B.15}$$

$$y_{ramp} = (x_{int} - x)\tan\phi_R \tag{B.16}$$

where x_{int} is the x-intercept of the function.

$$x_{int} = x_L + x_{base} \tag{B.17}$$

where x_{base} is the total length of the port ramp triangle.

$$x_{base} = \frac{1}{2}\frac{W_{port}}{\tan\phi_R} \tag{B.18}$$

Setting eq. (B.15) and (B.16) equal to each other allows the x-value for the intersection of the port ramp and the valve to be calculated, eq. (B.19).

$$\sqrt{r_v^2 - x^2} = (x_{int} - x)\tan\phi_R$$

$$0 = (1 + \tan^2\phi_R)x^2 + (-2x_{int}\tan^2\phi_R)x + \left(x_{int}^2\tan^2\phi_R - r_v^2\right)$$

$$x_I^+, x_I^- = \frac{2x_{int}\tan^2\phi_R \pm \sqrt{4x_{int}^2\tan^4\phi_R - 4(1+\tan^2\phi_R)\left(x_{int}^2\tan^2\phi_R - r_v^2\right)}}{2(1+\tan^2\phi_R)} \tag{B.19}$$

This information allows a piece-wise definition for the area profile, eq. (B.20), to be established. Each bound of the piece-wise function corresponds to a case from Figure B.7.

$$A(x) = \begin{cases} 0 & \text{Case A: } r_v < x_L \\ \displaystyle\int_{x_L}^{r_v} \sqrt{r_v^2 - x^2}\,dx & \text{Case B: } x_I^+ < x_L < r_v \\ \displaystyle\int_{x_L}^{x_I^+} (x_{int} - x)\tan\phi_R\,dx + \int_{x_I^+}^{r_v} \sqrt{r_v^2 - x^2}\,dx & \text{Case C: } x_I^- < x_L < x_I^+ < r_v \\ \displaystyle\int_{x_L}^{x_I^+} (x_{int} - x)\tan\phi_R\,dx + \int_{x_I^+}^{x_R} \sqrt{r_v^2 - x^2}\,dx & \text{Case D: } x_I^- < x_L < x_I^+ < x_R \\ \displaystyle\int_{x_L}^{x_R} (x_{int} - x)\tan\phi_R\,dx & \text{Case E: } x_I^- < x_L < x_R < x_I^+ \\ \displaystyle\int_{x_L}^{x_I^-} \sqrt{r_v^2 - x^2}\,dx + \int_{x_I^-}^{x_R} (x_{int} - x)\tan\phi_R\,dx & \text{Case F: } -r_v < x_L < x_I^- < x_R \\ \displaystyle\int_{-r_v}^{x_I^-} \sqrt{r_v^2 - x^2}\,dx + \int_{x_I^-}^{x_R} (x_{int} - x)\tan\phi_R\,dx & \text{Case G: } -r_v < x_I^- < x_R \\ \displaystyle\int_{-r_v}^{x_R} \sqrt{r_v^2 - x^2}\,dx & \text{Case H: } -r_v < x_R < x_I^- \\ 0 & \text{Case I: } x_R < -r_v \end{cases} \tag{B.20}$$

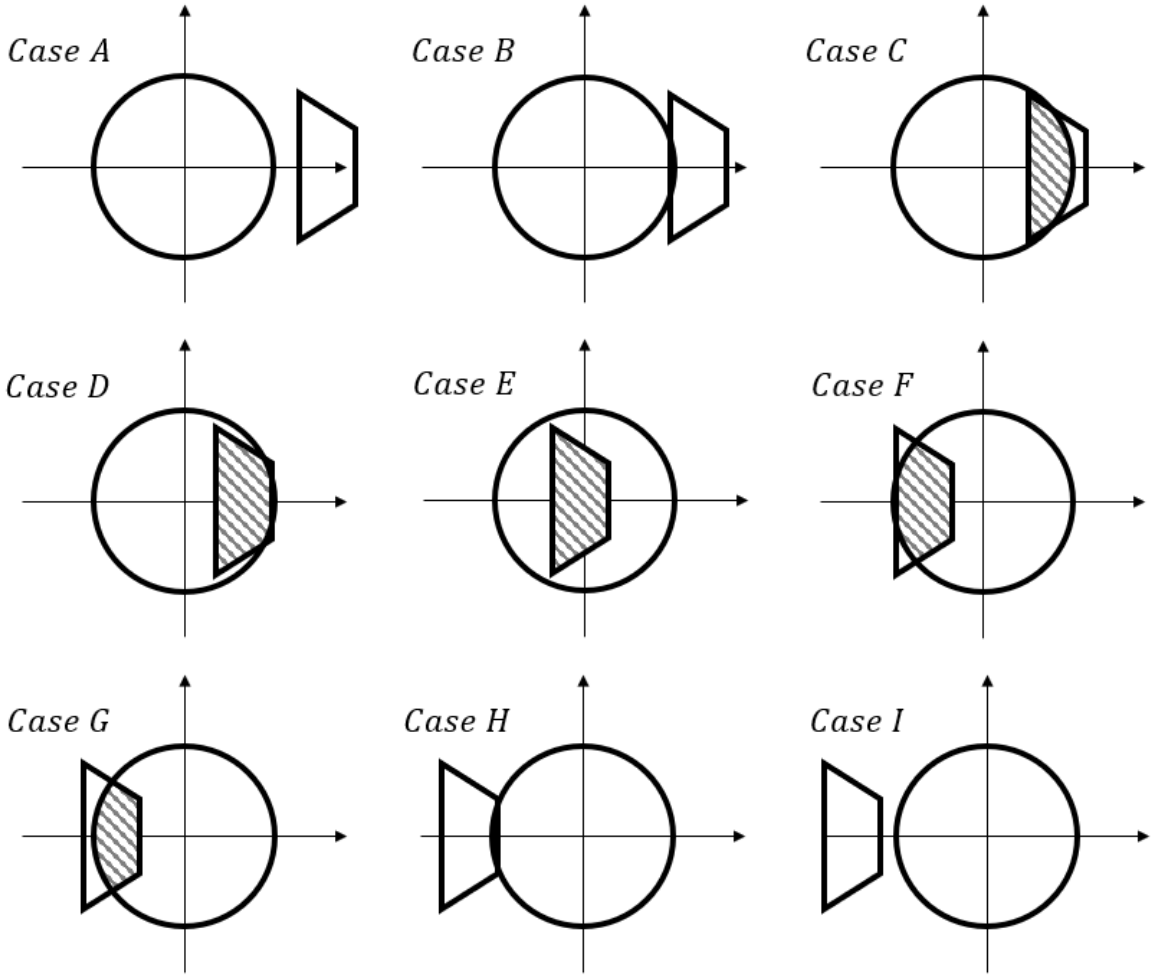

FIGURE B.7: VALVE CYLINDER AND CLOSING RAMP INTERSECTION CASES

The integral for the area under a circle is given in eq. (B.8) and for under the closing ramp, eq. (B.21) is used.

$$\int_a^b (x_{int} - x) \tan \phi_R \, dx = \tan \phi_R \left[x_{int} \cdot b - \frac{b^2}{2} - x_{int} \cdot a + \frac{a^2}{2} \right] \qquad \text{(B.21)}$$